HIGH-BRIGHTNESS PLASMA-BASED COMPTON BACKSCATTERING SOURCE FOR HIGH ENERGY PHYSICS

by

Paul Scherkl

A thesis presented for the degree of
Doctor of Philosophy in Physics

University of Strathclyde
Department of Physics

2019

SUPERVISORS:
Bernhard Hidding
Dino Jaroszynski

DECLARATION

This thesis is the result of the author's original research. It has been composed by the author and has not been previously submitted for examination which has led to the award of a degree.

Signed: Paul Scherkl
Date: November 11, 2019

To Vivian and Tom

" ..xcd vöä´´G h mzgn<zs "
T.O.M. Scherkl

ABSTRACT

Exciting, probing and manipulating the quantum states of nuclei is crucial to many scientific, industrial, medical and defence applications of high energy physics. Inverse Compton scattering (ICS) offers the necessary MeV-level photon energies along with highly directed and collimated pulse profiles. However, respective facilities are scarce as the large underlying particle accelerators cause high costs. Plasma accelerators, in contrast, offer orders of magnitude higher accelerating fields and can operate sensibly priced in considerably smaller laboratories. State-of-the-art experiments have routinely shown generation of dense electron beams suitable for MeV-photon pulses with extremely high peak brilliance. Yet, plasma accelerators suffer from large energy spread and emittance that cause spectral broadening impractical for many nuclear applications.

This work investigates the prospects of plasma photocathode wakefield accelerators generating low-emittance, high-quality electron beams for ICS. An important component is the experimental demonstration of a novel, plasma-based diagnostic for spatiotemporal synchronisation and alignment of electron and laser beams. This multi-shot method yields absolute time-of-arrival accuracy of ~$16\,\mathrm{fs}$ and alignment accuracy of $4\,\mu\mathrm{m}$. It has facilitated the word's first experimental realisation of a plasma photocathode and the plasma torch injection method. These experiments represent milestones towards highest-quality electron beam production, and are fundamental to plasma-based generation of brilliant, narrow-bandwidth and MeV-level γ-ray sources. Extensive simulations investigate their production and reveal unprecedented single-shot peak brilliance of ~1×10^{25} photons $\mathrm{s}^{-1}\ \mathrm{mm}^{-2}\ \mathrm{mrad}^{-2}\ 0.1\%\mathrm{BW}$ at $0.4\,\mathrm{MeV}$ to $9\,\mathrm{MeV}$.

This work further outlines the generation of inherently synchronised and brilliant γ-ray pairs, which constitute temporally and spectrally fully separable multi-colour radiation. The underlying effect can further minimise electron beam energy spread. This is shown to shrink the relative γ-ray bandwidth to $2.3\,\%$ at $2.4\,\mathrm{MeV}$, and overcomes one of the major problems in plasma accelerators and ICS sources. Each part of this work advances its respective research area, yet combined they promise the highest-quality photon sources for nuclear physics applications.

ACKNOWLEDGEMENTS

Great people have accompanied and encouraged me during the course of this work in very different aspects.

First of all, I'd like to bring my excellent supervision by Bernhard Hidding into prominence. Working with him has substantially amplified my scientific and professional abilities. These lessons were always accompanied by challenging, exciting and occasionally baffling activities, which gifted me with extremely comprehensive experiences in various situations. I particularly give thanks to his commitment for grooming all of his students throughout.
I'd also like to thank Dino Jaroszynski for being my second supervisor, for his support and interesting discussions during vivas and in stressing publication processes.

The experimental E-210 campaign at FACET has been one of the most exciting – and exhausting – ventures during my studies. Only by great mutual endeavour this campaign could be brought to a satisfying and successful end. I therefore thank everyone involved in this project. Specifically, Oliver Karger, Alexander Knetsch, Thomas Heinemann and Aihua Deng grew to a dedicated team I still appreciate to have worked with.

In the succeeding period, my team in Glasgow turned out to consist of likewise dedicated and awesome fellows and friends. I give special thanks to Fahim Habib, Thomas Heinemann, Grace Manahan, Daniel Ullmann and Andrew Beaton for great cooperation, discussions and leisure times during and after work. I further thank Andrew Sutherland and Panos Delinikolas.

I express special thanks to SUPA, the Scottish Universities Physics Alliance, for funding of my PhD and various travels, internships and conferences.

Most of all, I express my highest gratitude to Vivian, who extraordinarily supported me during the whole time of my studies.

PUBLICATIONS

The author has produced or contributed to the following publications during this study:

[1] Paul Scherkl et al. "Plasma-photonic spatiotemporal synchronization of relativistic electron and laser beams." In: (Aug. 2019). arXiv: `1908.09263`.

[2] Ahmad Fahim Habib et al. "Plasma accelerator-based ultrabright x-ray beams from ultrabright electron beams." In: *Proc. SPIE* 11110.September (2019). DOI: `10.1117/12.2530976`.

[3] Aihua Deng et al. "Generation and acceleration of electron bunches from a plasma photocathode." In: *Nature Physics* (Nov. 2019). DOI: `10.1038/s41567-019-0610-9`.

[4] Bernhard Hidding et al. "Fundamentals and applications of hybrid LWFA-PWFA." In: *Applied Sciences (Switzerland)* 9.13 (June 2019). ISSN: 20763417. DOI: `10.3390/app9132626`.

[5] Grace G. Manahan et al. "Advanced schemes for underdense plasma photocathode wakefield accelerators : pathways towards ultrahigh brightness electron beams." In: *Phil. Trans. R. Soc. A* 20180182 (2019).

[6] Bernhard Hidding et al. "First Measurements of Trojan Horse Injection in a Plasma Wakefield Accelerator." In: *Proceedings of IPAC2017* TUYB1 (2017).

[7] Grace G. Manahan et al. "Single-stage plasma-based correlated energy spread compensation for ultrahigh 6D brightness electron beams." In: *Nature Communications* 8 (2017), p. 15705. ISSN: 2041-1723. DOI: `10.1038/ncomms15705`.

[8] Paul A. Walker et al. "Horizon 2020 EuPRAXIA design study." In: *Journal of Physics: Conference Series* 874 (2017), p. 012029. DOI: `10.1088/1742-6596/874/1/012029`.

CONTENTS

LIST OF FIGURES

1

INTRODUCTION

Investigating, manipulating and exploiting the quantum states of nuclei still represents a major challenge of high energy physics. This is because of their excitation energies between $0.2\,MeV$ to $100\,MeV$, which significantly exceed all energy scales known from electronic states in atoms by orders of magnitude. Generating photon pulses, e.g. γ-rays, of such high energy naturally causes problems, as inversion required by the laser principle can not be maintained and optics suitable for MeV-class radiation do not exist. Other sources for γ-rays such as fission of radioisotopes do not provide sufficiently high radiation quality, and their properties can neither be controlled nor tuned.

As a consequence, γ-ray pulses tailored for professional applications are to be produced by different means. Exploiting fundamental electrodynamics, electric charges can be made to emit photons simply by applying accelerating forces to them. If these electrons, typically packed in dense bunches, move at relativistic velocities, this radiation is subject to Doppler blue shifts into the x-ray or γ-ray regime [1]. Famous examples are synchrotron radiation generated in circular accelerators, bremsstrahlung in solid targets or radiation caused by oscillating electrons. All of them offer different advantages and issues, but one mechanism particularly suits the generation of most energetic photons: *inverse Compton scattering* (ICS) [2, 3]. Here, an intense laser pulse interacts head-on with a relativistic bunch of electrons. In the reference frame of each electron, laser photons appear blue-shifted, and their interaction changes the energy and velocity states of both particles according to classical Compton scattering. In the laboratory frame, however, a second Doppler shift tremendously increases the energy of all interacting photons proportional to the electrons kinetic energy squared. The Doppler shift further scatters these photons into the electron beams propagation direction forming a directed and partially collimated pulse. Apart from the single-particle picture, the incident laser pulse can also be considered as electromagnetic undulator imposing oscillations on ambient electrons [4]. If the electron experiences negligible recoil in its rest frame, this process represents the low-energy limit of Compton scattering and is referred to as *Thomson backscattering*. In this work, ICS stands synonymously for Thomson backscattering, according to partially indistinct phrasing in literature. Furthermore, only linear interactions are considered, e.g. one electron and one photon in contrast to multiple photons simultaneously scattering off the same electron.

As direct consequence of the generation mechanism, ICS offers a straightforward way for transferring moderate electron energies into hard γ-rays. Combined with directional, collimated and pulsed properties, ICS sources provide high peak brilliance corresponding to homogeneous illumination of any target at high photon flux. Applications well-suited for this kind of radiation are, among others, radioisotope production for medical applications [5], photo fission experiments [6] and, particularly, nuclear resonance fluorescence [7–12]. The latter probes nuclear states of matter, and as such generates characteristic responses for specific materials and isotopes. Machines capable of producing suitable photon pulses facilitate *isotopic assay and detection of materials, an application that spans the domains of non-destructive evaluation, homeland security, nuclear waste assay, stockpile stewardship or mining* [12]. ICS radiation is therefore highly interesting for research, industry, as well as military and civil usage of nuclear materials. Requirements are, next to high photon energy, maximal photon flux and brilliance along with narrow, e.g. sub-2 %[11, 12], spectral distribution for sufficiently high signal-to-noise ratio.

Providing this combination remains a challenging aspiration. The very generation of MeV-level photons relies on electrons with kinetic energies in the range of hundreds of MeV up to GeV, which inevitably requires particle accelerators. Most ICS sources realised so far employ accelerator technology involving radio-frequency cavities. Famous facilities are SLAC [13], PLEIADES [14, 15], HIγs [16, 17], SPARC_LAB [18], or the ELI-NP facility [19, 20] being constructed. These sources currently deliver highest photon energies and by far highest average photon flux and brilliance. Commonly, the ICS bandwidth in these schemes is limited via collimators with variable acceptance angles, and can be lower than 2 %. Yet, the *conventional* particle accelerator technology takes a lot of space such that large laboratories are required. This, naturally, drives the overall costs to the level of hundreds of millions or even billions of £, limits the number of dedicated facilities and their availability. Beam time is therefore valuable and rare, such that only high-priority research and development (R&D) by science and industry can be supported.

Miniaturisation of particle accelerators is one of the major drivers of plasma-based accelerator technology [21–23]. The plasma medium can sustain accelerating electric fields orders of magnitude higher than radio-frequency cavities such that the required space shrinks dramatically along with the costs. Being linear accelerators, plasma-based schemes avoid significant energy loss due to synchrotron radiation known from circular accelerators, and might therefore be candidates for a plasma-based version of the international linear collider approach [24]. ICS sources, fortunately, require substantially less electron energy and have already been realised experimentally by a variety of groups [4, 9, 25–36]. These experiments routinely generate ~100 MeV up to 10GeV electron beams in ultra-compact accelerators, and have produced *quasi-monoenergetic* γ-ray pulses with spectral relative bandwidth between 10 % to 100 %. Due to the immense electron beam charge density and small dimensions, the radiation inherently provides high peak-brilliance per shot. However, the low average brilliance, poor shot-to-shot reproducibility and large spectral bandwidth –deteriorated by large electron beam energy spread and emittance– do not yet suffice for most applications [11, 12, 37]. Worldwide, many groups and collaborations such as at FACET [38, 39] or EUPRAXIA [40] therefore work on further improving plasma-based accelerator technology towards industrial quality.

The *underdense plasma photocathode wakefield accelerator* concept [41], also termed *Trojan Horse*, combines the high accelerating fields typical for plasma accelerators with substantially concentrated electron beam phase spaces. Consequently, these beams inherit ultra-low emittance and promise photon pulses of similar energy as other plasma-based techniques, but even higher brilliance and substantially reduced bandwidth. This thesis investigates the capabilities of inverse Compton scattering off electron beams generated via the plasma photocathode approach. Inspired by the promised electron beam quality, this study aims at generation of brilliant γ-ray pulses with energies of the order of 1 MeV to 10 MeV and relative bandwidth below 10 % without any collimating acceptance.

As the ICS pulse properties are primarily defined by the electron beam, the first part of this work begins with introducing fundamental plasma parameters and presents different ways of producing this state of matter. This chapter is succeeded by thorough discussions of plasma wakefield acceleration, focusing on energy gain and quality-related aspects of plasma wakefield accelerated electron beams. The subsequent chapter introduces the most relevant parametric dependencies of the ICS mechanism. Finally, the most relevant computational methods applied in this work are outlined.

The second part of this work presents the development of integral technologies required for potential realisation of such a radiation source. First, a novel plasma-based approach for diagnosing the spatiotemporal coincidence of intense electron and laser beams is investigated. It has been successfully applied experimentally and represents a key-capability for ICS sources: ensuring that the scattering laser actually hits the electron beam. This technique furthermore can be applied in many other scenarios involving electron beams and laser pulses. One of these is the world's first experimental realisation of a plasma photocathode wakefield accelerator following in a dedicated chapter. The spatiotemporal diagnostic has provided the required information that facilitates laser-triggered generation of electrons directly inside a plasma wave. This experimental result further encourages the beneficial combination of plasma photocathodes and ICS shown in the last chapter. There, different aspects and schemes outline the considerable synergies between these mechanisms, including the generation of tunable multi-colour radiation with high brilliance in the MeV-regime. Strategies and techniques for minimised spectral bandwidth are presented by means of exemplary simulations and close this work. Finally, the results obtained during this work are summarised and discussed along with an outlook sketching the path towards brilliant, narrow bandwidth γ-rays produced in compact and accessible laboratories.

Part I

THEORETICAL FOUNDATIONS

Before discussing the studies and results this work consists of, their fundamental theoretical background must be established such that the interested reader understands the most relevant effects and connections between them. This first part introduces the very basics of plasma physics, important quantities of collective behaviour, together with the generation and recombination of plasma. Those topics are fundamental to plasma electron acceleration techniques. These represent the core technology in this work and their characteristics, advantages and problems are thoroughly discussed. Generation and acceleration of high-quality electron beams by a plasma photocathode is shown and linked to the physics of inverse Compton scattering. For the latter, strategies for creation of brilliant gamma ray pulses are outlined. This part closes with a short overview of methods applied in this work.

2

FOUNDATIONS OF PLASMA

In comparison with the well-know states of matter –namely solids, liquids and gases– the fourth state called *plasma* exhibits unique and most fascinating properties. This more exotic substance consists of charged particles, e.g. mobile electrons and ions, which normally balance their electric charges [42]. As such, the plasma becomes quasi-neutral and the combined net charge density ρ is small compared to those of electronic or ionic constituents individually. As a consequence of the simultaneous presence of these charge carriers, plasma particles can react collectively to any (external) perturbation and Maxwell's equations determine their behaviour.

The first sections introduce the most relevant plasma parameters in this work: plasma oscillations and Debye shielding. These collective phenomena are succeeded by an excerpt describing important processes for plasma generation. An overview of different channels for ending this exotic state after its lifetime lasting for the fraction of a second ends this chapter.

2.1 PROPERTIES OF PLASMA

2.1.1 *Plasma Oscillations*

Perturbations of plasma, caused by e.g. inserting or removing charged particles or by applying electromagnetic fields, commonly lead to local imbalances of charge density and evoke strong electric fields. Those counteract the perturbation by accelerating and displacing electrons and ions, which consequently excites collective oscillations. In the linear approximation of a cold unmagnetised plasma, the electronic *plasma frequency* [43] reads

$$\omega_p = \sqrt{\frac{n_e e^2}{\epsilon_0 m_e}}. \tag{2.1}$$

Here, n_e is the electron density, e the elementary charge, ϵ_0 is the the vacuum permittivity and m_e denotes the electron mass. In this study, the typical plasma electron density of $n_e \approx 1.1 \times 10^{23}\,\mathrm{m}^{-3}$ yields

$$\omega_p \approx 56.4 n_e^{1/2}\ \mathrm{Hz} \approx 1.9 \times 10^{13}\ \mathrm{Hz}. \tag{2.2}$$

The plasma frequency describes local harmonic oscillations of electrons (not propagating waves) and defines the characteristic timescale for electronic plasma effects: $\tau_p = 1/\omega_p \approx 53.5\,\mathrm{fs}$ for the exemplary density.

In the special case of plasma acceleration where a laser pulse or a relativistic particle beam drive a plasma wave, ambient plasma electrons oscillate locally at the plasma frequency. The plasma wave, however, inherits the phase velocity of the drive beam $v_b \approx c$ which is close to the speed of light c. As such, the propagation of the wave can be approximated in first order by means of the *plasma wave number* [44, 45]:

$$k_p = \frac{\omega_p}{v_b} \approx \frac{\omega_p}{c}. \tag{2.3}$$

Its inverse k_p^{-1} is called *skin depth* and, having the unit of length, represents a common normalization scale in underdense (see Section 3.1) plasma applications. In the linear plasma wave regime, the wave number in Eq. (2.3) defines the *plasma wavelength*

$$\lambda_p = \frac{2\pi}{k_p} = \frac{2\pi v_b}{\omega_p} \approx \frac{2\pi c}{\omega_p}. \tag{2.4}$$

In this study, typical plasma wavelengths are of the order of

$$\lambda_p \approx 3.3 \times 10^{13} n_e^{-1/2}\ \mu\mathrm{m} \approx 99.5\ \mu\mathrm{m}. \tag{2.5}$$

As a side note it should be mentioned that the scalings shown above consider homogeneous ionic charge density, e.g. the ions form a constant positively charged background. However, ions also perform plasma oscillations with their individual amplitude and frequency (e.g. by substituting n_e with the ion density $Z_i n_i$ and m_e with the ion mass m_i in Eq. (2.1)). Due to $m_i \geqslant 1863 m_e$, ions react much slower on perturbations than electrons and are commonly neglected. As most effects in the context of this study take place on the fast electronic time scale, the terms plasma frequency and wavelength always correspond to the electronic quantities. In addition, the terms plasma density and electron density are used synonymously.

2.1.2 *Debye Shielding*

As mentioned above, local perturbations of plasma charge density, e.g. from inserting a test charge into a neutral plasma, excite fast oscillations. On time scales much longer than $\tau_p = 1/\omega_p$, however, these oscillations cease and the plasma adapts to the perturbation: its constituents rearrange due to Coulomb interactions and shield the potential $\Phi_0(r)$ of the perturbation. This *Debye shielding* or screening scales like $\Phi(r) = \Phi_0(r)e^{-r/\lambda_D}$ compared to the electrostatic potential that follows $\Phi_{vac}(r) = \Phi_0(r)/r$, and the corresponding 1/e range is known as *Debye length* [46]

$$\lambda_D = \sqrt{\frac{\epsilon_0 k_B T}{n_e e^2}}, \tag{2.6}$$

where k_B is Boltzmann's constant and T is the temperature of the electronic component of the plasma. Due to this screening the plasma appears to be quasi-neutral at distances much larger than λ_D, strongly confining the perturbations potential. In this work, any unperturbed plasma fulfils two conditions: First, the spatial extent of the plasma is much larger than λ_D ensuring quasi-neutrality. Second, any sphere of radius λ_D contains many particles (e.g. the *plasma parameter* $N_D = \frac{4}{3}\pi n_e \lambda_D^3 \gg 1$), meaning that all particles in this volume interact with –and react to– each other. A plasma in this configuration is called weakly coupled and its interaction is governed by collective Coulomb interactions instead of binary collisions where $N_D \ll 1$.

2.2 GENERATION AND RECOMBINATION OF PLASMA

Any plasma represents an ensemble of charged particles, and its generation requires at least partial *ionisation* of atoms or molecules. This paragraph outlines two very different methods to systematically generate plasma. Both underlying effects can ionise matter spatially controlled and even material-selective, and facilitate various most interesting applications as shown during the course of this study.

2.2.1 *Optical ionisation*

The probably most familiar approach for ionisation relies on the interaction of matter with electromagnetic radiation. This interplay can excite of one or multiple electrons from their bound states –characterised by their binding or ionisation potential

$|\xi_i|$– into unbound or continuous states of motion. In the research area focused on plasma acceleration, the radiation typically originates from laser systems capable of ionising large volumes of gas or solids. The laser field inherits a ponderomotive potential $U_p = e^2 E_0^2/(4 m_e \omega_l^2)$ and provides photons of energy $E_l = \hbar\omega_l$ and frequency ω_l. Here, E_0 corresponds to the electric field amplitude of the laser and $\hbar$ denotes Planck's reduced constant. U_p is the averaged quiver energy of an electron within an electromagnetic field oscillating with frequency ω_l.

Both the field and individual or multiple photons can cause ionisation and *Keldysh's adiabaticity parameter* [47]

$$\gamma_K = \sqrt{\frac{|\xi_i|}{2U_p}} \tag{2.7}$$

identifies the dominant effect in each individual application. Discussing the limits of this parameter differentiates individual advantages and disadvantages of the different regimes of optical ionisation, e.g. following [48].

The case where $\gamma_K \gg 1$ describes the well-known *photoionisation* of single atoms by single or multiple photons. For $E_l \geqslant |\xi_i|$, a single photon provides the energy required for ionisation. This intuitive textbook example, however, leads to significant problems in some practical applications if the electrons to be removed from their atoms are tightly bound. For example, hydrogen and helium are widely used in plasma accelerators and their ionisation requires 13.6 eV (~91 nm photons, atomic hydrogen) or 24.6 eV (~50 nm photons) corresponding to extreme ultra-violet radiation. Powerful laser systems in this range do not exist and radiation sources rely on (inefficient) higher harmonic generation or already existing plasma sources. Other materials used in plasma acceleration such as alkali metals can be disintegrated by single photon ionisation, and corresponding laser systems exist. However, these materials often inherit their individual problems such as explosive behaviour (e.g. see [49]). The other photon-related effect, where $|\xi_i| > E_l$, requires *multiple photons* to coincide and deposit their energy into a single atom. This non-linear effect [50] depends on the frequency and intensity I of the incoming photon distribution, and the ionisation probability P scales strongly with the number of participating photons N: $P \propto I^N$. This effect can efficiently be triggered by current laser systems, which easily provide 100-TW-scale power levels. Both single- and multiphoton ionisation are outlined in Fig. 2.1.

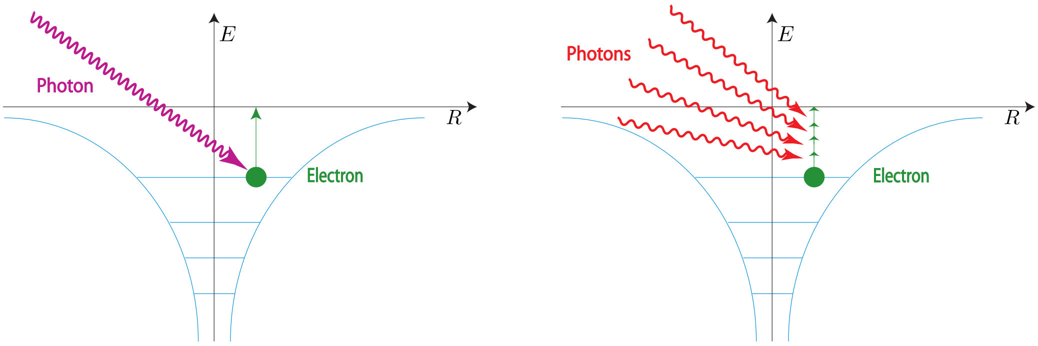

(a) Single-photon ionisation

(b) Multi-photon ionisation

Figure 2.1: **Comparison of ionisation by single and multiple photons. (a)** Ionisation of an atom by a single photon. The latter provides at least the energy to remove the electron from its bound state.**(b)** Multiple low-energetic photons coincide within short time at the atom and mutually provide the energy to release the electron from its bound state. Figures taken from [51].

The most intense laser systems, however, reliably ionise most materials based on a very different effect. In this regime $\gamma_K \ll 1$, meaning that the strong ponderomotive potential of the laser field overwhelms the binding potential $|\xi_i|$. In the limit where the electric component of the laser field reaches the critical value $E_{crit} = |\xi_i|^2/4Z_i$ with Z_i being the ionic charge of the nucleus, the binding potential diminishes such that the electron classically leaves the atom. This process shown in Fig. 2.2 is called *Barrier-Suppression-Ionisation* [52] (BSI) and becomes dominant for intensities larger than

$$I_{BSI} = \frac{1}{2} n c \epsilon_0 E_{crit}^2 = \frac{|\xi_i|^4}{16Z^2}, \tag{2.8}$$

with refractive index n, which yields

$$I_{BSI} \approx 4 \times 10^9 \frac{|\xi_i|^4 (eV)}{Z^2} (W\ cm^{-2}). \tag{2.9}$$

For the first level of hydrogen, $I_{BSI} \approx 10^{14}\ W\ cm^{-2}$. At these intensities, released electrons immediately interact with the laser pulse and get accelerated, which leads to hot plasma particles and, for even higher intensities, to propagating plasma density waves. Being a feature for laser-driven wakefield acceleration (LWFA), where the laser instantaneously removes many up to all electrons from the target material and partially accelerates them, this behaviour that can be disadvantageous for applications trying to selectively ionise specific electronic levels or relying on cold, static plasma distributions.

Finally, the optical ionisation process most relevant in this study is called *tunnelling ionisation*. Here, the field amplitude is smaller than the ionisation potential, e.g. $\gamma_K < 1$, but still represents a substantial fraction. The laser field, therefore, reduces the effective binding potential for electrons without compensating it completely and consequently increases the probability of electrons tunnelling through the remaining potential wall (e.g. see Fig. 2.2). If $E_l \ll |\xi_i|$ [52], the corresponding ionisation rate can be described semi-classically by averaging the field over one laser oscillation as done in the widely-used *ADK theory* [53]. It requires the tunnelling time, related to the orbital frequency of the electron, to be faster than the oscillation of the laser field allowing for adiabatic treatment [54]. This theory can be approximated in practical units to describe the rate in which valence electrons are released from their atoms [55]

$$\begin{aligned} W_{ADK} \approx 1.52 \times 10^{15} \frac{4^{n^*}|\xi_i|(\mathrm{eV})}{n^*\Gamma(2n^*)} \left(20.5 \frac{|\xi_i|^{3/2}(\mathrm{eV})}{E_o(\mathrm{GV\ m^{-1}})}\right)^{2n^*-1} \\ \times \exp\left(-6.83 \frac{|\xi_i|^{3/2}(\mathrm{eV})}{E_o(\mathrm{GV\ m^{-1}})}\right) \end{aligned} \tag{2.10}$$

using the gamma function Γ and the effective principal quantum number for the considered ground state of an atom or ion $n^* \approx 3.69 Z |\xi_i|^{-1/2}(\mathrm{eV})$. This formalism is valid as long as the field amplitude does not exceed $E = \left(\sqrt{2}-1\right) E_a \left(|\xi_i|(\mathrm{eV})/27.2\ \mathrm{eV}\right)^{3/2}$ [54, 55], which marks the transition to the BSI regime. Here, $E_a = (4\pi\epsilon_0)^{-3}\, m_e^2 e^5/\hbar^4 \approx 5.14 \times 10^{11}\ \mathrm{V\ m^{-1}}$. Tunnelling ionisation most commonly releases valence electrons and, combined with low intensity just enough for reliable ionisation rates, allows for the precise generation of cold, quasi-static plasma distributions. For most gases or mixtures of gases with sufficiently separated binding energies, tunnelling ionisation can even address one specific kind of valence electrons to be ionised while keeping all others unperturbed (e.g see [41, 56] or Fig. 2.3 and Chapter 7). This effect is therefore suitable in applications demanding high precision and quality.

As a side note, the mechanisms of field ionisation presented above do not necessarily rely on the presence of a laser pulse. Other sources of strong electric fields, e.g. highly compressed electron beams, can also lead to substantial tunnelling ionisation quantified by Eq. (2.10). In regimes where tunnelling *and* multiphoton ionisation processes can happen simultaneously, e.g. $\gamma_K \approx 1$, the model proposed in [57] yields more accurate results than the ADK approach.

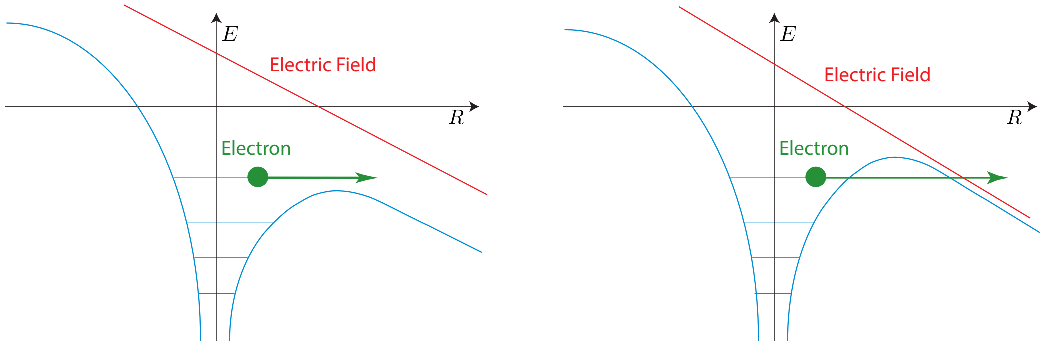

(a) Barrier suppresion ionisation (b) Tunnelling ionisation

Figure 2.2: **Comparison of field ionisation mechanisms (a)** An extremely strong external electric field acts on the binding potential of the atom and suppresses it for a sufficiently long time such that the initially bound electron can leave the atom classically. **(b)** A strong external electric field reduces the atoms binding potential such that the tunnelling probability for the electron increases substantially. Figures are modified version from [51].

In summary, many different approaches can generate plasma by optical means and the optimal one depends on the individual application and laser system available. Most of them, however, can be shaped and controlled by well-known and broadly applied techniques developed for optical sciences as done in the experiments presented in Chapters 6 and 7. Optical generation of plasma is therefore extremely versatile and broadly used in plasma-related science.

2.2.2 *Impact ionisation*

Collisions of one or multiple particles with atoms or molecules represents another important mechanism for the generation of plasma. This *impact ionisation* requires the incident particles to provide kinetic energy $W_{\text{kin}} > |\xi_i|$. The corresponding increase of density n_p can be described by a general rate equation for collision events [46]

$$\frac{dn_p}{dt} = n_i n_g \sigma_i v, \tag{2.11}$$

where an incoming electron or ion density distribution n_i moves with velocity v through the (gaseous) target with atom or molecule density n_g. The cross section σ_i as function of the kinetic energy (or velocity v) of the incoming particles represents the core of this interaction, being proportional to the statistical likelihood of ionising

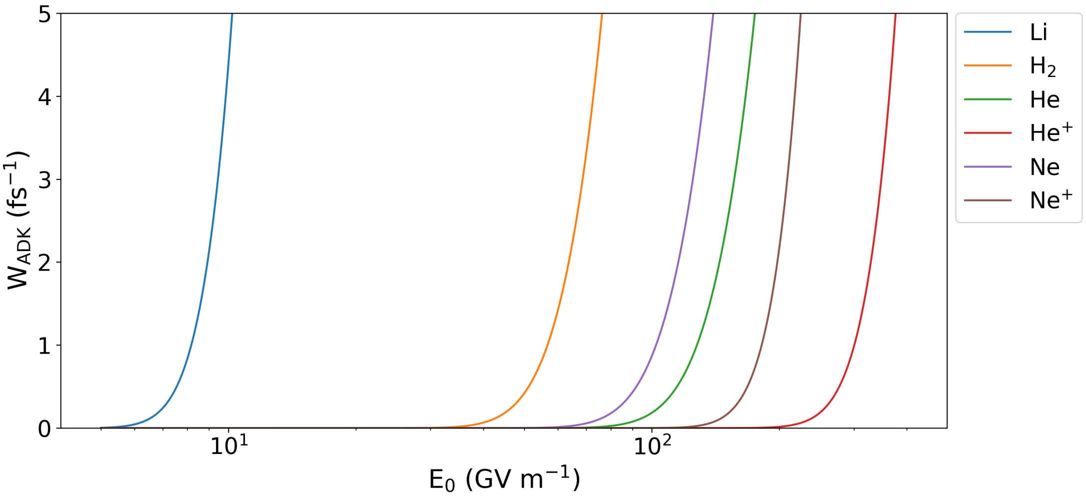

Figure 2.3: **Tunnelling ionisation rates for various gases.** Solving Eq. (2.10) for different gases reveals that each bound electron requires its individual range of peak electric fields E_0 to be ionised at sufficient rate. The lines are separated, which allows for species-selective ionisation of specific gases or ionisation levels, respectively, provided the electric field can be controlled sufficiently well.

scattering events. Using Eq. (2.11) and the generally good assumption of a Maxwell-Boltzmann-like plasma velocity distribution $f(v, T)$, the rate for releasing electrons bound in states of quantum number n reads

$$R_n = \frac{dn_p}{dt} = n_i n_g \int f(v, T)\sigma_{i,n}(v) v dv = n_i n_g \alpha_n(T). \tag{2.12}$$

The function $\alpha_n(T)$ denotes the ionisation coefficient with unit volume per time for the given ionisation level. For a complete description, the coefficients for all levels (all quantum numbers) must be calculated and their effects combined. Various approaches [58–62] for an adequate description of the functional dependency of σ_i and $\alpha(T)$ have been published, some of them being empirical scaling laws based on [63]. Their major problems arise from the huge range of energies available for incoming particles and their highly complex interplay with the targets electronic configuration, and thus some models agree with experimental data in very limited regimes, only. The work in [62] provides an empirical scaling that fits well to the experimental data obtained for electrons:

$$\sigma_i = \frac{8 r_0^2 \pi |\xi_{i,H}| A_1}{m_e c^2 \beta^2} f(\beta) \left(\ln \frac{2 A_2 m_e c^2 \beta^2 \gamma^2}{|\xi_{i,H}|} - \beta^2 \right). \tag{2.13}$$

This expression involves the Bohr radius $r_0 = 0.53 \times 10^{-10}$ m and the ionisation potential of atomic hydrogen $|\xi_{i,H}| = 13.6\,eV$ or Rydberg energy, and A_1 and A_2 are material-specific empirical constants. $\beta = v/c$ and $\gamma = (1-\beta^2)^{-1/2}$ describe the electron velocity and Lorentz or gamma factor, respectively. The function $f(\beta)$ corrects the low energy regime by fitting the data near the threshold where the kinetic energy of the incoming particles is close to the ionisation potential [46]. The corresponding cross sections for molecular hydrogen and helium are shown in Fig. 2.4. It may be noted that the velocity dependency in Eq. (2.11) describes two competing effects: faster particles encounter more atoms or molecules per time, but their cross section $\sigma_i(v)$ is substantially lower than for electrons with energy slightly above the ionisation potential.

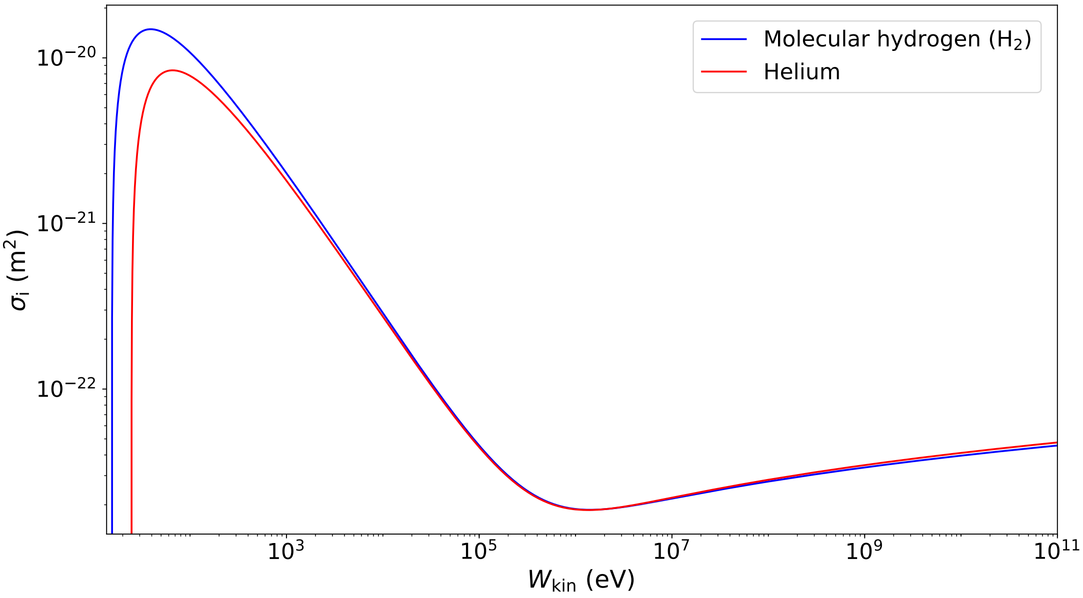

Figure 2.4: **Impact ionisation cross sections for electrons scattering off molecular hydrogen and helium gas based on Eq. (2.13) in a double-log plot.** Both curves peak at low energy (molecular hydrogen at ~39 eV and helium at ~66 eV) and rapidly drop until the keV-level. At elevated energies, the cross sections increase steadily. It may be noted that both curves differ particularly at low kinetic energy because of the strongly scaling β in Eq. (2.13). Above several hundred keV, both curves converge because of the increasing γ and saturating β.

Typically, impact ionisation generates plasma in electric discharge devices, which rely on currents propagating through gas to be ionised (e.g. as already done in the time of [64]). In the low-current regime, electric fields set up by external voltages accelerate randomly released electrons or ions, which then collide with ambient gas and create additional free charges experiencing the external field. This avalanche effectively creates more plasma, which can be exploited e.g. to excite the well-known colourful illumination in gas-discharge-lamps. Another, more vigorous approach directly delivers kA-level currents e.g. from large capacitors, which impact ionise gas targets and produce large-volume plasma. These strong discharges find application as waveguides for laser-driven [65–67] or beam-driven [68] wakefield acceleration or as plasma lenses [69, 70]. Having the advantage of easily producing voluminous plasma targets even of radial-symmetric shapes [65], discharge techniques lack the ability for large and controlled variations of the plasma extent or the density profile. Changing the targets geometry or profile commonly requires newly designed discharge devices. Further, the high voltage and current necessary for operation limit their applicability in sensitive experimental conditions and increase the risk for serious accidents. As a side note, discharges typically cannot address specific bound electrons for ionisation because of the current and subsequent avalanche. However, a distribution of low-energy particles can, in principle, selectively release electrons from their bound states.

2.2.3 *Recombination of Plasma*

Consisting of free charged particles restricts the lifetime of plasma substantially compared to the other states of matter. Particularly quasi-neutrality indicates that a balanced number of positively and negatively charged particles coexists, which eventually will re-form neutral atoms or molecules. This process is known as *recombination* and includes various microscopic effects [71]. Being the inverse effect of ionisation, recombination can be described by a formalism like Eq. (2.12). As the densities of ions and electrons are commonly of similar magnitude, this equation shows that recombination scales with approximately the electron density squared, while the temperature dependence is a feature of the individual ionic species and physical circumstances in the plasma.

The most prominent effect is radiative recombination

$$A^{+} + e^{-} \rightarrow A + \hbar\omega, \tag{2.14}$$

where an ion A^+ captures an electron e^- and forms a neutral atom A. Kinetic energy exceeding the binding energy is released as photon $\hbar\omega$. Similarly, another electron can absorb the excess energy in a process called three-body recombination:

$$A^+ + e^- + e^- \rightarrow A + e^-. \tag{2.15}$$

Other recombination modes include the dissociation of short-living molecules formed during the life time of the plasma into atoms [43, 72, 73], or the exchange of charges between anions and cations forming two neutral atoms. The dominating recombination channel depends on the individual cross section, which typically is a function of temperature, density and the ionic or atomic quantum-mechanical configuration [43]. It may be noted that the neutral atom resulting from any recombination process can embody bound electrons in excited states [74, 75], which eventually relax and emit photons in the material-specific, characteristic spectral lines. Together with the photons from radiative recombination, bremsstrahlung (in case of high electronic temperature) and other excitation/relaxation processes happening during the plasmas lifetime, this radiation constitutes the so-called *plasma afterglow*. This characteristic signal reveals valuable information of each individual plasma and has been investigated from the earliest days of plasma science, e.g. in plasma generated by cathode rays and arcs.

Recombination processes define the lifetime of plasma: as soon as they dominate the combined effect of all sources of ionisation, the number of plasma particles reduces until they form neutral gas again. The lifetime can be expressed roughly as $\tau_p \approx 1/n_e\alpha_{\text{total}}(T)$, with $\alpha_{\text{total}}(T)$ being the coefficient combining all recombination channels. This simple argument, however, becomes highly complex in a detailed analysis. For example, the complete plasma evolution between ionisation and recombination depends on the density and temperature of constituting particles, the individual properties of the ions involved, the presence of (external or internal) electromagnetic fields, collisions, various excitations, expansion and shock, etc. Therefore, the lifetime of plasma covers a huge range from hundreds of picoseconds up to milliseconds [75–79].

3

PLASMA WAKEFIELD ACCELERATION

Generally, particle accelerators rely on strong electric fields to transfer kinetic energy. Established machines, however, rely on chains of radio-frequency cavities that cannot support accelerating electric fields above approximately 100 MV m^{-1}. Their performance is limited due to heating resistance effects [80] and material-specific damage thresholds which can lead to breakdowns in their structure [81]. Higher fields can even ionise and substantially damage the structures integrity. In contrast, the unique nature of plasma, being an already ionised medium, allows it to sustain substantially higher field magnitudes. This property of plasma was identified as key feature for the miniaturisation of particle accelerators [21]. In the model of a one-dimensional (1D) cold plasma, the maximum field that can be sustained is the *cold non-relativistic wave breaking field*

$$E_{WB} = m_e c \omega_p / e \approx 96\sqrt{n_p(\mathrm{cm}^{-3})}\ \mathrm{V\ m^{-1}} \tag{3.1}$$

of the order of 10 GV m^{-1} for plasma density $n_p = n_e \approx 10^{16}\,\mathrm{cm}^{-3}$, which exceeds the fields in conventional accelerators by at least two orders of magnitude. Substantial parts of this study aim at realisation, optimisation and application of this new class of particle accelerators, with particular regard to the technique called *plasma wakefield acceleration* (PWFA) [22, 23]. In contrast to the intense *oscillating* pulses used in laser-driven wakefield acceleration (LWFA) with intensities of the order of $10^{18}\,W\,\mathrm{cm}^{-2}$ [21], PWFA applies the much weaker but *unipolar* transverse fields of relativistic dense electron beams for achieving very similar effects. Positron [82] and even proton [83] beams can similarly serve this purpose, but facilities providing sufficiently dense or short beams are extremely scarce, large and expensive such that these approaches remain highly exotic.

The following sections describe the mechanisms of particle acceleration through electron beam driven PWFA, starting with the excitation of plasma waves and many beneficial features resulting from their characteristic properties.

3.1 PLASMA WAVES

Inside plasma, strong electric fields suitable for acceleration of charged particles can occur if the electric potentials of electrons and ions don't equalise for a sufficiently long time. All plasma acceleration techniques deliberately achieve this state by introducing electron density perturbations δn_p and thereby generate their tremendous electric fields (e.g. see Eq. (3.1)) for the time scale given by some plasma oscillations ω_p. To eventually reach energies competitive with conventional accelerators, however, the bunches or beams of charged particles to be accelerated must experience these fields sufficiently long. Intense relativistic electron (or laser) *driving beams* modulating the electronic plasma component can provide these desired effects by excitation of *plasma density waves* [21–23]. These co-propagate with the driver at phase velocity $v_{ph} \approx c$ and take their associated electric fields along, similarly to the *wakefield* of a boat moving quickly in water. Ambient charged particles rapidly reaching or directly providing this velocity thus can stay inside the same phase of the plasma wave and, therefore, get accelerated over extended distances.

This section introduces the foundations of plasma waves excited by electron beams moving in z-direction through homogeneous plasma. For simplicity, these drive beams are modelled by a bi-Gaussian density distribution with longitudinal and radial root-mean-square (r.m.s.) dimensions σ_z and σ_r, respectively,

$$n_b(z, r) = n_{b,0} \exp\left(-\frac{(z - v_{ph}t)^2}{2\sigma_z^2}\right) \exp\left(-\frac{r^2}{2\sigma_r^2}\right) \tag{3.2}$$

with total charge Q and peak number density $n_{b,0} = Q/\left(e(2\pi)^{3/2}\sigma_z\sigma_r^2\right)$. Their radial electric field

$$E_b(z, r) = \frac{Q}{(2\pi)^{3/2}\sigma_z\epsilon_0 r}\left[1 - \exp\left(-\frac{r^2}{2\sigma_r^2}\right)\right] \exp\left(-\frac{(z - v_{ph}t)^2}{2\sigma_z^2}\right) \tag{3.3}$$

interacts with the plasma constituents, introduces a density perturbation δn_p and consequently sets up a trailing wakefield described by a pseudo potential ψ.

The following formalism normalises length scales to k_p^{-1} and applies the *quasi-static* [84] or *frozen-field* approximation by choosing the co-moving coordinate frame $\xi = z - v_{ph}t$. This approach implies that the drive beam does not evolve on the time scale τ_p of the plasma responding to its presence, e.g. $\partial_t n_p = -c\partial_\xi n_p$. In this case, the relevant properties of a plasma wakefield can be decoupled [44, 85] into the longitudinal electric field

$$E_\xi = -\frac{E_{WB}}{k_p}\partial_\xi \psi \tag{3.4}$$

and the transverse focusing force field

$$E_r - cB_\theta = -\frac{E_{WB}}{k_p}\partial_r \psi \tag{3.5}$$

consisting of the radial electric field E_r and the azimuthal magnetic field B_θ [86]. For conditions as expressed here, the Panofsky-Wenzel theorem [87] states that any transverse variations of the longitudinal force field equals the longitudinal variations of the transverse force field, e.g.

$$\partial_r e E_\xi = \partial_\xi e(E_r - cB_\theta). \tag{3.6}$$

It origins from the propagation of charged particles through accelerating structures with transverse boundaries such as radio-frequency cavities yet can be applied to the blowout regime. The expression links the transverse kick the particle receives during propagation with the accelerating field. Combined, Eqs. (3.4) to (3.6) are powerful relations and express the relevant physics inside plasma wakefields.

In analogy to the dispersion relation of electromagnetic waves of frequency ω_l in plasma which allows ($\omega_p/\omega_l < 1$) or prohibits ($\omega_p/\omega_l \geqslant 1$) penetration depending on the plasma density (e.g. see [45]), the interaction of electron beams with plasma can roughly be classified by means of the density ratio. If $n_b/n_p < 1$, the plasma is called *overdense* and the interaction is *linear*, whereas the term *underdense* corresponds to $n_b/n_p \geqslant 1$ and plasma waves exhibit substantially different and *nonlinear* behaviour. Another quantity called *normalised beam charge* [88]

$$\tilde{Q} = \frac{N_b k_p^3}{n_p} \tag{3.7}$$

can differentiate the degree of (non-)linearity in a beam-plasma interaction more precisely. It conveys the ratio of beam to plasma electron charge within a volume of cubic skin depth (e.g. see Eq. (2.3)) with N_b denoting the number of beam electrons. For $\tilde{Q} \ll 1$, the plasma response is *linear*. Increasing this parameter above unity also enhances the non-linearity until the *blowout* regime is reached. Both very different regimes are introduced and discussed subsequently.

3.1.1 *Linear Regime*

If the particle density n_b of the driving electron beam fulfils $n_b/n_p \ll 1$, it slightly disturbs the plasma density n_p. In this *overdense* interaction regime, the plasma responds linearly to the beam and the wake potential becomes $\psi \ll 1$. Adapting the formalism in [44, 89] for a particle beam with density distribution $f(\xi, r) = n_b(\xi, r)/n_p$, the wake potential reads

$$\psi(\xi, r) = -k_p \int_0^\infty d\xi' \sin(k_p(\xi - \xi'))f(\xi', r). \tag{3.8}$$

For a bi-Gaussian beam density distribution of magnitude $f_0 = n_{b,o}/n_p$

$$f(\xi, r) = f_0 \exp\left(-\frac{\xi^2}{2\sigma_z^2}\right) \exp\left(-\frac{r^2}{\sigma_r^2}\right) \tag{3.9}$$

the corresponding wake potential from solving Eq. (3.8) yields

$$\psi(\xi, r) = -k_p\sqrt{2\pi} f_0 \sigma_z \exp\left(-k_p^2\sigma_z^2\right) \sin(k_p\xi) \exp\left(-\frac{r^2}{2\sigma_r^2}\right). \tag{3.10}$$

This expression is valid for positions behind the rear of the drive beam, e.g. $\xi/\sigma_z \gg 1$. Combining this result with Eqs. (3.4) and (3.5) gives the longitudinal and transverse fields of the wake [44]:

$$E_\xi = k_p E_{WB}\sqrt{2\pi} f_0 \sigma_z \exp\left(-k_p^2\sigma_z^2\right) \cos(k_p\xi) \exp\left(-\frac{r^2}{2\sigma_r^2}\right) \tag{3.11}$$

and

$$E_r - cB_\theta = -\frac{r}{\sigma_r^2} E_{WB}\sqrt{2\pi} f_0 \sigma_z \exp\left(-k_p^2\sigma_z^2\right) \sin(k_p\xi) \exp\left(-\frac{r^2}{2\sigma_r^2}\right). \tag{3.12}$$

Consequently, the wake potential and the resulting fields of linear plasma waves exhibit simple oscillating behaviour with wavelength ~λ_p. Note that the density gets modulated in the *longitudinal* direction. From these two equations follows the maximum amplitude from setting $k_p\sigma_z = \sqrt{2}$ for fixed f_0. This is the *resonance condition* for linear wake fields. It may be noted that in common accelerators $f_0 \propto n_b(\sigma_z, \sigma_r)$

is a function of the beam dimensions, and higher beam density can lead to increased wake field amplitudes.

As mentioned above and as consequence of the overdense interaction, the electron beam represents a small perturbation to the plasma and thus partially displaces plasma electrons. In addition to exciting a linear density wave, plasma electrons can effectively mirror the beam charge in an adiabatic scenario, e.g. if the current rising time of the beam fulfils $\sigma_z/c \gg \tau_p$. This effect shields the expanding Coulomb or *space charge* self-field of the beam, but not the current and its associated magnetic field. Thus, the rear part of the beam interacting with this shielding plasma gets effectively compressed by this *overdense plasma lens* [**Lotov1996**, 86, 90].

3.1.2 *Blowout Regime*

In the other, highly nonlinear regime where $n_b/n_p \gg 1$, $\tilde{Q} \gg 1$ and $\sigma_z < \lambda_p$, the interaction between electron beam and plasma becomes more severe. The drive beam dominates this *underdense* interaction and its strong transverse electric fields originating from high charge density expel all plasma electrons *radially* away from its propagation axis [91]. As the ions remain nearly stationary during the characteristic time scales of the drive beam and ambient plasma electrons, the region behind the beams head forms a homogeneous ion channel. This positively charged region asserts tremendous restoring forces on the expelled electrons forcing them back to the central longitudinal axis of the system. In the co-moving coordinate system introduced above, these electrons form a dense *sheath* before they cross at the central axis. The thereby formed, closed structure is called *blowout* [92] and its fields substantially differ from the linear case. Due to their highly complex nature, the dynamics associated with the blowout regime are not yet completely described by analytical models. However, different phenomenological approaches [85, 93–95] exist and their predicted density and field distributions agree well with extensive simulations. Assuming a blowout with radial function $r_b(\xi)$ and maximal radius $R_{max} \gg k_p^{-1}$ moving with the speed of light and applying the quasi-static approximation, the wakefield potential reads [85]

$$\psi(\xi, r) \approx k_p^2 \frac{(r_b^2(\xi) - r^2)}{4}. \tag{3.13}$$

Combined with Eqs. (3.4) and (3.5), this potential defines the longitudinal and transverse fields inside the blowout:

$$E_\xi = \frac{k_p E_{WB}}{2} r_b(\xi) \partial_\xi r_b(\xi) \approx \frac{k_p E_{WB}}{2} \xi \tag{3.14}$$

and

$$E_r - cB_\theta \approx \frac{k_p E_{WB}}{2} r. \tag{3.15}$$

For the acceleration of charged particle beams, this set of fields provides almost ideal conditions. Generally, they scale linearly with their respective coordinate in good agreement between theory and simulation within the central region of the wake, e.g. compare Figs. 3.1 and 3.2. Linearity is a beneficial property for any physical application as it reduces complexity. Further, the longitudinal field and force $F_z = eE_\xi$, respectively, are independent of the transverse coordinate, and the transverse force component $F_r \approx e(E_r - cB_\theta)$ does not depend on the longitudinal coordinate. Referring to Eq. (3.6), $\partial_r eE_\xi = \partial_\xi e(E_r - cB_\theta) = 0$. Consequently, a test electron within the blowout regime will perform transverse harmonic *betatron oscillations*, while the longitudinal electric field accelerates the particle at constant rate irrespective of the transverse oscillations phase. Particularly, variations in the longitudinal field configuration do not change the transverse properties of the wake. A more careful discussion of these effects follows in Sections 3.2 and 3.3.

It may be noted that Eqs. (3.14) and (3.15) hold for the typical cases of spheric and elliptical cavity shapes as long as the drive beam expels all electrons. The exact cavity shape expressed by $r_b(\xi)$ is a function of the plasma density and its distribution as well as the drive beam particle density, current and form factor [85, 95].

Finally, the field amplitudes in nonlinear plasma waves can exceed the linear ones significantly. For example, the *1D cold relativistic wave breaking field* [45, 81]

$$E_{WB,rel} = \sqrt{2(\gamma_{ph} - 1)} E_{WB} \tag{3.16}$$

involves the gamma factor γ_{ph} associated with the plasma wake and can reach several 100 GV/m. Note that this value can differ from the fields in a three-dimensional (3D) blowout.

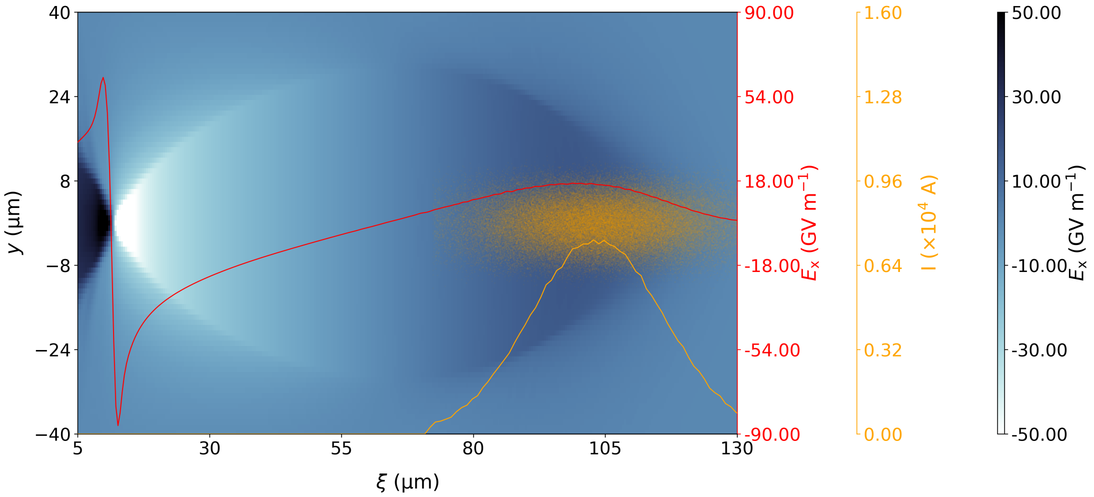

Figure 3.1: **Longitudinal electric field in a beam-driven blowout** Particle-in-cell simulation of a relativistic drive beam (orange dots) propagating in positive ξ-direction with energy $W_{\mathrm{kin}} \approx 10\,\mathrm{GeV}$ and charge density $n_b = 1.5 \times 10^{24}\,\mathrm{m}^{-3}$ drives a blowout in homogeneous plasma of density $n_p = 1.1 \times 10^{23}\,\mathrm{m}^{-3}$. This beam is transversally matched ($\epsilon_n = 100 \times 10^{-6}\,\mathrm{m\,rad}$ yielding $\sigma_{r,m} = 4.0\,\mu\mathrm{m}$ (r.m.s)), e.g. its envelope does not change during interaction with the plasma until all its energy is depleted. The beam duration $\sigma_z = 12.7\,\mu\mathrm{m}$ (r.m.s.) yields $k_p\sigma_z = 0.8$, which is slightly below the linear PWFA resonance condition. The orange line describes the beams current distribution. In the background, the central slice of the longitudinal electric wake field is shown, which acts decelerating (positive sign) for electrons at the drive beam position and accelerating (negative sign) in the rear of the wake. Its central, on-axis (e.g. at $y = x = 0\,\mu\mathrm{m}$) longitudinal electric field is plotted as red line. In the central region, the field scales linearly with the longitudinal coordinate in agreement with Eq. (3.14).

3.2 LONGITUDINAL DYNAMICS IN PWFA

Now that the fundamental properties of the blowout regime are established, the behaviour of electron beams inside this structure demands for a more detailed discussion. This section focuses on the longitudinal dynamics inside the wake field. Aside from the huge accelerating gradients being the major selling point for plasma accelerators, trapping of electron distributions inside the wake for subsequent acceleration and effects on the wake field caused by their presence are outlined.

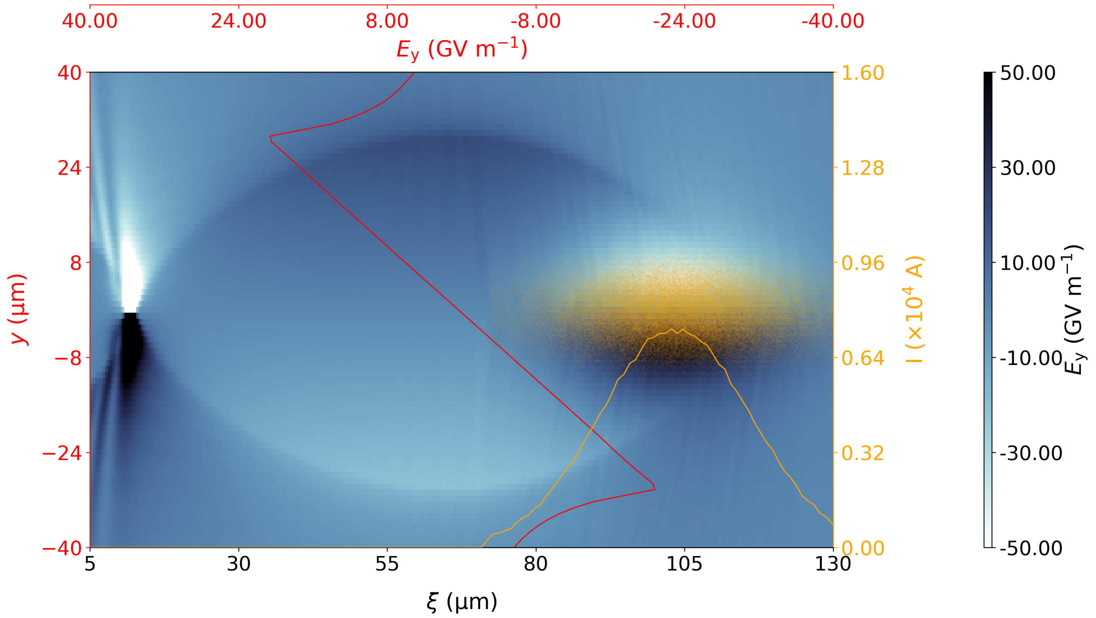

Figure 3.2: **Transverse electric field in a beam-driven blowout** This figure shows the electric fields y-component present in the simulation snapshot shown in Fig. 3.1. The red curve denotes the fields taken at $\xi = 63\,\mu m$, e.g. represents a vertical line approximately through the centre of the wake. In agreement with Eq. (3.15), the transverse field scales linearly with increasing distance from the central axis and therefore provides excellent focusing conditions for any electron distribution propagating inside the wake field.

3.2.1 *Deceleration and Acceleration*

By expelling plasma electrons and forming the blowout structure, the drive beam transfers its kinetic energy $W_{kin} = m_e c^2 \gamma_b$ successively into the plasma. The formalism of the longitudinal electric field in Eq. (3.14) expresses this behaviour by a positive sign of the field at the drive beam position with peak field E_- approximately at the centre of the beam. E_- yields the approximate rate at which this beam gets *decelerated* and defines the ultimate *depletion* length over which the drive beam can sustain a blowout, e.g. until all its kinetic energy is absorbed by the plasma [23]:

$$L_d = \frac{m_e c^2 \gamma_b}{e E_-}. \tag{3.17}$$

For typical relativistic drive beams, this quantity can be on the metre-scale and commonly represents a minor issue compared to transverse effects (e.g. see Section 3.3).

In the second half of the wakefield, however, the electric field switches sign as seen in Fig. 3.1 and becomes accelerating for negatively charged particles. This particular phase in the back can be exploited for example by accelerating the tail of a long drive beam [96] or a second *witness* beam, e.g. externally generated and trailing the drive beam [97, 98]. Similarly, this second beam can be generated right inside the wake as discussed in Section 3.2.2. Due to the almost identical velocities of drive and witness beam in the plasma accelerator (except for the duration of any trapping process described below), the witness beam stays in the same phase of the wake (e.g. does not *de-phase*) and gains energy at constant rate. Consequently, the drive beam transforms its energy via the plasma medium linearly with the acceleration length into the witness beam. A quantity describing the energy transfer effect is called *transformer ratio* [99, 100]

$$R = \frac{E_+}{E_-} \tag{3.18}$$

and represents the ratio between maximal accelerating field E_+ to the maximal decelerating field. This parameter also quantifies the ratio of the energy gain of the witness beam to the energy loss of the drive beam. R can maximally assume 2 for symmetric beams [101]. In the highly nonlinear blowout regime, R can exceed this value [23, 102]. It may be noted that due to conservation laws, the total energy absorbed by the witness cannot exceed the energy loss by the driver. Exploiting the maximal transformer ratio therefore requires the number of witness particles to be lower than $1/R$ times the particle number in the drive beam. In turn, the more witness particles are to be accelerated, the less energy can be gained by each particle. This effect tightly relates to *beam loading* (e.g. see Section 3.2.4). Similar to the linear regime, the duration of the drive beam can influence the amplitude of the accelerating field. It can be shown that [102] that the maximum field is achieved for a duration fulfilling $k_p \sigma_z = \sqrt{2}$.

3.2.2 *Trapping*

In order to exploit the deceleration-acceleration mechanism of the blowout regime, a population of charged particles (here we focus on electrons) termed *witness beam* must be injected into the blowout and rapidly reach or initially provide the phase velocity of the wake. This process is called *trapping*. Various methods for this purpose have been proposed, for both beams generated inside the wake or being injected externally, and [44, 45] provide a decent overview. Generally, trapped beams are few to tens of femtoseconds long and shorter than half the blowout length, e.g. $\sigma_z/c \ll \lambda_p/2$.

In the context of this work, a trapping mechanism associated to *ionisation injection* schemes is of crucial importance. Further, the general concept represents an excellent example to establish fundamental understanding. These techniques rely on at least one non-ionised atomic level (or even neutral gas with high ionisation threshold) to be present in the vicinity of the plasma wake, just expecting a source of ionisation for liberation of electrons. The formalism for trapping of these particles has been established for laser-driven plasma accelerators [103, 104] and pleasantly reduces in PWFA. It expresses the necessary condition of trapping, which requires a test particle inside the blowout to reach the wakes phase velocity before the wake passes by. In first order, this condition is expressed by [105]

$$\Delta\Psi_{\text{trap}} = \Psi(\xi_f) - \Psi(\xi_i) = m_e c^2/e. \tag{3.19}$$

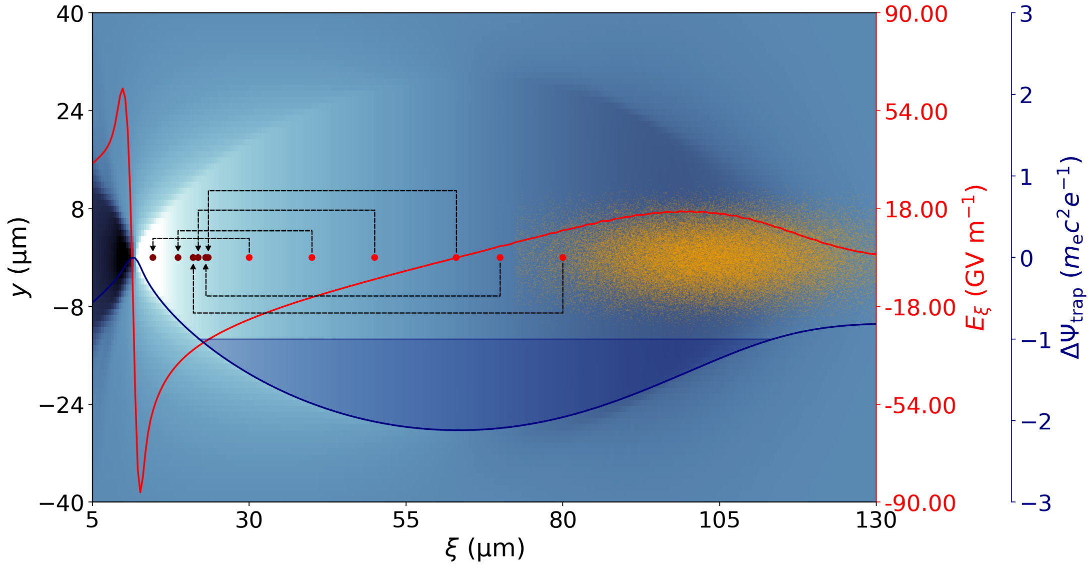

Figure 3.3: **One-dimensional trapping potential** This figure shows the same snapshot as Fig. 3.1. The dark blue line displays the trapping potential $\Delta\Psi_{\text{trap}} \propto \int E_\xi d\xi$ normalised to $m_e c^2/e$. Particles released at rest within the longitudinal extent of the highlighted area denoting $\Delta\Psi_{\text{trap}} \leqslant -1$ gain sufficient energy to stay within the relativistic blowout. Based on Eq. (3.20), various release positions (red dots) of initially resting electrons are mapped to their respective trapping positions (maroon dots) in the rear of the blowout.

Hence, the test electron born at rest must reach relativistic speed while being accelerated in the *trapping potential* Ψ associated to the longitudinal electric field from its initial position ξ_i to its final position ξ_f. In this formalism, $\xi = 0$ corresponds to the minimum of Ψ. In case of ionisation injection, ξ_i describes the position where the electron is released from its atom. Note that in the co-moving coordinate frame, the test electron slips backward within the wake. Inserting $\Psi \propto \int E_\xi \propto \xi^2$ either from the first order approximation in Eq. (3.13) or by integrating Eq. (3.14) for more special wake fields, the final or trapping position of the test electron assumes the form given by Eq. (A.8c)

$$\xi_f = -\left(\xi_i^2 + \frac{2\alpha}{k_p^2}\right)^{1/2} . \tag{3.20}$$

This formula has several important consequences. First, particles released in the minimal trapping potential, corresponding to the flipping sign of the longitudinal electric field approximately in the blowout centre, end up at the foremost possible trapping position. With increasing $|\xi_i|$, released particles get trapped closer to the blowout rear. This intriguingly applies also to particles released closer to the drive beam as a consequence of the parabolic shape of Ψ. Further, any initial particle distribution with finite extent gets longitudinally compressed during trapping. [105] calculates this *velocity bunching* approximately for the linear part of the longitudinal wake field. It may be noted that the trapping formalism expressed by Eq. (3.20) also allows for the generation of multiple longitudinally separated beams in the same wake by means of different release position, e.g. by using multiple laser pulses focused to individual positions within the wake as done in Chapter 8.

In this work, all electrons injected into the blowout by any effect aside from the desired one are considered *dark current*. This additional population of trapped electrons can get accelerated similarly to a witness beam, but commonly inherits very different properties as its generation typically happens in uncontrolled manner. Especially probabilistic processes injecting particles represent an obstacle for the development of reliable, high-quality accelerator technology. The presence of dark current can deteriorate the performance of any subsequent application and even damage the corresponding apparatus. Furthermore, unwanted populations trapped in the wake can cause beam loading (e.g. see Section 3.2.4) and change the witness beam parameters unpleasantly. Two particular sources of dark current can affect witness beams generated in this study: tunnelling ionisation by either the drive or witness beam due to extremely high transverse fields and ionisation by the wake field itself [106]. Both effects can be mitigated by a) reducing the drive (or witness) beam density and b) by decreasing the wake field amplitude. The latter can result from a) or by lowering the plasma density. As these quantities also influence the acceleration process of the witness beam, e.g. by modifying the accelerating and focusing fields, the mitigation of dark current can require substantial trade-offs.

3.2.3 *Energy spread*

Any realistic particle beam represents a velocity distribution with finite spread. In the longitudinal direction, this creates varying kinetic energies across all particles and is termed *energy spread*. This quantity results from multiple effects that can coarsely be divided into two categories.

One component typically results from the beam generation process. The width ΔW_{res} of the corresponding spectral distribution can be considered as *thermal limit*, and this *uncorrelated* or *residual* energy spread fundamentally defines the achievable minimum of a given electron beam generation process. In case of beams produced via ionisation injection in a plasma accelerator, multiple electrons are released and trapped inside the wake as described in Section 3.2.2. Their initial spatial distribution together with the overall trapping duration determines the residual energy spread. The spatial component of the trapping process, e.g. defined by the ionisation volume, causes different trajectories from initial to final position. Thus, particles subject to this process reach the speed of light at different rates imposing energy spread on the beam. A finite injection duration extends this effect because the first trapped particle already gains energy before the last one arrives. In reality, ΔW_{res} may become substantially larger than the theoretical minimum due to inhomogeneous ionisation, gas density or the wake field amplitude.

The second major reason for energy spread results from inhomogeneous acceleration: As a consequence of the *slope* $\mathrm{d}E_\xi/\mathrm{d}\xi$ of the accelerating field (e.g. see Eq. (3.14)), each longitudinal slice of a particle distribution experiences its own field. Any beam of finite duration thus accumulates *correlated energy spread* or chirp ΔW_{corr} in the presence of a blowout. Generally, this applies to both the drive beam and the witness beam, yet with different sign and strength. The correlated energy spread increases with the duration those beams are subject to the longitudinal field. In the limit of a linear field slope, ΔW_{corr} grows at constant rate.

Together, residual ΔW_{res} and correlated ΔW_{corr} energy spreads define the effective spectral distribution of any relativistic electron beam.

As can be seen from many quantities introduced in the following sections, energy spread potentially influences both longitudinal and transverse properties of any particle beam. It can cause severe problems in all stages along a beam line, e.g. during acceleration and in subsequent applications. In the accelerating stage, the energy spread couples with the transverse phase space of the beam by altering betatron oscillation amplitude and phase (e.g. see Sections 3.3.2 and 3.3.3), particularly when the transverse forces are not matched [107–110]. This can lead to reduced charge density, mixing phase space rotations, chromatic focusing, and consequently increased emittance and low current. At the end of a beam line, either during the decoupling from the accelerating field or within final focusing devices, large energy spread can cause similar problems [111]. Finally, most applications of electron beams require low absolute and relative energy spread for (optimal) operation, one of them being inverse Compton scattering sources.

3.2.4 *Beam Loading*

The presence of a trapped witness beam inside a blowout can alter the wake field distinctively. In the linear wake regime, *beam loading* [112] by a short beam delivering sufficiently high charge can partially compensate the ionic background, which flattens the longitudinal electric field. The beam thus experiences different – typically reduced and longitudinally more homogeneous– acceleration. However, the beam also loads the linear wake *transversely* (e.g. see Eqs. (3.11) and (3.12)), leading to a radial energy chirp. Working in the blowout regime, in contrast, ensures that each transverse slice experiences the same variation due to beam loading [113], since the longitudinal field typically does not depend on the radial coordinate in the blowout regime (e.g. see Eqs. (3.14) and (3.15)).

Having high charge density can be advantageous for the witness beam energy distribution. For example, if it flattens the accelerating field over the entire beam length all its particles uniformly gain energy at approximately the same rate. Thus, beam loading can suppress the accumulation of correlated energy spread (e.g. see Section 3.2.3) and de-phasing of the betatron oscillations (e.g. see Section 3.3), which otherwise can cause emittance growth. As beam loading reduces the accelerating field, the transformer ratio diminishes as well. However, it can allow for overall high acceleration efficiency [98] and conservation of beam quality.

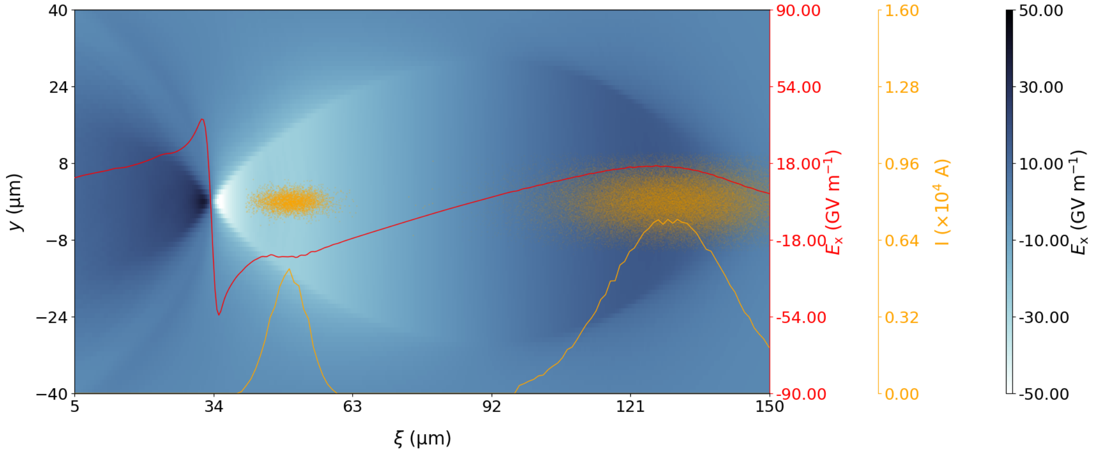

(a) Beam loading by narrow beam

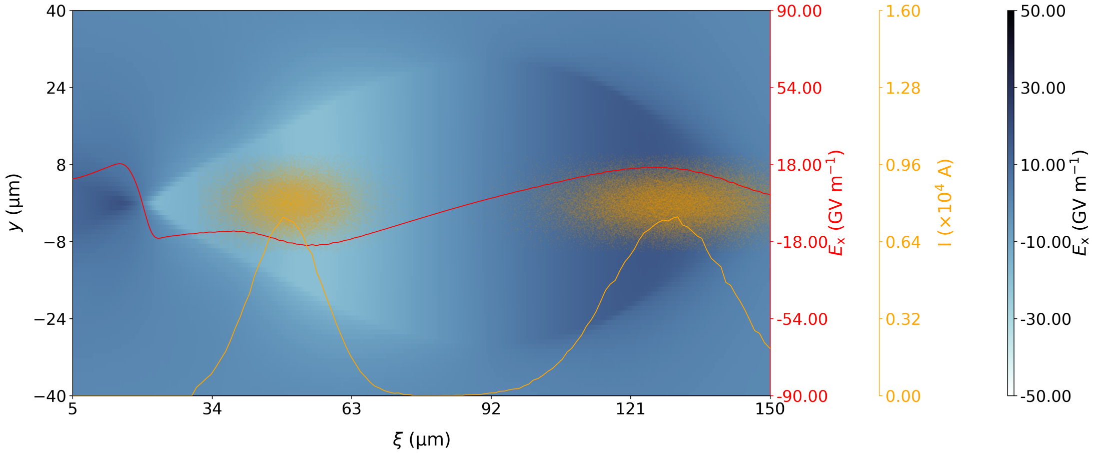

(b) Beam loading by wide beam

Figure 3.4: **Beam loaded PWFA**. Similar simulation settings as in Fig. 3.1, but with two different trailing beams. **(a)** A narrow beam co-propagates with the drive beam in the rear of the wake field. Its charge density partially compensates the positive ion background and locally flattens the accelerating electric field. **(b)** A wide trailing beam with same charge density as the drive beam co-propagates with the drive beam. Because of the large radial extent of this high-charge, high-current distribution, plasma sheath electrons returning to the axis get expelled. This shifts their crossing point further to the rear and thus elongates the wake structure. As a consequence, the changed radial wake function influences the longitudinal electric field according to Eqs. (3.13) and (3.14). Here, this effect over-compensates the wake field, leading to a slope of opposite sign compared to the unloaded case.

A perfectly flat profile requires a trapezoidal witness beam distribution *tailored* to the specific wake field [113], while other or more typical density configurations lead to deviations particularly at the edges of the loaded field region. Although beam loading has been accomplished experimentally with an externally generated witness beam [98], it becomes impractical already when a single part of the involved systems, e.g. the drive beam, the witness beam or the plasma source, varies or gets exchanged during operation. Then, the witness beam loses its fit to the wake, which can drastically modulate the energy distribution and lead to transverse decoherence. Further, if this beam is generated inside the wake, huge charge density required for beam loading can immediately cause massive losses of beam quality due to space charge forces long before the beam gathers sufficient energy for mitigation of this effect (e.g. see Section 3.3.3).

This study involves another possible application of tailored beam loading aiming at the minimisation or even elimination of correlated energy spread accumulated during the acceleration phase of a witness beam. It deliberately decouples the charge dedicated for acceleration from the charge distribution causing beam loading, and thereby grants high flexibility and opportunities. The corresponding description follows in Section 8.2.

3.3 TRANSVERSE DYNAMICS IN PWFA

Where the longitudinal fields mostly account for energy gain –the core characteristic of a particle accelerator– the transverse fields greatly determine the *quality* of witness beams. This abstract term refers to the transverse distribution and its (r.m.s) extent σ_r (or σ_x and σ_y in a Cartesian coordinate frame) of the beam and its transverse momentum distribution p_r (or p_x, p_y, respectively). The latter can be expressed by the (r.m.s) beam divergence σ_θ, which essentially represents the *angular velocity spread* relative to the longitudinal momentum component p_z.

A beam of perfect quality in this context exhibits no divergence, meaning that all particles arrive absolutely parallel at their target (e.g. the beam is *collimated*), and provides small radius for high particle density and correspondingly intense interactions. In practice, any mechanism generating electron beams exhibits an intrinsic *thermal velocity spread* limiting the homogeneity of all particle velocities similarly to the consideration made for the residual energy spread earlier. Thus, particle beams always adopt a finite radial momentum distribution. This section describes primary mechanisms leading to large radial momentum distributions together with strategies for their minimisation.

3.3.1 *Transverse Trace Space*

The transverse *trace space emittance* ϵ of particle beams combines the spatial density with the homogeneity of particle velocities [46, 108]. It is proportional to the area a projected beam distribution occupies in the trace space defined by the transverse coordinates $x, x' = dx/dz \approx p_x/p_z$ and is similarly defined in the $y-$ direction. x' denotes the single-particle divergence. By statistical means, the r.m.s emittance reads

$$\epsilon_x = \sqrt{\langle x^2 \rangle \langle x'^2 \rangle - \langle xx' \rangle^2}, \tag{3.21}$$

where the brackets denote second central momenta of the respective distributions. Note that ϵ_y is defined analogously. In Eq. (3.21), the spatial extent and the divergence of a particle beam are correlated by $\langle xx' \rangle^2$ expressing convergent or divergent behaviour of a beam. In the limit of an infinitesimally narrow beam, this term becomes zero at the minima or maxima in a focusing structure, e.g. when the beam performs betatron oscillations in a plasma channel (see Section 3.3.2). Due to reasons similarly as for the divergence, a beam of high quality commonly has as low emittance as possible. Low-emittance beams can be focused to smaller spot size and therefore can increase the beams interaction with a target. As consequence of *Liouville's theorem*, the area of a beams *phase space* (e.g. set up by x, p_x) is constant given that there is no coupling with the other planes in y and z [46]. This also applies to the trace space area and the emittance as long as the beam energy stays constant ($\beta\gamma_b = \text{const.}$). However, in an accelerating environment, the beam is supposed to gain energy and the transverse trace space density reduces accordingly (e.g. recall $x' \approx p_x/p_z$). A more suitable description results from the *normalised emittance*

$$\epsilon_{n,x} = \beta\gamma_b\epsilon_x, \tag{3.22}$$

which stays constant under acceleration in an ideal system with linear forces and without coupling between the individual trace space planes. Currently, plasma-based accelerators produce normalised electron beam emittance of the order of 1×10^{-7} to 1×10^{-5} m rad [114–117].

Recalling Eqs. (3.14) and (3.15), the conditions for emittance conservation apply to the blowout regime allowing for rapid *and* high-quality particle acceleration. Within such a linear system, any emittance change results from nonlinear effects in the accelerating system [46]. Examples are the space charge fields of the beam, non-linearities in the wake field e.g. due to inhomogeneities of the plasma profile or the driving beam, mismatching to the focusing field of the wake (e.g. see Section 3.3.3), chromatic aberrations e.g. from substantial energy spread (e.g. see Section 3.3.2), or collisions with ambient gas or other beam particles. Some of these effects can be reversed, particularly when they follow deterministic dependencies. If they obey stochastic laws like collisions do, these effects tend to increase the beams entropy without hope for reversion [118]. Certain nonlinear effects can reduce the beam emittance, such as radiative, electron, and stochastic cooling. Unfortunately, these techniques rely on extremely long interaction times and thus require large and expensive storage rings [46].

Although the emittance measures transverse quality of a beam, most applications require multiple optimised parameters. Therefore, combining transverse and longitudinal figures of quality seems adequate as done for the (5D) *beam brightness* [46]:

$$B_{n,5D} = \frac{2I_p}{\epsilon_{n,x}\epsilon_{n,y}}. \tag{3.23}$$

This definition quantifies the particle flux per transverse area and per solid angle and couples the normalized emittance of both transverse planes with the peak current defined as

$$I_p = \left.\frac{dQ}{dt}\right|_{max} = \frac{Q}{\sqrt{2\pi}\beta c\sigma_z}. \tag{3.24}$$

By following this strategy, the brightness parameter can further be expanded to ultimately include all relevant quality terms particle beams can provide. The new definition called *6D brightness* [119] additionally includes the relative energy spread in units of charge within 0.1 % bandwidth (BW) around the peak energy:

$$B_{n,6D} = \frac{B_{n,5D}}{0.1\%BW} = \frac{2I_p}{\epsilon_{n,x}\epsilon_{n,y}\ 0.1\%BW}. \tag{3.25}$$

Here, $\langle W \rangle$ is the averaged kinetic energy of the beam.

Regardless of the 5D or 6D definition, high brightness is generally regarded as high quality, particularly with respect to light source applications. Those typically benefit from high longitudinal and transverse particle density, excellent collimation and a mono-energetic spectrum simultaneously. The strong dependence of the normalised emittance, scaling quadratically for symmetric beams, emphasises the production of low-emittance beams and the need for emittance-conserving particle accelerators.

3.3.2 *Betatron Oscillations*

Following the considerations about trace space outlined above, the blowout regime provides ideal properties for high-quality beam acceleration because of the linear transverse fields expressed by Eq. (3.15). They originate from the complete expulsion of electrons from the drive beam path, leaving the heavy ions as stationary and positively charged *ion channel* behind. As a consequence, any electron inside the blowout structure having radial displacement or velocity gets accelerated towards the central axis and performs harmonic *betatron oscillations* with frequency

$$\omega_\beta = \omega_p/\sqrt{2\gamma} \tag{3.26}$$

depending on the electrons kinetic energy and the plasma frequency. These forces act on trapped beams and most parts of the drive beam in PWFA. As a side note, betatron oscillations, consisting of accelerated electric charges, emit electromagnetic radiation that can be exploited e.g. for diagnosing the beam [115] or even as light source [4, 37, 120].

Betatron oscillations correspond to particles rotating in the transverse trace space and integrating over all particle trajectories yields the beam emittance (e.g. see Section 3.3.1). Generally, many particles at different phase of their individual oscillation or with varying frequency or amplitude compose a larger area and increase the emittance compared to the case where they all rotate in the same phase with identical frequency and amplitude. There are two fundamental, yet complex mechanisms how betatron oscillations define the beam emittance or cause it to grow. The first one results from the individual generation process of any electron beam, and the minimally achievable value for a given parameter set is called residual or *thermal* emittance. Externally generated beams subsequently injected into a blowout already inherit a pre-defined emittance, which is then subject to the linear focusing forces of the wake field. In contrast, beams generated inside the wakefield obtain their emittance based on the duration and initial volume of ionisation injection schemes as discussed in Section 3.2.2 and [121], similarly to the residual energy spread. The second effect results from Eq. (3.26) and the spectral distribution of the beam. As ω_β depends on the individual electron energy, any sort of spectral spread leads to more or less rapid longitudinal *phase mixing* of individual electrons, increasing the overall beam emittance. *Residual* energy spread (e.g. see Section 3.2.3) causing this *de-phasing* or decoherence affects *all* electrons within the beam, and the resulting increase of projected emittance cannot be inverted. By accumulating *correlated* energy spread (e.g. see Section 3.2.3) by an accelerating field with non-zero gradient, in contrast, de-phasing occurs between all longitudinal *slices* of the beam [122]. Thus, the trace space areas of each slice overlap and combine to a much larger emittance than each slice normally inherits. This effect can be reversed or at least reduced by inverting the slope of the accelerating field for a sufficiently long time, e.g. by tailored beam loading as done in Section 8.2.

3.3.3 *Transverse Matching*

The transport of an electron beam inside a blowout is of fundamental relevance for its transverse quality. This process is a highly complex interplay of very different effects, and each of them can severely deteriorate the emittance and even integrity of the respective beam.

For any particle distribution experiencing the blowout such as the driver or witness, the linear focusing forces of the wakefield act against the expanding ones set up by the beam. Those consist of the natural defocusing behaviour due to finite transverse velocity spread expressed by the beam emittance, and the space-charge force, a nonlinear repulsive Coulomb interaction between all electrons in the beams distribution. A large variety of effects caused for example by external fields or scattering events can influence the transverse dynamics as well, but is beyond the scope of this introduction.

If all expanding and focusing forces balance, the beam is *transversely matched*. This state implies that the radial envelope of the beam stays constant throughout propagation in the ion channel, even though single particles still perform their individual betatron oscillations. Particle accelerators strongly benefit from transverse matching because it ensures optimal and *stable* interaction with the plasma medium and a wake field. Particularly, beam emittance is conserved in this state as all nonlinear effects are balanced [46].

Transverse matching mitigates undesired effects related to evolving beam envelopes that occur in non-matched wake structures. Generally, large fractions of mismatched electron beams contract and/or expand simultaneously, which typically manifests as collective betatron oscillations along the beam inside a plasma channel, As a consequence, the emittance of mismatched beams tends to increase until it saturates at maximal decoherence between all longitudinal slices [122]. Global oscillations along the beam facilitates the hose instability [123], where a displacement of the beam centroid gets exponentially amplified [124], and can be reduced by transverse matching [125]. Similarly, losses due to synchrotron radiation at elevated beam energy can be minimised [126]. In strong cases, considerable betatron oscillations along the beam cause *pinching*, which locally increases the charge density substantially. The beam fields grow accordingly and can trigger tunnelling ionisation (e.g. see Section 2.2.1). Released electrons can get trapped and form a witness beam [127], but is considered undesired dark current in this work (e.g. see Section 3.2.2). A pinching drive beam can also influence the wake field amplitude as it changes the expulsion of plasma electrons. The other limit occurs when the drive beam emittance or space charge continuously expand the beam against all focusing forces such that its density decreases and, eventually, the blowout collapses. Summarising all these arguments, matching of beams to the plasma is highly desirable and should always be considered.

For an electron beam propagating in z-direction inside a homogeneous ion column or wake field, the following differential equation describes the r.m.s. envelope evolution where primes denote derivatives in the longitudinal z-direction

$$\sigma_x''\beta^2 = -K^2\sigma_x + \frac{\epsilon_n^2}{\gamma^2\sigma_x^3} + \frac{I_p}{\gamma^3 I_0(\sigma_x+\sigma_y)} - \frac{\beta^2}{\gamma}\gamma'\sigma_x' \tag{3.27}$$

and combines various expressions from [46, 125, 128–130]. Other terms, e.g. scattering off ions or atoms, can be added if required by an individual applications. Here, $I_0 = ec/r_e$ denotes the *characteristic current* and r_e is the *classical electron radius*.

The first term on the right hand side of Eq. (3.27) expresses the linear focusing force of a homogeneous ion column or wake field by using the parameter

$$K = k_p/\sqrt{2\gamma}. \tag{3.28}$$

It determines the focusing strength and is closely related to the betatron frequency defined by Eq. (3.26). High K associated to large plasma density can compensate the effect of large defocusing forces. If the latter are weak, however, the focusing forces are not balanced and can imprint considerable transverse momentum and expand the beam envelope. Typically in plasma acceleration schemes, the focusing forces dominate the expanding ones as shown in Fig. 3.5.

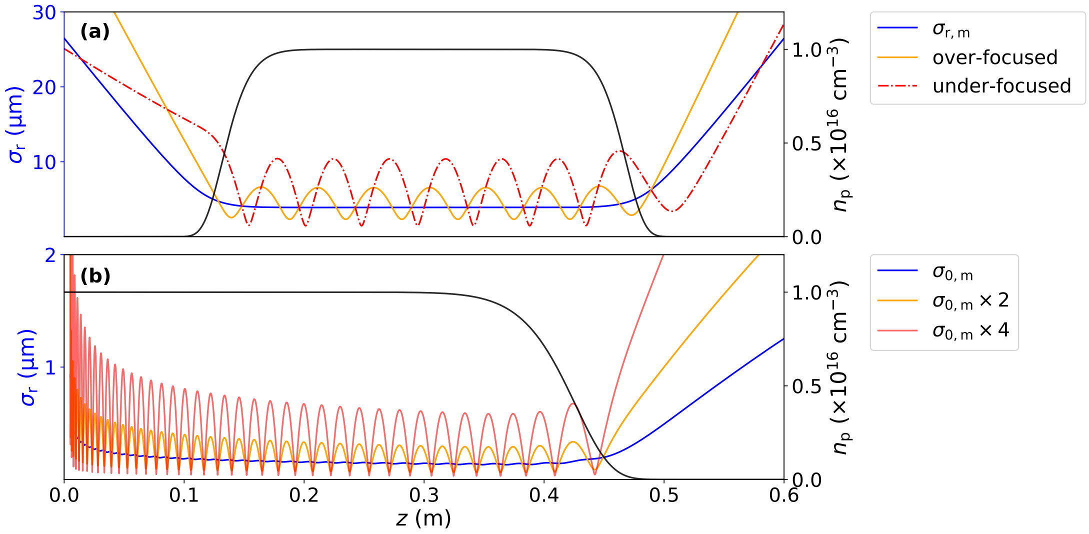

Figure 3.5: **Numerical solutions of Eq. (3.27) in a typical homogeneous ion channel. (a)** Electron beams with constant energy $W_{\text{kin}} = 24\,\text{GeV}$ and initial emittance $\epsilon_n = 40 \times 10^{-6}$ m rad are focused to different spot sizes at approximately the same location into the ion channel and experience its transverse forces. Only the matched beams envelope stays constant, whereas larger and smaller spot sizes yield global betatron oscillations and substantially increased averaged beam radius. Both non-matched cases are dominated by the focusing term, and space charge effects are negligible at these energies. Combined with constant beam energy, neither the betatron period nor its amplitude change during the interaction.
(b) Slow beams with initial energy 1 MeV and low emittance $\epsilon_n = 20 \times 10^{-9}$ m rad subject to constant acceleration of 10 GV m^{-1}. Small deviations from the matched *initial* radius $\sigma_{0,m} \approx 0.9\,\mu\text{m}$ for the given plasma density cause betatron oscillations. These small beam envelopes are extremely challenging to achieve experimentally, and thus matching of beams generated e.g. by ionisation injection requires operation in lower plasma density regimes. Due to the constant acceleration, the betatron frequency and amplitude reduce until the beams reach the plasma exit. There, only the matched beam can be decoupled adiabatically, while the non-matched beams depend strongly on their current betatron phase on the down-ramp. As a consequence, these beams are much harder to capture in a subsequent beam line and sensitive to all sorts of jitter. Note that deliberately defining low beam charge diminishes space charge effects in (b). This is required as their influence at low energy would lead to substantially increased beam radius, and therefore prevent decent comparison between matched and slightly mismatched beams.

The two middle terms primarily cause expansion because of emittance and space charge forces, respectively. As the latter scales considerably with γ, it can dominate all other contributions at low beam energy. In particular, electrons released at rest inside the wake field with high peak current I_p (e.g. see Eq. (3.24)) or charge density can be strongly affected. In this case, rapid expansion of the beams envelope and nonlinear emittance growth deteriorate the beam quality regardless of any initially low thermal emittance. Thus, space charge effects limit the maximal beam charge or current trapped with considerable quality by any injection mechanism involving slow electrons. Rapid energy gain can restrict the duration of this effect. Furthermore, even if a high-quality witness beam is trapped and accelerated to moderate energies, any high charge density such as other beams or dark current overlapping the witness can cause substantial distortions in its transverse distribution. Gaining sufficiently high energy before other charge densities appear close to the witness can immunise it against space charge effects.

Often, identifying the dominating expanding term can improve the particle accelerator and help to match the beam. For a transversally symmetric distribution with $\sigma_x = \sigma_y$, the ratio of space charge to emittance terms

$$R_0 = \frac{I_p \sigma_x^2}{2 I_o \gamma \epsilon_n^2} = 2 k_{p,b}^2 \beta_x^2 \tag{3.29}$$

quantifies the *space charge dominance over emittance* [129]. Here, $\beta_x = \langle x^2 \rangle / \epsilon_x$ denotes the r.m.s. *beta function* of the beam and $k_{p,b} = \omega_p / c \approx (4\pi r_e n_b / \gamma^3)^{1/2}$ is the plasma wave number associated to the beam density.

The very last term in Eq. (3.27) accounts for changes of kinetic beam energy, with high importance in an decelerating/accelerating system such as the blowout regime. This term can be important for the drive beam when it is about to deplete (e.g. see Eq. (3.17)) and its γ-factor approaches unity. In this case, the beam envelope expands due to space charge effects until the blowout and this differential equation collapses. As mentioned earlier, this term also determines the trapping behaviour and emittance of a slow witness beam as rapid acceleration can reduce the duration over which space charge effects act.

The various and strong dependencies on the γ-factor influence many different transverse effects of the electron beam. In addition to the arguments above, this dependence can also deteriorate transverse properties of a beam that inherits substantial correlated or uncorrelated *energy spread*. During propagation inside the ion channel, broad energy distributions yield many different effective forces within the beam, which can chromatically modulate envelope evolution and lead to emittance growth.

Equation (3.27) can be solved for propagation of a matched electron beam inside the plasma channel at constant energy. In this case, the non-evolving envelope requires

$\sigma_x' = \sigma_x'' = 0$. In the limit of an emittance-dominated beam, e.g. $R_0 \ll 1$, the matched beam r.m.s. radius yields [130]

$$\sigma_{x,\mathrm{matched}} = \left(\sqrt{\frac{2}{\gamma}}\frac{\epsilon_n}{k_p}\right)^{1/2} \propto \epsilon_n^{1/2}\left(\gamma n_p\right)^{-1/4}. \tag{3.30}$$

This expression is dominated by a weak dependence of the beams emittance, and varies even weaker with its energy. The same applies to the effect caused by the plasma, such that the matched radius of a given beam does not change significantly over a large range of densities. In context of PWFA, Eq. (3.30) shows that large emittance increases the matched radius for a given drive beam and plasma density, which can be particularly important for avoiding drive beam ionisation. This behaviour simultaneously lifts the requirements on the final focusing elements in the beam line upstream of the plasma. If the delivered beam emittance yields an undesirable small matched radius for a given plasma target, scattering foils can increase it in a controlled manner [46]. For driving a blowout, the beam density after scattering and focusing must still exceed the plasma density. Figure 3.5 presents various solutions of Eq. (3.27) with matched and non-matched beams in situations typical for this work, e.g. for high energy driver focused into the plasma and slow beams getting accelerated.

Equation (3.27) expresses that an initially matched beam can stay close to this state even during acceleration or changes of the plasma density provided this process happens *adiabatically* [130]. Similar considerations apply to the witness beam *extraction* from the wake when the plasma ends [107–109]. If the density profile drops (or increases) rapidly, e.g. not adiabatically, the witness beam cannot adapt to the focusing associated to the varied K-parameter and the beam emittance grows massively. This effect can become even stronger for beams of high energy spread. Complete destruction or beam loss might happen in this case.

Summarising, the transverse forces within the plasma accelerator are crucial for electron beam quality, transport and any subsequent application. If transverse matching can be achieved, the propagation is highly stable, suppresses many potential obstacles and facilitates high-quality electron beams.

3.4 PLASMA PHOTOCATHODE WAKEFIELD ACCELERATION

The prime witness beam generation process exploited in this study is the *underdense plasma photocathode* [41]. This technique generalises the mechanism of ionisation injection (e.g. see Section 3.2.2) and exploits the advantages of an *independent, low-intensity* laser pulse propagating behind the drive beam. Once the pulse reaches its focal position, the laser releases electrons directly inside the blowout which subsequently get trapped and form the witness beam. Figure 3.6 depicts this process. By decoupling wake excitation and beam generation, multiple unique features in terms of *quality* and *flexibility* arise from this scheme.

Following the arguments discussed in Sections 3.2 and 3.3, high quality beams in terms of low emittance and residual energy spread demand for rapid ionisation within well-defined, small volumes. The plasma photocathode approach achieves these two conditions by tightly focusing the laser pulse of wavelength λ_l to a focal waist w_0 into the blowout, ionising e.g. an undisturbed *dopant* gas species overlapping the plasma. For typical Gaussian focusing $w(z) = w_0\sqrt{1 + z^2/z_R^2}$ with *Rayleigh range* $z_R = \pi w_0^2/\lambda_l$ the ionisation duration can be estimated as

$$\tau_{\text{ion}} \approx \frac{2z_R}{c} \propto w_0^2\lambda_l^{-1} \tag{3.31}$$

for constant yet low laser intensity $a_0 = eE_0/m_e c\omega_l \ll 1$ above the level for reliable ionisation. In this case the ionised volume scales approximately like

$$V_{\text{ion}} = \pi\int_{-z_R}^{z_R} w(z)^2 dz \propto\ w_0^4\lambda_l^{-1} \tag{3.32}$$

with strong dependence on the focal spot size, which is commonly of the order of $<10\,\mu\text{m}$ [41]. Note that calculating the actually ionised charge and the resulting beam profile requires more sophisticated means such as ADK theory expressed by Eq. (2.10) and illustrated in Fig. 3.7.

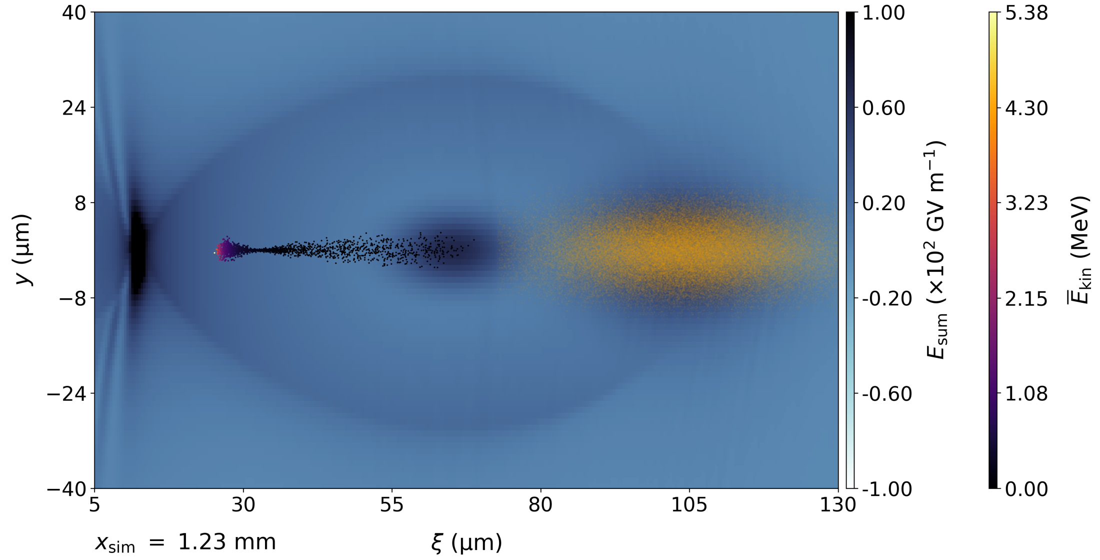

(a) During injection

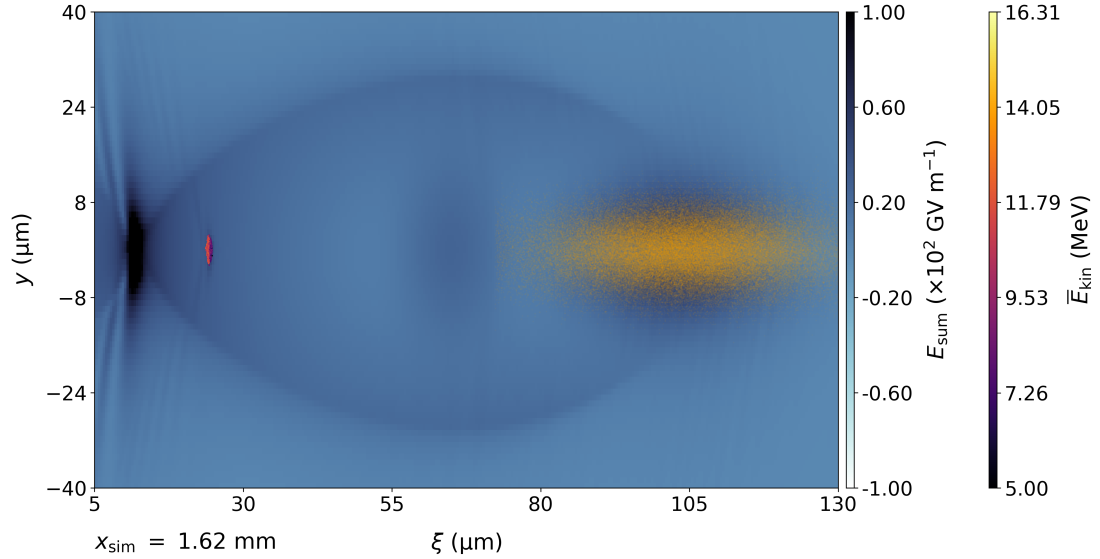

(b) After injection

Figure 3.6: **A plasma photocathode in the co-moving coordinate frame (a)** Similar simulation settings as in Fig. 3.1, but with a focused laser pulse (dark region in the centre) co-propagating with the drive beam delayed by ~130 fs. Due to its intensity just above the ionisation potential of homogeneously distributed helium, released electrons are born cold and experience minimal interaction with the laser pulse. In this co-moving coordinate frame, particles slip backwards in the wake, gain energy and eventually get trapped when they reach the wakes phase velocity. Colour-coded particles show the generation of residual energy spread. **(b)** After the laser intensity has dropped due to defocusing, ionisation stops and the trapped low-emittance beam (in this case $\epsilon_n \approx 25 \times 10^{-9}$ m rad at 5.2 pC charge) gets accelerated in a stable phase relation to both drive beam and wake field. Due to the linearly varying longitudinal field, the absolute energy spread increases and assumes a linear chirp.

For laser intensities yielding high ionisation ratios, e.g. Fig. 3.7 (b) and (c), the actual release process happens inside a thin slice of the laser pulse located at its forepart. In this slice referred to as *ionisation front* the integrated ADK rate yields maximal ionisation. The plasma photocathode laser, then, generates electrons mostly within a very finite length of initial positions, leading to even finer trapping (e.g. see Section 3.2.2) and thus very dense beams. For (Gaussian) focused laser pulses, the ionisation front can move slightly to the front and back due to changing laser intensity profile and therefore elongates the trapped beam depending on w_0 [105].

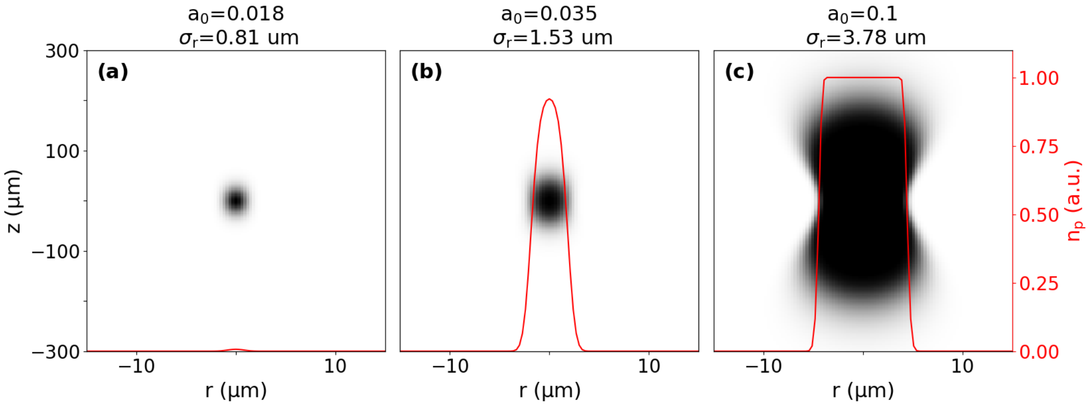

Figure 3.7: **Comparison of plasma photocathode ionisation volumes in the laboratory frame based on ADK.** A 800 nm Gaussian laser pulse with duration $\tau = 8.0\,\text{fs}$ propagates in positive z direction, and reaches its focus defined by $w_0 = 4.0\,\mu\text{m}$ at $z = 0$. The radial coordinate is expressed by r. **(a)** Ionisation profile for injector laser used in [41]. Due to the low intensity, the laser ionises a small fraction of the dopant gas helium in a volume much smaller than given by Eq. (3.32). The red line represents the radial ionisation ratio at the focus position. Its r.m.s. width σ_r is displayed at the top of each figure and defines the initial beam envelope relevant for matching. **(b)** Increasing the laser intensity almost yields full ionisation at $z = 0$. Substantially more charge than in the first case is released as the higher intensity elongates and extents the ionisation volume. The Distribution still displays a Gaussian radial shape. **(c)** Further increasing the laser intensity reveals the typical "bone"-like structure expected from Gaussian focusing. Both the flat-top density distribution at $z = 0$ and the transverse broadening will deteriorate the witness beam quality in the blowout, as the projected beam envelope increases due to both effects. As such, more particles receive a larger kick from the transverse wake fields. Additionally, the non-negligible kick caused by the high laser intensity also increases the emittance in the laser polarisation direction. Figures are based on an ADK script developed by D. Ullmann.

Another advantage of low laser intensity $a_0 \ll 1$ than confining the ionisation volume comes from the weak interaction between released electrons and the polarised laser field. Then, for $a_0 \ll 1$, the interaction remains linear and ponderomotive effects are suppressed such that the laser does not transfer significant momentum to released particles. This leads to low thermal velocity spread, particularly in the transverse direction. Together with small volume and short ionisation duration, the plasma photocathode generates ultracold electron beams with *thermal divergence* [131]

$$\sigma_\theta \approx \gamma^{-3/4} k_p w_0 \Delta_i / 2. \tag{3.33}$$

The associated *thermal emittance* in each transverse plane [131]

$$\epsilon_{n,th} = k_p w_0^2 a_0 \frac{3\pi r_e}{4\sqrt{2}\alpha^4 \lambda_l} \left(\frac{13.6\ (\mathrm{eV})}{U_I} \right)^{3/2} \tag{3.34}$$

is of the order of 10^{-9} m rad to 10^{-8} m rad. Here, α denotes the fine structure constant and $\Delta_i = (3\pi r_e a_o / \alpha^3 \lambda_L)^{1/2} (13.6\ (\mathrm{eV})/U_I)^{3/3} a_o^{3/2}$ relates the laser field with the ionisation potential U_I of the target gas. Even though the laser intensity should be as low as possible for weak influence on released electrons, the laser should ionise the respective charge state such that minimised thermal emittance [131] coincide with moderate trapped charge. Further dependencies of beam emittance determined by a plasma photocathode can be found in [132]. Similarly to any other beam inside the blowout, beams formed by the plasma photocathode perform global and incoherent betatron oscillations unless the beam is matched to the focusing forces. [131] suggests using a laser pulse causing a radial ionisation profile with extent very close to the matched radius for the given wake field. This would yield constant and low emittance along the whole particle accelerator. However, according to Eq. (3.30), low-emittance beams of the order of 10 nm to 40 nm yield very small matched radii across a large range of plasma densities. The released charge for such laser foci <1 µm is either low or, if increased, can cause rapid beam expansion via space charge. Further, the trapped beam will present high charge density and the associated strong electric fields could ionise the dopant gas leading to dark current. Generating beams slightly mismatched to the plasma wake can avoid these problems partially at cost of slowly growing emittance [41] until maximal decoherence is reached [122]. As can be seen in Chapter 8, the beam emittance can be ultra-low even if this growth occurs.

The residual energy spread from a plasma photocathode can be estimated by [133]

$$\Delta W_{res} \approx \frac{2\pi}{5} \frac{w_0^2 E_{\xi,trap}}{\lambda_l}, \tag{3.35}$$

where $E_{\xi,\mathrm{trap}}$ denotes the accelerating field at the witness beam trapping position. It may be noted that Eqs. (3.33) to (3.35) all depend on the plasma density and, hence, on the wake field amplitudes. Generally, these quantities can be optimised by operating in low density plasma because any *thermal* injector effects caused by the wake lessen. Applying this strategy nonetheless reduces the accelerating and focusing fields, leading to lower energy gain. At the same time, transverse matching requirements relax.

In the plasma photocathode scheme, the dopant substance serving as witness electron reservoir can be decoupled from the wake excitation and most laser parameters. As indicated above, this dopant, e.g. neutral gas distributed within the plasma volume, must provide higher ionisation potential than the substance dedicated for the plasma medium and also sustain the passing electron drive beam according to Sections 2.2.1 and 2.2.2. Note that multiple, separated ionisation energies allow for *species-selective* electron beam injection. If the dopant stays neutral during the PWFA process, it can cover various densities and linearly tune the ionised charge until space charge deteriorates the emittance (e.g. see Section 3.3.3). It may be noted that the gas dopant can in principle be confined, e.g. by a gas jet or other sophisticated devices, such that various profiles different to the homogeneous case can be generated.

The plasma photocathode pushes the obtained beam emittance *one to three orders of magnitude* below the level of any competing electron beam source. Correspondingly it offers ultra-high beam brightness $B \propto \epsilon_n^{-2} \Delta W^{-1}$ facilitating future light source and collider applications. The high quality obtained through small ionisation volumes, however, comes at the price of low overall charge. Even though it only affects brightness linearly, some applications strongly benefit from high absolute particle numbers. Yet, increasing laser parameters (w_0 or a_0) or the dopant gas density for higher charge will inevitably cause undesired beam loading, space charge forces and mismatching. Those rapidly blow up the witness and immensely increase the emittance once they overwhelm the wakes transverse forces. This effect is of exceptional strength at the low particle velocities during trapping because of the inverse cubic scaling of the gamma factor. Trying to solve this problem, e.g. by redistributing charge density by beam elongation or longer trapping duration, in turn nurtures the irreversible residual energy spread, while radial expansion either leads to larger thermal emittance or subsequent growth due to mismatching. Fighting the latter, e.g. by increasing the focusing force of the wake to again balance the broadening, in turn negatively impacts thermal velocities again. Consequently, the generation of relativistic beams providing superior quality along with high charge is either fundamentally prohibited or requires new, possibly exotic approaches.

The independence of drive beam and injector laser opens immense opportunities regarding flexibility: it allows laser operation under arbitrary angle and at any specific position within the blowout [134]. Such variations of the initial electron distribution subsequently affects the trapping mechanism shown in Section 3.2.2 and the radial evolution governed by Eq. (3.30). Different laser incidence can create exotic beams with larger transverse velocity distributions, among other effects leading to large betatron amplitudes suitable for x-ray sources (e.g. compare [37, 56]). This high flexibility paired with ultra-high quality, however, comes at a prize, as it bears the challenge of alignment and synchronisation of the injector with the electron beam and its trailing plasma wave. Comparing the length scales shows how demanding these tasks can be. For example, in a spherical blowout with radius $\sim\lambda_p = 100\,\mu\mathrm{m}$ the already tight laser waist $w_0 \approx 10\,\mu\mathrm{m}$ corresponds to 10 percent of the wake structure. Considering the high fields inside the wake, transverse misalignment or jitter of this magnitude could severely impact the witness beam quality, or even prevent it from getting trapped. Similar arguments apply to longitudinal inaccuracies of the laser timing. Temporal jitter can vary the trapping position and change the acceleration and accumulation of energy spread, or release electrons before or behind the wake. However, in the collinear geometry between laser and drive beam, the parabolic trapping potential can compensate partially for timing jitter as the density of trapping positions increases with larger deviation from the central injection position as a consequence of Eq. (3.20). Measuring and controlling the spatiotemporal overlap of laser pulse and plasma wake is of crucial importance for this scheme, and a promising method has been developed as part of this study (see Chapter 6).

3.5 DISCUSSION OF PWFA

In summary, PWFA offers the high fields inherent to the nonlinear blowout regime and therefore can, in principle, boost particle beams to high energies within short acceleration lengths. The linear accelerating and focusing fields are ideal properties and allow for high quality beams superior to any conventional accelerator if combined with the plasma photocathode.

Yet, there are some limiting factors deserving reference. Firstly, the relativistic drive beam must be delivered externally with sufficiently high density for driving the wake and energy for sustaining it adequately long. So far, most PWFA experiments were concluded at large linear accelerator facilities, which counteracts the promise of *compactness* and responsible costs. This is why huge research and technology is performed around *staging* concepts [70, 122, 134–137]. A possible layout can be found in Fig. 3.8, where a high-power laser system generates the dense drive beam in a first plasma stage, which then drives a blowout in a subsequent one. These hybrid LWFA→PWFA concepts are the future of university-scale and industrial particle accelerators, but inherit their own essential problems such as beam transfer between plasma stages and waves.

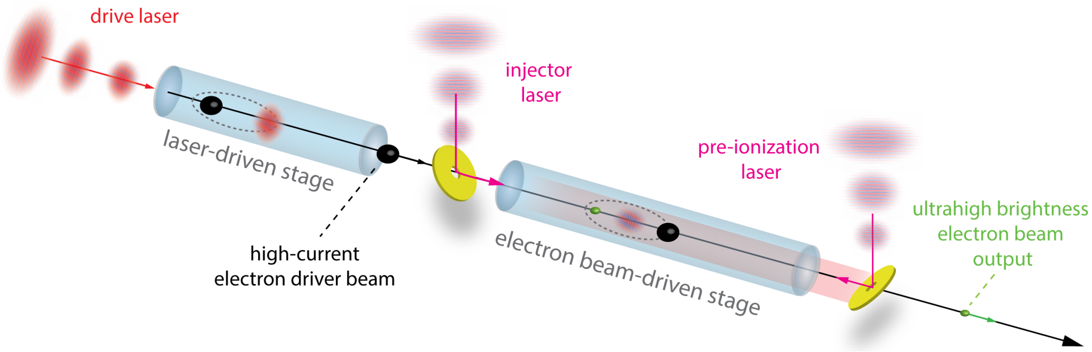

Figure 3.8: **A staged plasma photocathode wakefield accelerator in the laboratory frame.** An intense laser pulse drives a nonlinear plasma wave in the first stage. Electrons injected and accelerated there form an intense, yet low-quality electron beam (black ball). Afterwards, this beam is coupled into a second, pre-ionised stage and drives a plasma wakefield accelerator. A plasma photocathode injects a high-quality witness beam, which eventually can be exploited for subsequent applications such as light sources. This setup represents a truly compact plasma photocathode wakefield accelerator. Figure produced mutually by A. F. Habib and the author.

Secondly, even though generating *any* plasma is comparably easy, the production of wide and long plasma volumes that can spatially sustain large wakes, e.g. $\lambda_p = 300\,\mu m$ to $500\,\mu m$ suitable for highest brightness beams and stability, over several metres of acceleration bears a considerable challenge. This task complicates when a potential dopant gas in the background shall remain undisturbed by this process, which excludes discharge devices and requires well-controlled laser pulses. As it turns out, e.g. during the experiment done in Chapter 7, the plasma source remains the major bottle neck in the production of ultra-high brightness electron beams using the underdense photocathode.

Plasma accelerators have been shown to produce dense electron beams up to the 10 GeV-level per shot. However, all plasma-based techniques suffer from low time-averaged output as they operate at up to 10 Hz repetition rate for the most advanced systems, and typically much less. Most of the time, the high-power laser system required for LWFA or creating the plasma source is the limiting factor, and recombination time scales of heated plasma may turn out as another one even if laser technology advances rapidly. Consequently, subsequent applications such at light sources also run at much lower repetition rate than conventional accelerators can deliver.

Another issue related to the laser system both in LWFA and laser-based plasma sources in PWFA relates to the shot-to-shot stability of the respective laser pulses. This involves pulse energy and shape, but more crucially its pointing and alignment. This leads to considerable shot-to-shot parameter jitter of the generated and accelerated electron beam and thus strongly influences subsequent applications.

Finally, the physics involved in the beam generation and acceleration is highly complex. As discussed in Sections 3.2 to 3.4, most experimentally accessible parameters directly or indirectly influence the same set of beam properties. In some regimes these parameters constructively improve the beam quality, in others they counteract each other and the beam deteriorates or gets lost. Similarly, improving one parameter almost always goes on cost of at least another important one, which constantly requires careful trade-offs depending on the individual situation.

Overcoming all these problems by dedicated studies nevertheless offers extremely fascinating opportunities for the development of new and highly improved accelerator technology, light sources and applications.

4

INVERSE COMPTON SCATTERING

Now that the foundations of plasma and beam driven wakefield acceleration are laid out and pave the way for generation of ultra-bright electron beams, their appropriability for driving scientific progress should be illuminated. In this work, these (high-quality) electron beams are fundamental to the production of brilliant γ-ray pulses from the interaction with (optical) photons in a process called *inverse Compton Scattering* (ICS). The interaction between an electron beam and a laser pulse in *head-on* geometry is sketched in Fig. 4.1.

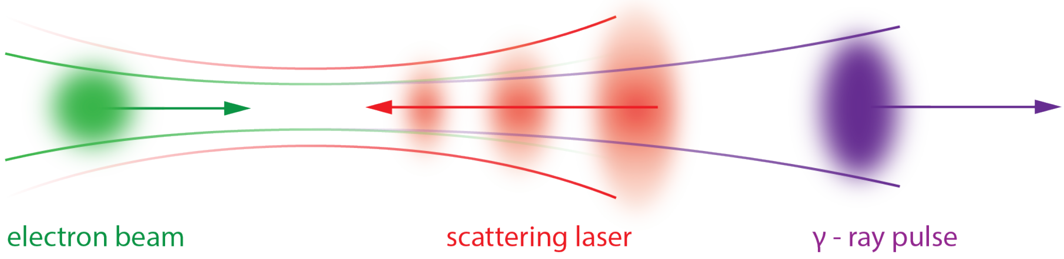

Figure 4.1: **Concept of Inverse Compton Scattering in head-on geometry** The electron beam (green) propagates from left to right and is subject to Gaussian focusing indicated by the green lines. The scattering laser (red) propagates in the opposite direction and is also subject to Gaussian focusing indicated by the red lines. Here, the laser hits the electron beam head-on, which produces maximal γ-ray energies according to Eq. (4.9). The interaction produces a pulse of γ-rays (purple) which propagate in the electron beam direction.

In the underlying mechanism of ICS, photons scatter off relativistic electrons and their energy gets Doppler - shifted by several orders of magnitude, e.g. from initially about $1\,eV$ into the regime of $0.2\,MeV$ to $100\,MeV$. The strong scaling behind this effect commonly requires large and expensive electron accelerators, but the recent developments in exploiting plasma wakefields even allow university-scale laboratories to generate γ-ray pulses. Particularly laser-driven plasma acceleration and ICS synergize well as they rely on intense laser systems and in principle offer inherent synchronization between all beams within small spatial footprint. As high electron beam quality is not necessarily required for exploiting the Doppler-shift, ICS offers decent experimental applications of plasma accelerators. The resulting radiation is commonly ultrashort, dense and collimated and exhibits spectral distributions typically about 10 % to 100 % *on-axis*, e.g. in the centre of the radiation pulse on the electron beam orbit [9, 11, 26, 29, 30, 34, 36].

Detailed investigations of nuclear physics and exploiting corresponding processes, however, often require well-defined peak energies $E_\gamma = \hbar\omega_\gamma$ with narrow absolute $\Delta\omega_\gamma$ and relative $\Delta\omega_\gamma/\omega_\gamma$ bandwidth, respectively. These demands together with high photon flux facilitate reliable operation and excitation of the effects of interest. All these properties together constitute –similarly to *brightness* in the context of electron beams– the quantity *brilliance*:

$$B_\gamma = \frac{N_\gamma}{\tau_\gamma \sigma^2_{\gamma,\theta} \sigma_{\gamma,x} \sigma_{\gamma,y} 0.1\%\ BW}. \tag{4.1}$$

It describes the quality of radiation pulses and allows for comparison of different approaches and facilities. Brilliance describes the number of photons N_γ within 0.1 % bandwidth (BW, or $\Delta\omega_\gamma/\omega_\gamma$) of the peak energy within duration τ_γ. All photons are emitted from an area called *source size* $\sigma_{\gamma,x} \times \sigma_{\gamma,y}$, given by the transverse overlap of electron beam and laser pulse, and diverge via $\sigma^2_{\gamma,\theta} = \sigma_{\gamma,\theta,x} \times \sigma_{\gamma,\theta,y}$, where the last two terms denote the divergence angles in x and y-direction, respectively. Typical values of measured single-shot, on-axis peak brilliance range from $B_{ICS} \approx 1.5 \times 10^{15}$ to 3×10^{22} photons s^{-1} mm^{-2} $mrad^{-2}$ $0.1\%BW$ [9, 32, 36]. γ-rays created by plasma-accelerated electron beams typically inherit ultra-high single-shot peak-brilliance because the electron beams are short and dense, but the average brilliance is low as a result of the repetition rate of the laser system of the order of 1 Hz.

The following chapter introduces the most relevant mechanisms generating γ-rays from ICS. These dependencies then allow discussing strategies that translate the ultra-high brightness electron beams from plasma photocathode wakefield accelerators into brilliant γ-ray pulses.

4.1 GENERAL DEPENDENCIES

Before introducing the more famous characteristics of ICS, the *stochastic* nature of this mechanism should be emphasised shortly. In the picture of particle-particle interactions, and very similarly to the arguments in Sections 2.2.2 and 2.2.3, the scattering rate depends on the densities of participating particles and the cross section being proportional to the probability of events taking place. The same applies to the electrons and photons interacting in ICS, and the governing cross section is of comparable magnitude as the *classical Thomson cross section*

$$\sigma_T \approx \frac{8\pi}{3} r_e^2 \approx 6.65 \times 10^{-29}\,\mathrm{m}^2. \tag{4.2}$$

This quantity represents a widely used low-energy approximation which neglects recoil of scattering electrons. More general formulations exist for both absolute and differential cross sections, e.g. the *Klein-Nishina formula* [138] or [139, 140] and references therein, but are beyond the scope of this work. σ_T is very small and almost diminishes compared to e.g. the 7 to 9 *orders of magnitude* larger cross section for impact ionisation of hydrogen gas (e.g. from Eq. (2.13)). That is why ICS unfortunately works very inefficiently, and the number of scattered photons is just a tiny fraction of the incoming photon pulse. Generating significant scattered flux therefore requires dense beams of electrons and photons.

The more general picture of the ICS process can be derived by integrating the *Lienard-Wiechert* potentials [140, 141]. This yields the *differential spectral photon flux density*

$$\frac{d^2 I}{d\omega d\Omega} = \frac{q^2}{16\pi_0^{\epsilon} c} \left| \int_{-T/2}^{T/2} dt[\vec{n} \times (\vec{n} \times \vec{\beta})] \exp\left[i\omega(t - \vec{n} \cdot \vec{r}/c)\right] \right|^2 \propto \frac{d\sigma_T}{d\Omega}, \tag{4.3}$$

which describes the energy spectrum per frequency $d\omega$ and solid angle $d\Omega$ emitted during the time T by a *single electron* [140]. The functions $\vec{r}(t)$ and $\vec{\beta}(t)$ describe the electron orbit and $\vec{n}$ is a unit vector pointing in the direction of observation. This expression generally describes the interaction of a single electron with an electromagnetic wave, and convoluting it with electron beam and laser pulse distributions yields a complete description of the final γ-ray pulse.

For electrons of relativistic energies $\gamma_e^2 \gg 1$ in the presence of a low-intensity $a_0 \ll 1$ laser field and for small scattering angles $\theta \ll 1$, it can be shown that Eq. (4.3) is proportional to the resonance function [26, 140]

$$R(\omega_\gamma, \omega_l) = \left(\frac{\sin(\bar{k}L/2)}{\bar{k}L/2} \right)^2, \tag{4.4}$$

where $L = N_0\lambda_l$ denotes the interaction length. It is given by number of periods N_0 the electron experiences oscillations in an electromagnetic field of wavelength λ_l. Further,

$$\bar{k} = k_\gamma(1+\gamma_e^2\theta^2)/(4\gamma_e^2) - k_l. \tag{4.5}$$

The resonance function in Eq. (4.4) has finite bandwidth given by

$$\Delta\omega_R = \int d\omega_l R(\omega_\gamma, \omega_l) = \frac{\omega_\gamma}{N_0}. \tag{4.6}$$

Equation (4.4) generates sharp peaks in the spectral flux density depending on the interaction duration (e.g. $N_0 \gg 1$) and Eq. (4.5), which relates the wave numbers of the laser pulse $k_l = \omega_l/c$ and the scattered radiation $k_\gamma = \omega_\gamma/c$. Setting $\bar{k} = 0$ yields the well-known energy relation of Compton scattering in the *head-on geometry*

$$E_\gamma = \hbar\omega_\gamma \approx \frac{4\gamma_e^2\hbar\omega_l}{1+\gamma_e^2\theta^2} \tag{4.7}$$

with resonant frequency ω_γ. Due to the γ_e^2-dependency resulting from two Doppler shifts, relativistic electrons can boost even optical or infrared photons of energy $E_l = \hbar\omega_l \approx 1\,\text{eV}$ –where state-of-the-art lasers can provide high photon density– into the x-ray or γ-ray regime. This equation is the key for any ICS source. It particularly addresses compact plasma accelerators because their electron output routinely reaches few hundreds of MeV, which is sufficient for the generation of MeV-level photons. The term $\gamma_e^2\theta^2$ is commonly small as almost all scattered photons are confined *within* a cone of opening angle

$$\theta_{\max} \approx 1/\gamma_e \tag{4.8}$$

centred on the electron beam axis as consequence of the Doppler shift [1, 4]. This means that scattered photons propagate in the same direction as the electron beam, regardless of the angle of incidence of the laser pulse. Clearly, this angular dependency decreases the scattered photon energy for increasing deviation from the electron beam axis. This effect causes an off-axis redshift, which can be exploited for selecting or limiting the final spectrum using apertures and collimators. However, because of the finite spread of incident angles of both the electron and laser distributions, spectral *cleaning* by small acceptances has limited effect [142].

Equation (4.7) inherits several approximations and can be further generalized for describing more relevant effects. Those are included in the following term (summarised in [51] and references therein) that describes the scattered photon energy of the n-th harmonic:

$$E_{\gamma,n} \approx \frac{2\gamma_e^2 E_l(1-\beta_e \cos(\alpha_i))}{1+\gamma_e^2\theta^2+4\gamma_e\frac{E_l}{m_e c^2}+\frac{a_0^2}{4}} \times n. \tag{4.9}$$

The nominator of this expression shows that maximal energy can be transferred from electron to photon if they scatter head-on, e.g. the angle of incidence $\alpha_i = \pi$ between laser photon and electron. Any deviating angle $\alpha_i \neq \pi$ reduces the achievable peak energy. The denominator now inhibits two additional terms causing further red shifts: the recoil term $4\gamma_e E_l/(m_e c^2)$ and the laser intensity $a_0^2/4$. The former expresses the momentum transfer from electron to photon and can be neglected for few interactions per electron and if the incident photon energy in the electrons rest frame is smaller than the particles rest energy, e.g. $E_{l,rest} \ll m_e c^2$, which is the *Thomson limit*. The single-particle interaction geometry captured by Eq. (4.9) is shown in Fig. 4.2.

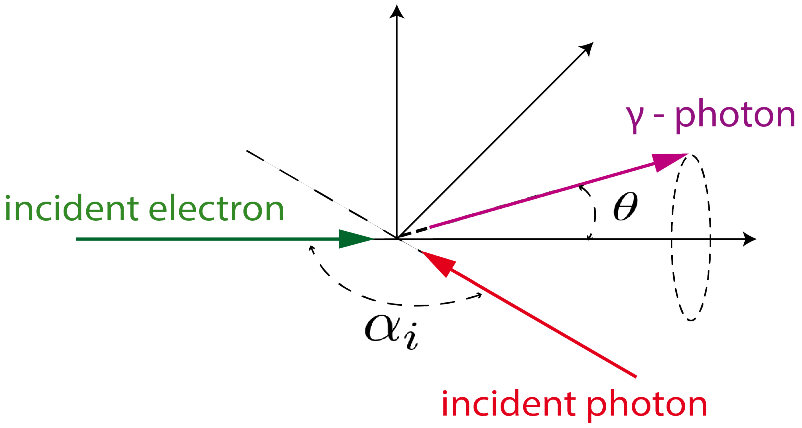

Figure 4.2: **Single-particle picture of Inverse Compton Scattering** A single photon, e.g. from a laser pulse, approaches an electron (green) under an angle of incidence α_i. If both particles interact, the photon experiences two Doppler shifts and obtains substantial energy from the electron. The resulting γ-photon is emitted along the electron propagation axis under the angle $0 \leqslant \theta \propto \gamma_e^{-1}$. The energy of the scattered photon decreases with increasing θ.

The laser term expresses the ponderomotive effect of intense fields with $a_0 \approx 1$ on electrons. This effect accelerates particles to relativistic energies within half an oscillation cycle of the field and increases their coupling with the magnetic field component of the laser. This results in varying *longitudinal* momentum, changes γ_e and causes anharmonic, figure-8-like trajectories. Emitted radiation therefore obtains a widened spectral distribution, but the number of scattered photons increases substantially. The same argument applies to higher harmonics, which require large laser intensity $a_0 \approx 1$ to yield significant photon flux [140]. These *nonlinear* interaction regimes can be mitigated by simply reducing the laser intensity, or deliberately entered by the opposite procedure [32, 143]. This work only considers the linear ICS regime for minimal bandwidth and to concentrate the whole photon distribution into the fundamental harmonic.

At this point another highly important characteristic of the scattered radiation should be mentioned. As the electric field of the incident laser pulse oscillates in a specific way, e.g. it is polarised either linearly or circularly, the interacting electrons follow this motion such that the emitted or scattered radiation inherits the same degree of polarisation [2]. This behaviour can also be seen from the dependence of the differential cross section on the degree of laser polarisation P [144]:

$$\frac{d\sigma}{d\Omega} \propto (1 + P\cos(2\alpha_p - 2\alpha_s)). \tag{4.10}$$

Here, α_s denotes the azimuthal angle of the scattered photon, and α_p is the angle between the plane of the polarisation of the laser and the coordinate system of the electron. As a consequence of this equation, linearly polarised ICS radiation displays an oval radial intensity distribution, e.g. its opening angle in the polarisation direction of the laser is larger than in the perpendicular plane. This can even cause a bone-like or *lobe* structure, as measured in [9]. Polarised γ-rays are beneficial for many applications, e.g. for photodisintegration studies or measurements of the parity of nuclear states [145]. Equation (4.10) also expresses that the transverse angular spread of the electron beam, e.g. its divergence, strongly influences the homogeneity of the ICS polarisation by means of α_p. As such, particularly low-emittance, low-divergence electron beams can yield a high degree of overall polarisation, while large divergence causes deteriorations [145]. In this work, only linearly polarised laser pulses are employed.

4.2 BRILLIANT γ-RAY PULSES

Next follows the introduction for generating brilliant γ-ray pulses from electron and photon *distributions*. Optimisation of pulse brilliance in Eq. (4.1) can be boiled down to very few connected relations introduced earlier.

Starting with optimising the number of generated photons N_γ also called *integrated dose*, the standard event rate for particle-particle interactions simply estimates this quantity to be [143]

$$N_\gamma \approx \frac{\sigma_T N_e N_l}{4\pi\sigma_x^2} \tag{4.11}$$

in the most efficient case where the transverse envelopes σ_x of electron and laser beams are identical such that both beam fully overlap. Here, N_e and N_l are the numbers of electrons and laser photons, respectively. This equation can become unprecise in practice, but outlines the linear dependencies on the number of involved particles and the strong influence of smaller laser spot size meaning higher laser intensity. More refined predictions for the number of scattered photons by focused lasers in vacuum and even the presence of plasma guiding the laser can be found in [9, 11]. It may be noted that the short interaction time between the laser pulse and the electron beam, the generated radiation is typically incoherent.

However, simply increasing the number of scattered photons by using more incident particles in electron or laser beams sooner or later is detrimental to the ultimate goal of high brilliance, as this partial victory comes at cost of massive spectral broadening and deterioration of the ICS pulse behaviour. Reasons are of fundamental nature: in practice, any particle distribution involves variations and spreads in all their parameters, which particularly applies to relativistic electron beams depending on their generation and acceleration process. On the optical side, higher laser intensity correspond to stronger nonlinear effects and shorter pulses to larger intrinsic bandwidth. Most of these problems arise directly from the ICS master equation Eq. (4.9) when considering multiple particles: each quantity changing the scattering energy also threatens the goal of high brilliance. Individual effects, e.g. explained and derived in [11, 139, 142, 146], can be summarised in an approximate, engineered formula yielding the relative scattered on-axis bandwidth

$$\frac{\Delta\omega_\gamma}{\omega_\gamma} \approx \sqrt{4\frac{\Delta\gamma_e^2}{\gamma_e^2} + \frac{\gamma_e^4\sigma_\theta^4}{16} + \left(N_{SC} 2\gamma_e \frac{\hbar\omega_l}{m_e c^2}\right)^2 + \frac{a_0^4}{4} + \frac{\Delta\omega_l^2}{\omega_l^2} + \left(\frac{M^2\lambda_l}{2\pi w_0}\right)^4}\,. \tag{4.12}$$

It describes a linear influence of electron beam energy spread $\Delta\gamma_e/\gamma_e = \Delta W_e/W_e$ and a strong, quadratic coupling between the electron beam divergence and its gamma factor expressed by $\gamma_e^2\sigma_\theta^2/4$, which broadens the spectrum particularly at elevated energies. As electron beam divergence and emittance are related, this term can also be expressed in terms of a quadratic dependence on beam emittance [9]. Further, the effect of multiple electron recoils also broadens the ICS bandwidth and is proportional to the number of scattering events N_{SC} per particle. This effect is typically small in the linear parameter regime as individual electrons scatter just once or few times during the interaction because of the small cross section [11]. This also means that the electron beam does not significantly deteriorate in the ICS process, which makes the interaction quasi-non-invasive and allows for diagnostic applications such as the *laser wire* [147]. The last three constituents relate to the laser pulse intensity, inherent bandwidth and the focal spread with beam quality factor M^2 describing deviations form Gaussian focusing. As this study investigates the applicability of *electron beams* from a plasma photocathode, their influence on Eq. (4.12) are of particular interest and subject to optimisation. In turn, all laser-related terms are excluded from deep analysis by setting them to typical, yet sufficiently small values such that they do not unnecessarily broaden the spectrum. It may be noted that maintaining high peak brilliance typically becomes increasingly challenging at elevated γ-ray energies because the spectral broadening described by Eq. (4.12) reduces the number of photons in the 0.1 % spectral band around the peak energy.

The scattered pulse duration is basically determined by the electron beam duration and energy, e.g. [4, 148]

$$\tau_\gamma \approx \frac{\sigma_z}{c} + \frac{\tau_l}{\gamma_e^4}. \tag{4.13}$$

γ-ray pulses from plasma accelerators are therefore intrinsically short and inherit durations on the few-femtosecond scale.

Finally, the effect of imperfect alignment and synchronisation between electron beam and incident laser pulse must be considered. Following [11], the transverse misalignment can substantially decrease the integrated dose as the overlap between beam and plasma foci changes, while longitudinal misalignment is typically small for current laser systems. Further, temporal jitter of common scattering lasers can be neglected as their pulse duration typically covers several Rayleigh lengths to provide high photon density for the whole time the electron beam traverses the laser focal region. However, the spatiotemporal overlap between laser and electron beam should be well-known and measured on a shot-to-shot basis to ensure optimal scattering efficiency, e.g. by the diagnostic developed in Chapter 6.

The combined effects of Eqs. (4.8), (4.9), (4.12) and (4.13) outline the requirements for a brilliant γ-ray source defined by Eq. (4.1). Generally, the electron beam energy is of primary importance as its quadratic scaling fundamentally causes the strong photon blueshift. It also strongly limits the scattered pulse duration to the electron beam length for relativistic energies and can reduce the opening angle of the cone containing most radiation. Thus, defining the target energy, e.g. for a specific nuclear application, automatically determines multiple parameters constituting the final brilliance.

The final step for optimising the γ-ray quality for demanding nuclear physics applications requires minimal spectral width. Low-energy spread electron beams are therefore required as this quantity sets the lower limit of the spectral γ distribution. Yet, the influence of beam divergence can massively exceed this value at electron energies larger than few hundreds of MeV due to the quadratic scaling, and thus is of particularly high importance. Beam divergence directly relates to beam emittance via $\epsilon_n \approx \beta_e \gamma_e \sigma_\theta \sigma_x$, such that ultra-small emittance is required for maintaining small divergence and beam radius simultaneously. At higher emittance, low divergence can be achieved at cost of large beam radius, which trades small bandwidth for reduced brilliance because of larger γ-ray source size $\sigma_{\gamma,x}$. Summarised, these dependencies demand that the electron beam source, e.g. a particle accelerator, must be considered as integral part of any ICS source, and optimising the electron beam yields improved pulse quality in terms of brilliance and bandwidth.

So far, conventional facilities such as HIγS [16, 17] precisely deliver requested energies up to $100\,\mathrm{MeV}$ combined with highest beam charge and by far lowest energy spread, and consequently provide highest integrated dose on target. These advantages must we weighted by the tremendous costs and large spatial footprint, rather high emittance and beam durations from hundreds of femtoseconds up to several picoseconds. Most of these sources achieve high brilliance from beam charge, repetition rate and intense laser pulses (HIγS even uses a free-electron laser). Most facilities deliver low bandwidth typically by application of apertures and monochromators such as [149], and sacrifice large fractions of their generated photon flux.

Plasma electron accelerators, in contrast, offer small spatial footprint at much lower costs, and routinely accelerate electron beams to $0.4\,\mathrm{GeV}$ to $4\,\mathrm{GeV}$ [66, 150, 151]. These energies allow for boosting photons up to some ten MeV [34, 36], and both quantities steadily increase with developing technology. The electron beams from plasma accelerators, however, have several to tens of percent energy spread [30, 33, 152] and large divergence because of their emittance and the strong transverse fields in LWFA, imprinting substantial transverse momenta to accelerated electron beams. Even beams with $\sim 1\,\mathrm{mrad}$ divergence inside a plasma wave, corresponding to $\epsilon_n \approx$

10^{-7} m rad [115], would broaden the ICS bandwidth to above 20 % for $\gamma_e \approx 1000$ (e.g. for 500 MeV electrons) [11]. This effect increases substantially for higher beam energies. Thus, electron beams must be decoupled from the plasma and refocused in a beam line to raise at least some hope for generation of narrow bandwidth radiation. Being linear accelerators, the beams can currently not be recycled or irradiate the same target multiple times with similar pulse properties. Combined with repetition rates of the order of 1 Hz and lower charges, plasma accelerators yield much lower integrated dose than a conventional facility. Summarised, even though experiments have shown high electron and γ-ray energies, the broad energy distributions and transverse velocity spreads cause deterioration of current ICS brilliance and prevents applications demanding narrow bandwidth without substantial spectral cleaning.

The plasma photocathode approach (e.g. see Section 3.4) could avoid fundamental problems inherited by plasma accelerators by generating brightest, ultra-low emittance electron beams. The ultra-low emittance facilitates small beam radius along with low divergence, which can completely suppress the associated spectral broadening for a huge parameter range and allow for low bandwidth even at high photon energies. Then, the spectral width of produced γ-rays is governed by the electron beam energy spread, which can be compensated by the technique developed in Section 8.2. As the ICS brilliance is optimised via quality-related properties, it compensates even low electron beam charge and integrated dose. Combined, ICS radiation obtained from plasma photocathode wakefield accelerated electron beams is expected to deliver high peak-brilliance, high energy and narrow bandwidth and presents a considerable advantages over most accelerators.

5

METHODOLOGY

Many aspects of this work involve highly complex interactions. These include plasma dynamics in the presence of strong dynamic electromagnetic fields, plasma wakefield acceleration and the plasma photocathode in a relativistic reference frame, and finally stochastic scattering between generated particle beams and intense laser pulses. All these topics employ huge, arbitrarily shaped particle distributions in their typically non-linear interactions, which are challenging to solve –or even express– analytically.

Addressing these issues caused development of highly specialised numerical methods. These allow precise definition of the physical problem and can include or exclude specific effects. Currently, substantial parts of whole experimental campaigns can be *simulated* such that researchers can investigate to be measured effects or address potential issues way in advance. Simulations also work the other way around, and can reveal effects and dynamics generating formerly inexplicable experimental results.

Depending on the complexity of the problem, normal computers or even high-performance clusters must be employed for simulations. But even then, the computational resources necessary for a 1:1 representation of all effects are immense and typically not feasible. This is why several strategies must be applied for reduction of information load. One major approach combines multiple, typically thousands of physical particles to so-called *macro particles*. Each of those represents a statistical distribution and behaves like its realistic counter part, yet reduces the computational load substantially. Problems involving electromagnetic fields are commonly solved on a grid, which spans the spatial interaction region. The corresponding cell sizes Δx, Δy, and Δz reduce the computational load, but must be sufficiently small to sample the physical effects of interest. The same applies to the finite time step Δt, which must be sufficiently small to resolve dynamics of interest.

The following sections describe the two major simulation tools applied in this thesis. The first one known as *particle-in-cell simulation* (PIC) is broadly used in plasma and plasma accelerator science. The second one describes a software capable of generating ICS pulses from arbitrary particle distributions. Both codes solve highly complex physical problems which are not accessible by means of analytical models.

5.1 PARTICLE-IN-CELL SIMULATIONS

5.1.1 *Concept*

Particle-in-cell simulations are the most advanced tool for simulating electrodynamics and plasma physics, e.g. used for [21]. Their general structure provides a self-consistent set of operations that solves Maxwell's equations for electromagnetic fields and charged particles, and moves the latter by means of the Lorentz force. Technically, this calculation is done by means of a *finite difference time domain* (FDTD) scheme also known as *Yee's method* [153]. It describes electric $\vec{E}$ and magnetic $\vec{B}$ fields on two grids shifted against each other by half a cell (*Yee grid*). Dynamics result from solving the time-dependent Maxwell equations approximated by central-difference stencils with the leapfrog algorithm. The latter periodically solves the electric field in a specific grid cell at one time, and the magnetic component one instance of time later. In PIC codes, these two operations together represent one time step. The latter is commonly defined as

$$\Delta t \leqslant (\Delta x^{-2} + \Delta y^{-2} + \Delta z^{-2})^{-1/2}/c, \tag{5.1}$$

which is called *Courant condition* [154] and closely couples to the grid size. Simulations fulfilling this inequality converge numerically.

After solving the electromagnetic fields, charged particles are moved based on their own phase space and the calculated fields. This process is referred to as *particle pusher*, which typically follows the highly stable Boris formalism [155]. In PIC codes, the push consumes most computational resources as it must be applied to each particle individually. Even in case that macro particles are used, typically more than 1×10^6 operations per time step must be carried out. The resulting charge and current distributions after the push are then again transformed into electromagnetic fields and the whole process advances by another time step. This PIC cycle is shown in Fig. 5.1.

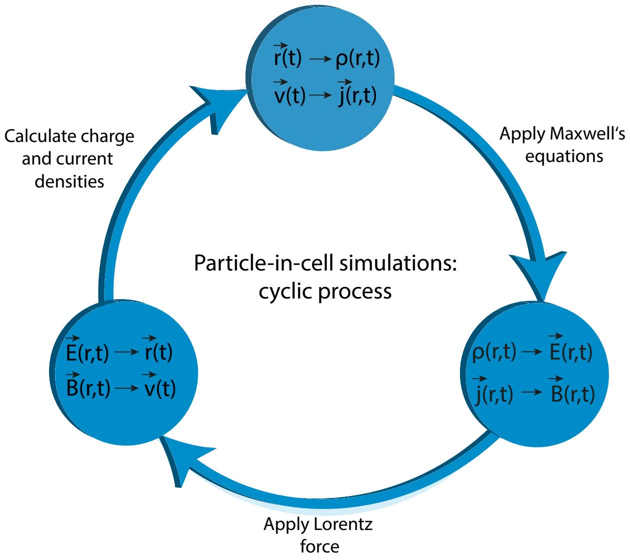

Figure 5.1: **PIC cycle.** In each time step, one complete cycle of different actions is performed. Macro-particle positions $\vec{r}(t)$ and velocities $\vec{v}(t)$ are transformed into densities $\rho(t,r)$ and currents $\vec{j}(r,t)$. These yield, based on Maxwell's equations, the current state of the electric $\vec{E}(r,t)$ and magnetic $\vec{B}(r,t)$ fields in the leapfrog method. Finally, the particle pusher applies the Lorentz force on all macro particles and the cycle continues with the next time step. Figure taken from [51].

This work simulates all electron beam-plasma interactions with *VSim* [156], a highly parallelised PIC code optimised for high-performance computing with large numbers of processors. Simulations with this code take place within a simulation box, which is decomposed in sub-domains individually solved by a single processor such that even large numbers of macro particles can be sustained.

VSim facilitates arbitrary particle distributions, e.g. for defining electron drive beams, modulated plasma channel distributions and other plasma target geometries. Typically, at least one macro *particle per cell* is required for homogeneous distributions with not too many particle per macro, e.g. 1×10^4 to 1×10^5. If expressed as higher order particles, they cause smooth charge density and current fields within the PIC cycle. Increased number of particles per cell yield better resolution at the cost of more expensive particle pushes. Additional current smoothing also helps for accurately solved electromagnetic fields. These depend on the cell size of the Yee grid and small cells resolve finer effects. As this quantity couples with the time step and the particles per cell, small grid size rapidly causes tremendous computational costs: in 3D grids, the number of cells to be solved scales roughly with the third power of cell size.

The code further offers various side packages to model additional effects. In this work, particularly tunnelling ionisation based on ADK theory expressed by Eq. (2.10) is used extensively, e.g. when simulating a plasma photocathode. The corresponding algorithm calculates the ionisation rate in each cell and creates additional particles such as electron-ion pairs from neutral gas macro particles or fluids. These are then subject to the ambient electromagnetic fields and, for example, form a witness beam getting accelerated in a blowout.

5.1.2 *Challenges*

Although PIC codes offer large capabilities in simulating complex electrodynamic problems, they do have intrinsic weaknesses and instabilities.

The first and most crucial one relates to the grid resolution, which causes high costs for small grid size. This is particularly problematic for a plasma photocathode, as its physics evolves on three different length scales. The largest one is associated to the plasma accelerator in terms of the drive beam and its excited blowout with $\lambda_p \approx 100\,\mu\mathrm{m}$ to $300\,\mu\mathrm{m}$ in all three spatial directions.

The second one relates to the witness beam, which is typically few micrometres long and wide and therefore substantially smaller than the blowout. As VSim does not support variable or adaptive cell size, the whole simulation box must be sampled on resolution of the witness beam. This can become highly expensive and even prohibitive for the desired long plasma wavelengths yielding optimal beam quality (e.g. see relations in Section 3.4). Fortunately, the linear transverse fields in the blowout regime in principle allow for comparably large transverse cell size without sacrificing significant physical information.

The last length scale relates to the injector laser creating the witness beam: as the laser wavelength is typically $0.8\,\mu\mathrm{m}$ [41] or even less [56, 157], fully resolving its oscillating field is far beyond responsible use of computational resources in three dimensions, particularly at long plasma wavelengths. This is why all laser pulses in this thesis are implemented in an envelope model using the paraxial approximation for Gaussian beams. Then, the laser pulse is expressed as unipolar electric field following the envelope equation. Combined with an averaged ADK model, this field approximates ionisation sufficiently well as long as its small intensity would not transfer significant energy to released electrons, e.g. $a_0 \ll 1$. Even though this approach lifts some restrictions regarding resolution, the laser field must still be sufficiently well sampled, otherwise its spatial information will cause poorly defined ionisation volumes. The envelope approximation further neglects heating of ionised particles, which would require a properly resolved laser pulse. As the envelope approximation neglects coupling between the laser field and the plasma, its propagation is not self-consistent. Effects such as dispersion, spectral broadening or ionisation-defocusing are not included. Operation at low laser intensities avoids these relativistic effects and reduces complexities of laser beam control and propagation when compared to simulations of LWFA. Interestingly, while the laser pulse propagates inside the electron-cavitated plasma blowout behind the driver beam, such effects would be completely absent due to lack of plasma electrons.

Other issues are connected to the finite grid size for electromagnetic fields. As a consequence of the Yee algorithm, electromagnetic waves on this grid travel slower than the speed of light, and particularly slower than highly relativistic particles along their axis [158, 159]. This unphysical dispersion causes emission of electromagnetic waves known as *numerical Cerenkov* radiation. These waves in turn couple to the particles and can modulate the 6D phase space of a trapped beam and cause emittance growth [160]. Next to highly increased resolution, controlled dispersion schemes can address this issue partially [161].

Another effect observed in PIC simulations causes unphysical beam loading. Particularly dense, narrow beams such as witness beams are typically not sufficiently well sampled because of lacking computational resources. This obstacle creates substructures within the longitudinal wake field along a loaded region, as can bee seen in [113] and even stronger in [133], where numerical Cerenkov adds further disturbances. Here, only extremely small longitudinal cell size along with large numbers of macro particles yields satisfying results. [162] has investigated this effect by systematic scans in PIC.

5.2 COMPTON SCATTERING CODE

A second code called COMPTON [139] simulates the ICS interaction between particle distributions generated in VSim and a 3D laser pulse. This code has been benchmarked against experimental data obtained at PLEIADES [15]. This section shortly introduces its underlying maths and assumptions.

The fundamental equation in this algorithm describes the differential scattering rate per solid angle $d\Omega$, frequency $d\omega_s$, and unit time dt expressed as [139]

$$\frac{dN_s}{d\omega_s d\Omega dt} = c\left(1 - \vec{\beta}_e \cdot \vec{k}\frac{c}{\omega}\right) n_\gamma \frac{d\sigma}{d\Omega}\delta\left[\omega_s - \omega g(\theta)\right]. \tag{5.2}$$

Here, $\vec{\beta}_e$ represents the electrons dimensionless velocity vector, $\vec{k}$ the laser pulse wave vector and ω its frequency. n_γ is the Lorentz-invariant number of scattered photons, e.g. identical in the laboratory and electron rest frame. ω_s denotes the angular frequency of the scattered photon and $g(\theta)$, closely related to Eq. (4.9), represents its relativistic Doppler shift as a function of the scattering angle θ. Using the differential Thomson cross section $\frac{d\sigma}{d\Omega}$ requires the scattering to be linear, e.g. the formula neglects electron recoil and assumes small normalised intensity $a_0 \ll 1$. Further, space charge effects during the interaction time with the laser must be small.

Integrating Eq. (5.2) over an arbitrary 6D electron beam phase space distribution $f_e(\xi_{xe}, \xi_{ye}, \gamma_e, \mathbf{r}_e(t = 0))$ containing N_e particles yields the final photon spectral density flux

$$\frac{dN_T(\theta, \phi, \omega_s, t)}{d\omega_s d\Omega dt} = N_e \int f_e(\xi_{xe}, \xi_{ye}, \gamma_e, \mathbf{r}_e(t)) \frac{dN_s(\xi_{xe}, \xi_{ye}, \theta, \phi, \omega_s, t)}{d\omega_s d\Omega dt} d\xi_{xe} d\xi_{ye} d\gamma_e d^3r. \tag{5.3}$$

This expression yields the temporal, spatial, and spectral photon flux for an ICS scattering event between an electron beam and a focused laser pulse. The angle ϕ denotes the azimuthal laser observation angle, and the angles ξ_{xe}, ξ_{ye} denote the angle of individual electrons deviating from the beams propagation axis. Note that this formalism only captures incoherent superposition of scattered photons.

The code calculates the number of scattered photons per solid angle and frequency for each time step and electron macro particle on a detector plane located at arbitrary observation angle and distance. Eventually, it yields the integrated dose and radiation source size, the projected intensity distribution and the temporal and spectral density observed by the detector screen.

Part II

RESULTS

Based on the preparatory considerations introduced earlier, the following part describes the studies carried out during this work and presents major results. First, a novel approach for the precise diagnosis of the spatiotemporal overlap between intense electron and laser beams is presented, which has been investigated theoretically and experimentally. This technique has substantially contributed to the first experimental demonstration of the plasma photocathode presented afterwards, which promises electron beam quality far beyond of any other accelerating scheme. Combined with a short overview of a newly developed method for the compensation of correlated energy spread in plasma accelerators, all these findings amalgamate and form a conceptual study on the generation of brilliant multicolour gamma ray pulses.

6

PLASMA-BASED ALIGNMENT AND SYNCHRONISATION

Spatial and temporal coordination of electron and laser beams is of major importance for many applications such as exciting and probing ultrafast processes in ultrasmall structures of all states of matter [37, 163, 164]. Large errors in alignment and time-of-arrival (TOA) can substantively change the triggered and excited physics or even prohibit experimental success, e.g. if the target is missed in space and time.

Free-electron lasers, for example, benefit from stable electron beam orbits at the centre of an undulator, or require well-defined overlap of seed lasers and electron beams [165]. The same applies to diagnostic applications [166]. For inverse Compton scattering acting as radiation source [14, 26, 29, 33] or diagnostic [167, 168], the scattering laser must precisely hit the electron beam well-timed as discussed in Chapter 4.

Similarly, advanced plasma accelerators [41, 169–172] demand for controlled coordination of laser pulses, electron beams and plasma waves with high accuracy. Particularly the plasma photocathode introduced in Section 3.4, which decouples plasma wave and electron beam generation, requires a laser precisely hitting a specific phase in a $\sim 100\,\mu\mathrm{m}$ small wake field moving at the speed of light. Eventually, however, all plasma accelerators must diagnose and control the spatiotemporal coincidence of laser and electron beams as natural consequence of the ultra-small accelerating structures and beams, specifically when staging concepts discussed in Section 3.5 are required for extending the acceleration length for truly high electron energies. The plasma photocathode scheme pulls these requirements into the spotlight, as it relies on spatiotemporal overlap at the very starting point of the plasma accelerator. Summing up, precise coordination of laser and electron beams is of paramount importance for the realization and exploitation of basically any plasma-based accelerator scheme.

Synchronisation and alignment of relativistic electron and laser beams therefore represents an integral challenge for both brilliant photon sources and particle accelerators that must be overcome. In the context of this work, a high level of spatiotemporal stability is required firstly for the low-emittance electron beam generation and secondly for the subsequent, high-quality scattering event. As both stages of a combined light source define the γ-ray brilliance, spatiotemporal drifts and jitter must be accurately measured and compensated.

State-of-the-art diagnostics typically measure *either* TOA *or* alignment. For example, beam viewer or optical transition radiation (OTR) screens quantify spatial alignment and electro optic sampling (EOS) crystals [173, 174] characterise temporal coincidence. These techniques must be placed at different positions of a beam line because of their spatial footprint: they typically exclude each other as they require close proximity to the electron or laser beams, exposure or even passage of either beam through a detector material. In addition, diagnostics exploiting direct interactions generally prohibit application at high intensities due to their material damage thresholds. Typical cases are focused or ionising beams with intensities above the material damage or ionisation threshold, or the presence of plasma in novel accelerator concepts. Consequently, these techniques rely on operation at attenuated intensity levels or must be placed away from the relevant interaction point of an experiment. This can hide crucial information as results obtained conventionally, e.g. in low-power modes or far away from the interaction point, inherently imply considerably reduced accuracy and resolution.

This chapter describes a novel plasma-based technique developed during the E-210 collaboration campaigns at the Facility of Experimental Tests (FACET) at the Stanford Linear Accelerator Center. This diagnostic measures the temporal and spatial overlap of the relativistic, dense FACET electron beam with a focused, ionising laser pulse within one and the same setup. As the author was the principal investigator for the experimental and theoretical exploration and analysis of this part of the E-210 efforts (manuscript submitted to peer-review [175]), this study represents a major project within this thesis. The following chapter is a synopsis of this work.

6.1 CONCEPT

Before describing the actual experiment in the following sections, the fundamental physics of the diagnostic must be established. It exploits the response of a thin, bounded plasma column generated by a laser pulse focused into a gas reservoir at sub-atmospheric pressure. Following the short introduction in Section 2.2 and [77], released plasma electrons gain modest kinetic energy of about ~100 eV from the ionising laser field, while the much heavier ions remain almost undisturbed. Laser-based ionisation generates sharp plasma boundaries because of the strong dependence of tunnelling ionisation rate on laser intensity (e.g. recall the ADK model in Eq. (2.10)). This corresponds to a steep pressure gradient between the non-equilibrium plasma electrons and the ambient neutral gas. Consequently, electrons are driven out of the initial plasma filament during shock expansion at the speed of sound, and the ions are pulled along via strong Coulomb fields [77]. After several nanoseconds, the resulting plasma density profile displays almost parabolic radial shape, which is commonly used for guiding intense laser pulses [176–178]. As the expansion ends eventually, the plasma constituents can thermalise and recombine, emitting the afterglow signal characteristic to the employed gas species [75, 179]. Further heating the initial plasma electron distribution, e.g. by a second laser pulse [77, 180], changes the plasma dynamics such that the afterglow emission increases.

In the early stage of the E-210 campaign at FACET, a differently triggered yet pronounced amplification of the afterglow signal has been observed after a dense, relativistic electron beam has propagated within a plasma channel or traversed a small, confined filament generated in the beam path. Figure 6.1 compares the very different afterglow signals emitted by the laser-only plasma and one where the electron beam has heated the filament.

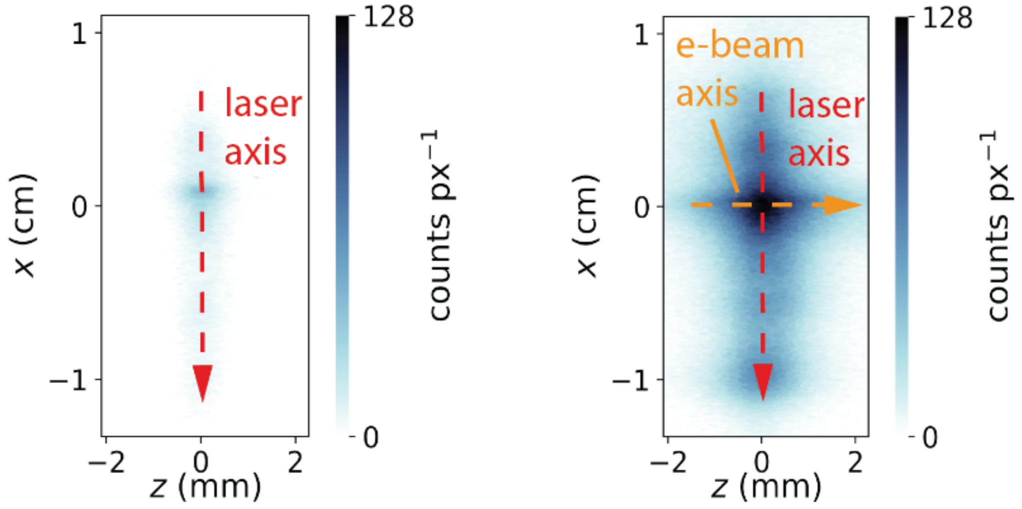

(a) Laser-only afterglow

(b) Amplified afterglow

Figure 6.1: **Comparison of measured plasma afterglow signals**. Raw images of the laser focal region are taken by a CCD camera with 25 ms integration time attached with a bandpass filter centred on the He-I spectral line at $\lambda_{\mathrm{He}} \approx 587\,\mathrm{nm}$. The intense laser propagates in the negative x-direction. **(a)** The laser-only afterglow signal displays a confined extent. **(b)** The electron beam propagates from left to right at $x \approx 0\,\mathrm{cm}$. Its interaction with the pre-formed plasma filament substantially and globally amplifies the afterglow in terms of larger volume and higher signal amplitude. The former increases from ~$8.40 \times 10^{-3}\,\mathrm{cm}^3$ to $0.13\,\mathrm{cm}^3$ (r.m.s) corresponding to a factor of ~15 assuming rotational symmetry. The integrated counts increase from ~6.23×10^4 counts to 2.64×10^6 counts (r.m.s), which corresponds to a factor of ~42. Images produced by the author for [175].

In order to understand the involved dynamics and pronounced differences to laser-based heating in more detail, three-dimensional (3D) particle-in-cell (PIC) simulations model the interaction with experimental parameters (for more details see Section 6.2) using the code VSim [156]. The corresponding three-dimensional box consists of $633 \times 533 \times 266$ cubic cells of size $3\,\mu\mathrm{m}$ in each direction for all shown simulations except for the scan in Section 6.2.2, which is set up in a box with $399 \times 333 \times 466$ cells. The 6D-Gaussian electron beam inherits 16 macro particles per cell, and is initialised by a Poisson solve at the beginning of the simulation in vacuum. It carries a total charge of $3\,\mathrm{nC}$ and provides a central energy of $20\,\mathrm{GeV}$. The beam dimensions are $\sigma_z \approx 64\,\mu\mathrm{m}$, $\sigma_x \approx 22\,\mu\mathrm{m}$ and $\sigma_y \approx 44\,\mu\mathrm{m}$ (all r.m.s), which corresponds to a particle density $n_b \approx 1.1 \times 10^{22}\,\mathrm{m}^{-3}$. The beam propagates through a neutral gas medium consisting of helium and hydrogen which is modelled by 8 nominal macro particles per cell each. This gas is ionised by a Gaussian laser pulse of $5\,\mathrm{mJ}$ compressed to $\tau_l \approx 60\,\mathrm{fs}$ (FWHM) focused to $w_0 \approx 38\,\mu\mathrm{m}$ (r.m.s), which corresponds nominally to a Rayleigh range of $z_R \approx 5.6\,\mathrm{mm}$. The electron beam traverses the resulting plasma filament of electrons density $n_p \approx 1.9 \times 10^{23}\,\mathrm{m}^{-3}$ with diameter $d_{\mathrm{plasma}} \approx 100\,\mu\mathrm{m}$. The interaction between beam and plasma happens in the *overdense* regime as $n_b/n_p \approx 0.1$, and triggered dynamics are shown in Fig. 6.2. The electric fields of the electron beam couple briefly with the plasma filament for a duration given by $\tau_{\mathrm{int}} = \tau_{\mathrm{beam}} + d_{\mathrm{plasma}}/c$ and accelerates surrounding electrons. Due to the brevity of this process, the beam transfers just a tiny fraction ($0.93\,\mathrm{mJ}$) of its total kinetic energy $W_{\mathrm{kin,total}} = 67\,\mathrm{J}$, e.g. approximately 0.001 %, making the process almost non-invasive. Similarly, effects related to overdense plasma lensing or linear plasma waves (e.g. see Section 3.1.1) can be neglected for this thin column.

In contrast to an *oscillating* laser field heating the plasma due to its ponderomotive force, which is a second order effect and requires high field intensities, the *unipolar* field of the electron beam transfers energy much more efficiently regardless of its significantly smaller amplitude. This behaviour analogously facilitates PWFA and the plasma photocathode, where the unipolar drive beam fields are capable of driving a blowout without simultaneously ionising any ambient (dopant) gas. In the given setup, the immediate range of this energy transfer from electron beam to plasma is strongly confined along the direction of the filament as plasma electrons rapidly screen the fields (e.g. $\lambda_D \approx 4\,\mathrm{nm}$, see Section 2.1.2, and $k_p^{-1} \approx 12\,\mu\mathrm{m}$, see Section 2.1.1).

Plasma electrons *within* the vicinity of the beam get accelerated to non-relativistic, broad-band velocities with peak energies up to hundreds of keV, and get partially expelled from the column. The simulations further reveal multiple highly complex electronic dynamics triggered by this initial interaction. When the electron beam passes the plasma boundaries, an electromagnetic pulse launches and associated surface waves are excited (a decent overview can be found in [181] and references therein). The latter are shown in Fig. 6.3 and exhibit electric fields of comparable magnitude as the beam fields themselves, transport the initial perturbation along the overall plasma filament and heat electrons which are not directly affected by the near-field of the electron beam.. Their existence and importance arises from the *finiteness* of the ionised column with respect to the electron beam dimensions. Inside the filament, currents and density waves accompany the surface waves and further distribute parts of the initial energy.

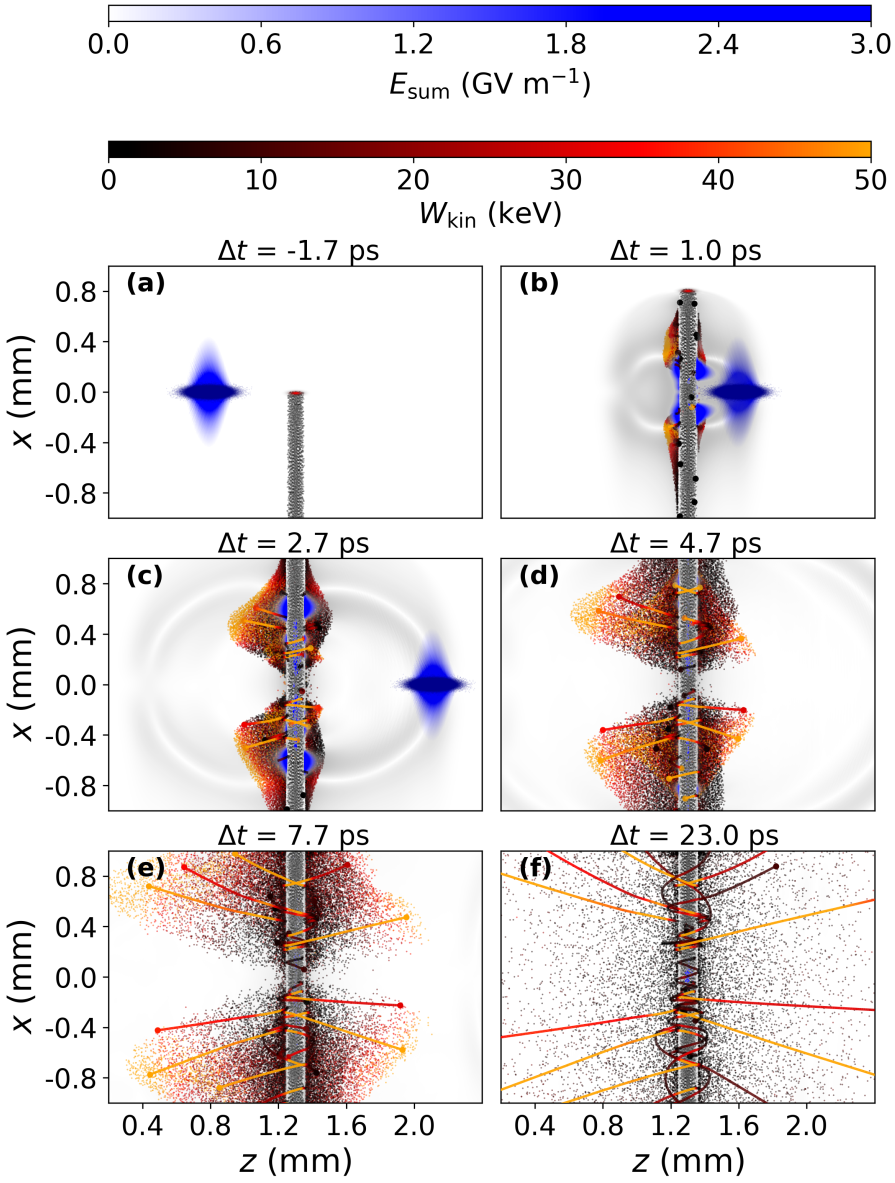

Figure 6.2: **Snapshots from particle-in-cell simulation.** **(a)** The FACET electron beam propagates in positive z-direction through a neutral hydrogen/helium gas mixture. A focused laser pulse generates a thin plasma filament along the perpendicular x-direction shortly before the beam arrives. **(b)** The beam crosses the filament and transfers energy to plasma electrons in its close vicinity. In addition, an electromagnetic pulse is launched accompanied by surface waves of amplitude comparable to the beam fields. These propagate along the filament, further heating and expelling plasma electrons far away from the beams reach as shown by **(b)-(d)**. In **(e),(f)**, large fractions of accelerated electrons propagate on oscillating trajectories around the initial filament volume as indicated by selected coloured trajectories. In the surrounding neutral gas, these electrons have particularly low kinetic energy located close to the peak of impact ionisation cross section shown in Fig. 2.4. Figure produced by the author for [175].

Finally, the attractive potential generated by the ions causes many expelled electrons to oscillate around the filament, e.g. they undergo *local*, confined motion. As the plasma wavelength $\lambda_p \approx 80\,\mu m$ is of comparable size as the diameter $d_{plasma} \approx 100\,\mu m$ of the filament, these oscillations are inherently anharmonic. Several of these electrons therefore periodically propagate in ambient neutral gas, where their kinetic energies are particularly low.

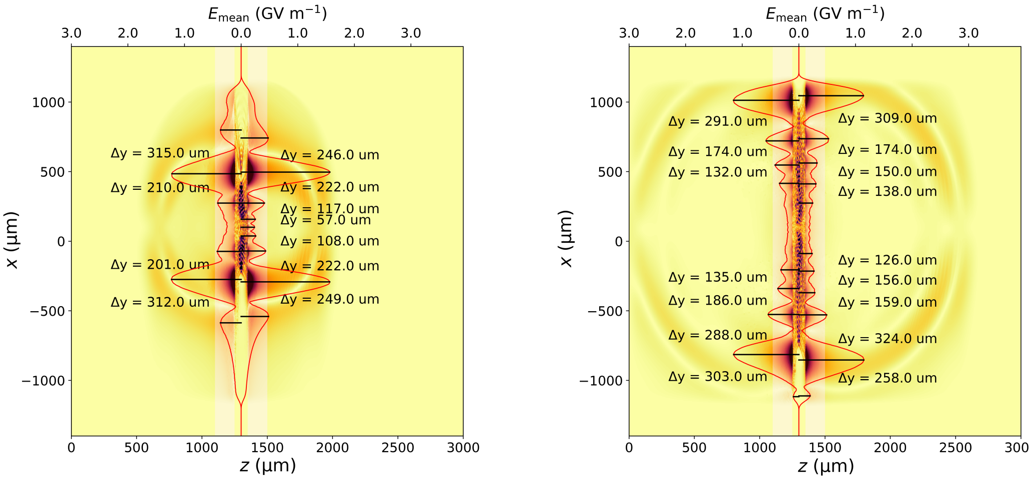

(a) Electric fields associated to the plasma ~1.5 ps after the electron beam has passed

(b) Electric fields associated to the plasma ~1.8 ps later

Figure 6.3: **Evolution of plasma surface waves**. This figure consists of snapshots from the simulation shown in Fig. 6.2. **(a)** The interaction between the electron beam (not shown) and the plasma filament centred on $z = 1300\,\mu m$ launches an electromagnetic pulse (EMP, expanding wave structure) that propagates with the speed of light away from the filament. This pulse is accompanied by surface waves (black-red contours) excited at $x = 0\,\mu m$ where the beam has passed the plasma. These waves are attached to the plasma boundary and do not reach inside its initial volume. It may be noted that the surface waves propagate along the filament at lower speed than the EMP in vacuum, which is characteristic for them [181]. The red line represents the absolute electric field component E_{mean} averaged over each slice in x, and peak values are of the order of $E_{mean,p} \approx 1.6\,GV\,m^{-1}$. The black horizontal lines mark the individual peak positions, and their spacing is indicated by various Δy-values. **(b)** After ~1.8 ps, several additional maxima with reduced amplitude appear and follow the maximum peak in decreasing distances Δy. The overall Bessel-shaped field structure transports the initial perturbation induced by the electron beam along the filament.

The measurements shown in Fig. 6.1 convey substantially amplified plasma afterglow signal. Particularly, the plasma response reaches well beyond the initially, laser-generated *seed plasma* bounds and its integrated number of counts increases substantially. For the displayed images and assuming rotational symmetry of the filament, the observed volume grows from ~$8.40 \times 10^{-3}\,\mathrm{cm}^3$ to $0.13\,\mathrm{cm}^3$ (r.m.s) corresponding to a factor of ~15. Meanwhile, the integrated counts increase from ~6.23×10^4 counts to 2.64×10^6 counts (r.m.s), which corresponds to a factor of ~42. By means of the quantum efficiency of the camera, the solid angle of the imaging system and the transmission factor of the bandpass filter, the total number of generated photons with $\lambda_{\mathrm{He}} \approx 587\,\mathrm{nm}$ can be estimated as 4.54×10^8 for the laser-only case and 1.92×10^{10} for the amplified afterglow signal. The initial seed charge can be approximated by inserting the given laser parameters into the ADK theory used in Chapter 3 and Fig. 3.7 and integrating over the resulting plasma volume, which yields $10.90\,\mu\mathrm{C}$ for the combined charge of helium and hydrogen plasma. The laser-only plasma therefore emits ~6.67×10^{-6} photons with wavelength $587\,\mathrm{nm}$ per electron, and only ~1.73×10^{-9} photons with wavelength $587\,\mathrm{nm}$ per electron are actually collected by the camera due to the small solid angle and the detection efficiency.

Consequently, the induced heating must generate significant amounts of additional plasma compared to the laser-only case. As discussed earlier, plasma electrons expelled by the interaction with the electron beam or succeeding plasma dynamics oscillate around the initial filament with energies close to the peak of impact ionisation (e.g. see Fig. 2.4). Combined with massive Coulomb expansion of the remaining ions, this effect causes additional ionisation depending on the long-term dynamics inside the plasma. Hydrodynamics and shock expansion discussed above for the laser-only case happen on longer time scales. All these effects cumulate in the recombination and relaxation of the overall plasma and generate the observable afterglow. Connecting the initial interaction with the emitted signal amplitude turns out to be challenging as the finiteness of the plasma breaks many common assumptions and the complex electrodynamics require highly advanced treatment far beyond this study (e.g. see [182]).

Regardless of this obstacle, the obtained experimental and conceptual results yield two very important consequences. Firstly, the afterglow signal increases *substantially* and *globally* along and across the seed plasma filament after passage of the electron beam. Secondly, the effective range of the electron beam is *strongly confined* due to Debye shielding. The transferred energy available for plasma dynamics and the subsequently emitted afterglow signal therefore distinctively change with varying spatiotemporal *overlap* volumes of electron beam and plasma. As the latter gets generated by the laser, these dependencies can be exploited for measuring the degree of spatial and temporal coincidence of electron beams and ionising laser pulses.

6.2 RESULTS

6.2.1 *Setup*

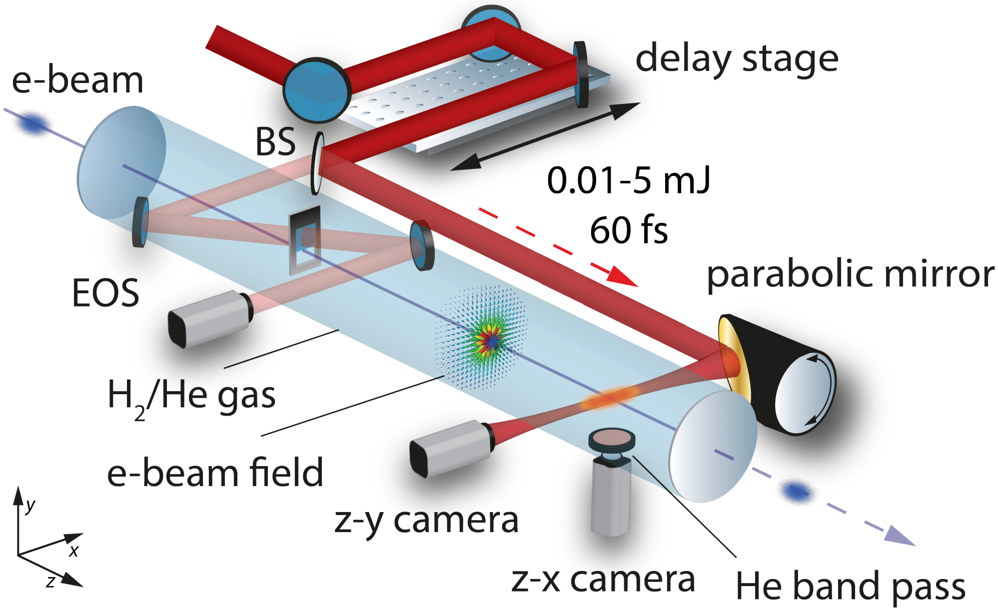

Figure 6.4: **Experimental layout.** Experimental setup at FACET. The electron beam propagates in the z-direction through a H2/He gas mixture and its transverse electric field signature is imprinted upon a laser pulse when it passes by a gallium phosphide (GaP) crystal for electro-optic sampling (EOS). A beam splitter (BS) sends the main laser arm downstream, where an off-axis parabolic mirror (OAP) focuses it to produce a narrow plasma filament perpendicular to the path of the electron beam. The interaction point is monitored by two CCD cameras, one for diagnosing the laser and the other one, attached with a helium bandpass filter, for observing the interaction. The laser can be delayed with respect to the electron beam time-of-arrival by means of a mechanical stage. Similarly, the OAP can be rolled in y-direction for introducing spatial displacement between electron beam and laser axis. Figure produced by the author for [175].

In the experimental setup shown in Fig. 6.4, the FACET electron beam provides energy $W = 20.4\,\mathrm{GeV} \pm 2.0\%$ (FWHM) and charge $Q = 3.0\,\mathrm{nC} \pm 0.6\%$ (r.m.s.) within its r.m.s.-dimensions $\sigma_z \approx 64\,\mu\mathrm{m} \pm 1.9\%$, $\sigma_x \approx 22\,\mu\mathrm{m}$ and $\sigma_y \approx 44\,\mu\mathrm{m}$ (uncertainty unknown). It traverses a multi-litre chamber homogeneously filled with a gaseous mixture of H_2 and He in 1:1 ratio at $5.3\,\mathrm{mBar}$. The repetition rate of $1\,\mathrm{Hz}$ ensures that any plasma thermalises and recombines, and that the re-established gas mixture assumes a homogeneous distribution before the next shot. At the beginning of this interaction chamber, the electric field of the electron beam is superimposed in a gallium phosphide crystal for EOS with a collimated, low-intensity split-off fraction of the 800 nm Ti:Sapphire main laser pulse compressed to $\tau_l \approx 60\,\mathrm{fs}$. The EO crystal is placed a few millimetres away from the electron beam orbit and gets irradiated by the laser at an angle of 45°. This benchmarking diagnostic provides relative shot-tot-shot TOA information and its characterisation yields TOA resolution $\tau_{\mathrm{EOS}} = 25.8 \pm 2.5\,\mathrm{fs\,px^{-1}}$ [105, 183] along with the facility-inherent TOA jitter between laser pulse and electron beam as $\Delta t_{\mathrm{FACET}} = 109 \pm 12\,\mathrm{fs}$. The major fraction of the laser pulse carries $E_l = 4.9 \pm 0.1\,\mathrm{mJ}$ and is focused by an off-axis parabolic mirror (OAP) perpendicular to the electron beam orbit. Approximately one metre downstream of the EOS, the laser generates a several millimetre long plasma column at the electron beam focus. The density of this filament is approximately $n_p \approx 1.9 \times 10^{23}\,\mathrm{m^{-3}}$ because ADK theory predicts full ionisation of molecular hydrogen and the first level of helium for the delivered pulse intensity $I_l \approx 3 \times 10^{15}\,\mathrm{Wcm^{-2}}$ [105]. A dedicated CCD images the lasers focus and yields strong evidence of astigmatism at a spot size of approximately 38 µm by 40 µm [105]. The pointing jitter of this laser amounts to $\sigma_{j,l,x} \approx 9.4\,\mathrm{\mu m}$ and $\sigma_{j,l,y} \approx 7.6\,\mathrm{\mu m}$ (all r.m.s.), while the electron beam orbit measured by ~100 shots on a removable OTR screen jitters by $\sigma_{j,b,x} \approx 4.2\,\mathrm{\mu m}$ and $\sigma_{j,b,y} \approx 6.6\,\mathrm{\mu m}$ [184] and can be seen in Fig. 7.7. Since the jitter in y-direction changes the electron beam-plasma overlap, the corresponding error values can be combined by means of error propagation to yield the effective shot-to-shot alignment jitter $\sigma_{j,\mathrm{eff},y} \approx 10.1\,\mathrm{\mu m}$. A second CCD camera attached with a 10 nm-wide bandpass filter centred on the strong helium-I spectral line at $\lambda_{\mathrm{He}} \approx 587\,\mathrm{nm}$ [185] monitors the interaction region and images the afterglow signal originating from this specific line with 25 ms integration time. The quantum efficiency of this camera is ~53 % for the spectral range of the band pass filter. The effective solid angle observed by this camera amounts to $\sim 4.65 \times 10^{-3}\,\mathrm{sr}$, which corresponds to $\sim 3.70 \times 10^{-2}\,\%$ of the 4π-sphere. As such, only a tiny fraction of emitted photons is actually detected.

From analysing the laser-late afterglow region, e.g. when the electron beam arrives before the laser pulse, the dataset shown in Fig. 6.7 yields the resolution limit of the imaging system. All raw images are subject to a morphological filter with mask size of 2×2 pixels that removes hot spots. By selecting fields of view in each image that are not influenced by the plasma afterglow signal, e.g. see Fig. 6.5, the background counts per shot can be extrapolated to the whole image. Then, these counts are analysed in a series of approximately 150 shots in the laser-late mode (e.g. the electron beam does not amplify the afterglow) and yield 707 ± 248 counts as background signal. As such, the average value of 707 counts is considered as the minimally distinguishable signal and thus determines the resolution of the imaging system. This value corresponds to ~1.1 % of the laser-only afterglow signal shown in Fig. 6.1 (a).

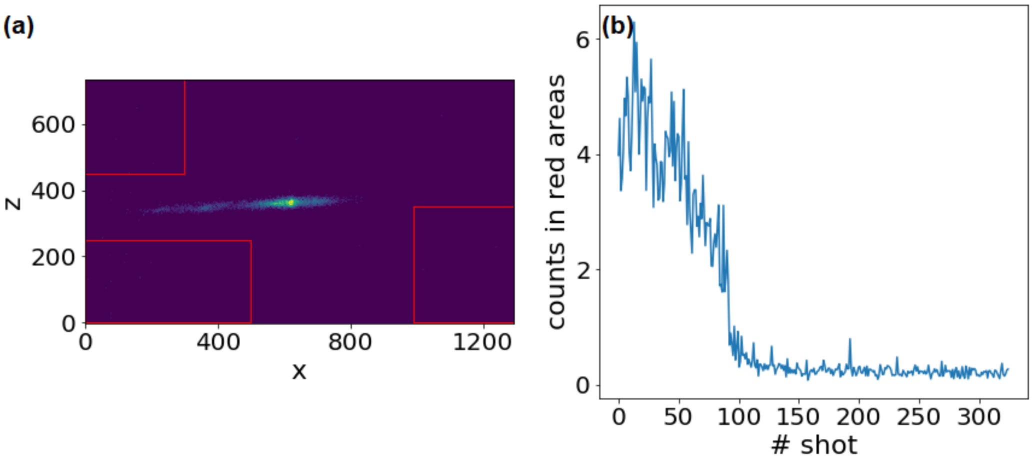

Figure 6.5: **Camera noise evaluation**. **(a)** Single shot taken from the laser-late mode (laser propagates in negative x-direction). As the afterglow signal is confined, the camera noise of the imaging system can be obtained from areas outside this region. Therefore, all pixels (~3×10^5) within the red rectangles are considered in the analysis and summed. Note that the region above the afterglow signal is not taken into account because it displays a reflection visible in the laser-early mode. **(b)** Dataset of the time-of-arrival scan shown in Fig. 6.7 only considering pixel counts in the red rectangles shown in (a) and without sorting by EOS time stamps. For shot numbers larger than 150, the electron beam does not heat the plasma and data inside the rectangles represents noise. Taking the mean and standard deviation of the summed counts for all shots larger 150, extrapolated to the whole image, the camera noise amounts to 707 ± 248 counts.

The shot-to-shot variations of the minimal plasma afterglow signal can be retrieved by a similar approach: selecting a field of view containing the afterglow in the laser-late mode and analysing the same series of shots as in the evaluation of camera noise, the laser-only afterglow signal consists of $2.99 \times 10^4 \pm 0.51 \times 10^4$ counts. The jitter of 0.51×10^4 counts describes parameter jitter of the laser as well as inhomogeneities of the gas volume. These information, unfortunately, cannot be deconvolved from the present set of diagnostics. However, relative to the maximum level of 3×10^6 counts at full interaction with the electron beam, this jitter is small compared to other shot-to-shot variations.

It is important to note that the electron beam propagating through the gas mixture does not generate any observable afterglow signal, e.g. because its fields do not cause field ionisation and its high energy, corresponding to high velocities and small cross sections, prevents significant impact ionisation per volume.

This experimental layout allows exploitation of the conceptual results obtained earlier: the electron beam transfers most energy to the plasma if their overlap volume is maximal. Changing the latter, e.g. by deliberately misaligning the OAP or by varying the TOA between electron beam and laser pulse, also affects the energy absorbed by the plasma and any subsequently observable afterglow signal. These two modes are conducted and characterized sequentially in the experimental campaign.

6.2.2 *Spatial alignment Mode*

In the spatial measurement mode, the TOA $\Delta t_{\text{delay}} = TOA_{\text{laser}} - TOA_{\text{e-beam}} \approx 2.1\,\text{ps}$ is fixed within accuracy of the facility. This large delay decouples any temporal dependence and ensures that the laser has fully formed the seed plasma filament before the electron beam arrives. Then, rotating the OAP introduces vertical spacings Δy between electron beam orbit and plasma, such that the long and narrow filament effectively samples the transverse density distribution of the electron beam.

For this measurement, the collected afterglow signals are correlated with the vertical focus position determined by the centroid of the imaged focus of the laser. Integrating the pixel counts for each image in a Δy-scan consisting of 99 consecutive shots results in the Gaussian-like curve with r.m.s. width of ~64.8 μm shown in Fig. 6.6 that exhibits a steep decrease of amplified afterglow signal. The resulting data is fit by a bi-Gaussian distribution $f(y) = a1 \cdot exp(-((y-b1)/c1)^2) + a2 \cdot exp(-((y-b2)/c2)^2)$. The first term describes the amplified plasma afterglow signal from the interaction with the electron beam and agrees well with PIC simulations. The second one (not shown) results from systematic aberration errors due to movements of the OAP which reduces the plasma volume with increasing misalignment. The aberration function is subtracted from the measured curve signal. Calculating the detector function $f(y)^{-1}$ for the first fit yields a measured accuracy of 4.1 μm at the peak of the curve from error propagation.

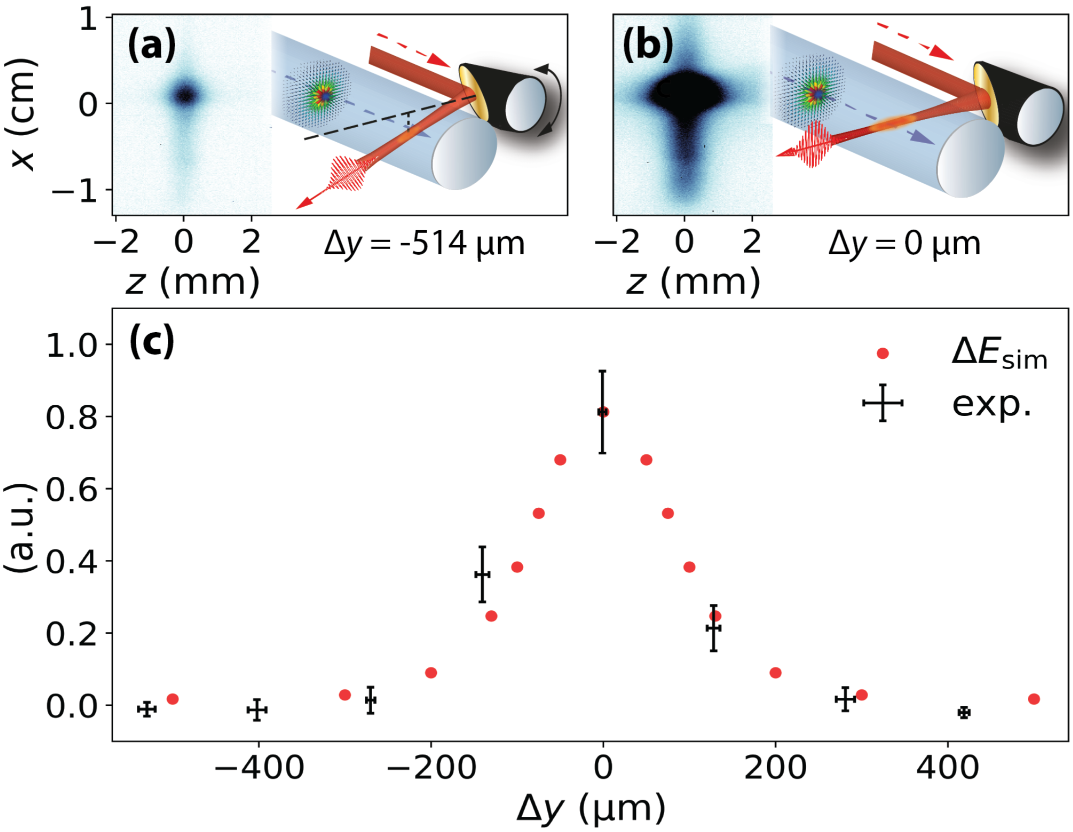

Figure 6.6: **Spatial alignment scan between electron beam and laser pulse.** Rotating the OAP in the y-direction shifts the laser pulse axis from optimal alignment with respect to the electron beam orbit (b) such that the seed plasma is increasingly positioned off-axis (a). This decreases the afterglow amplification substantially. To decouple any potential influence of varying TOA, a fixed $\Delta t_{\text{delay}} = -2.1\,\text{ps}$ ensures interaction with a fully formed plasma. The complete alignment scan with 8-10 shots per setting (red, crosses denote r.m.s. for each setting) reveals a strong dependence of integrated amplified afterglow signal and distance between plasma and electron beam. Fitting a Gaussian distribution to the data yields a r.m.s. width $\sigma_y \approx 64\,\mu\text{m}$. This curve can be obtained from particle-in-cell simulations as the relative energy transferred into the plasma (black) agrees well with the measured afterglow amplification. Applying this information, best overlap of beam and laser corresponds to the peak afterglow signal. This position can be determined with accuracy of $4.1\,\mu\text{m}$ from the experimental data. Figure produced by the author for [175].

The kinetic energies transferred from the electron beam into the plasma simulated in a set of PIC simulations agree well with this curve as shown in the same figure, which suggests a linear relation between initial energy and amplification of the afterglow signal. Comparing simulation and experiment supports the conceptual argument that the position with maximal counts corresponds to optimal overlap between electron beam and plasma. It can, therefore, readily be established experimentally within the accuracy of the imaging system. From fitting the measured data and by applying error propagation, the central overlap can be determined within $4.1\,\mu m$ accuracy from the given dataset. This plasma afterglow response in Fig. 6.6 further directly yields the statistical influence of alignment jitter on the afterglow signal. Applying the effective, combined alignment jitter $\sigma_{j,\mathrm{eff},y} \approx 10.1\,\mu m$ to the Gaussian fit, this curve simultaneously yields the precision of this measurement, e.g. the shot-to-shot afterglow amplification changes by $0.7\,\%$ (r.m.s).

The obtained curve constitutes a multi-shot alignment diagnostic that directly yields the optimal spatial overlap between beam and laser pulse. The associated accuracy depends on the sensitivity of the imaging system and experimental limits. For the former, the collection efficiency is primarily limited by the small solid angle, such that most emitted afterglow photons are not detected. Furthermore, selecting the specific spectral line $587\,nm$ with a bandpass filter excludes all photons from other excited lines, which potentially display a very similar amplification behaviour as the investigated one and could increase the photon yield. Increasing the collection volume and considering more spectral lines potentially improve he sensitivity of the imaging system. Finally, the experimental accuracy can substantially be improved by obtaining larger numbers of shots per setting as well as by reducing or externally quantifying electron beam and laser pulse parameter jitter and drifts. Characterising the Gaussian dependency shown in Fig. 6.6 sufficiently well either from experiment or theory yields a gauge curve for the given interaction and parameter regime. Then, this technique can measure absolute alignment between electron and laser beams on a single-shot basis.

6.2.3 *Time-of-arrival Mode*

The second measurement mode fixes the spatial overlap to $\Delta y = 0$ within the experimental accuracy by simply maximising the measured afterglow signal, and then varies the timing between electron and laser beams. This delay scan shown in Fig. 6.7 consists of 256 consecutive shots in the range of $-2.5\,ps < \Delta t_{\mathrm{delay}} < 4.0\,ps$ and, reveals a pronounced transition from maximal amplification when the laser arrives before the electron beam, e.g. at negative delays, to the mere glimmer generated by the laser-only case for positive delays.

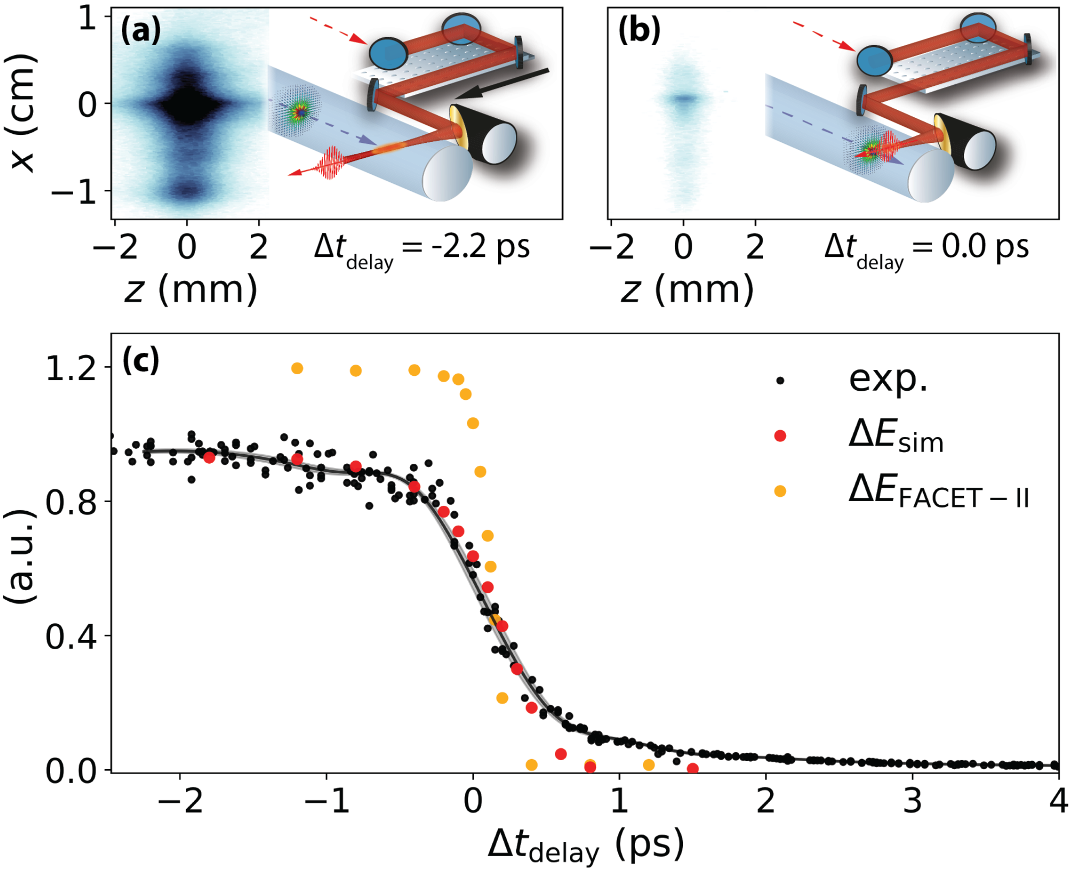

Figure 6.7: **Time-of-arrival scan between electron beam and laser pulse.** Moving the laser delay stage varies the TOA between electron beam and laser pulse from the case where the laser arrives way before the electron beam (a) to the case where it arrives after the electron beam (b). The respective afterglow amplification reduces substantially. In this mode, the spatial dependence is reduced to shot-to-shot alignment jitters by fixing the OAP pointing at maximum glow. This figure shows a TOA scan over 256 consecutive shots between $-2.5\,\text{ps} < \Delta t_{\text{delay}} < 4.0\,\text{ps}$. Large negative timings correspond to the situation where the beam interacts with a fully formed plasma (e.g similar to the maximum glow case in Fig. 6.6) producing maximal afterglow amplification, while for large positive timings the laser generates plasma after the beam has passed the interaction point leading to the laser-only glimmer shown in Fig. 6.1. The background raw data reveals a sharp drop of measured signal. Calibrated by EOS time stamps the relative integrated photon count of those images exhibits a sharp transition allowing shot-to-shot TOA measurements with 16 fs accuracy (54 fs without EOS calibration). The data agrees well with the relative simulated energy transfer from electron beam into the plasma. For a FACET-II class electron beam, the transition gradient becomes substantially steeper (more details can be found in Fig. 6.10). Figure produced by the author for [175].

In contrast to the alignment mode, where the energy transfer depends on the overlap of the electron beam distribution (expressed by the rapid field screening) with a displaced yet fully formed seed plasma, altering the TOA in this scenario varies the *amount of already generated plasma* when the beam crosses the interaction point. As a consequence, the integrated afterglow counts per shot do not yield a Gaussian transition curve, but the *sigmoid* shape shown in Fig. 6.7. Essentially, the afterglow displays maximal amplification if the laser arrives sufficiently early (laser-early mode), corresponding to large negative delays, such that the already generated plasma covers the whole radial extent of the electron beam. In contrast, no amplification is observed when the laser arrives later than the electron beam (laser-late mode), corresponding to large positive delays, and the generated plasma does not overlap with beam particles at all. In both cases, rapid Debye shielding restricts the range of the electron beam such that larger $|\Delta t_{\mathrm{delay}}|$ does not change the transferred energy and the afterglow signal saturates at high or low level, respectively. These plateaus are connected by a steep, quasi-linear transition region of width ~315 fs (r.m.s), which is given by the duration the electron beam distribution overlaps with plasma particles (e.g. recall the rapid field screening discussed earlier). Within this time, the laser generates plasma available for energy transfer *close to and even inside* the passing radial electric field distribution of the electron beam. Experimentally, this steep transition region is crucial to identify the coarse temporal coincidence between electron beam and laser. This method has been applied for finding and calibrating the signal on the small EOS crystal during the demonstration of a plasma photocathode presented in Chapter 7.

However, the coarse accuracy achieved from comparing these plateaus and the associated minimal and maximal afterglow amplification can significantly be exceeded by measuring *directly on* the transition. In this region approximately around $\Delta t_{\mathrm{delay}} = 0$, small changes in TOA cause large variations of the measured signal. Applying error propagation to a sigmoid fit through the measured transition yields the TOA accuracy of ~55 fs via error propagation through a sigmoid fit function $s(t) = a/(1 + \exp((t - t_0) \cdot k))$. This measurement represents a multi-shot approach and its accuracy is limited by the number of shots and shot-to-shot parameter jitter. Unfortunately, the large facility-inherent TOA jitter of approximately 109 fs critically impacts all datasets retrieved in this measurement mode.

Applying the obtained EOS information for benchmarking every shot can nonetheless partially compensate for this effect. Correlating each image produced by the z-x-CCD with an individual relative TOA determined by the EOS unit, which accounts for temporal jitter between laser and electron beam, the dataset can be sorted by EOS time stamps. The resulting transition modelled by the sigmoid function and subsequent error propagation of the detector function $s(t)^{-1}$ yields the improved TOA accuracy of ~16 fs, e.g. approximately 15 % of the timing jitter.

It should be noted that even though this measurement strongly benefits from *relative* TOA benchmarking by EOS, the presented diagnostic can serve as an accurate, stand-alone apparatus delivering *absolute* TOA information in the multi-shot approach. If either the sensitivity of the imaging system or the number of shots per setting is substantially improved or the shot-to-shot jitter of electron and laser beam parameters reduces, the accuracy of this technique can be improved substantially as indicated by the linear agreement with the simulated transferred energy.

The measured afterglow benchmarked by EOS time stamps agrees well with the simulated transferred energy and strengthens the findings obtained earlier regarding a linear relation between these parameters in the given interaction regime. This agreement shows that the measurement sorted by EOS time stamps is actually close to the jitter-free optimum, and that the simulation represents a gauge curve. Similarly to the arguments earlier, characterising this curve sufficiently well can enable single-shot operation with higher accuracy than achieved by the multi-shot approach. Again, this requires substantially reduced jitter of electron beam and laser pulse properties, or their quantification by additional diagnostics.

6.2.4 *Further Dependencies*

The influence of parameter variations apart from timing and alignment could not be investigated experimentally due to limited beam time within the E-210 campaign at FACET. In addition, extending the computational analysis over significantly longer runtime than the 16 ps shown in Fig. 6.2, or in larger simulation boxes for covering the whole plasma filament, are practically limited by the excessive computational costs. On the other hand, hydrodynamic simulations cannot properly simulate electrodynamics as these require well-resolved grids and particle pushes. Combined with the lack of a closed model predicting the amplified afterglow signal for arbitrary electron beam and seed plasma distributions, expanding the parameter space via simulations is restricted to small changes within the investigated overdense regime. This ensures the linear relation between energy and afterglow amplification revealed by experiment and simulations. Leaving this regime in either direction can radically change the overall plasma dynamics. On the one hand, weakening the electron beam relative to the plasma can prevent global energy dissipation, e.g. when surface and density waves of sufficient amplitude are not excited. Then, only the small fraction of the filament interacting with the beam generates amplified afterglow signal stronger than usual hydrodynamic effects. On the other hand, strengthening the beam relative to the plasma can cause a snowplough-like effect. This situation is very similar to the excitation of nonlinear plasma waves where the beam viciously expels all electrons within its vicinity. In both cases, the linear relation between initially transferred energy and signal amplification is not guaranteed to hold.

Close to the experimental regime experimentally encountered at FACET within E-210, however, certain established or simulated variations to the interaction parameters can be considered to maintain the linear relation between these quantities.

Generally, energy loss by an electron beam propagating inside plasma scales linearly with the (normalised) beam charge [88] from the linear into the deeply nonlinear interaction regime, meaning both overdense and underdense cases. Thus, small variations in beam charge should linearly change the afterglow signal.

The plasma geometry plays another crucial role and its parametric dependency with the afterglow amplification is not fully understood. So far, only qualitative arguments can be brought forward. As the most common plasma effects such as oscillations act inherently locally, their influence gets damped or shielded on length scales much shorter than the millimetre-long filament axis. Further, plasma waves along this axis cannot be sustained without a mechanism perturbing the density. Amplifying the *overall* afterglow signal therefore requires global heating mechanisms. One of these can be strong Coulomb fields caused when the beam accelerates considerable fractions of plasma electrons so strongly that they do not stay in close vicinity to the plasma. Remaining ions will attract other electrons from the filament, which in turn leave a positively charged region behind and create a perturbation moving along the filament, e.g. plasma density waves. Second, remaining ions can also undergo space charge and hydrodynamic expansion, which similarly causes distortions of the global plasma density distribution and can cause secondary ionisation of ambient gas. Finally, surface waves can dissipate the locally absorbed energy along the macroscopic filament axis. All these effects require the plasma geometry to be *finite* in at least one dimension with respect to the electron beam extent. As a side note, small plasma dimensions are relevant for sampling the beam extent, e.g. particularly in the alignment mode.

The plasma geometry relative to the electron beam dimensions defines another relevant quantity for the energy transfer. As the immediate response of plasma on the external perturbation is a *dynamic* effect, e.g. the electron beam excites a linear plasma wave for the duration it traverses the filament, field screening and energy transfer depend on the perturbations speed (together with its magnitude). Therefore, the rise time of the electron beam current defined by its longitudinal distribution compared to the plasma extent is relevant and defines how adiabatic an interaction takes place [**Lotov1996**].

For [175], several small parameter scans were performed in PIC simulations to roughly understand their influence on the transferred energy, e.g. as potential source of jitter. First, the electron beam duration is varied at constant charge in Fig. 6.8. A second scan changes the radius at constant charge and duration in Fig. 6.9. Both dependencies are weakly non-linear.

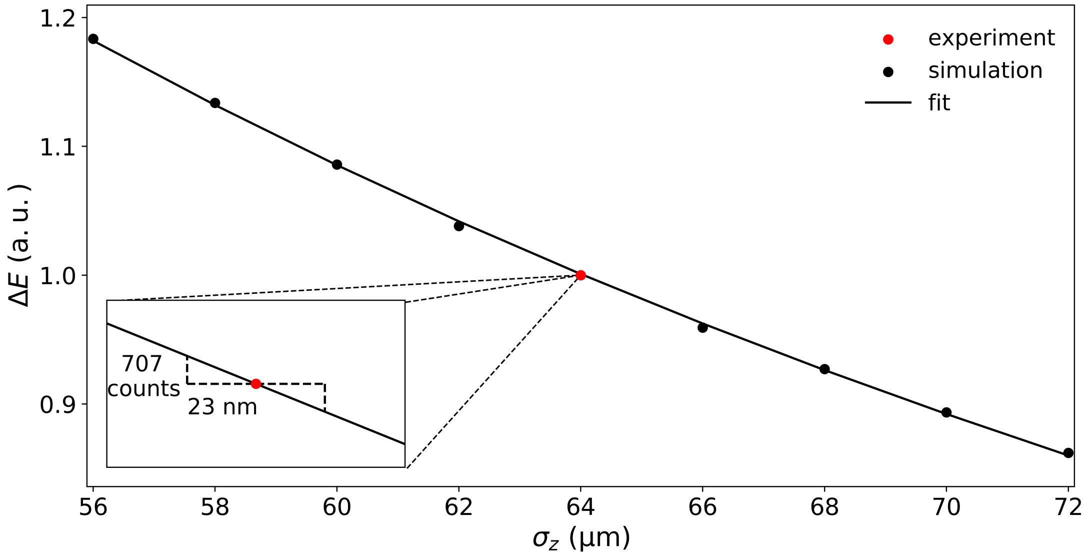

Figure 6.8: **Simulated parameter scan for electron beam duration** Variations of beam duration with all other parameters similar to the experiment. For constant charge, shorter (longer) electron beams have stronger (weaker) electric fields, which increases (reduces) the strength of the beam-plasma interaction. Following Figs. 6.6 and 6.7, the change in amplified afterglow signal is expected to linearly follow this line as long as the overdense, adiabatic interaction regime holds. Therefore, this curve represents the effect of electron beam duration jitter in our experiment. Applying the experimental resolution limit to this simulated curve implies a relative beam duration metrology limit of 23 nm (77 as) in a jitter-free configuration. Figure produced by the author for [175].

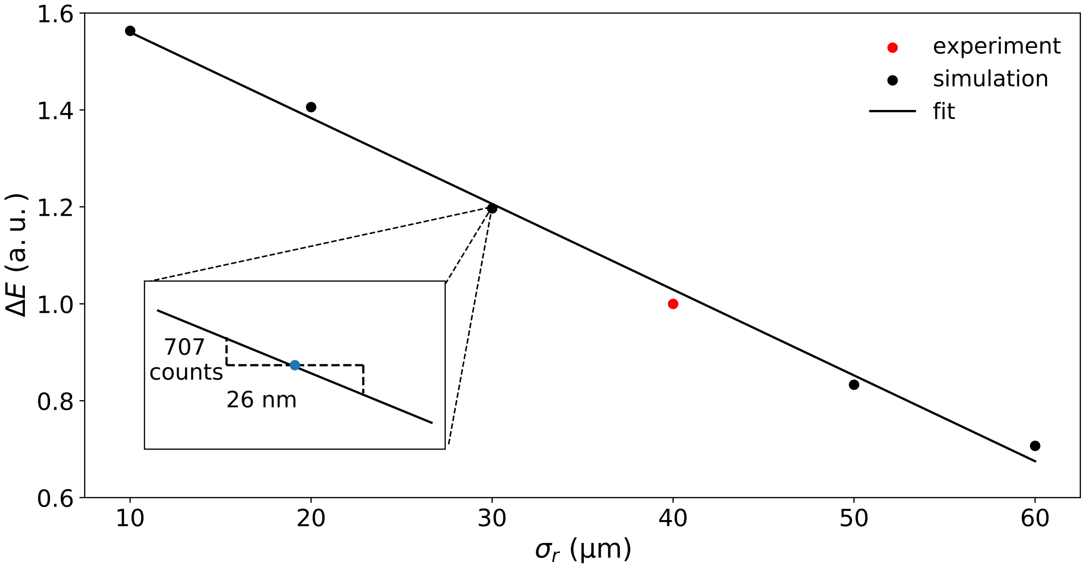

Figure 6.9: **Simulated parameter scan for electron beam radius** Variations of beam radius with all other parameters similar to the experiment. For constant charge, narrower (wider) electron beams have stronger (weaker) electric fields, which increases (reduces) the strength of the beam-plasma interaction. Following Figs. 6.6 and 6.7, the change in amplified afterglow signal is expected to linearly follow this line as long as the overdense, adiabatic interaction regime holds. Therefore, the curve represents the effect of electron beam radius jitter in our experiment. The experimental-specific imaging system resolution limit of 707 counts applied to this simulated curve yields a relative beam radius metrology limit of 26 nm in a jitter-free configuration. Figure produced by the author for [175].

Figure 6.10 compares TOA scans using the electron beams from FACET and FACET-II. The latter is particularly relevant as it represents the next world-leading PWFA facility. There, experimental beam time for further developing and exploiting the presented technique has been approved. In the corresponding simulated TOA scan, $n_b/n_p \approx 0.1$ and $\sigma_z/d_{\text{plasma}} = \text{const.}$ ensure comparable, overdense interaction regimes, similar current rise times and adiabaticity. The stronger transverse compression possible with the FACET-II electron beam results in a narrowed transition region together with higher transferred energy. The resulting gradient is therefore steeper than in the experimental showcase in the E-210 case and promises improved temporal resolution by a factor of 4 from the amplified afterglow diagnostic.

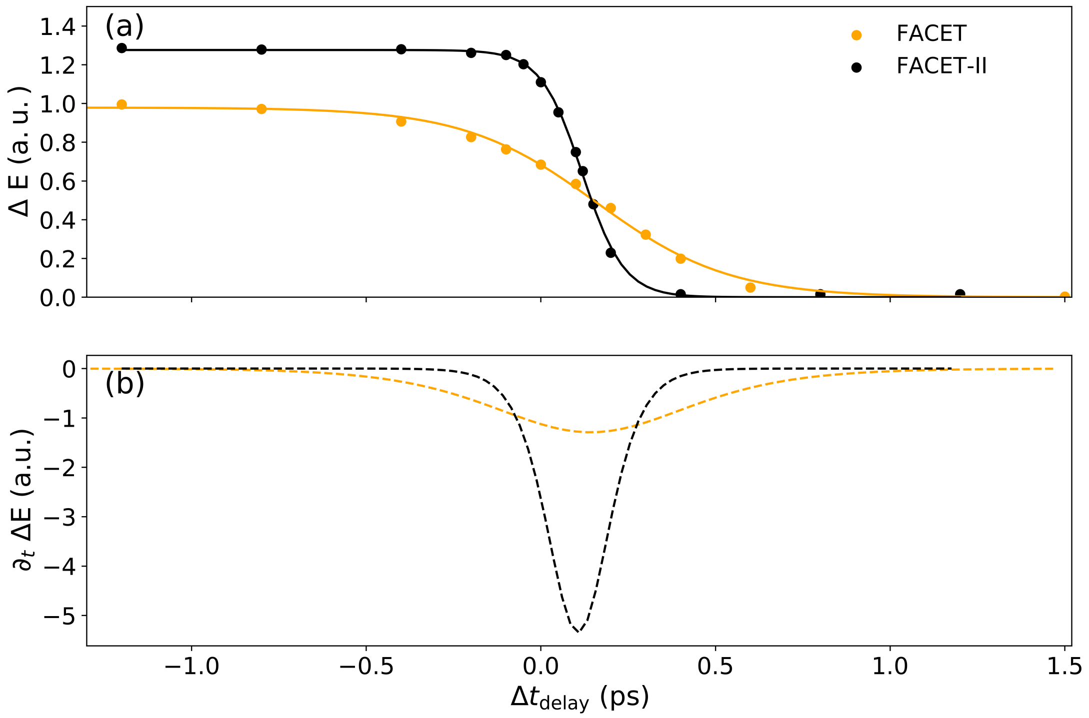

Figure 6.10: **Simulated time-of-arrival scan for FACET and FACET-II beams.** This figure compares the time-of-arrival (TOA) scan of the employed FACET electron beam shown in Fig. 6.7, with simulations of the anticipated energy deposition at FACET-II, which delivers more compressed electron beams ($\sigma_z = 20\,\mu m$ r.m.s., $\sigma_{y,x} = 10\,\mu m$ r.m.s., black). Keeping the ratio of beam to plasma density $n_b/n_e = 0.1$ and the ratio of beam duration to plasma radius identical to the experiment ensures the same comparable, adiabatic interaction regime. **(a)** The FACET-II beam generates a shorter transition of width $0.35\,ps$ FWHM compared to $0.67\,ps$ FWHM simulated in Fig. 6.7. Additionally, more energy is transferred during the interaction, which results in a slope steepened by a factor of 4 as shown in **(b)**. More compressed beams therefore may allow for further increased sensitivity in TOA measurements, or to adjust the TOA with higher accuracy, respectively. Such short and even shorter electron beams are relevant for various applications, e.g. for photon science, and can be produced particularly by plasma-based accelerators. Figure produced by the author for [175].

All discussed quantities such as the density ratios along with electron beam and plasma filament form factors, influence the transferred energy and, therefore, the expected afterglow amplification. They represent potential sources of jitter and opportunities for optimisation. On the other hand, this multi-parameter dependency typical for beam-plasma interactions (e.g. see [186]) also promises versatile applications for diagnosing any of them. This can, for example, be done by setting up several identical filaments simultaneously, e.g. one in the alignment mode, one in the timing mode, a third one to measure the laser-only signal as background and so on. Then, several composite measurements could decouple and isolate many parametric dependencies, allow for much higher accuracy and yield comprehensive information of the electron and laser beams.

Finally, one very simple variation of the procedure could significantly improve the obtained resolution: selective ionising the hydrogen gas (at adequate density) while keeping the helium component undisturbed allows independently tunable *seed* and *detector* medium densities. In this case, the electron beam transfers its energy solely into hydrogen plasma, which then undergoes the complex plasma dynamics and successively ionises ambient helium via impact ionisation. As the immediate plasma dynamics do not depend on the helium component, its density can be increased substantially, thus yielding stronger afterglow signal enhancement without changing the electron beam-seed plasma density relation. On the other hand, if minimal or no energy is transferred, almost no signal will be detected because of the bandpass filter. Thus, the signal-to-noise ratio can be increased by simplest means and the diagnostic might yield much better accuracy. This configuration could not be established experimentally because of lacking beam time, but will be employed to future experimental campaigns.

6.3 SUMMARY

The experimental and conceptual work summarised in this chapter constitutes a highly promising approach for measuring the spatiotemporal coincidence of intense, focused electron and laser beams directly at their interaction point and in the presence of plasma. The complex plasma dynamics outlined here transform the ultra-short and ultra-fast interaction of the beam with a plasma column into a macroscopic effect observable by a simple CCD camera. These features combined with high resolution are unique for comparable diagnostics and promise application in many experiments and facilities.

This technique has already been successfully applied in demonstrating the plasma photocathode, which is subject to Chapter 7. There, the TOA resolution of $16\,\mathrm{fs}$ corresponds to $1/20$th of the $\sim 100\,\mu\mathrm{m}$ long wakefield. As such, the given diagnostic has enabled a milestone towards high-quality electron beam generation. Furthermore, this kind of diagnostic suits very well to ICS sources as it can determine the spatiotemporal overlap between electron beam and scattering laser even in high-power mode and in the interaction point. This might be particularly useful in the context of plasma-based ICS sources, which are prone to pointing and timing jitter. This diagnostic therefore may facilitate major progress in this field.

Future studies must address the remaining open questions. Particularly, an adequate model linking initial energy transfer and ultimate afterglow signal should be established for optimising interaction parameters and geometry. Then, the diagnostic might even yield low or sub-femtosecond and sub-micrometre resolution, and can be applied for electron beam metrology applications.

Apart from developing a diagnostic, some last thoughts should be raised regarding the plasma surface waves excited by the electron beam. As surface waves propagate without radiation [181] on the interface between two media, corresponding to different permittivity, they are attached to the respective boundary. In the given study, this boundary exists between plasmas and neutral gas. Therefore, propagation behaviour of surface waves can be influenced by geometric means. For example, simulations show that they can be guided around edges with angles up to 90°, lose intensity when the filament radius increases, and even get reflected at the plasma columns ends. Their longitudinal, Bessel-like structure might even allow resonant excitation with multiple, properly delayed electron beams. This might even generate standing waves along a finite plasma filament, at least until too many electrons get expelled causing Coulomb-explosion of the remaining ions. For a short time, e.g. tens or hundreds of picoseconds, these waves might cause emission of terahertz or microwave radiation depending on the plasma electrons orbits. Combined with the comparably easy experimental requirements, these dynamics may constitute a highly interesting research topic.

7

EXPERIMENTAL REALISATION OF A PLASMA PHOTOCATHODE

At the time this study started, the plasma photocathode injection concept introduced in Section 3.4 has been proposed for several years [41]. The experimental verification, however, could not be realised until this time. One of several reasons was the low number of facilities capable of delivering relativistic and highly compressed electron beams suitable for PWFA. Other concerns were raised with respect to the supposedly demanding synchronisation between plasma wake and decoupled injector laser, which was anticipated to require challenging accuracy on the 10 fs-level. Nonetheless, a collaboration consisting of multiple international universities and industrial partners eventually formed for realising this promising technique: the E-210 experimental campaign received beam time at FACET [38], the globally most advanced PWFA facility at that time.

The author has joined the group assembled at FACET in the last six months of beam time. After tremendous mutual effort, the worlds first experimental demonstration of two different modes generating electron beams from laser-triggered ionisation directly inside a plasma wakefield accelerator has been achieved and published [187, 188]. The author has contributed significantly to the experimental realisation together with conceptual and computational work.

This chapter represents a synopsis of the challenges, strategies and obtained results. Many more information and details can be found in [105, 184], whose authors lead large parts of the campaign.

7.1 EXPERIMENTAL DESIGN

The theoretical description in Section 3.4 shows that a plasma photocathode can be established by (a) driving a nonlinear wake field and (b) releasing electrons inside this blowout by means of an independent laser pulse. Experimentally, the temporal synchronisation and spatial alignment of the plasma photocathode laser at the right position and phase of the blowout are of paramount importance for accomplishing the plasma photocathode wakefield accelerator. These include fundamental problems such as achieving accurate temporal synchronisation and spatial alignment between plasma wave and laser pulse. This is a key requirement which is independent from the plasma photocathode geometry and the employed laser pulse. This fundamental requirement depends on the facility-specific capability of spatial and temporal accuracy of electron and laser beams, and the capability of the measurement of spatial and temporal overlap at the interaction point. Examples are electron beam timing, alignment and pointing jitter caused by parts of the conventional accelerator technology. Likewise, energy, pointing and wavefront stability of the laser system are limited, which also applies to space and access to and for employed equipment.

Following, the relevant steps and solved problems on the path towards realisation of the plasma photocathode are introduced and discussed in logical order. These milestones, together with many unsuccessful iterations, eventually culminated in the successful proof-of-concept measurements, which were recently published in [187].

7.1.1 *Plasma Source*

The linear accelerator at FACET offered unique capabilities for delivering highly compressed, dense electron beams with short duration well-suited for driving plasma wakefield accelerators. Next to this drive beam, the second major ingredient of plasma wakefield accelerators is the plasma source maintaining the wakefield structure. This plasma must be tens of centimetres long for GeV-level acceleration of electrons.

Previous PWFA experiments at FACET [82, 96, 98, 189, 190] exploited an oven filled with alkali metal vapour. These materials, e.g. lithium, can be ionised easily by the electron beam fields or laser pulses because of their low ionisation threshold, which are presented in Fig. 2.3. Laser-based *pre-ionisation* allows for metre-long and sufficiently wide alkali-based plasma sources [191], which facilitate stable interaction of the electron beam. This oven, however, could not be used in the plasma photocathode experiment as its metallic enclosure prevents diagnosing alignment and synchronisation of the injector laser with respect to the plasma wake. The actual plasma source for the E-210 experiment is therefore generated in an alternative beam line with multiple access ports for diagnostics. Replacing the oven requires an alternative plasma medium, as the new beam line does not provide the necessary heating and gas buffering mechanisms. Choosing molecular hydrogen has multiple reasons: it is gaseous and therefore easily poured into the interaction chamber, and it provides comparably low ionisation potential compared to many elements at room temperature. Furthermore, hydrogen does not provide higher ionisation states, which promises homogeneous plasma sources as long as full ionisation of the molecule is guaranteed. The hydrogen plasma medium is superimposed by helium as dopant gas, which inherits much higher ionisation potential and allows for selective ionisation by the plasma photocathode injector. As the helium component must be ionised at a specific position and at a different time than the plasma medium, a plasma discharge device as discussed in Section 2.2.2 is not employed. Instead, tunnelling ionisation by a well-controlled laser pulse offers species-selective ionisation and simultaneously provides comparably cold plasma temperature.

During this experiment, the $170\,\mathrm{mJ}$ FACET laser pulse compressed to $55\,\mathrm{fs}$ (FWHM) is focused into the gas mixture by a holographic axilens [192]. This optic pre-ionises the hydrogen component $\sim 20\,\mathrm{ps}$ before the drive beam arrives and forms the Bessel-shaped plasma channel shown in Fig. 7.1. It is supposedly $\sim 1\,\mathrm{m}$ long and, theoretically, produces a suitable plasma source for generation of GeV-class witness beams. In addition to appropriate length, the channel must be sufficiently wide such that it fully engulfs the wake fields sheath. For channel radii close to or smaller than the nominal blowout radius, simulations carried out for this publication show that the wake fields envelope elongates and alters the wake field potential defined by Eq. (3.13), also see [106]. Both the radial as well as the longitudinal geometric conditions are necessary as they facilitate high final energy and, more fundamentally, allow stable propagation of the wake field (e.g. see Chapter 3).

Generating a suitable plasma source involves different trade-offs between physical constraints and restrictions imposed by the setup. In principle, two strategies with individual advantages and challenges can provide channels of sufficiently wide radius: either fitting the blowout to a given channel or vice versa. Considering the first case, the wake field dimensions can simply be controlled by changing the hydrogen gas pressure as both the blowout radius as well as its length scale with the plasma density similar to $\lambda_p \propto {n_p}^{-1/2}$. However, the wake field amplitudes vary inversely with the plasma density, e.g. $E_{WB} \propto n_p^{1/2}$, and increase for smaller blowouts. For a given plasma channel radius defined by the pre-ionisation laser pulse profile, the plasma density can, therefore, simply be increased until the blowout is small enough to fit into that channel of given radius. Tunnelling ionisation of the helium dopant by the wake field can cause dark current that overlays, hides or deteriorates any intentionally trapped witness beam, e.g. as discussed in Section 3.2.2 and [106]. Further, PWFA requires an underdense interaction regime with $n_b \geqslant n_p$. These arguments set an upper limit for the hydrogen plasma density and a lower limit for the channel radius.

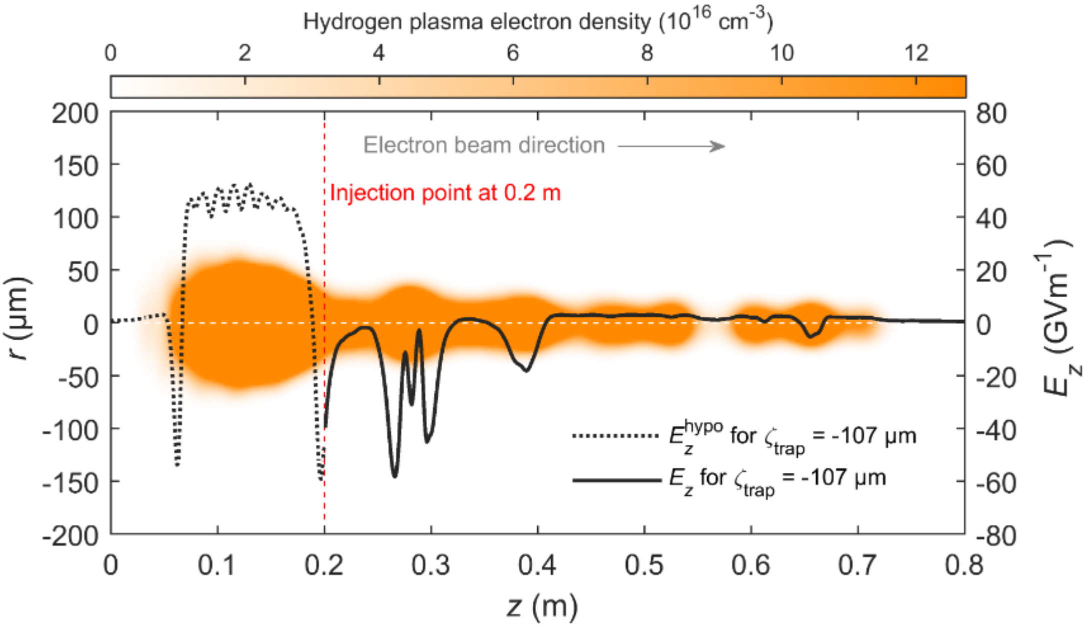

Figure 7.1: **Calculated plasma channel during the E-210 campaign** The orange structure depicts the hydrogen plasma density profile calculated by ADK theory for the FACET laser pulse focused by an axilens. The first maximum of the Bessel profile is wide and can engulf the blowout at plasma wavelength $\lambda_p \approx 100\,\mu m$. Towards the downstream end corresponding to large z-positions, the radial extent narrows due to limited laser energy. Further increasing the latter can cause undesired ionisation of the helium dopant. Unfortunately, the experiment shows that varying transverse plasma profile distorts the electron trajectories in the PWFA process. This modulates the shape and strength of the blowout along z. Consequently, a trapped beam experiences different accelerating fields during propagation through the plasma, e.g. its phase relation to the wake is not fixed. For a typical trapping position in the co-moving coordinate frame (here: $\chi_{trap} = -107\,\mu m$, and $\chi_{trap} = 0$ corresponds to the centre of the blowout), the black lines describing the longitudinal fields express this effect. The dashed red line at $z \approx 0.2\,cm$ indicates the position of the transverse injection laser pulse in the laboratory frame. This figure is taken from [187].

Therefore, generating a suitable plasma source also applies parts of the second strategy, which aims at increasing the radial profile of the plasma. This can be done by raising the transverse laser intensity distribution for a given focusing optic and target medium, e.g. by means of increased pulse energy or shorter pulse duration. This consideration generally holds for any ionising laser pulse independent of the given optic. On the other hand, the laser intensity must be balanced between generating a large hydrogen plasma and avoiding ionisation of the dopant gas. Even for the much larger helium ionisation potential (e.g. see Fig. 2.3), this condition requires careful adjustment of the laser intensity. It may be noted here that, theoretically, the focusing optics can be replaced by another one with varied diffraction pattern such that a wider channel is created. Both spatial constraints as well as limits regarding the available laser power at FACET during the E-210 experiments restrict the range of accessible plasma channel widths and densities.

In between these experimental constraints, the plasma wakefield acceleration theory outlined in Chapter 3 expresses that high beam quality corresponds to low plasma density or large blowout dimensions, respectively. Particularly beams formed by a plasma photocathode benefit from this situation as both their emittance and energy spread decrease with decreasing plasma density. Low densities also relax requirements of alignment and synchronisation between plasma wave and injector laser as their spatiotemporal coincidence range increases. Additionally, overlapping plasma channel and drive beam orbits is less susceptible to laser-to-electron beam jitter and drifts if the plasma channel is wide.

Combining all these considerations, the plasma density is adjusted to yield $\lambda_p \approx 70\,\mu\mathrm{m}$ to $100\,\mu\mathrm{m}$. Then, the blowout supposedly fits to most parts of the approximately ~$88\,\mu\mathrm{m}$ (FWHM) wide plasma channel and dark current can be mitigated.

Finally, the plasma channel must be centred on the electron beam orbit for capturing the beam and optimally driving a plasma wake. This has initially been done by a two-point alignment procedure, which overlaps electron beam and laser spots on removable OTR screens. To avoid damaging their materials, this happens in vacuum, e.g. not in the presence of plasma, and at low laser intensity. Typically, this procedure takes approximately one hour, and pumping and flooding the chamber can cause new misalignments. Furthermore, the substantial electron beam and laser pulse pointing drifts require several re-adjustments during each beam time. This whole procedure can, in principle, be substantially improved and sped up by applying the spatial alignment mode of the diagnostic presented in Chapter 6.

As the average channel radius is of comparable size as the beams radial extent, even small inaccuracies in the initial alignments, pointing jitter and drifts can affect the acceleration process. For example, the beam experiences transverse attracting forces if the channel is misaligned [193], which can disturb excitation of blowouts.

The final focusing quadrupole magnets of the FACET beam line do not allow transverse matching of the drive beam to the plasma density as introduced in Section 3.3.3. As such, the drive beam is bound to pinch periodically and may cause localised ionisation of ambient helium gas. However, this kind of dark current is not observed during data acquisition for [187]. This is partially due to reduced fields from non-resonant excitation of the plasma wake, e.g. $k_p\sigma_z \approx 2.0$, which results from the constraints related to the plasma channel and limited longitudinal drive beam compression.

7.1.2 *Injector laser*

A plasma photocathode requires an independent laser pulse for ionising the dopant gas directly within a blowout. Due to limited space close to the axilens optic for the pre-ionisation laser, the injector laser focal optic is set up in 90° geometry further downstream, e.g. at $0.2\,\mathrm{m}$ in Fig. 7.1. This decision offers several opportunities for the whole experimental campaign.

First, and particularly important for the given setup, the focal position of the injector laser intersects the beam axis right *after* the first, broad Bessel peak of the plasma channel shown in Fig. 7.1. Again, spatial constraints and the limited number of windows allowing transverse optical access to the beam line are reasons for this situation. While in principle it is straightforward to shift the pre-ionised plasma channel, e.g. by means of a linear stage, this was not possible either due to experimental boundary conditions.

Secondly, while 90° injection geometry is perfectly suitable for first realisations of the plasma photocathode and the plasma afterglow metrology concept, it is not suitable to straightforwardly obtain the best emittance and brightness promised by the collinear geometry in [41]. This is because the ionisation volume set up by the laser, having a comparably large spot size and correspondingly long Rayleigh length, spreads across the whole transverse extent of the wake field such that released particles obtain large thermal velocity spread (e.g. see Sections 3.3 and 3.4). While the residual momentum imposed by the plasma photocathode is still negligible because $a_0 \approx 0.039$, the released electrons sample a large wide radial volume, and correspondingly obtain large transverse momentum spread imposed by the plasma wakefield.

The final injector geometry employs the same setup used for the amplified afterglow diagnostic discussed in Chapter 6. Recalling this passage, the pulse is an individually compressed split-off fraction of the main laser pulse with duration $60\,\mathrm{fs}$ (FWHM) and tunable energy up to $5\,\mathrm{mJ}$. An off-axis parabolic mirror focuses this pulse with spot size $w_0 \approx 38\,\mu\mathrm{m}$ onto the electron beam orbit. The pulse can be delayed relative to the pre-ionisation laser and the wake field by means of a mechanical stage.

For the plasma photocathode, the injector laser must fulfil multiple requirements: it must *ionise* the dopant gas helium, and this must be done *inside* the wakefield precisely *when* the wake crosses the focal position of the injector laser. The first condition is readily satisfied as confirmed by a CCD camera monitoring the focal region of the laser pulse. By means of a bandpass filter centred on the strong helium-I line $\lambda_{\mathrm{He}} \approx 587\,\mathrm{nm}$, the camera detects a clearly visible helium plasma, for example shown in Fig. 6.1 (a). To unambiguously verify *laser*-based ionisation instead of potential impact ionisation caused by hydrodynamic expansion of hydrogen plasma, this test is also done in pure helium gas.

Spatial overlap between plasma wake and injector laser pulse is established by aligning the injector laser focal spot to the signal from the electron beam on a removable OTR screen. This overlap can be improved and achieved without need to evacuate the chamber or to reduce the laser intensity by exploiting the alignment mode presented in Chapter 6.

The EOS system introduced in Chapter 6 provides relative temporal synchronisation between electron drive beam and injector laser. However, the *absolute* temporal coincidence of injector laser and wake field at the focal position of the OAP can not be retrieved by the EOS. The scheme presented in Chapter 6, however, provides absolute information and allows for finding the correct TOA with accuracy corresponding to ~1/20 th of the plasma wake duration. Once found, the EOS gives well-resolved relative TOA and jitter information.

7.2 EXPERIMENTAL RESULTS

Figure 7.2 contains the final setup based on all considerations and trade-offs discussed above. The developed experimental procedure for demonstrating a plasma photocathode is straightforward: after establishing alignment and synchronisation between all beams and pulses, the pre-ionisation laser generates a pure hydrogen channel 20 ps before the electron beam arrives to excite a dark current-free plasma wake. If now the plasma photocathode injector laser precisely hits the wake and releases helium electrons inside the plasma wake, these can get trapped provided the wake potential in Eq. (3.13) is sufficiently deep such that the particles reach the speed of light and stay within the blowout at their trapping positions given by Eq. (3.20). The subsequently formed witness beam gets accelerated and detected on the downstream-end spectrometer. As last challenge remains an unambiguous proof that accelerated electrons are released by the plasma photocathode.

The 90° injector geometry provides several crucial assets for this problem in spite of all challenges imposed by the setup. In this geometry and together with the comparably large spot size and available energy, the injector can form a wide helium plasma filament that locally increases the effective plasma density. If this filament is generated *ahead* of the wake, this configuration exactly constitutes a *plasma torch* [194, 195], an optical variation of the density-downramp injection approach. Interestingly, the plasma photocathode differs from plasma torch only in two critical points: the witness beam of a plasma photocathode must be generated *directly inside* the wake and within *small ionisation volume*. Figure 7.3 compares simulations for both injection schemes and outlines these fundamental differences.

As plasma torch injection has low requirements for synchronisation between electron beam and injector laser, it is employed first. Even if the laser pulse arrives hundreds of picoseconds before the electron beam, injection into the wake field can be measured. Figure 7.4 shows an "on-off" scan of the injector laser. Trapped beams correspond to excess charge measured on the beam position monitor (BPM) downstream of the interaction point. Only when the injector laser operates, substantial amounts of excess charge are registered. If this is the case, almost every shot yields traps and accelerates charge, meaning that this scheme is comparably robust against the substantial shot-to-shot parameter and pointing jitter. This dataset represents the worlds first demonstration of plasma torch injection, or, in other words, optically triggered density downramp injection into a plasma wakefield accelerator.

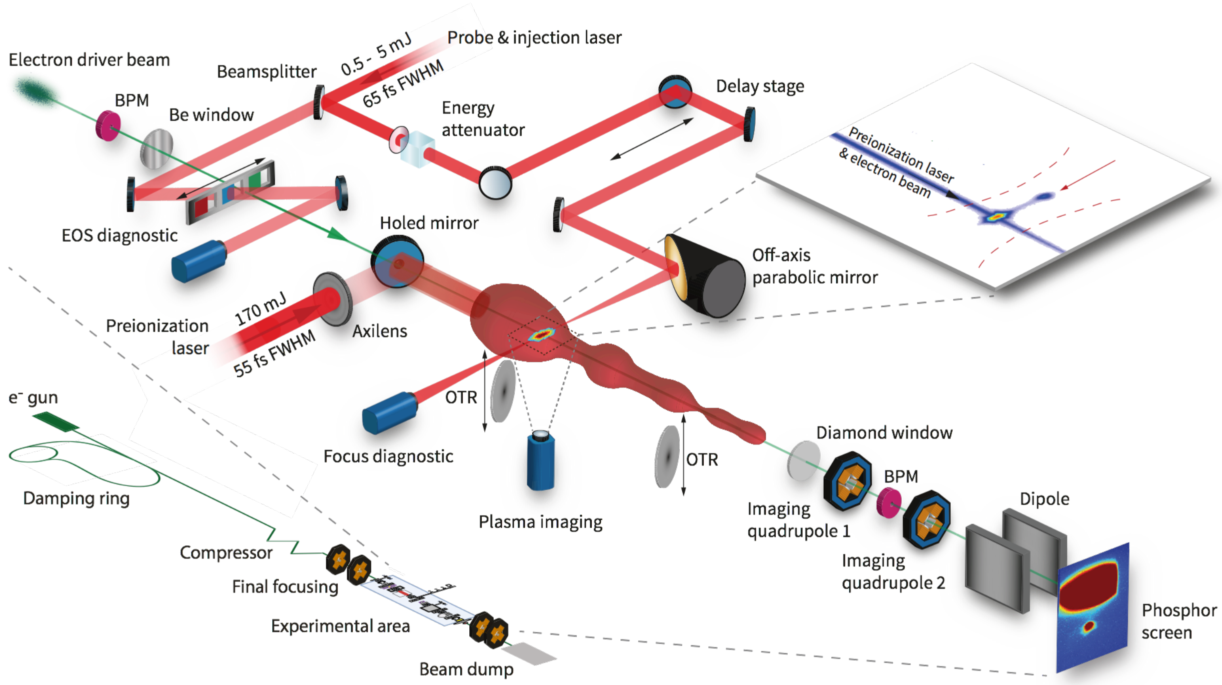

Figure 7.2: **Experimental layout of the photocathode injector] Experimental layout of the photocathode injector** The electron drive beam delivered by the FACET linear accelerator propagates from left to right. After passing the first beryllium window, the interaction chamber is homogeneously filled with the hydrogen-helium gas mixture. First, the electron beam is superimposed by a low-intensity split-off fraction of the injector laser in an electro-optic sampling crystal yielding relative time-of-arrival measurements. Then, it passes a mirror with a hole, which previously was used for alignment of the preionisation laser to the beam orbit and generation of the metre-long plasma channel. Inside the channel, the beam drives a nonlinear plasma wake. There, the injector laser focus intersects the beam orbit in 90° geometry aiming at controlled ionisation of the helium dopant and corresponding injection of electrons into the wake. This laser pulse can be attenuated by a beam splitter and a rotatable wave plate, and its TOA relative to the wake field can be varied by a delay stage. After acceleration in the plasma wave, the electron beam leaves the vacuum chamber through a thin diamond window and can be analysed in an electron spectrometer at the downstream end of the beam line. Figure produced by the author for [187].

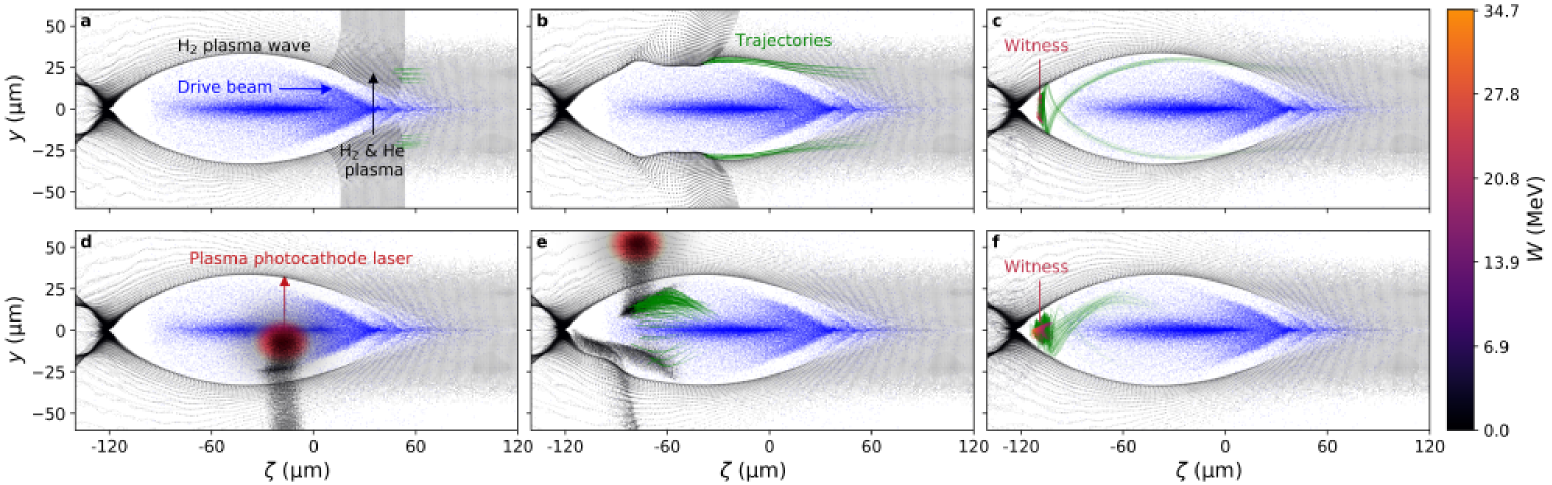

Figure 7.3: [**Comparison of simulated plasma photocathode and plasma torch injection.**] **Comparison of simulated plasma photocathode and plasma torch injection.** The electron beam (blue dots) propagates from left to right in the plasma channel shown in Fig. 7.1 and drives a blowout. **a-c** show the plasma torch injection scheme. The laser pulse creates a helium plasma filament ahead of the electron beam. The resulting density spike changes the blowout radius temporarily and varies its phase velocity. Some electrons originating from the filament (indicated by green trajectories) can get scattered inside the wake, and subsequently get trapped and accelerated. In **d-e**, the laser pulse indicated by the red circle releases electrons directly inside the blowout, which get trapped and accelerated. Again, green trajectories show the spatial evolution of injected electrons. The large transverse spread in initial positions directly relates to beam emittance much larger than in the original, collinear plasma photocathode scheme. Figure taken from [187].

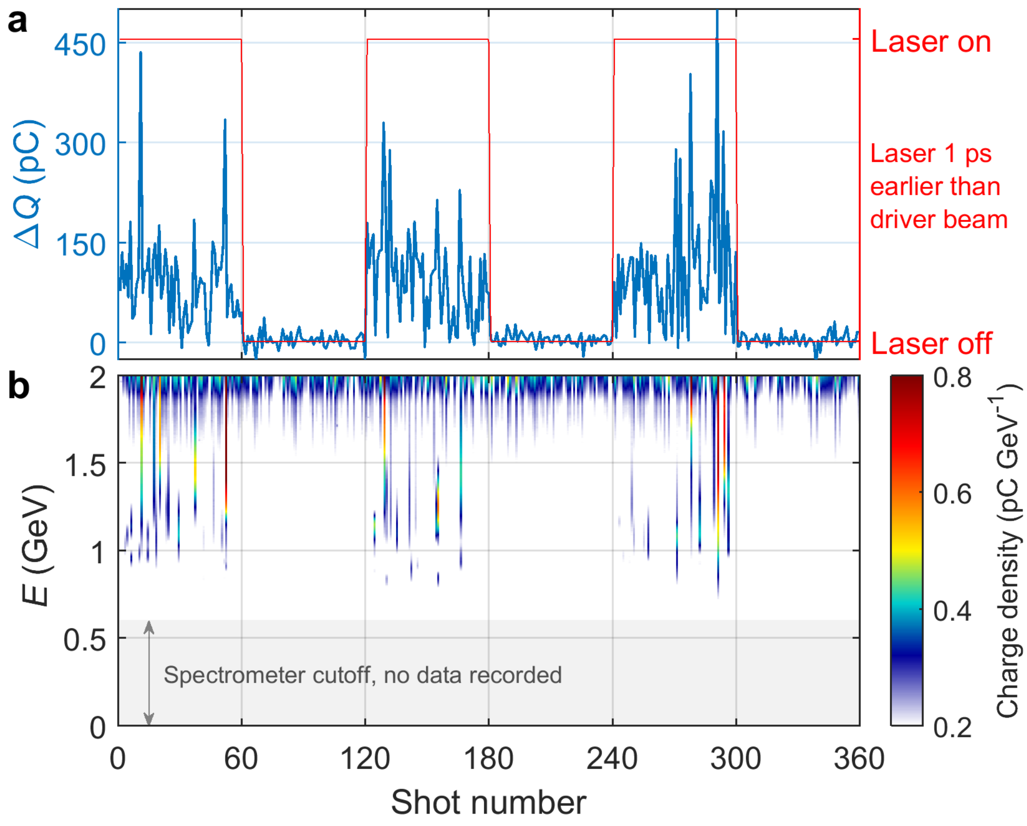

Figure 7.4: **Measured excess charge and corresponding spectra from plasma torch with injector laser turned on or off** The scan performed in the plasma torch mode contains 360 consecutive shots. Every 60 shots, the injector laser is either turned on or off as indicated by the red line in **a**. The blue line corresponds to the witness beam charge measured as charge difference between the beam-position-monitors (BPM) located up- and downstream of the interaction chamber. **b** shows the corresponding electron spectra measured on the electron spectrometer at the end of the beam line. Most spectra display large energy spread. They are subject to substantial shot-to-shot variations, likely due to alignment jitter between electron beam and pre-ionisation, paired with the narrowing plasma channel geometry shown in Fig. 7.1. However, almost every shot shows injected charge and demonstrate that plasma torch injection works considerably robust. Parts of the drive beam appear at the top of the spectrometer image, e.g. at 2 GeV. Figure taken from [187].

After establishing plasma torch injection, its close relation to the plasma photocathode can be exploited as stepping stone: by varying the TOA between electron beam and laser pulse and successively reducing the laser energy, torch injection can be converted into a plasma photocathode. Experimentally, this connection is exploited as follows. First, plasma torch is realised by sending the injector laser with maximal pulse energy several picoseconds ahead of the beam. This mode is particularly robust as the generated filament has comparable dimensions as the electron beam. Then, a TOA scan similarly to the one in Fig. 6.7 is performed, such that the filament is not generated ahead of the electron beam but later. This procedure reveals a transition regime between the limits of torch injection and the case where the laser arrives too late for beam generation. In between, the laser releases electrons just within the blowout. Successively reducing the laser energy reduces the density gradient of the filament and extent such that beam generation from plasma torch ceases completely to work. This particularly manifests for negative TOA, where the laser ionises helium before the drive beam arrives, but the generated density ramp is insufficient for torch injection and the transition region vanishes. Only when the laser releases electrons within the wake, e.g. in a narrow TOA range, these particles can get trapped and accelerated. Repeating the TOA scan in this situation reveals the desired plasma photocathode shown in Fig. 7.5 (c) unambiguously. Establishing and employing this two-dimensional connection, namely the effects of the torch and the narrow time-of-arrival, represents one of the major achievements of this campaign.

A series of shots captured by the electron spectrometer in the plasma photocathode regime is shown in Fig. 7.6 along with two exemplary spectrometer images. Similarly to the torch mode, accelerated beams can only be observed if the injector laser is turned on. Then, witness beams gain energy in the range of $0.3\,\mathrm{GeV}$ to $0.7\,\mathrm{GeV}$. These beams inhibit energy spread of ~2 % (r.m.s) and the derived emittance is of the order of $\epsilon_n = 1 \times 10^{-6}\,\mathrm{m\,rad}$. These comparably low energy values –given the pre-ionised plasma is nearly $1\,\mathrm{m}$ long– results from the shape of the plasma channel. Extensive simulation studies emphasize the deteriorating influence of the plasma channel shown in Fig. 7.1. As its radial extent narrows substantially after the first Bessel peak, the channel does not fully engulf the blowout. This periodically elongates and compresses the wake field, and the correspondingly varying radial function influences the wake potential defined by Eq. (3.13). Formed witness beams hence experience dynamically changing phases of the wakefield including decelerating ones. Additionally, considerable shot-to-shot alignment jitter of the electron beam orbit relative to the pre-ionisation laser axis is observed and illustrated in Fig. 7.7. Particularly the pre-ionisation laser jitters with ~$23\,\mu\mathrm{m}$ (r.m.s.), which represents a large fraction of the plasma channel radius and likely de-stabilises the plasma wakefield accelerator. This is one of the largest contributions to significant shot-to-shot variations in Fig. 7.5.

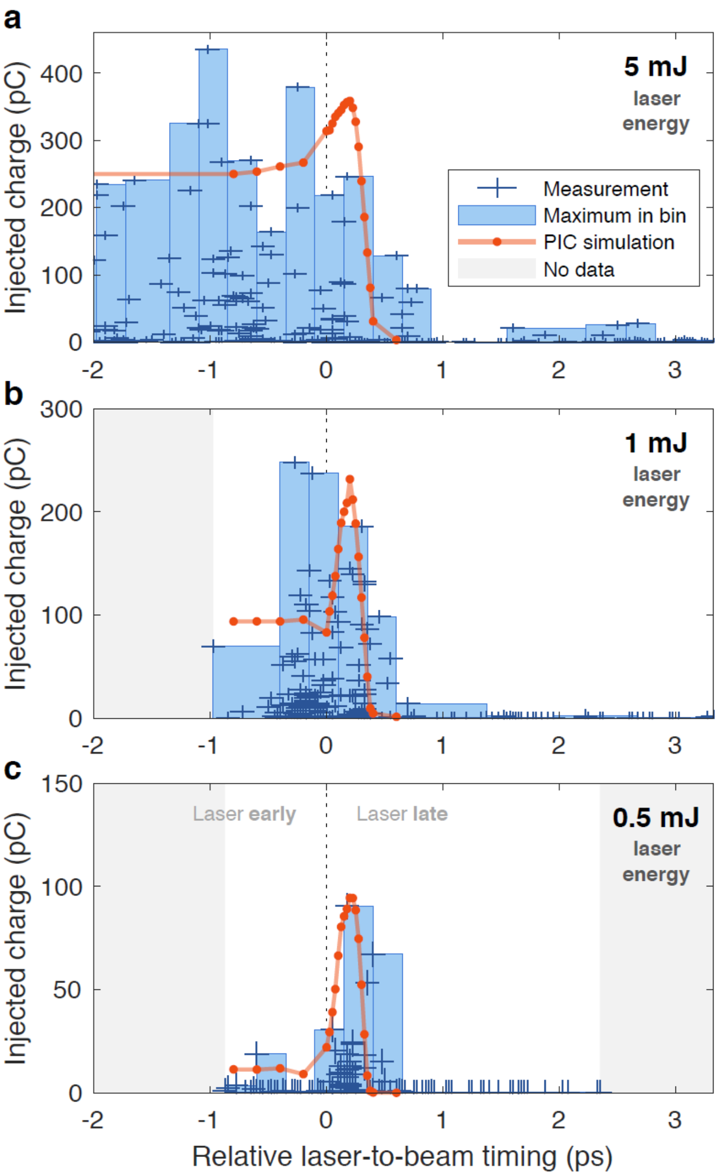

Figure 7.5: **Measured transition from plasma torch to plasma photocathode** All figures show the witness beam charge measured on the downstream spectrometer (blue crosses) in a TOA scan. The blue bars indicate the maximum charge per bin. The red line shows charge values obtained from PIC simulations. For negative TOA, the laser arrives ahead of the electron beam, while negative timings correspond to the case where the laser arrives after the beam. **a** The injector laser at maximal pulse energy of 5 mJ produces the largest helium filament corresponding to the most pronounced density spike. If the laser arrives ahead of the electron beam, substantial amounts of charge are trapped and accelerated. **b** Reduction of laser energy changes the impact of the torch density spike on the wake field, and less charge is injected. At TOA slightly larger than 0, a spike of trapped charge already hints injection of a plasma photocathode. **c** Further reduction of laser energy diminishes torch injection completely. Only when the laser releases electrons inside the blowout, trapped charge is detected on the spectrometer. This measurement unambiguously demonstrates electron beam generation by a plasma photocathode. Figure taken from [187].

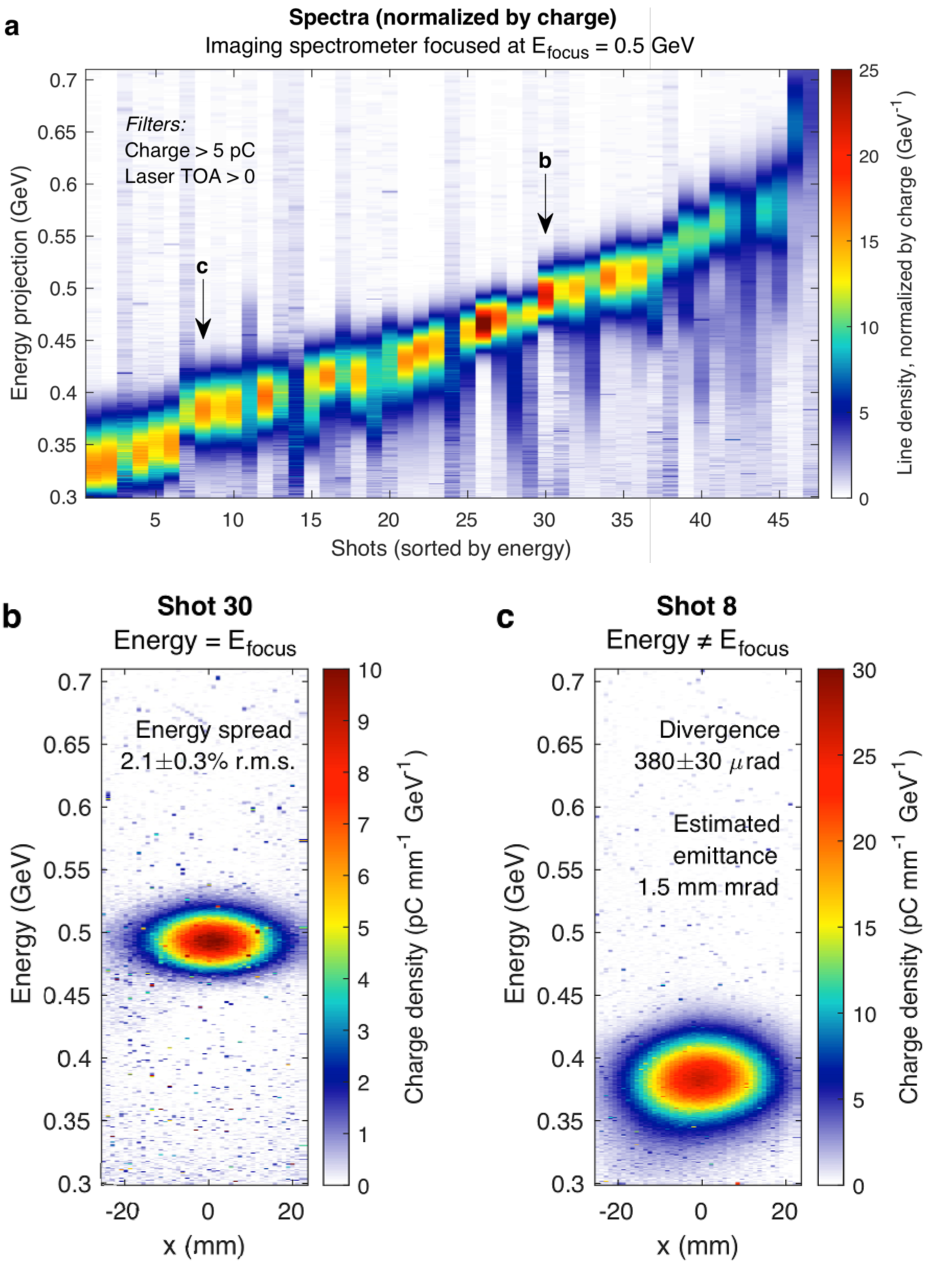

Figure 7.6: **Spectrometer data for shots in the plasma photocathode regime**. **a** Spectra sorted by mean energy for shots with charge Q > 5 pC colour-coded by charge density. **b** Exemplary shot taken close to the imaging energy og 0.5 GeV with energy spread of 2.1 ± 0.3 % (r.m.s.). **c** Exemplary shot with energy away from the imaging energy. The horizontal divergence can be estimated as 380 ± 30 µrad (r.m.s.) and the corresponding emittance as $\epsilon_n = 1.5 \times 10^{-6}$ m rad. Figure is a modified version from [187].

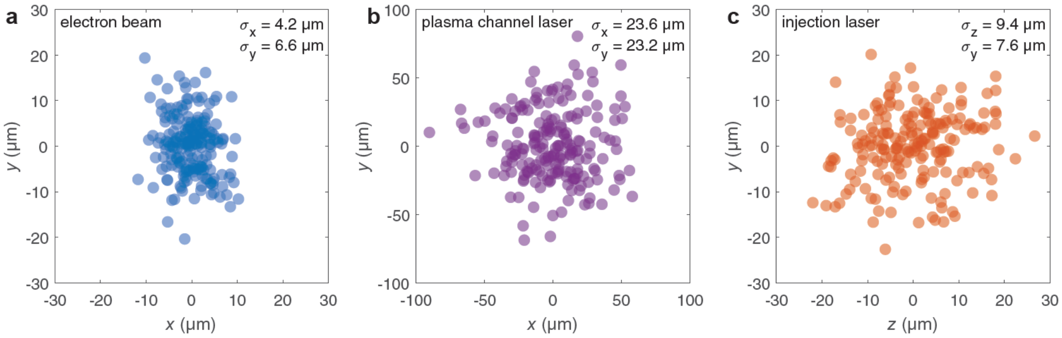

Figure 7.7: **Measured shot-to-shot jitter of all electron and laser beams**. Three sets of ~100 consecutive shots each measured on different OTR screens. For all beams, the alignment jitters by more than 10 % of the respective length scale. Combined with the already tight plasma channel geometry, this jitter most likely represents the major source of measurement error in the experimental campaign. **a** Shot-to-shot jitter of the electron beam pointing. The r.m.s. spread in both dimensions amounts to 4.2 µm and 6.6 µm, both r.m.s. **b** Shot-to-shot jitter of the pre-ionisation laser pointing. The r.m.s. spread in both dimensions amounts to 23.6 µm and 23.2 µm, both r.m.s. **c** Shot-to-shot jitter of the injector laser pointing. The r.m.s. spread in both dimensions amounts to 9.4 µm and 7.6 µm. Figure created by O.S. Karger for [184, 187].

7.3 SUMMARY

The experimental E-210 programme has systematically developed building blocks which eventually have allowed demonstration of controlled injection of electron beams by an independent laser pulse inside a plasma wakefield accelerator. Exploiting optically-triggered density downramp injection effectively locates and accesses the complementary plasma photocathode regime. Both schemes are realised for the first time and can now be considered feasible, established techniques.

The revealed transition between these injection schemes allows seamless transition from one mode to the other. Combined with the developed procedures and systems, particularly the plasma afterglow diagnostic presented in Chapter 6, this study provides a clear path towards reproduction and optimisation of the plasma photocathode wakefield accelerator.

Future studies must address multiple essential issues experienced in the E-210 campaign. Realising a wide and long plasma source turns out to be the most challenging building block, which can substantially influence all aspects of a plasma photocathode wakefield accelerator. Particularly the varying and narrow radial extent along the Bessel-shaped channel in the E-210 experiment deteriorates the PWFA process such that all generated beams display low energy and quality. Furthermore, the shot-to-shot alignment jitter between electron beam and pre-ionisation laser is responsible for low injection stability and large witness beam parameter variations. Wider channel radius as shown in Fig. 7.8 can mitigate most of these problems as the electron beam can be captured more easily, which relaxes the requirements on shot-to-shot pointing stability. Additionally, the injected witness beam then obtains a fixed phase relation inside the wakefield and therefore experiences constant energy gain. Wide plasma sources further maintain larger wakefield structures. This reduces requirements of shot-to-shot alignment between injector laser and drive beam, and simultaneously allows for significantly improved witness beam quality as discussed in Section 3.4. Long and wide plasma sources compatible with species-selective ionisation must therefore be employed.

Additionally, even though the 90° injector geometry facilitate the exploited transition, this setup limits achievable witness beam emittance compared to the collinear scheme proposed in [41]. Collinear or shallow-angle injection can provide ultra-low emittance in both transverse planes and must therefore be employed for unleashing the full potential of the plasma photocathode towards generation of lowest-emittance electron beams.

All remaining challenges discussed earlier are of *technical* nature and can be addressed by established technology. Particularly, delivering higher laser pulse energy for pre-ionisation combined with a focusing optic tailored for the generation of wider plasma channels is feasible already. Similarly, the substantial TOA jitter experienced in the E-210 campaign can be reduced to the 10 fs level [163, 196]. Both improvements can immediately stabilise the injection and acceleration processes.

Considering the presented results and the strategies developed for further improvement will lead to the production of highest quality electron beams in future experimental studies. These will be particularly suitable for generation of brilliant radiation from advanced light sources.

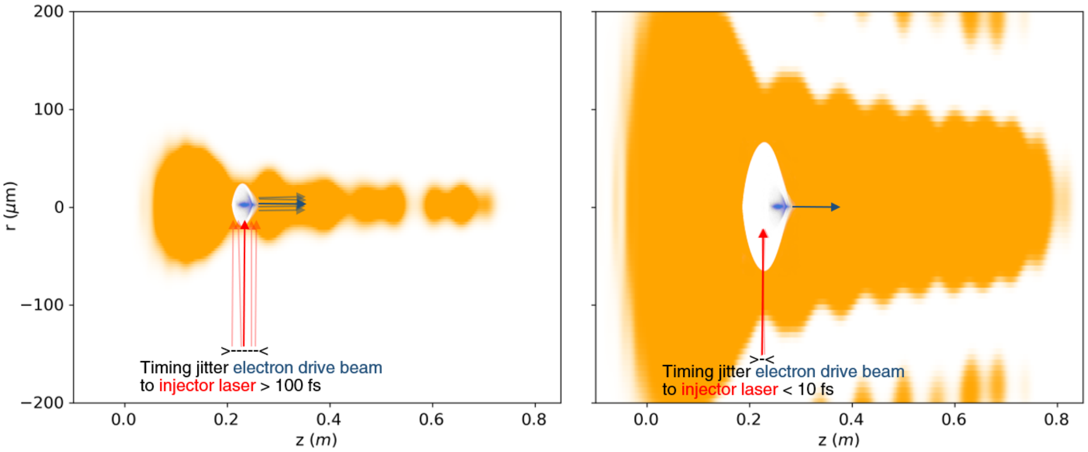

Figure 7.8: **Conceptual comparison of the experimental and and an optimised plasma channel**. **Left:** Plasma wakefield accelerator present in the experiment, similar to the case shown in Fig. 7.1. The pre-ionised channel (orange) just barely engulfs the blowout structure. Consequently, the acceleration process is compromised by varying accelerating and focusing fields, which limits the final witness beam energy. Furthermore, the accelerator displays high sensitivity to pointing jitter of the electron drive beam and the pre-ionisation laser indicated by blue horizontal arrows. The small plasma wavelength furthermore facilitates the strong influence of synchronisation jitter of the injector laser as indicated by the red vertical arrows. These effects combined are the reason for the high shot-to-shot jitter in all witness beam parameters. **Right:** Optimised plasma wakefield accelerator. Increasing the radial profile of the pre-ionised plasma channel, e.g. by choosing a different focusing optic, can allow for highly improved stability of the PWFA. This configuration ensures that the plasma always engulfs the blowout structure, which facilitates non-evolving electric fields inside the blowout even for increased plasma wavelength. Furthermore, the deteriorating effect of alignment jitter between electron drive beam and pre-ionisation laser diminishes. If, additionally, the synchronisation of injector laser and electron drive beam gets optimised towards state-of-the-art levels of ~10 fs, the witness beam can be generated approximately at the same phase of the wakefield for every shot. Combined, the parameter stability of the accelerated witness beams can improve substantially. Figure created for the review process of [187] by the authors of this publication.

8

THEORETICAL STUDY OF ICS γ-RAYS

The prospects of plasma-based accelerators facilitating brilliant, narrow bandwidth γ-ray sources substantially improve due to the results presented in Chapters 6 and 7. These experiments have solved considerable problems arising from any system involving (decoupled) electron and laser beams, for example accurate spatiotemporal coordination of electron and laser beams. Furthermore, demonstration of the plasma photocathode wakefield accelerator encourages further explorations towards its applications. As such, both experimental results are important milestones towards the generation of highest-quality ICS radiation in compact experimental environments, which may be suitable for demanding nuclear physics applications.

The given chapter, eventually, outlines the path towards generation of brilliant and narrow bandwidth ICS pulses and steps to be taken for meeting this goal. High electron beam density, short duration, low divergence and ultra-low emittance are crucial obligations according to the introduction in Chapter 4, but also low energy spread.

Interestingly, investigating the generation of *two* or multiple radiation pulses from individual plasma photocathodes at the beginning of this chapter has several advantages. First, this approach increases the amount of generated electron beams and associated ICS pulses, which emphasises several effects fundamental –and unique– to the plasma photocathode. Furthermore, each one of these pulses represents an individually tunable signal separable from the other ones in space and energy, but all of them are inherently synchronised. Generation of such multi-colour radiation is a fascinating research area in its own right, yet enables further advances of ICS quality from plasma accelerators. This is shown in the succeeding section, where the multi-beam approach combined with fundamental PWFA effects reveals the enabling key milestone for substantial reduction of the ICS spectral bandwidth. The last section combines all obtained results and showcases a highest-quality radiation source.

8.1 MULTI-COLOUR γ-RAY PRODUCTION

Application of several radiation pulses is widely used in science. Most prominent examples are pump-probe experiments, where the first signal excites specific dynamics or transitions within a target, and the second signal scans its momentary state. Varying the delay between both signals then resolves the triggered dynamics in a multi-shot approach. Thus, generation of multiple pulses is a highly important and rewarding research topic itself.

In the x- or γ-ray regime, the temporal spacing of multicolour radiation is determined by the pair or sequence of relativistic electron beams emitting the radiation. Therefore, concepts generating multiple electron beams automatically offer multiple radiation pulses. Conventional accelerators can deliver beams separated in energy and time, yet these approaches remain challenging and limited. Multiple beams are either directly produced by a photo injector [18, 197], or by splitting a high-energy beam [97, 98, 198]. Controlling the spatial and spectral separation can be tough as these beams must be accelerated by the same radio-frequency cavity in case of two generated beams, or the beam subject to splitting must be chirped substantially. Finally, conventionally generated beams inherit the mutual disadvantage of limited longitudinal compression, which in optimal cases produces beam durations of at least hundreds of femtoseconds, which directly translates to equivalently long radiation pulses via Eq. (4.13).

Plasma accelerators, in contrast, inherently produce electron beams with duration on the low femtosecond scale and correspondingly short radiation pulses. However, the fundamentally different acceleration process discussed in Chapter 3 commonly causes large-divergence beams with high energy spread [37, 150, 152]. Furthermore, injecting multiple beams with specific yet tunable longitudinal and spectral spacing represents a challenge as well. Techniques employed so far are mostly LWFA schemes such as self-injection from modulated plasma waves [199, 200] and ionisation injection, e.g. by dual-colour [201] or colliding pulses [202]. For PWFA, multiple injection due to beam pinching [203] has been proposed. In all schemes where beam injection and beam acceleration are strongly coupled, e.g. for modulated plasma waves or the dual-colour scheme, the spectral and/or spatial separation of these beams can be changed, but typically on cost of a substantially varied wake field. This limits applicability of these schemes.

This problem can be solved by employing two or more plasma photocathodes [204], which can produce multiple electron beams in a well-controlled manner. Being independently generated, both distributions inherit the high beam quality associated to a regular plasma photocathode. If the corresponding laser pulses are split-off fractions from the same original pulse, their relative temporal spacing is free of jitter and the resulting electron beams are intrinsically synchronised. Exploiting the confined ionisation volume and the mapping between release ξ_i and trapping positions ξ_f expressed by Eqs. (A.8c) and (3.20) can longitudinally separate multiple released electron populations. Experimentally, this can be achieved by changing the focus position of one laser pulse in the co-moving frame, which corresponds to the TOA in the laboratory frame. This varies the trapping position within the wake field and, thus, the timing relative to the other beam. The resulting temporal spacing between two beams can be approximated in first order as

$$\Delta t_{\mathrm{ICS}} = \Delta t_{e,1-e,2} \tag{8.1a}$$

$$\approx |\xi_{f,1} - \xi_{f,2}|/c \tag{8.1b}$$

$$\overset{\text{Eq. (3.20)}}{\approx} \left| \left(\xi_{i,1}^2 + \frac{2\alpha}{k_p^2} \right)^{1/2} - \left(\xi_{i,2}^2 + \frac{2\alpha}{k_p^2} \right)^{1/2} \right| /c. \tag{8.1c}$$

where the subscripts 1 and 2 denote the first and second beam, respectively, and $\alpha \approx 1.69$. Note the linear influence of the plasma density via $k_p^{-2} \propto n_p^{-1}$. Increasing it reduces the time between release and trapping and causes released particles to be trapped closer to the centre of the wake. Based on Eq. (8.1), large k_p can allow for more precise separation of released beams within a wider relative longitudinal range (e.g. recall the $n_p^{-1/2}$-scaling of the blowout length in Eq. (A.4)). The maximum spacing between the two beams is given by the blowout dimensions and, more restricting, the trapping potential amplitude.

The plasma photocathode can further produce beams with almost arbitrary spectral spacing. The final energy of a single beam is proportional to the electric field at its trapping position $E_z(\xi_{\mathrm{trap}})$ and the acceleration length d, e.g. $W_{\mathrm{kin}} \approx E_z(\xi_{\mathrm{trap}})d$. The latter is valid in a de-phasing-free plasma accelerator with non-evolving wake field. The final ICS pulse energy for a single beam and the mentioned constraints can be computed via Eq. (4.7):

$$E_{\mathrm{ICS}} \approx 4E_L\gamma_e^2 \tag{8.2a}$$

$$= 4E_L\left(\frac{W_{\mathrm{kin}}}{m_e c^2}\right)^2 \tag{8.2b}$$

$$\approx \frac{4E_L}{m_e^2 c^4} E_z^2(\xi_f)d^2 \tag{8.2c}$$

$$\approx \frac{4E_L}{\alpha^2} k_p^4\, d^2(\xi_i^2 + 2\alpha k_p^{-2}) \tag{8.2d}$$

Thus, simply injecting one beam later than the other yields large capabilities for spectral separation, and the spectral spacing of two ICS pulses reads

$$\Delta E_{ICS} \approx 4E_L \left|\gamma_{e,1}^2 - \gamma_{e,2}^2\right| \tag{8.3a}$$

$$\approx \frac{4E_L}{\alpha^2} k_p^4 \left|d_1^2(\xi_{i,1}^2 + 2\alpha k_p^{-2}) - d_2^2(\xi_{i,2}^2 + 2\alpha k_p^{-2})\right| . \tag{8.3b}$$

Here, d_1 and d_2 are the individual acceleration lengths of the two beams until the ICS interaction point, respectively. Equation (8.3) shows that the spectral spacing is mostly given by the individual acceleration lengths d_1 and d_2. The specific accelerating field at the individual trapping positions, here expressed in terms of the release positions $\xi_{i,1}$ and $\xi_{i,2}$, is of comparable strength. As expected, the absolute energy is proportional to $k_p^4 \propto n_p^2$, such that smaller wakes associated to stronger electron beam acceleration produce high-energy ICS signals within a shorter plasma accelerator. If beam 1 is injected first at laboratory frame position P_1, and beam 2 is injected later at P_2, their acceleration lengths are connected via

$$d_2 = d_1 - (P_2 - P_1) \tag{8.4}$$

Integrating Eqs. (8.1c) and (8.3b) over longitudinal release positions yields dependences for trapped beams instead of single particles. Together, Eqs. (8.1c), (8.3b) and (8.4) fully determine the temporal and spectral spacing between two ICS pulses generated by a plasma photocathode inside the same blowout in terms of experimentally accessible parameters.

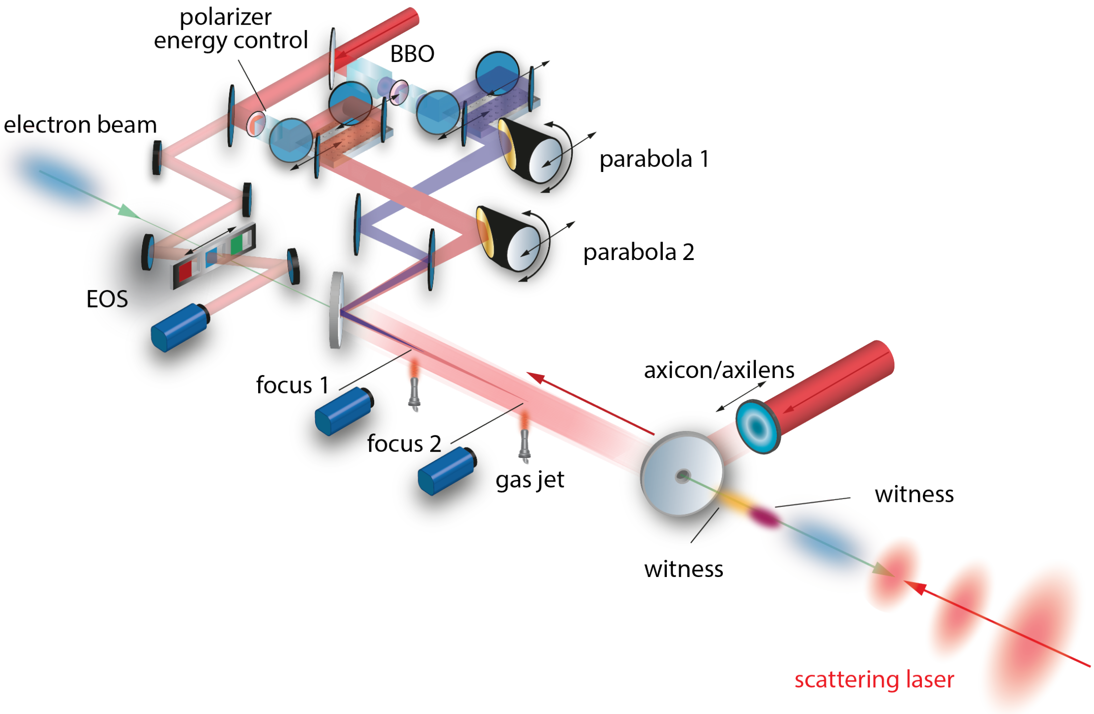

Figure 8.1: **Exemplary layout of a two-beam plasma photocathode wakefield accelerator** This schematic represents a collinear version of Fig. 7.2, which generates a low-emittance witness beam at focus 1 inside a plasma wakefield accelerator. Here, a second, independently tunable laser path (purple), e.g. frequency doubled by passing a beta barium borate (BBO) crystal, creates another injection volume further downstream. Using two gas jets for witness beam generation decouples the pre-ionisation process, e.g. when the dopant gas is released locally after the plasma has been generated. This allows for higher pre-ionisation intensities and thus wider and longer plasma channels, which were both bottlenecks experienced in Chapter 7. At the end, driver and witness beams are decoupled from the plasma and can be transported to a subsequent beam line or application. In this case, the ICS scattering laser interacts head-on with the electron beams. This setup can further be applied for the energy spread compensation technique shown in Section 8.2.

The following passage describes the concept of producing multi-colour radiation by means of the plasma photocathode. The plasma wakefield accelerator based on pre-ionised hydrogen gas of density $n_p \approx 1.8 \times 10^{22}\,\mathrm{m}^{-3}$ corresponding to $\lambda_p \approx 250\,\mu\mathrm{m}$ is driven by a transversally matched Gaussian electron beam with peak current $I_p \approx 3\,\mathrm{kA}$ with parameters accessible by FACET-II [39], the upcoming PWFA facility. Its density fulfils the blowout condition, e.g. $n_b \approx 55 n_p$, and creates a deep trapping potential. This beam-plasma system is free of dark current as neither the wake nor the beam ionise ambient helium gas. The beam duration is off-resonance, e.g. $k_p \sigma_z = 0.95$

to avoid overlap of beam particles and electrons released by the plasma photocathode lasers. One laser releases electrons from the neutral dopant gas helium of density $n_{\mathrm{He}} \approx 1.75 \times 10^{23}\,\mathrm{m}^{-3}$ directly in the centre of the wake and represents the reference case. A second laser focused to different laboratory-frame and co-moving coordinate frame positions releases another electron beam. A potential layout depicts this situation in Fig. 8.1. Fig. 8.2 shows two snapshots of this configuration obtained from PIC simulations.

All PIC simulations shown in this chapter origin from a single input deck of numerical and physical parameters modelled in VSim[156]. The three-dimensional box consists of $352 \times 192 \times 192$ cubic cells of size $1\,\mu\mathrm{m}$ in each direction. Each cell contains 1 macro particle for the hydrogen plasma medium with physical density $n_p \approx 1.8 \times 10^{22}\,\mathrm{m}^{-3}$ corresponding to $\lambda_p = 250\,\mu\mathrm{m}$. The 6D-Gaussian PWFA drive beam consists of 32 macro particles per cell. It has $10\,\mathrm{GeV}$ $\pm 5\,\%$ energy and normalised emittance $\epsilon_n = 50 \times 10^{-6}\,\mathrm{m\,rad}$. Its radius is matched to the plasma with $\sigma_{x,y} \approx 4.48\,\mu\mathrm{m}$ corresponding to $k_p\sigma_{x,y} = 0.11$, and its duration $\sigma_z \approx 37.8\,\mu\mathrm{m}$ corresponds to $k_p\sigma_z = 0.95$. The beam is initialised in vacuum by a Poisson solve before it enters the plasma region via a linear density up-ramp of length $1.2\lambda_p$. The plasma photocathode injector lasers are implemented by a Gaussian envelope model with $a_0 = 0.025$, $w_0 = 4.0\,\mu\mathrm{m}$ and duration $\tau = 20\,\mathrm{fs}$ if not otherwise stated. They are focused to different longitudinal positions inside the wake and in the laboratory frame. The lasers ionise neutral helium gas implemented by a fluid model by means of averaged ADK theory, and generate electron and ion macro particles with nominally 32 macro particles per cell. The nominal helium density $n_{\mathrm{He}} = 1.75 \times 10^{23}\,\mathrm{m}^{-3}$. All particle species are subject to a third-order Boris push, and all fields are interpolated by third order between cells. Current fields are smoothed by a 1-2-1 digital filter before being solved by the Yee-PIC-cycle.

Following, the injection of three different electron beam pairs into similar plasma wake field accelerators is presented. In all of them, the foremost beam is injected first, in the centre of the wakefield and by the same laser pulse as in Fig. 8.2. The second beam results from another injector laser with similar properties, but focused to a different position within the wake field and/or at different laboratory frame positions. Depending on these two parameters, the resulting beam pair can be separated in time and/or energy. As all electron beams are generated by similar laser pulses, they are all of short duration ~$1.6\,\mathrm{fs}$ (r.m.s), carry comparable charge of $Q \approx 2.7\,\mathrm{pC}$ and their normalised emittance ranges from $\epsilon_n \approx 30 \times 10^{-9}\,\mathrm{m\,rad}$ to $35 \times 10^{-9}\,\mathrm{m\,rad}$.

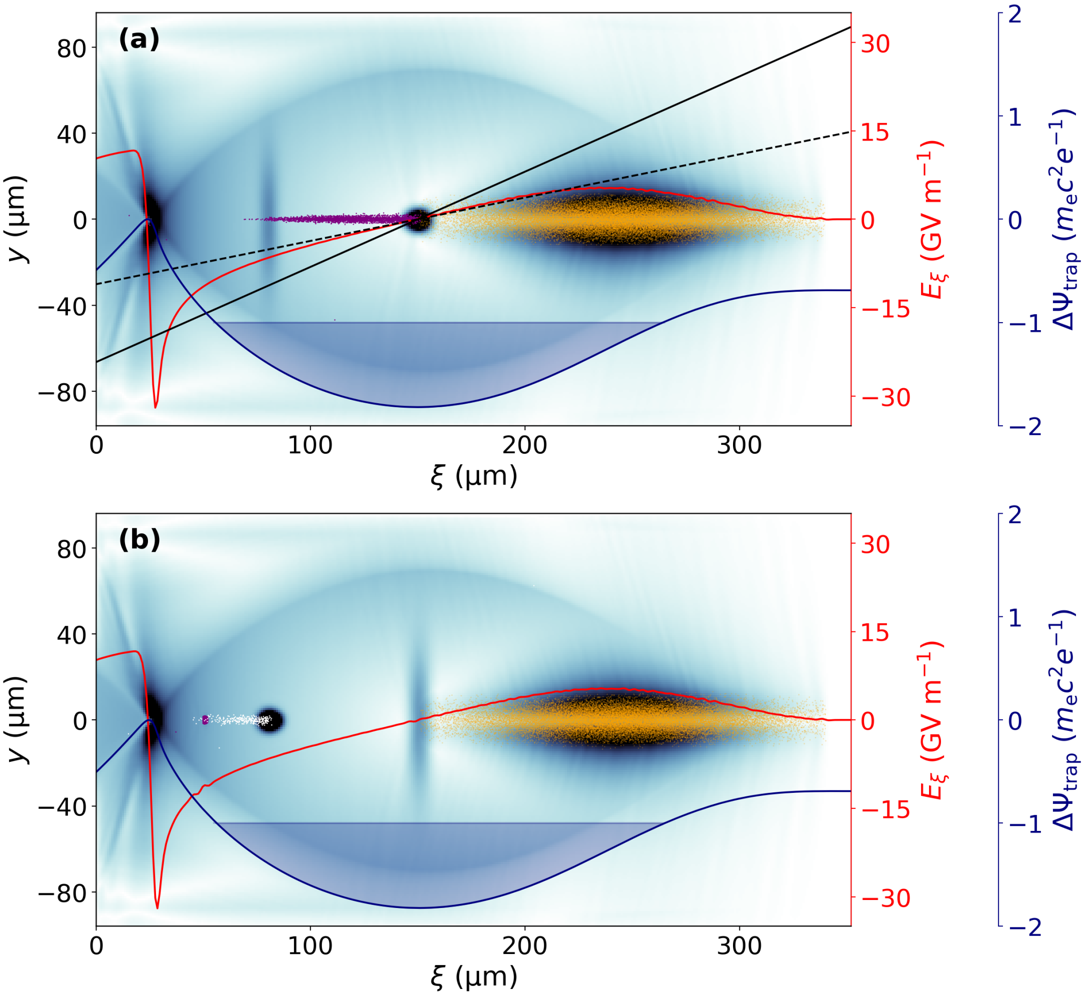

Figure 8.2: **Plasma wake field accelerator with two plasma photocathodes. (a)** The first plasma photocathode releases electrons (purple) at the centre of the blowout (the background field represents the normalised absolute field values), which slip back and get trapped in the rear. The black solid line represents the theoretically predicted accelerating field based on Eq. (3.14). It deviates from the simulated field (red), probably because the beam does not fulfil the longitudinal resonance condition. The dashed black line corresponds to the field from Eq. (A.6) scaled by $k_p\sigma_z\exp(-(k_p\sigma_z)^2)$ [102] with $k_p\sigma_z = 0.95$ used in the simulation, which compensates for the off-resonant configuration. **(b)** The first laser pulse has defocused. A second plasma photocathode laser located further in the rear of the blowout releases a second electron population (white). Due to the trapping dynamics given by Eq. (3.20), the second population gets trapped behind the first witness beam and thus forms an individual distribution independent of the first one. In principle, the whole longitudinal region where $\Delta\Psi_{\mathrm{trap}} \leqslant 1$ (indicated by transparent blue area) allows injection of electron beams. However, witness beams trapped very close to the blowout vertex, e.g. at the electric field spike, will experience highest transverse forces which can cause beam hosing or even loss. It may be noted that the longitudinal field at the trapping position of the purple witness displays beam loading due to its high charge density. The resulting shape, however, is unphysical due to comparably large cell size which under-samples the self-field of the witness beam.

All figures further display the simulated [15, 139], incoherent scattering events generated by the interaction with a low-intensity $a_0 \approx 0.044$ laser pulse focused to $w_0 = 4.0\,\mu m$. A description of the code can be found in Chapter 5. In this work, a $\lambda_L = 800\,nm$ laser pulse scatters head-on with the electron beam distribution obtained from PIC simulations. It is focused to $w_0 = 4\,\mu m$ and has a duration of $\tau = 4z_R/c \approx 0.8\,ps$ with $z_R = \pi w_0^2/\lambda_L$ being the Rayleigh range. This ensures photons are present during the whole time the electron traverses the focal region and increases the overall photon yield without non-linear spectral broadening caused by higher laser intensity. The corresponding normalised intensity $a_0 \approx 0.044 \ll 1$ ensures linear interaction and fulfils the requirements of the code. All ICS spectra are simulated on-axis. The spectral resolution is given by 400 evenly spaced bins spanning the range between 0.8 to 1.2 times the ICS frequency $4\gamma_e^2\omega_0$ for the average electron energy. As this implementation causes massive problems when simulating multiple beams with large energy gap, each beam is simulated individually and the spectra are combined afterwards. The temporal resolution is given by the duration of the electron beam, which is split into 300 evenly spaced bins. The obtained distributions are subsequently binned into a histogram with bin size $dt = 0.02\,fs$ and $dE = 2.0\,keV$ and smoothed by a convolution process to produce continuous curves. All temporal and spectral spacings here are defined as the distance between the weighted means of any two distributions. Electron beam energy spread and ICS pulse bandwidth are given as weighted r.m.s., e.g. via

$$< x >= \frac{1}{\Sigma y}\Sigma(yx), \tag{8.5}$$

and

$$< \Delta x >= \left(\frac{\Sigma y(x- < x >)^2}{(\Sigma y) - 1}\right)^{1/2}. \tag{8.6}$$

Each resulting ICS pulse consists of 2.6×10^6 to 2.9×10^6 photons. Note that the interactions neglect the presence of the plasma accelerator and particularly the drive beam. However, if the latter is energetically separated from the witness beam energy as in the given simulation, ICS radiation emitted from this beam is substantially separated from the desired pulse energy. In case this high-energy photon pulse is not tolerable for an application, the drive beam must be removed from the ICS process e.g. by means of a dispersive chicane in a beam line downstream of the plasma section.

In the first simulation shown in Fig. 8.3, the first witness beam has propagated $d_1 \approx 10.8\,\mathrm{mm}$ before the second beam is injected. In the co-moving frame, the associated injector laser is focused $\Delta\xi_i = 10\,\mu\mathrm{m}$ behind the first laser, which causes the released electron to be trapped almost at the first beams trapping position. This violates the trapping condition in Eq. (A.8c) that predicts stronger separation. Very likely, this effect results from beam loading caused by the first witness that changes the integrated electric field during the second trapping process. Nevertheless, the resulting beam pair propagates almost without temporal spacing over $2.08\,\mathrm{cm}$ where the shown snapshot is taken. As the second beam is injected after the first one in the laboratory frame, the pairs display an energy gap of $\Delta W_{\mathrm{kin}} \approx 125\,\mathrm{MeV}$. Individually, they provide $W_{\mathrm{kin},1} \approx 238.77\,\mathrm{MeV}{\pm}3.80\,\%$ and $W_{\mathrm{kin},2} \approx 113.49\,\mathrm{MeV}{\pm}5.75\,\%$. The phase space evolution of the first beam is exemplary presented in Fig. 8.9.

Consequently, the generated ICS pulse pair obtains negligible temporal delay and a wide spectral gap of $\Delta E_{\mathrm{ICS}} \approx 1\,\mathrm{MeV}$. The first pulse has a mean energy $E_{\mathrm{ICS},1} \approx 1.36\,\mathrm{MeV}{\pm}7.57\,\%$, and the second one $E_{\mathrm{ICS},2} \approx 0.31\,\mathrm{MeV}{\pm}10.38\,\%$. Note that the bandwidth of each pulse is approximately twice the energy spread of the associated electron beam in agreement with Eq. (4.12).

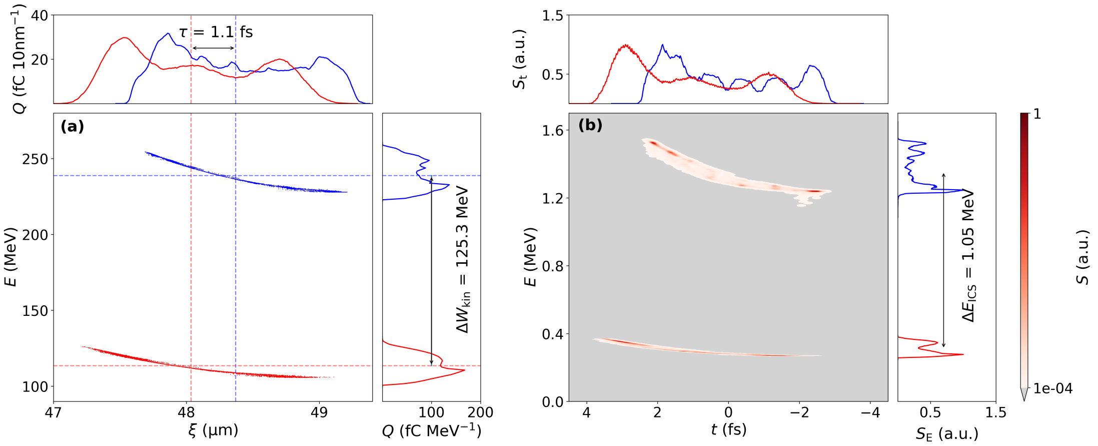

Figure 8.3: **Multi-colour radiation from two beams separated in energy. (a)** Longitudinal phase space of two beams trapped at approximately the same position within the plasma wakefield accelerator, but injected by two plasma photocathodes at different laboratory-frame positions spaced by $\Delta P = 10.8\,\mathrm{mm}$. This configuration leads to a spectral gap of $\Delta W_{\mathrm{kin}} \approx 125\,\mathrm{MeV}$. The inset on the top (side) shows the beam charge projected to time (energy). **(b)** Spectral ICS pulse density S in the energy-time phase space obtained from the beams shown in (a). The inset on the top (side) shows the spectral density projected to time (energy). The first pulse (blue) has a mean energy $E_{\mathrm{ICS},1} \approx 1.36\,\mathrm{MeV}{\pm}7.57\,\%$, and the second one (red) $E_{\mathrm{ICS},2} \approx 0.31\,\mathrm{MeV}{\pm}10.38\,\%$. The corresponding spectral gap amounts to $\Delta E_{\mathrm{ICS}} \approx 1\,\mathrm{MeV}$.

Figure 8.4 separates the injector position of the second laser within the co-moving coordinate frame by $\Delta\xi_i = 40\,\mu\mathrm{m}$ towards the blowout rear, while all other parameters remain unchanged. As a consequence, the second beam is trapped ~5.1 µm (or 17.1 fs) behind the first beam. Due to the different field and changed beam loading, the second beam gains more energy over the same propagation distance than in the first simulation. However, the first beam also changes its energy distribution, as its accelerating field is not influenced by the second beam any more. At the given charge level, this beam loading is likely a numerical effect caused by low longitudinal resolution. Due to these reasons, the electron beams have gained energy $W_{\mathrm{kin},1} \approx 243.88\,\mathrm{MeV}{\pm}3.38\,\%$ and $W_{\mathrm{kin},2} \approx 131.79\,\mathrm{MeV}{\pm}3.44\,\%$, and the resulting spectral spacing remains approximately the same as before: The first pulse has a mean energy $E_{\mathrm{ICS},1} \approx 1.41\,\mathrm{MeV}{\pm}7.29\,\%$, and the second one $E_{\mathrm{ICS},2} \approx 0.40\,\mathrm{MeV}{\pm}7.35\,\%$.

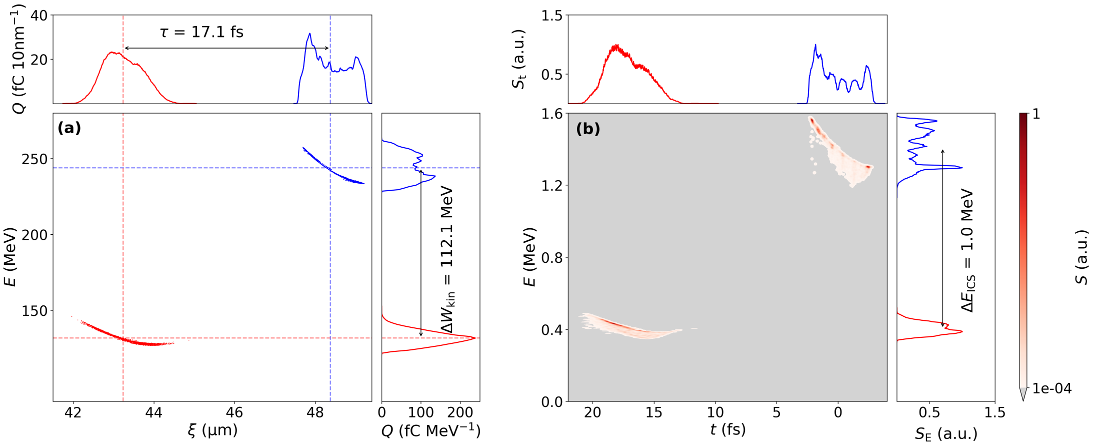

Figure 8.4: **Multi-colour radiation from two beams separated in energy and time. (a)** Longitudinal phase space of a beam pair released by two plasma photocathodes spaced by $\Delta\xi_i = 40\,\mu m$ in the co-moving coordinate frame and by $\Delta P = 10\,mm$ in the laboratory frame. This configuration causes a temporal spacing of $\tau \approx 17.1\,fs$ and a spectral gap of $\Delta W_{kin} \approx 112\,MeV$. The inset on the top (side) shows the beam charge projected to time (energy). **(b)** Spectral ICS pulse density S in the energy-time phase space obtained from the beams shown in (a). The inset on the top (side) shows the spectral density projected to time (energy). The first pulse (blue) has a mean energy $E_{ICS,1} \approx 1.41\,MeV \pm 7.29\,\%$, and the second one (red) $E_{ICS,2} \approx 0.40\,MeV \pm 7.35\,\%$. The corresponding spectral gap amounts to $\Delta E_{ICS} \approx 1\,MeV$.

The third simulation presented in Fig. 8.5 changes the injection position of the second electron beam in both the co-moving and the laboratory frame. Now, the beam is released $\Delta\xi_i = 70\,\mu m$ behind the first injector focus, which further increases the temporal spacing to ~47.2 fs. This time, the second beam is injected just $\Delta P = 4.8\,mm$ after the first one to deliberately alter the spectral spacing. As a consequence of this configuration, the second beam gains energy at much higher rate such that the spectral spacing reduces. For the given simulation snapshot, $W_{kin,1} \approx 135.91\,MeV \pm 3.69\,\%$ and $W_{kin,2} \approx 133.09\,MeV \pm 4.12\,\%$. This yields a mean ICS pulse energy $E_{ICS,1} \approx 0.42\,MeV \pm 6.88\,\%$, and $E_{ICS,2} \approx 0.44\,MeV \pm 6.02\,\%$ for the second one. Note that this simulations is stopped already after 8.1 mm of mutual acceleration of the beam pair, which reduces the final energy compared to the first two simulations. Continuing the acceleration process will, eventually, accelerate the second beam to higher energy than the first beam, which also affects the ICS pulses.

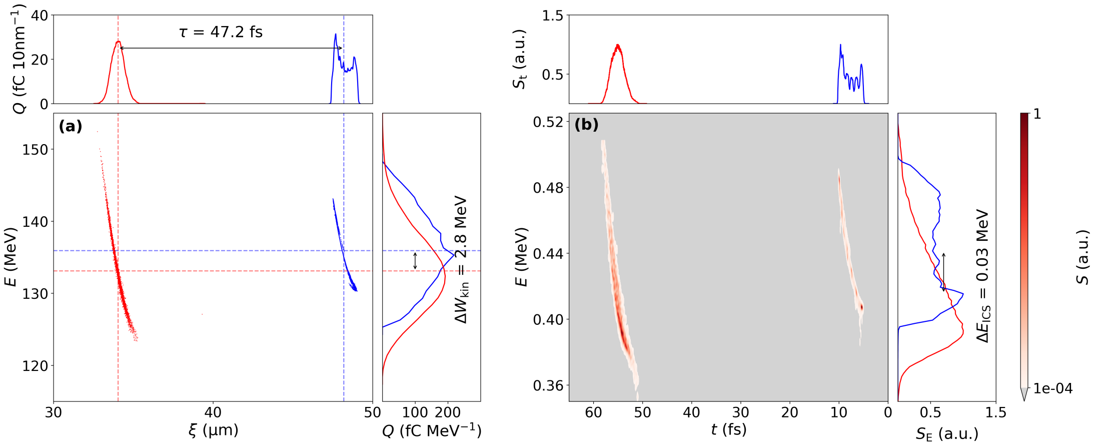

Figure 8.5: **Multi-colour radiation from two beams separated in time. (a)** Longitudinal phase space of a beam pair released by two plasma photocathodes spaced by $\Delta\xi_i = 70\,\mu\mathrm{m}$ in the co-moving coordinate frame and by $\Delta P = 4.8\,\mathrm{mm}$ in the laboratory frame. This configuration causes a temporal spacing of $\tau \approx 47.2\,\mathrm{fs}$ with minimal spectral gap. The inset on the top (side) shows the beam charge projected to time (energy). **(b)** Spectral ICS pulse density S in the energy-time phase space obtained from the beams shown in (a). The inset on the top (side) shows the spectral density projected to time (energy). The first pulse (blue) has a mean energy $E_{ICS,1} \approx 0.42\,\mathrm{MeV} \pm 6.88\,\%$, and the second one (red) $E_{ICS,2} \approx 0.44\,\mathrm{MeV} \pm 6.02\,\%$. The corresponding spectral gap amounts to $\Delta E_{ICS} \approx 0.03\,\mathrm{MeV}$.

Summarising, the plasma photocathode wakefield accelerator enables generation of multiple witness beams with large capacities for spectral and temporal separation. The subsequently produced ICS pulses inherit the temporal spacing 1:1 and the spectral separation follows the γ_e^2 dependence. It may be particularly noted that the generated beams and pulses are fully independent of each other and do not provide any low-energy tail typically present in most LWFA configuration. Generated spectra reach into the MeV level with bandwidth about ~7 % to 10 %. These directly result from the electron beam energy spread shown in the corresponding figures and must be overcome for further optimisation towards nuclear physics applications. In contrast, the low electron beam divergence associated to the low emittance in a plasma photocathode wakefield accelerator prevents additional, massive spectral broadening predicted by Eq. (4.12). As such, these pulses display much narrower bandwidth than all other plasma-based ICS sources. It may be noted that, in principle, more than two beams can be generated by adding more plasma photocathodes, which can lead to a train of single or multiple central ICS energies.

Most issues occurring in the presented simulations directly relate to the numerical electron beam generation in the PIC code. First, the number of macro particles per witness beam of the order of 3500 yields non-continuous radiation pulses. Decent statistical post-processing therefore requires binning and smoothing, which can be avoided by increasing the macro particle density at the cost of computational resources required for the particle pusher. Second, and more fundamentally, the grid resolution in these simulations is coarse. The chosen value of 1 µm cubed is a tradeoff between sampling of the witness beam and the extent of the simulation box, and ultimately originates from the very different length scales present in the plasma photocathode wakefield accelerator. The simulation box is comparably large to capture the $\lambda_p \approx 250\,\mu\text{m}$ long blowout chosen for high transverse beam quality according to Eqs. (3.33) to (3.35). Simulating a smaller wakefield, in turn, would allow for reduced box size and resolution, but sacrifice witness beam quality. Further, the high fields associated to small blowouts can cause wake ionisation and, in case of a dense drive beam, beam ionisation and associated dark current (e.g. see Section 3.2.2). Avoiding dark current in high-field scenarios requires more exotic combinations of plasma and dopant gas media, which represents a whole study on its own right. In a beam loading-free configuration, the given resolution would suffice as the accelerating field has an almost linear shape. However, the given beams do load the wake. Particularly the longitudinal resolution prevents sufficient sampling and causes unphysical spikes along each beam. As such, this affects all presented longitudinal phase space distributions. This problem can, in principle, be addressed by reducing the longitudinal cell size substantially, e.g. to $\Delta x \leqslant 0.2\,\mu\text{m}$ at the cost of fourfold increased computational costs.

8.2 ENERGY SPREAD COMPENSATION BY MULTIPLE ELECTRON BEAMS

Apart from multi-colour γ-ray production, the versatility of the plasma photocathode –expressed by the generation of multiple electron beams– provides further benefits for both particle accelerators and light sources. In fact, proper application can improve the electron beam brightness and subsequently generated pulse brilliance substantially, and at the same time solve several crucial problems in plasma accelerators. The author has contributed significantly to publishing the associated concept [133]. Setting the scene for this abstraction of multi-beam generation requires a short introductory paragraph recapitulating fundamental properties of electron beams and plasma wakes.

As outlined in Section 3.2, any particle beam inherits a non-zero spectral distribution. This *energy spread* can be divided into the uncorrelated or residual fraction originating from the distributions generation process, and the correlated spread that the beam accumulates during acceleration. More information can be found in Section 3.2.3. While the former represents the lower limit for achievable energy spread of a given generation process, the latter can be reversed.

Particularly plasma electron accelerators suffer from substantial energy spread due to their high wakefield amplitudes and corresponding field gradients. Typical energy spreads range from ~1 % at low electron energy [199, 205] up to tens of percent [37, 150, 152]. As the beam transport inside the accelerator along with any applications demand for mono-energetic spectra, several different methods for reducing accumulation of energy spread [98, 113] or for its compensating [206–209] have been proposed.

This sections describes a novel technique for energy spread compensation directly within the plasma wakefield accelerator. If applied correctly, this scheme can completely reverse the correlated energy spread, while maintaining optimal beam quality and current. At high final beam energy, the remaining, constant residual energy spread can yield relative values far below 1 %, allowing for unprecedented monochromaticity in plasma accelerator science.

This effect is caused by loading a nonlinear blowout with a high-current particle distribution. In contrast to other beam-loading techniques where the witness beam itself provides the charge density required for flattening the accelerating field, this scheme decouples the witness from the loading effect: Deliberately generating (or externally injecting) a high-charge beam inside the wake field can over-load the wake field at the position of a witness beam such that the fields slope changes its sign. This situation can be illustrated by a simplified 1D fluid model [133, 177]

$$k_p^{-2}\frac{\partial^2\phi}{\partial\xi^2} = \frac{n_b + n_d + n_w}{n_p} + \frac{1}{2(1+\phi)^2} - \frac{1}{2}, \tag{8.7}$$

where ϕ denotes the electrostatic wake potential generated by the drive beam of density n_b, while n_d and n_w correspond to the particle densities of loading and witness beams, respectively. Figure 8.6 displays solutions for different combinations of these three beams.

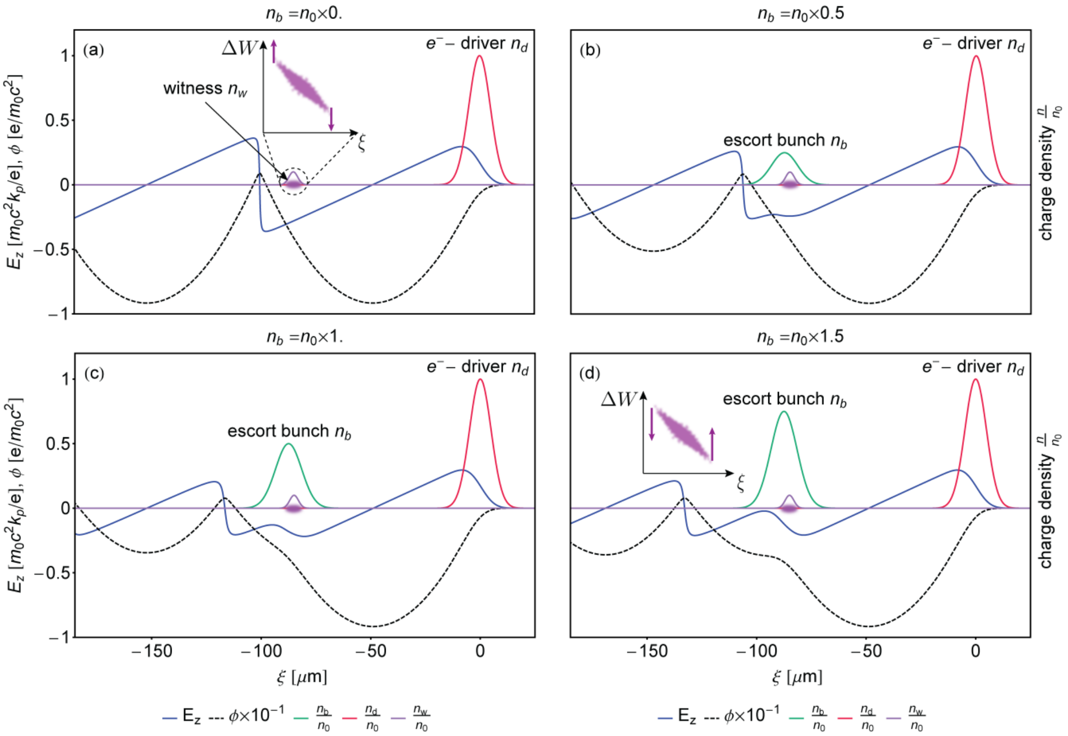

Figure 8.6: **Numerical solutions for the electrostatic wake potential for different beams.** This figure solves Eq. (8.7) for different variations of trapped beams. **a** The electron drive beam (red) generates the parabolic wake potential (black) associated to a blowout, which yields the typical saw-tooth shaped longitudinal electric field (blue). A low-charge witness beam (purple) trapped in the rear of this structure gains energy and accumulates energy spread due to the finite field slope. The inset depicts the longitudinal phase space and indicates that the tail of the beam gains more energy than its front. **b** Adding a second, high charge beam denoted as escort bunch to the witness beam flattens the electric field similar to the case proposed in [113]. This compensates the field gradient and reduces the accumulation of energy spread. **c** Increasing the escort charge density overloads the wake field such that the gradient switches sign. **d** Further increasing the escort charge density amplifies the effect shown in **c**. The witness beam now gains more energy at its front than in its back, which causes a counter-clockwise rotation in the longitudinal phase space. As long as the escort is present, the witness beam therefore reduces its energy spread. Figure produced by A. F. Habib for [133].

A witness beam inheriting accumulated energy spread will *de-chirp* if it resides in this special region: the overall longitudinal phase space distribution defined by ξ,W rotates adiabatically in a counter-clockwise direction. This process is shown in Fig. 8.7 for witness and escort beams generated by two individual plasma photocathodes in a layout similar to Fig. 8.1. Provided this beam has gained sufficient energy before the escort is trapped, it becomes relativistically stable and is immune against the additional space charge field. The witness, therefore, maintains its potentially high transverse quality while de-chirping reduces both absolute and relative energy spread. This scheme consequently increases the final 6D brightness defined by Eq. (3.25) as outlined in Figure 8.8.

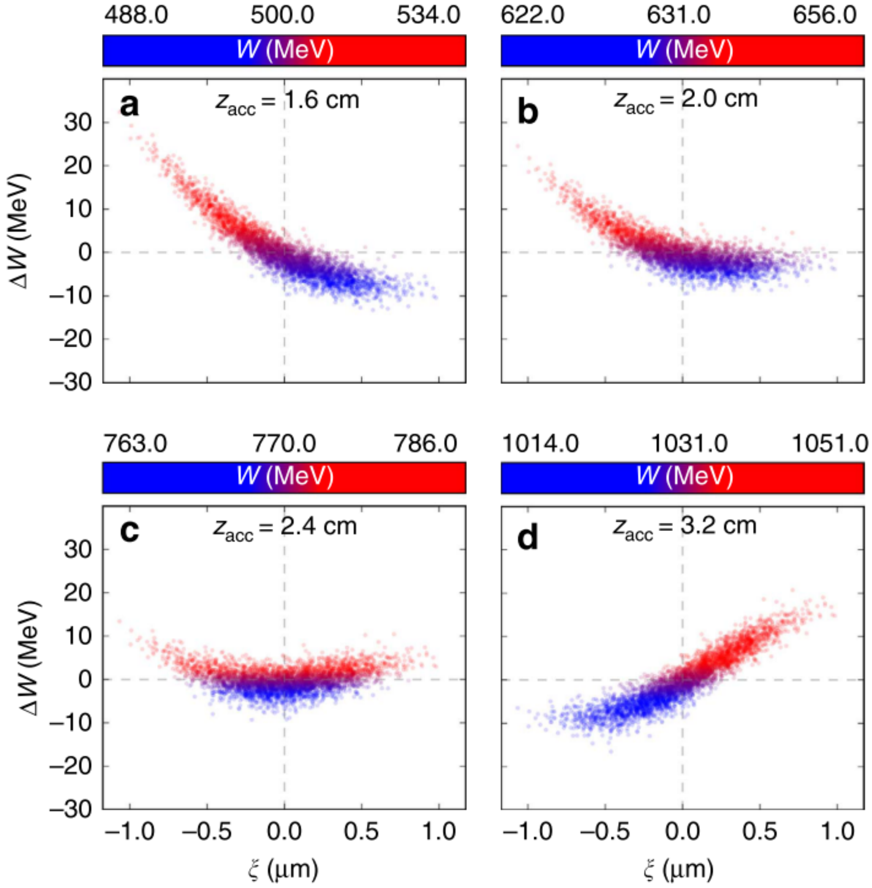

Figure 8.7: **Energy spread compensation caused by overloaded wake field** The witness beam shown has been generated by a plasma photocathode. **a** After propagating $z_{acc} = 1.6\,\mathrm{cm}$ in a $\lambda_p = 100\,\mu\mathrm{m}$ long blowout, the beam has accumulated considerable energy spread. Furthermore, its gained mean energy 500 MeV makes it relativistically stable against space charge effects. **b** After the escort beam has been released by a second plasma photocathode, the overloaded wake rotates the witness beams longitudinal phase space counter-clockwise and reduces its energy spread. The witness still gains energy in this configuration. **c** Experiencing the escort beam for a total propagation distance of $z_{acc} = 0.8\,\mathrm{cm}$ has almost completely removed the accumulated energy spread. It now amounts to $\Delta W_{res,min} \approx 2.6\,\mathrm{MeV}$ corresponding to 0.03 % at the given mean energy. This value agrees well with the approximation given by Eq. (3.35). **d** Further de-chirping continues the phase space rotation and causes a configuration opposite to **a**. Figure produced by A. F. Habib for [133]

Another beneficial effect results from the stronger acceleration at the beams head. Based on Eq. (3.26), this configuration partially compensates for mixed-up rotations of longitudinal slice emittance that occurred during acceleration in the non-loaded wake. This effect is illustrated in Fig. 8.8.

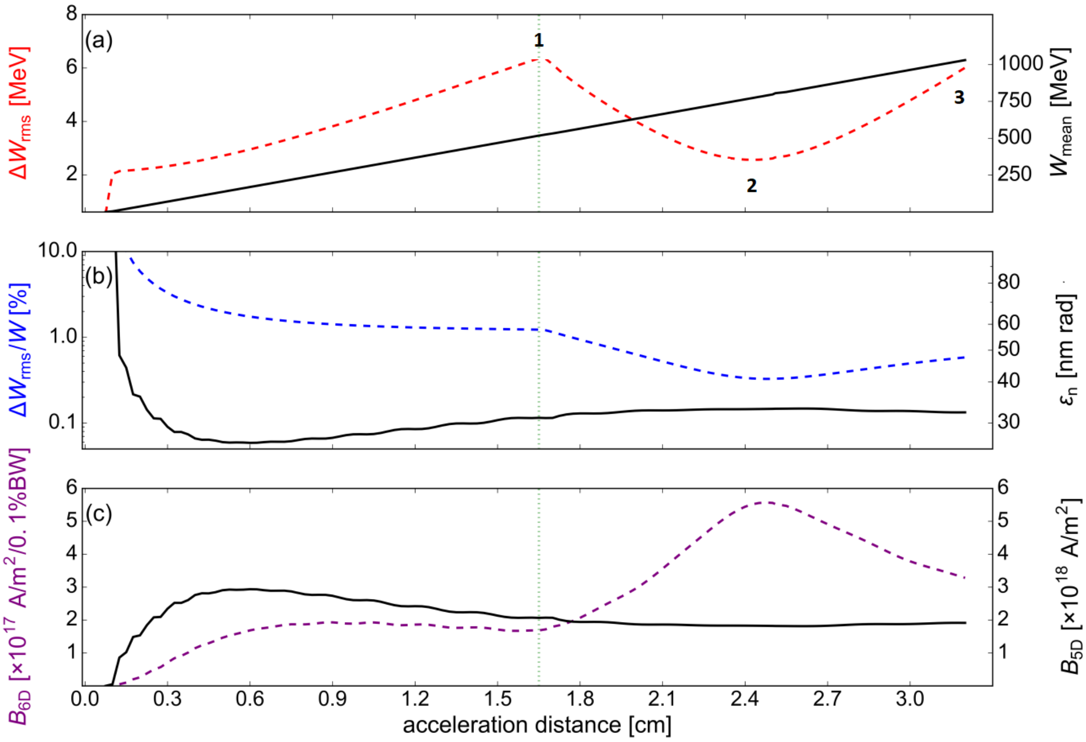

Figure 8.8: **Evolution of witness beam parameters before and during energy spread compensation (a)** Linear energy gain (black) and evolution of energy spread (red) during acceleration in the plasma wake. The witness beam forms with minimal energy spread slightly above 2 MeV and successively accumulates further spread from the wakes gradient. The green vertical line at **1** denotes the injection point of the escort beam. The witness energy spread reduces subsequently until it reaches its residual minimum **2**, after which over-compensation lasts until the simulations end **3**. Cases 1,2, and 3 correspond to Fig. 8.7 a,c, and d, respectively. **b** Relative energy spread (blue, log-scale) and normalised emittance (black) of the witness beam during the simulation. The former reduces to below 1 %, representing an exceptional value for a plasma-accelerated electron beam. In parallel, the emittance increases due to mismatching. When the escort beam starts acting, the emittance growth slows down, reaches a peak value slightly above $30 \times 10^{-9}\,\mathrm{m\,rad}$ close to position 2, and then even decreases. **c** Evolution of 5D- brightness (black) and 6D brightness (purple). While the former decreases similarly as the emittance grows, the latter advances substantially with decreasing energy spread. Figure is a modified version based on the illustration produced by A. F. Habib for [133]

After this study has been published, the theoretical analysis of the energy spread compensation technique has been expanded in [162]. This is neither result of the given work nor the authors original research. Yet, some developed dependences complete the description of the presented technique. Due to the lack of a suitable, self-consistent model describing beam loading for arbitrary combinations of wake fields and trapped beams, the following scalings are deduced from highly resolved particle-in-cell simulations. For fully capturing the witness beam within the over-loaded region, it can be shown that the (Gaussian) escort beam duration must be approximately twice the maximum length of the witness beam $\sigma_{\mathrm{witness,max}}$, e.g.

$$\sigma_{\mathrm{escort,fwhm}} \approx 2\sigma_{\mathrm{witness,max}}. \tag{8.8}$$

The propagation length until the witness energy spread reaches its residual value can be approximated by

$$z_{\mathrm{opt}} \approx \left| \frac{\Delta W_{\mathrm{res}} - \Delta W_0}{\Delta E_{z,\mathrm{lin}}} \right|. \tag{8.9}$$

Here, ΔW_0 represents the total energy spread when the de-chirping process starts, and $\Delta E_{z,\mathrm{lin}}$ expresses the difference of the over-loaded electric fields between the witness beams head and tail. The latter quantity is a function of the escort peak current $I_{p,\mathrm{esc}}$. These relations require that the escort beam actually over-loads the wake field, e.g. its peak current exceeds a certain, parameter-specific threshold. More information and studies extending this research will be presented in [210].

In summary, the presented technique applies multiple electron beams from plasma photocathodes to generate extremely low absolute and relative energy spread. This application of tailored beam loading promises to overcome the cardinal energy spread limit plasma-based ICS sources suffer from. Coincidentally, the transverse quality of the witness beam is maintained as it is inherently decoupled from the deteriorating aspect of space charge effects. In the shown simulations, constant emittance growth seems to get reduced and even reversed by the presence of the escort beam. This effect might come from a compensation of the betatron decoherence accumulated during acceleration, which reduces because the betatron frequency introduced in Eq. (3.26) that governs the speed of transverse phase space rotations changes due to the presence of the over-loaded wake field.

Apart from generating highest brightness electron beams for radiation sources and other applications, this method also stabilises the witness beam against transverse effects along the beam line. Low energy spread prevents incoherent betatron oscillations, and also limits chromatic beam expansion at the plasma exit and in subsequent focusing devices. Therefore, this scheme has large potential for plasma accelerator science, but can also be applied to beams generated and accelerated in other configurations. Finally, the witness-escort beam pair overlaps in time and must be separated for some applications such as free-electron lasers. Similar to the drive beam, this can be done by means of a dispersive beam line elements such as a chicane, but requires sufficient spectral spacing with respect to the witness. For ICS applications, a spectrally separated escort beam might be tolerable as long as its emitted radiation does not excite undesired dynamics in the target material.

8.3 GENERATION OF BRILLIANT γ-RAY PULSES

At last, the generation of brilliant γ-ray pulses, encouraged by the experimental achievements in Chapters 6 and 7 prorates this work. The strategy towards brilliant single-shot ICS radiation in the MeV regime was developed in instalments along this chapter and gets combined here.

To establish more understanding of the relevant dependences, the ICS bandwidth introduced in Eq. (4.12) can be expressed in terms of the plasma photocathode wakefield accelerator. The associated divergence and potential energy spread according to Eqs. (3.33) and (3.35) are both requirements for narrow bandwidth and high brilliance. For constant, linear accelerating fields, the influence of electron beam divergence can be estimated as

$$
\begin{aligned}
\frac{\Delta\omega_\gamma}{\omega_\gamma} &\propto \frac{\sigma_\theta^2\gamma_e^2}{4} && (8.10a)\\
&\approx \frac{k_p^2 w_0^2 \Delta_i^2 \gamma_e^{1/2}}{16} && (8.10b)\\
&\approx \frac{k_p^2 w_0^2 \Delta_i^2}{16}\left(\frac{E_z(\xi_f)d}{m_e c^2}\right)^{1/2} && (8.10c)\\
&\approx \frac{k_p^3 w_0^2 \Delta_i^2}{16\alpha^{1/2}}\sqrt{-\xi_f d} && (8.10d)\\
&\approx \frac{k_p^3 w_0^2 \Delta_i^2}{16\alpha^{1/2}} d^{1/2}\left(\xi_i + 2\alpha k_p^{-2}\right)^{1/4} && (8.10e)
\end{aligned}
$$

For a plasma photocathode, the bandwidth broadening due to the electron beam divergence scales effectively with $\gamma_e^{1/2} \propto d^{1/2}\xi_f^{1/2}$ in Eq. (8.10e). Thus, even at high electron energy, the low beam emittance enables low-bandwidth radiation pulses. This scaling furthermore outlines the non-linear dependence on the plasma density $k_p^3 \propto n_p^{3/2}$ and thus inherits the typical behaviour of all quality-related properties in plasma accelerators: low plasma density yields high electron beam and γ-ray quality.

The effect of residual and accumulated electron beam energy spread, in contrast, can be approximated by

$$\begin{aligned}
\frac{\Delta\omega_\gamma}{\omega_\gamma} &\propto 2\frac{\Delta\gamma_e}{\gamma_e} \tag{8.11a}\\
&\approx 2\frac{\Delta W_{\mathrm{corr}} + \Delta W_{\mathrm{res}}}{W} \tag{8.11b}\\
&\approx 2\frac{\frac{\partial E_z(\xi_f)}{\partial \xi}\sigma_z d_o + \frac{2\pi w_0^2}{5\lambda_L}E_z(\xi_f)}{E_z(\xi_f)d_o + E_{z,\mathrm{esc}}(\xi_f)d_{\mathrm{esc}}} \tag{8.11c}\\
&\approx 2\frac{\sigma_z d_o + \frac{2\pi w_0^2}{5\lambda_L}\xi_f}{\xi_f d_o + \xi_f d_{\mathrm{esc}}\kappa(n_{\mathrm{esc}})} \tag{8.11d}\\
&\overset{\Delta W_{\mathrm{corr}}=0}{\approx} \frac{4\pi w_0^2}{5\lambda_L(d_o + d_{\mathrm{esc}}\kappa(n_{\mathrm{esc}}))} \tag{8.11e}
\end{aligned}$$

Here, σ_z denotes the witness beam length, and d_o represents the length over which the witness beam has accelerated accumulated energy spread until the escort beam is released. Then, its space charge field depending on the escort beam density n_{esc} changes the longitudinal field expressed by $E_{z,\mathrm{esc}} = \kappa(n_{\mathrm{esc}})E_z$ and the energy spread reduces over the de-chirping length d_{esc}. Equation (8.11e) has additional beneficial consequences: the adverse influence of electron beam energy spread observed in Figs. 8.3 to 8.5 reduces linearly with the de-chirping length d_{esc}. It can reach the residual energy spread limit defined by the electron beams generation process at almost any final average beam energy, and thus get substantially reduced. The factor $\kappa(n_{\mathrm{esc}}) = E_{z,\mathrm{esc}}/E_z$ describes the influence from the loaded wake field.

The plasma photocathode wakefield accelerator already employed in Section 8.1 finds another application in this section to facilitate consistency. It has proven to be free of dark current and to generate low-emittance beams of the order of 30×10^{-9} m rad. The comparably large plasma wavelength $\lambda_p = 250\,\mu\mathrm{m}$ also promises low residual energy spread according to Eq. (3.35). The simulation shown in Fig. 8.4 represents the basis for this section and is extended for another $d \approx 3\,\mathrm{cm}$ without the second, low-energy beam. At the re-start position, the remaining beam has $W_{\mathrm{kin}} \approx 243.13 \pm 7.39\,\mathrm{MeV}$ corresponding to 3.04 % relative energy spread. In both transverse directions, the normalised emittance $\epsilon_n \approx 3 \times 10^{-8}$ m rad and the beam divergence amounts to $\sigma_\theta \approx 0.2\,\mathrm{mrad}$. As before, it carries $Q \approx 2.77\,\mathrm{pC}$. The evolution of quality-related properties can be found in Fig. 8.9.

Figure 8.10 contains the evolution of ICS scattering events for the electron beam for all simulation snapshots. The scattering configuration remains the same as Section 8.1, such that each pulse produces approximately 2.6×10^6 to 2.9×10^6 photons. ICS pulse energies are in the range of $E_\mathrm{ICS} \approx 1.8\,\mathrm{MeV}$ to $9.5\,\mathrm{MeV}$, while the relative bandwidth $\Delta E_\mathrm{ICS}/E_\mathrm{ICS} \approx 7.3\,\%$ stays approximately constant due to the relative electron beam energy spread shown in Fig. 8.9. At MeV photon energies, such bandwidths are uniquely low for ICS sources based on plasma accelerators. Note that no spectral filtering is applied at all. For the shot with minimal relative bandwidth in Fig. 8.10, the single-shot peak brilliance from Eq. (4.1) summarises the number of photons 2.96×10^6, the pulse duration $\tau_\mathrm{ICS} \approx 1.57\,\mathrm{fs}$, the source size $0.31 \times 0.32\,\mathrm{\mu m}^2$, and the divergence $0.94 \times 1.28\,\mathrm{mrad}^2$. All quantities are r.m.s. values and result from analysing the simulated data. The number of photons within $0.1\,\%$ bandwidth around the peak energy approximately amounts to 3.6×10^3 photons mrad^{-2}. Thus, the generated brilliance $B_\mathrm{ICS} \approx 2.3 \times 10^{25}$ photons s^{-1} mm^{-2} mrad^{-2} $0.1\%\mathrm{BW}$ at $E_\mathrm{ICS} \approx 1.9\,\mathrm{MeV}$ is ultra-high and exceeds even the brightest plasma-based sources realised so far. This directly results from the small source size and extraordinary transverse homogeneity of the incident electron beam. Figure 8.14 shows the spectrum and radial intensity profile of the ICS pulse for minimal relative bandwidth.

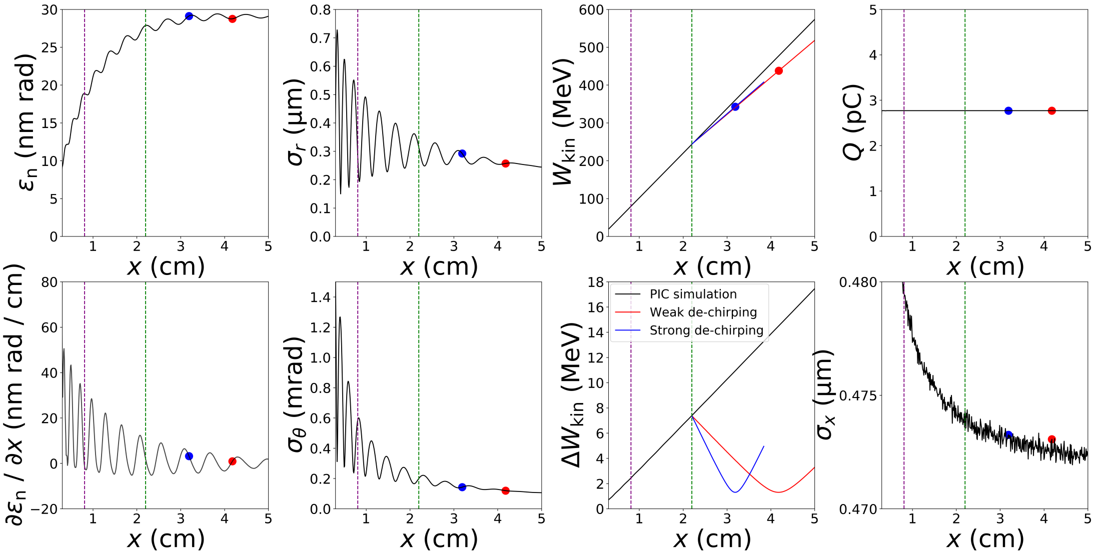

Figure 8.9: **Evolution of electron beam parameters along the plasma wakefield accelerator.** The black curves represent the electron beam shown in this section along with Figs. 8.3 to 8.5. The vertical lines represent the positions where the simulation snapshots were taken. Green corresponds to Figs. 8.3 and 8.4, and Fig. 8.5 to the purple line. Generally, these curves agree well with the dynamics introduced in Chapter 3. The beam is transversely slightly mismatched as can be seen by the oscillating radius and divergence. Consequently, the beam emittance grows (e.g. most of the time, $\partial\epsilon_n/\partial x > 0$) until expanding and focusing forces are balanced and saturation sets in. Energy and its spread both increase linearly during acceleration. The beam length appears to be irregular, but these variations occur on extremely low length scales such that they can be neglected. At the laboratory coordinate $P_{esc} = 2.2\,\text{cm}$, the witness beam gets de-chirped by two differently strong escort beams causing the red and blue lines, respectively. Thus, the beams energy spread reduces to $\Delta W_{kin,res} \approx 1.30\,\text{MeV}$. The red and blue dots correspond to the position where the respective beam inherits this minimal energy spread. Simultaneously, the energy gain reduces as the remaining accelerating field gets decreased in amplitude. As the de-chirping is applied externally, longitudinal and transverse phase space coordinates are decoupled such that the new energy distribution, or the space charge field of the escort beam, does not affect the betatron oscillations.

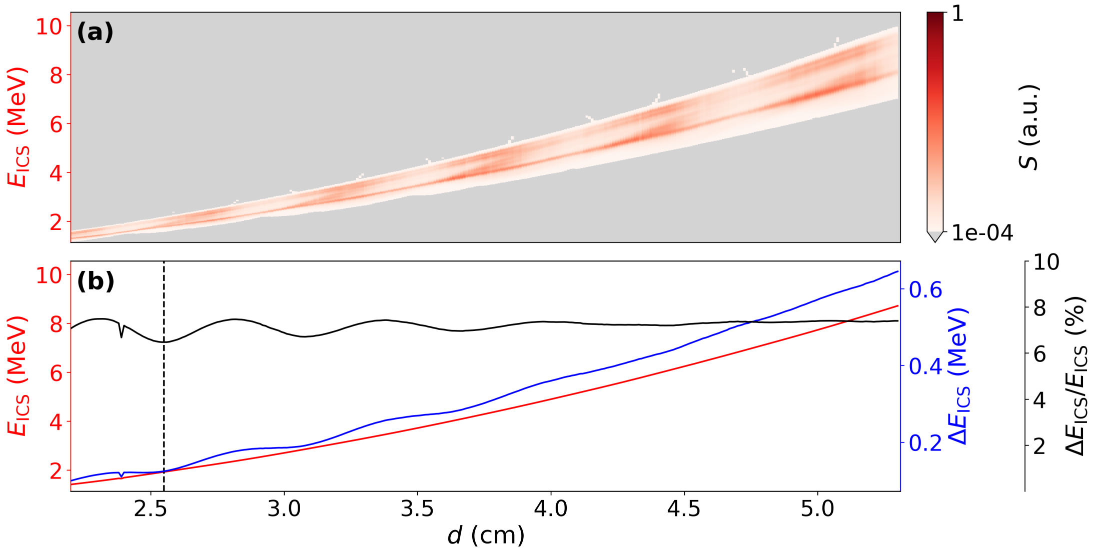

Figure 8.10: **Evolution of ICS radiation for the plasma photocathode beam shown in Fig. 8.9.** **(a)** Waterfall plot of normalised ICS spectra for each shot along the plasma accelerator. Each vertical slice corresponds to a whole spectrum as shown in Figs. 8.3 to 8.5 summed over the temporal axis. The grey background corresponds to zero generated photons. **(b)** Post-processed spectral data from (a). The red curve describes the central ICS energy and increases quadratically with increasing acceleration length d along the plasma accelerator. Its r.m.s. width (blue) closely follows this curve such that the relative bandwidth (black) stays approximately constant at 7.3 %. The vertical dashed line corresponds to the position with minimal relative bandwidth. In the earlier stages of the simulation, the ICS bandwidth oscillates in phase with the electron beam divergence as a consequence of the mismatched beam shown in Fig. 8.9. This behaviour ceases with increasing electron beam energy.

Even though the spectra shown in Fig. 8.10 are already narrow, they still inherit the ~3 % electron beam energy spread. Actually achieving the optimal state therefore demands for compensation of the accumulated energy spread already observed in Figs. 8.3 to 8.5.

As mentioned earlier in this chapter, coarse longitudinal resolution influences the associated phase space due to numerical beam loading, and simultaneously prevents correct over-loading by an escort beam. Unfortunately, the simulations in this study are subject to limited computational resources such that the grid resolution can not be further improved for centimetre scale simulation lengths. However, the energy spread compensation technique in Section 8.2 demonstrates the de-chirping approach and further shows that the transverse phase space of the relativistic witness beam becomes nearly immune to the space charge field of the escort beam. These two observations combined allow for approximating the de-chirping effect by manipulating the longitudinal phase space only. Here, this is achieved by accelerating the longitudinal phase space of the witness beam taken at $P_{\mathrm{esc}} = 2.2\,\mathrm{cm}$ by means of the *loaded* field generated by a dense escort beam in a short simulation with $\Delta x = 0.2\,\mu\mathrm{m}$. The effect of this approximation can be seen in Fig. 8.9 for the escort beam and another, even stronger one as shown in Fig. 8.11. Their fields are artificially amplified by stretching the well-resolved over-loaded area to reduce the computational load. These values – and escort beam densities– are clearly artificial and not feasible experimentally. In the given PWFA configuration, however, the wake potential is deep and robust against –properly resolved– space charge effects because of the extremely strong drive beam with $n_b \approx 55 n_p$. This setting is useful for wide longitudinal separation of multiple injected beams in Section 8.1, but turns out to be disadvantageous for the energy spread compensation technique. For sake of protecting computational resources and to maintain consistency, this study therefore outlines the *concept* of energy spread compensation by approximating its influence on the ICS radiation.

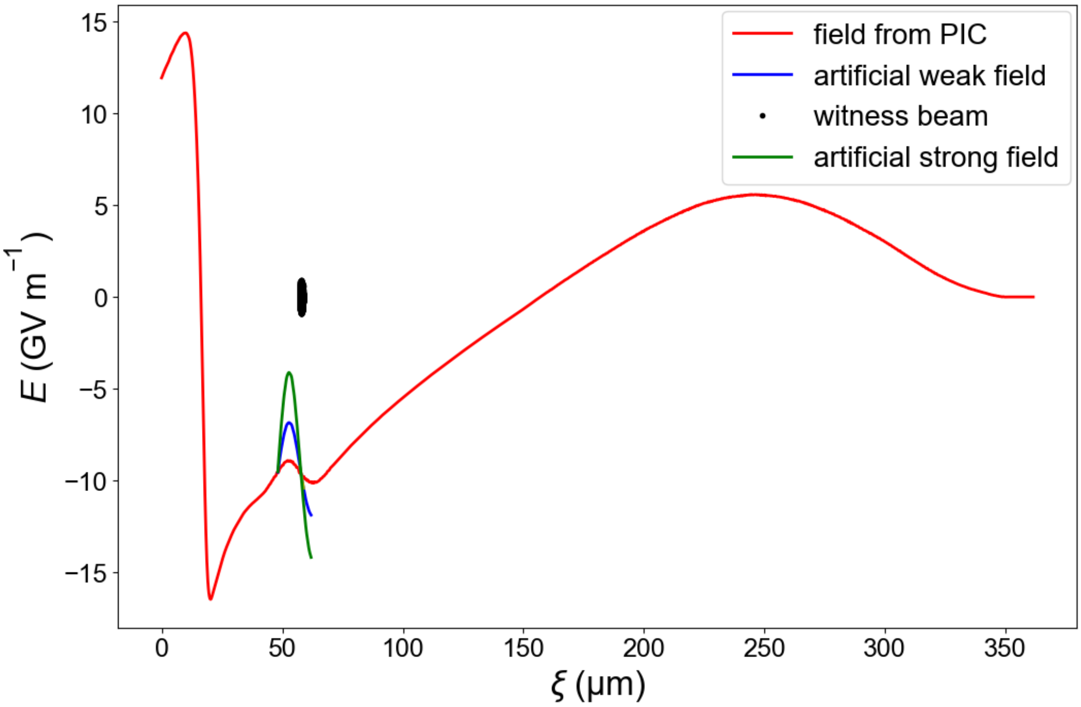

Figure 8.11: **Fields used for energy spread compensation.** Longitudinal electric fields obtained from PIC simulation (red) with an intense trailing beam. The longitudinal cell size $\Delta x = 0.2\,\mu m$ is substantially decreased for physical evaluation of beam loading, but cannot be maintained for a full-scale simulation. Therefore, the beam loading is approximated externally. The blue and green curves are stretched versions of the beam-loaded area. The black dots represent the witness beam subject to energy spread compensation located at the turning point of the overloaded region.

For the stronger escort beam, the energy spread reduces to the residual level after ~1 cm in the overloaded field region as shown as blue lines and dots in Fig. 8.9. Afterwards, the energy spread increases again due to the counter-clockwise rotation. The presence of the beam further reduces the accelerating field and thus the momentary electron beam energy. For the ICS process, Fig. 8.12 shows that energy spread compensation has substantial impact: the relative bandwidth drops significantly from more than 6 % at the start down to $\Delta E_{ICS}/E_{ICS}|_{min} \approx 2.34\,\%$ at the position indicated by the vertical dashed line. There, the central pulse energy $E_{ICS} \approx 2.66\,MeV$. So far, no plasma-based ICS source has produced that narrow bandwidth at these high energies without spectral filtering, as the combination of ultra-low electron beam emittance and low energy spread has not been produced yet. At the position with minimal relative bandwidth, the ICS pulse contains 2.9×10^6 photons within a pulse duration $\tau_{\mathrm{ICS}} \approx 1.57\,\mathrm{fs}$. The source of size is found to be $0.30\times0.30\,\mu\mathrm{m}^2$, and the pulse diverges under the angles $0.83\times1.13\,\mathrm{mrad}^2$. The number of on-axis photons within 0.1%BW amounts to ~$1.3 \times 10^4\,\mathrm{mrad}^{-2}$, which significantly exceeds the values of the first example and directly relates to the de-chirping process. Combining these quantities yields an exceptional peak brilliance of 1.0×10^{26} photons s^{-1} mm^{-2} mrad^{-2} 0.1%BW at even higher peak energy than before. Again, the corresponding spectrum and radial intensity profile can be found in Fig. 8.14.

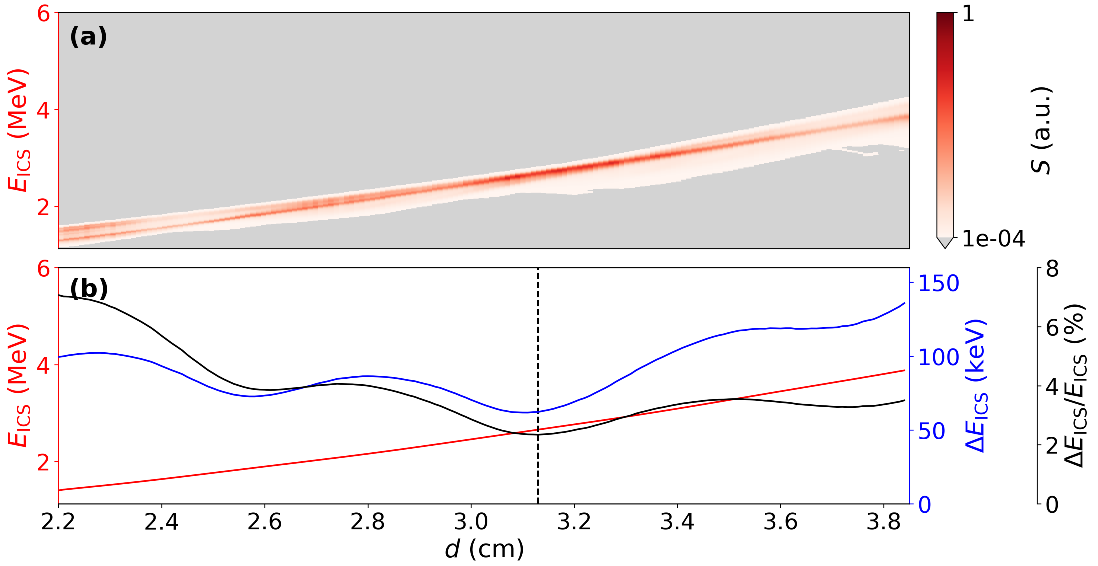

Figure 8.12: **Evolution of ICS radiation for a strongly de-chirped electron beam. (a)** Waterfall plot containing ICS spectra for each momentary electron beam configuration along the plasma wakefield accelerator. In comparison with Fig. 8.10, the bandwidth is substantially smaller close the the optimal de-chirping position. **(b)** Post-processed ICS information obtained from (a). De-chirping reduces the relative ICS bandwidth down to 2.34 % at the position with minimal electron beam energy spread. Coincidentally, the beam divergence is close to a minimum. As both energy spread and divergence increase shortly after the optimal position, the ICS bandwidth follows quickly.

For the second, weaker escort beam field, the position with minimal electron beam energy spread simply moves further downstream of the plasma accelerator, which can be seen in Fig. 8.9. The witness beam therefore gains more energy until the optimal scattering position is reached. Figure 8.13 presents the corresponding ICS evolution, which enters a quite interesting mixed regime where the influence of energy spread and divergence start overlapping.

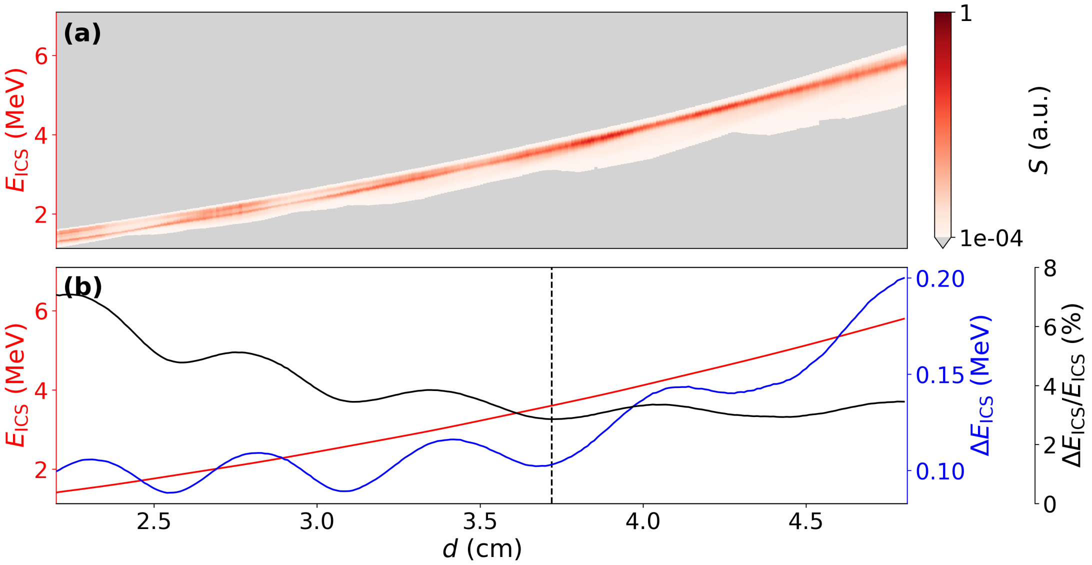

Figure 8.13: **Evolution of ICS radiation for a weakly de-chirped electron beam. (a)** Waterfall plot containing ICS spectra for each momentary electron beam configuration along the plasma wakefield accelerator. The central energy reaches almost 6 MeV as the electron beam accelerates longer than in Fig. 8.12. **(b)** Post-processed data obtained from (a). The minimal relative bandwidth 2.86 % is slightly increased compared to the stronger loaded wake. However, this quantity becomes minimal *before* the residual energy spread is reached, likely due to the coupling of electron beam divergence and energy. Both effects compensate each other: while the energy-divergence coupling intensifies, the energy spread decreases further. Effectively, the relative ICS bandwidth stays approximately constant along about $d \approx 1\,\mathrm{cm}$ of acceleration, and thus covers a wide range of E_{ICS}.

In contrast to the stronger case at lower electron beam energy, the last set of simulations assumes its minimal relative bandwidth of 2.86 % not at the position where the residual energy spread is reached. Instead, minimal bandwidth is achieved several millimetres *earlier* because of the influence of the electron beam divergence. At these elevated energies, e.g. $\gamma_e \approx 1000$, the divergence starts broadening the ICS spectrum according to Eq. (4.12) with comparable magnitude as the energy spread. However, while the electron beam energy spread further decreases, the relative ICS bandwidth stays approximately constant at 3 % for $d \approx 1\,\mathrm{cm}$ of acceleration and, in turn, compensates the divergence-driven broadening. This highly interesting mixed regime maintains the low relative bandwidth between ~3.5 MeV to 5.6 MeV for the given combination of electron beam energy, divergence and residual energy spread. As such, this regime offers narrow bandwidth radiation pulses over a large range of photon energies, which is unique for all ICS sources without application of spectral filtering. Reducing divergence and energy spread further is expected to extend this behaviour to even higher ICS photon energies, but becomes ever more challenging and should be investigated in future studies. It might be noted that this regime can only be accessed by techniques reducing the electron beam energy spread at a specific energy or position within the accelerator.

At last, the peak-brilliance at the minimal relative bandwidth position amounts to 8.3×10^{25} photons s^{-1} mm^{-2} mrad^{-2} $0.1\%BW$. The total number of photons is 2.91×10^{6}, the pulse duration $\tau_{\mathrm{ICS}} \approx 1.57\,\mathrm{fs}$, the source size $0.28{\times}0.28\,\mu\mathrm{m}^2$, and the divergence $0.73{\times}0.98\,\mathrm{mrad}^2$. The corresponding radial intensity profile can be found in Fig. 8.14, along with the on-axis spectrum. The latter yields the number of photons per $0.1\,\%BW$: 1.2×10^{4} mrad^{-2}.

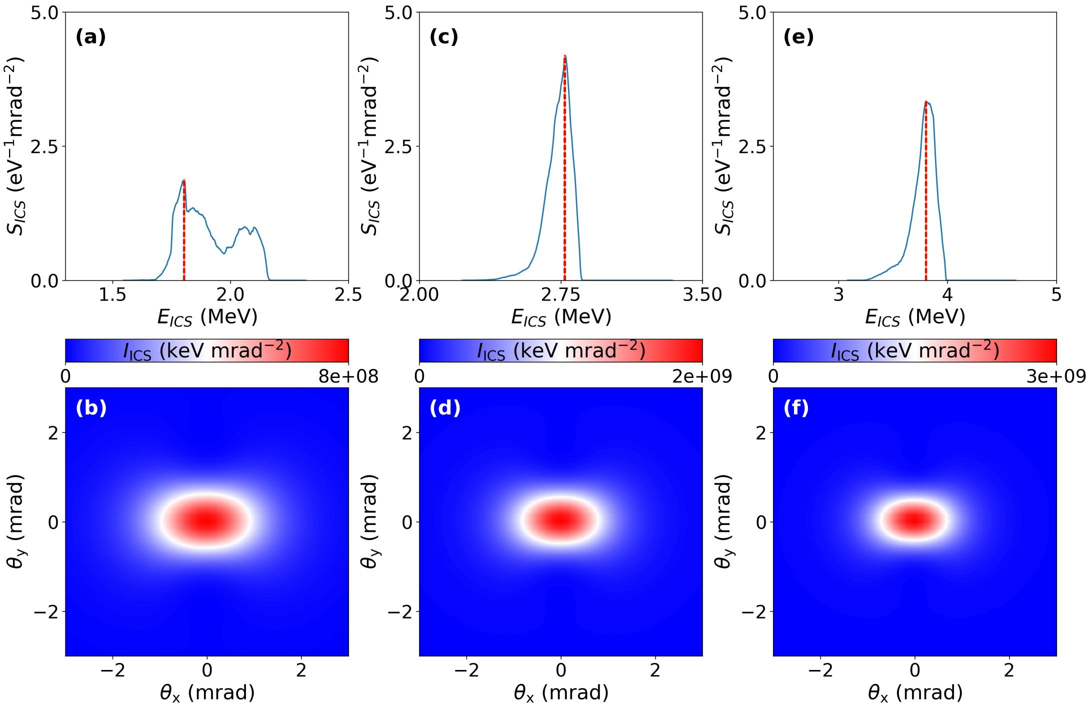

Figure 8.14: **On-axis spectral density and radial intensity profile. (a,c,e)** display the on-axis spectral density $S_{\rm ICS}$ for the scattering interactions with minimal relative bandwidth in Figs. 8.10, 8.12 and 8.13. More precisely, **(a)** represents the reference case for a regular witness beam from a plasma photocathode. **(c,e)** origin from witness beams subject to strong and weak energy spread compensation, respectively. As expected from Eq. (4.12), the spectra narrow substantially when the witness beam energy spread reduces. The vertical red lines mark the peak energy of each spectrum and define the 0.1 %BW-region required for calculating the peak brilliance. From left to right the on-axis spectral density within 0.1 % BW yields 3.6×10^3 photons mrad^{-2}, 1.3×10^4 photons mrad^{-2}, and 1.2×10^4 photons mrad^{-2}, respectively. **(b,d,f)** display the associated radial intensity profile of each ICS pulse. The oval shape directly results from the linear polarisation (x-direction) of the incident laser pulse and Eq. (4.10). Due to the low electron beam divergence combined with their relativistic energy, the ICS pulses are highly directed and diverge under small opening angles. Form left to right, the r.m.s. pulse divergence $\sigma_{\theta,y} \times \sigma_{\theta,x}$ reads $0.83{\times}1.13\,\mathrm{mrad}^2$, $0.83{\times}1.13\,\mathrm{mrad}^2$, and $0.73{\times}0.98\,\mathrm{mrad}^2$.

8.4 SUMMARY

All sections in the given chapter outline the capabilities offered by a plasma photocathode wakefield accelerator as versatile, high-quality source of electron beams and γ-ray pulses. These steps further represent and suggest concepts and strategies for improving the inherently excellent quality even further.

One aspect involves generation of multiple electron beams causing spectrally and temporally separable pairs (or even trains) of ICS pulses. These are intrinsically synchronised, but otherwise fully independent of each other and individually defined by the respective plasma photocathode. In a second step, injection of multiple electron beams is generalised and applied in a completely different context. The over-loading of the wake field by a high-charge, high current escort beam is shown to reduce the accumulated electron beam energy spread completely without deteriorating the witness beam quality. This technique may be a significant milestone towards narrow bandwidth ICS radiation without spectral filtering.

The latter is produced in the last section with relative bandwidth of the order of 2.3 % to 10 % at MeV-level photon energies. This represents a major progress as no plasma-based ICS source has achieved relative bandwidth below 10 % in this spectral regime so far. The optimal values are close to the 2 %-level exclaimed in [11] and therefore highly suitable for nuclear and high-energy physics applications as they facilitate high signal-to-noise ratios. Additionally, the low bandwidth combined with ultra-short, narrow and highly collimated pulses, the single-shot peak brilliance assumes levels above 1×10^{25} photons s^{-1} mm^{-2} $mrad^{-2}$ $0.1\%BW^{-1}$. These values are unprecedented for plasma-based ICS sources so far and origin from the high charge density and quality set up by the plasma photocathode. Finally, the transition regime between energy-spread limited and divergence-energy-limited bandwidth is shown to provide narrow, ~3 % ICS spectra over a large range of photon energies.

The given study demonstrates, therefore, the beneficial combination of inverse Compton scattering and the plasma photocathode along with encouraging results. However, some problems remain to be solved for both the simulations as well as of physical importance. For the former, all numbers and figures rely on highly expensive PIC simulations. These are widely used in plasma science and can, in principle, compute qualitative and quantitative results of the extremely complex physics of plasma acceleration. The plasma photocathode, however, inherently spans over several very different length scales such that all effects included require trade-offs between accuracy and costs. The given study implements the injector laser by an envelope model, which neglects oscillations and polarisation of the laser field. As a consequence, electron beam emittance and divergence are potentially underestimated in the plane of polarisation at the beginning of the simulation. The emittance growth observed in Fig. 8.9, however, is a superposition of physical and numerical effects. Further, modelling of correct beam loading is sacrificed here, such that all beams shown and employed are subject to unphysical modulations of the longitudinal field.

Tailored beam loading for energy spread compensation also requires high resolution over centimetre-scale propagation, otherwise the over-loaded area becomes highly irregular and spiky, which substantially deteriorates all electron beam coordinates. As such, the obtained 6D phase spaces shown here are approximations, and future studies should avoid this problem by acquiring more dedicated computational resources and by further optimising the PIC software and input configuration.

Apart from the demanding experimental implementation done in Chapter 7, some physical problems and challenges are excluded from the study. Generally, and typical for plasma photocathodes, the electron beam charge and resulting number of photons is much lower than in conventional schemes, and the repetition rate is limited by the drive beam source and the injection and scattering laser pulses. The problem related to low charge might be solved by systematic injection studies optimising laser parameters with respect to a given plasma wake. More pressing, however, is the technically restricted repetition rate. This can potentially be solved by new research and development of high-repetition rate laser systems, but requires substantial mutual effort from science and industry.

Next, and more subtle, this study assumes that the ICS event happens at any desired position inside the plasma accelerator. This interaction is furthermore calculated as if beam and laser were in vacuum. In reality, however, the beam resides inside plasma, and the incident laser must traverse it, potentially for significant lengths. This can cause laser-plasma interactions due to the plasma dispersion, which can cause multiple effects such as ionisation defocusing, filamentation and broadening of the bandwidth. Consequently, the laser will most likely not be perfectly Gaussian at the interaction point, might have accumulated significant bandwidth or might have lost large fractions of intensity due to filamentation. In case of high laser intensity, linear or even nonlinear plasma waves could be excited. Solving this problem basically follows two approaches: either reduce the duration of laser-plasma interactions, e.g. by limiting the plasma accelerator or refraining from scattering at all positions, or de-couple the electron beam from the accelerator stage combined with subsequent scattering in vacuum. While the first strategy can be employed easily on cost of tunable output energies, the second one is more challenging as the extraction from the wake must happen adiabatically for conservation of emittance. However, if done correctly, the second approach offers further benefits for ICS: while the electron beam expands slowly with decreasing plasma density, the divergence reduces accordingly. As such, the divergence term can be further suppressed at much higher electron energies, and thus offers even more narrow relative bandwidth than achieved in this work. Further optimisation seems to rely on operating in even lower plasma densities, trading electron beam quality for energy gain. Very similarly to Chapter 7, this is limited by the width and length of the plasma source.

9

CONCLUSIONS AND OUTLOOK

At last, the obtained and presented results amalgamate and conclude this narration. Reversing the former story line, the given work theoretically demonstrates the generation of γ-ray pulses via inverse Compton scattering off plasma wakefield accelerated electron beams. Obtained photon energies ~$0.4\,MeV$ to $9\,MeV$ are capable of exciting and probing nuclear states. These energies are rapidly reached because of the powerful γ_e^2-dependence, which synergises well with the strong accelerating fields provided by centimetre-long, state-of-the-art plasma accelerators.

The γ-rays simulated in the given work differ substantially from any pulse already produced in (laser-driven) plasma accelerators. Firstly, the de-phasing-free accelerator configuration in PWFA in principle supports constant energy gain until the drive beam has depleted, such that much higher photon energies than shown in this work are within reach of this technology. Secondly, the presented peak brilliance ~1×10^{25} photons $s^{-1}\ mm^{-2}\ mrad^{-2}\ 0.1\%BW$ exceeds any other plasma-based source by orders of magnitude. This directly relates to the very special electron beam generation by the plasma photocathode technique. The resulting high phase space density along with low thermal velocities surmount the effects of low electron beam charge with super-linear scalings in most quality-related terms: the ultra-low emittance translates to small beam radii and low divergence, which both quadratically increase the ICS pulse brilliance. Thus, the pulses shown in the present work facilitate intense, homogeneous and collimated illumination and is well-suited for nuclear physics applications.

Two related yet different generalisations of the plasma photocathode injector are employed sequentially and outline further capabilities of this scheme. One technique injects a second, high-quality witness beam dedicated for multicolour radiation production. Both resulting pulses are intrinsically synchronised, but can be shaped individually by their respective injector lasers. Furthermore, the plasma photocathode supports a large range of spectral and temporal spacing between these pulses by simple experimental means. In the second approach, a low-quality, high charge beam gets trapped at the first witness beams position. It overloads the accelerating field and causes counter-clockwise rotations of the longitudinal phase space of the first witness beam. Consequently, energy spread accumulated during acceleration can be compensated and reduced to a mere constant, such that the relative energy spread can reach sub-% levels particularly for high-energy electron beams. ICS pulses originating from these highly improved plasma photocathode beams assume relative bandwidths slightly above 2 %. This quantity represents the most challenging part of high-energy radiation sources, and the obtained values are unheard of for plasma-accelerated ICS sources. Summarised, the shown ICS pulses provide MeV energies, low relative bandwidth and ultra-high brilliance, and promise well-controlled experiments and applications. These outcomes directly originates from the plasma photocathode, which grants highest beam quality because of successive decoupling of plasma generation, excitation of the blowout, injection of witness beams and energy spread compensation paired with high flexibility.

Yet, these encouraging results are based on simulations, and although these may yield decent approximations of reality, only experimental demonstration can serve as ultimate proof. Realising all steps necessary for generating the simulated beam quality, however, represents a tremendous challenge: just a single plasma photocathode requires, next to the dense electron beam and plasma source fundamental to PWFA, excellent alignment and synchronisation between drive beam and injector laser, and unambiguous proof that any generated beam originates from the photocathode. For synchronisation and alignment of electron and laser beams, a novel plasma-based diagnostic was developed as major part of this work. Even though the whole long-term dynamics are not yet fully understood, the technique is shown to transfer the femtosecond-micrometre interaction dynamics of an electron beam with a thin, laser-generated plasma filament to millisecond and millimetre-scale observables. This has allowed multi-shot time-of-arrival measurements with approximately 16 fs and 4 μm accuracy, and offers high potential for improvements and optimisation. If the involved processes can be further investigated, highly-accurate single-shot measurements for time-of-arrival and alignment might be possible. Potentially, this technique may even yield exhaustive information of the electron beam phase space distribution. Because of the simple setup and easily accessible observable, this technique can be readily set up in any facility or experiment involving relativistic electron and laser beams. For example in light sources such as ICS or seeded FEL setups, it can measure their spatiotemporal synchronisation and alignment. Similarly, any laser-triggered effect in PWFA experiments can benefit from these results as laser pulses and drive beam are quite challenging to synchronise and align. This also applies to staging concepts, which are necessary for compact, hybrid LWFA→PWFA plasma accelerators and, on the long run, high-energy collider facilities based on plasma-based accelerator technology.

This diagnostic, furthermore, has facilitated the crucial synchronisation between electron beam and injector laser in the E-210 experimental campaign. As a direct consequence, it has enabled the world's first demonstration of a plasma photocathode along with plasma torch injection. These two approaches seem to differ fundamentally in both their mechanisms and resulting electron beams, but are shown to be closely related. The plasma torch even constitutes a reliable stepping stone towards the photocathode, and ultimately validates its operation. Developing these enabling techniques and procedures can be considered important milestones towards ultra-bright plasma accelerator research and development, and specifically for brilliant, narrow bandwidth ICS sources.

Experimentally, some problems and challenges remain to be solved. Most urgently, the plasma photocathode demonstrated in 90°-geometry must be realised in collinear geometry, including validations for unambiguity. Then, the dependencies between injector and final beam need to be carefully measured. This particularly includes quantification of beam emittance, which in itself represents a major challenge. ICS might offer an adequate tool for this purpose, as its spectrum sensitively depends on the electron beam phase space. Measuring the spectral distribution of generated ICS pulses accompanied by well-characterised electron beam energy, energy spread and scattering laser properties may indirectly yield the emittance based on Eq. (4.12). Realisation of the collinear plasma photocathode will take place at FACET-II, where the collaboration has received beam time. This facility will be substantially upgraded compared to the time of E-210, which involves a new drive beam source together with highly increased beam compression and density. Second, significant improvements to the laser output power and pointing stability are planned. As a direct consequence, a suitable plasma source is likely to be generated, capable of sustaining the blowout dimensions potentially at lower plasma densities than before. Even matching of the drive beam might become feasible and increase the overall stability. The plasma-afterglow diagnostic presented in this work is also subject to future research. Owing to the fact that PIC simulations cannot capture the revealed long-term dynamics, either new theoretical models or experiments can yield improved knowledge and optimised interaction parameters. Strategies advancing this concept towards a high-accuracy beam metrology diagnostic will be investigated experimentally at FACET-II. Eventually, this technique may improve particle accelerator and light source technology alike.

Current advances in research and development massively push towards all-optical particle accelerators and radiation sources. This is particularly relevant for PWFA schemes, as they rely on large, expensive and inaccessible conventional accelerator facilities. Truly compact schemes based on intense laser systems can substitute the conventional accelerator once staging concepts for hybrid LWFA→PWFA, e.g. sketched in Fig. 3.8, can be well-controlled. Once this technique becomes accessible above the proof-of-principle level, high-quality witness beams injected by plasma photocathodes may be produced in university-sized laboratories at low cost. Combining the ultra-low emittance and the minimal energy spread offered by this scheme, this configuration offers all-optical generation of brilliant, narrow bandwidth γ-ray pulses and promises new research, scientific progress and industrial applications.

Part III

APPENDIX

A

APPENDIX A: TRAPPING IN A PLASMAPHOTOCATHODE WAKEFIELD ACCELERATOR

A.1 ENGINEERED RELATIONS

Estimating the temporal and spectral spacing of generated ICS pulses requires knowledge of the trapping positions ξ_f and the different energies gained by the witness beam pair. As a plasma photocathode employs ionisation injection by means of an independent, low-intensity laser pulse, both quantities are functions of the wake potential and the release positions ξ_i inside the co-moving coordinate frame as expressed by Eq. (3.19).

The required wake potential, e.g. Eq. (3.13), depends on the radial function r_b of the blowout. It can be found by solving the differential equation [85] in the limit of an ultra-relativistic blowout

$$r_b \frac{d^2 r_b}{d\xi^2} + 2 \left(\frac{dr_b}{d\xi} \right)^2 = -1. \tag{A.1}$$

Note that all length scales are normalised to k_p^{-1}, and that beam loading is neglected throughout. $\xi = 0$ corresponds to the position with minimum trapping potential or, equivalently, the position where the longitudinal electric field becomes 0, e.g. close to the centre of the blowout. For the purpose of engineering an expression for the trapping position, the solution of Eq. (A.1) is approximated by the elliptical shape

$$r_b(\xi) \approx R_b \left(1 - \frac{\xi^2}{L_b^2} \right)^{1/2} \tag{A.2}$$

according to observations in PIC simulations and models [85, 95, 211]. This equation involves an approximation for the maximal blowout radius [113, 211]

$$R_b \approx 2 \left(\frac{n_b}{n_p} \sigma_r^2 \right)^{1/2} \tag{A.3}$$

and for half its longitudinal extent in a homogeneous plasma channel [95]

$$L_b \approx ((2+n)\pi)^{1/2} R_b \frac{\Gamma(\frac{n+3}{2n+4})}{\Gamma(\frac{1}{2n+4})} \overset{n=0}{\approx} 0.85 R_b \tag{A.4}$$

with Γ being the gamma function for a radial plasma profile given by a shape proportional to r^n. Combining all these terms for a homogeneous radial profile, e.g. $n = 0$, with the longitudinal field inside the blowout given by [113, 212]

$$E_z(\xi) \approx -\frac{1}{2} r_b \frac{dr_b}{d\xi} = -\frac{r_b}{2^{3/2}} \left(\frac{R_b^4}{r_b^4} - 1 \right)^{1/2} \tag{A.5}$$

yields the approximated on-axis electric field inside the blowout in *physical units*

$$E_z(\xi) \approx -\frac{E_{WB} k_p R_b}{2^{3/2}} \left(1 - \frac{\xi^2}{L_b^2}\right)^{1/2} \left(\left(1 - \frac{\xi^2}{L_b^2}\right)^{-2} - 1 \right)^{1/2} \approx -\frac{E_{WB} k_p}{\alpha} \xi \left(1 + \frac{\xi^2}{4L_b^2} + \mathcal{O}(4)\right). \tag{A.6}$$

$\alpha = 2 * (2\pi)^{1/2} \Gamma(3/4)/\Gamma(1/4) \approx 1.69$ summarises all constants and includes the radial profile of the plasma for $n = 0$. The last step in Eq. (A.6) results from a Taylor expansion at $x = 0$. It is linear in first order as expected, and higher orders lead to the distinct spike in the rear of the wake. Integrating this expression yields an approximation for the longitudinal component of the plasma wake potential:

$$\Psi(\xi) \approx -\frac{E_{WB} k_p}{2\alpha} \xi^2 \left(1 + \frac{\xi^2}{L_b^2}\right) \tag{A.7}$$

Recalling the trapping condition given by Eq. (3.19), an electron test charge released at rest at initial position ξ_i will get trapped at the final position ξ_f if it has gained relativistic energy. Thus, this expression links initial and final positions, restricted to the longitudinal extent of the blowout. Inserting Eq. (A.7) yields

$$\Delta\Psi = \frac{m_e c^2}{e} = \Psi_f - \Psi_i \tag{A.8a}$$

$$\frac{2\alpha m_e c^2}{E_{WB} k_p e} \approx \xi_i^2 (1 - \frac{\xi_i^2}{8L_b}) - \xi_f^2 (1 - \frac{\xi_f^2}{8L_b}) \tag{A.8b}$$

$$\xi_f \approx - \left(\xi_i^2 + \frac{2\alpha}{k_p^2} \right)^{1/2} \tag{A.8c}$$

Just keeping the first order, the trapping position behind the zero crossing of the electric field can be estimated by A.8c, which is independent of the drive beam as long as it maintains the blowout regime. This approximation is valid as long as the released particle experiences the wide linear region of the electric field. Including higher orders, e.g. from A.8b or A.5 further includes the electron beams effects by means of L_b which can elongate or extend the wake field according to Eqs. (A.3) and (A.4), and thus slightly changes the trapping position towards the rear of the blowout.

BIBLIOGRAPHY

[1] G Margaritondo. “A Primer in Synchrotron Radiation: Everything You Wanted to Know about SEX (Synchrotron Emission of X-rays) but Were Afraid to Ask.” In: *Journal of synchrotron radiation* 2.Pt 3 (1995), pp. 148–154. ISSN: 09090495. DOI: `10.1107/S0909049595001701`.

[2] F.R. Arutyunian and V.A. Tumanian. “The Compton Effect on Relativistic Electrons and the Possibility of Obtaining High Energy Beams.” In: *Phys. Letters* 4 (1963). DOI: `10.1016/0031-9163(63)90351-2`.

[3] Richard H. Milburn. “Electron scattering by an intense polarized photon field.” In: *Physical Review Letters* 10.3 (1963), pp. 75–77. ISSN: 00319007. DOI: `10.1103/PhysRevLett.10.75`.

[4] S Corde et al. “Observation of longitudinal and transverse self-injections in laser-plasma accelerators.” In: *Nature communications* 4 (2013), p. 1501. ISSN: 2041-1723. DOI: `10.1038/ncomms2528`. arXiv: `1309.6364v1`.

[5] D. Habs and U. Köster. “Production of medical radioisotopes with high specific activity in photonuclear reactions with γ-beams of high intensity and large brilliance.” In: *Applied Physics B: Lasers and Optics* 103.2 (2011), pp. 501–519. ISSN: 09462171. DOI: `10.1007/s00340-010-4278-1`.

[6] Micah S. Johnson et al. “Using quasi-monoenergetic photon sources to probe photo-fission resonances.” In: *AIP Conference Proceedings* 1336.May 2015 (2011), pp. 590–593. ISSN: 0094243X. DOI: `10.1063/1.3586171`.

[7] J. Pruet, D. P. McNabb, C. A. Hagmann, F. V. Hartemann, and C. P.J. J Barty. “Detecting clandestine material with nuclear resonance fluorescence.” In: *Journal of Applied Physics* 99.12 (2006). ISSN: 00218979. DOI: `10.1063/1.2202005`.

[8] W. Bertozzi et al. “Nuclear resonance fluorescence excitations near 2 MeV in U235 and Pu239.” In: *Physical Review C - Nuclear Physics* 78.4 (2008), pp. 1–5. ISSN: 05562813. DOI: `10.1103/PhysRevC.78.041601`.

[9] F. Albert et al. “Characterization and applications of a tunable, laser-based, MeV-class Compton-scattering γ-ray source.” In: *Physical Review Special Topics - Accelerators and Beams* 13.7 (2010), pp. 1–13. ISSN: 10984402. DOI: 10.1103/PhysRevSTAB.13.070704.

[10] F. Albert et al. “Design of narrow-band Compton scattering sources for nuclear resonance fluorescence.” In: *Physical Review Special Topics - Accelerators and Beams* 14.5 (2011), pp. 1–11. ISSN: 10984402. DOI: 10.1103/PhysRevSTAB.14.050703.

[11] S. G. Rykovanov et al. “Quasi-monoenergetic femtosecond photon sources from Thomson Scattering using laser plasma accelerators and plasma channels.” In: *Journal of Physics B: Atomic, Molecular and Optical Physics* 47.23 (2014). ISSN: 13616455. DOI: 10.1088/0953-4075/47/23/234013.

[12] F Albert et al. “Laser wakefield accelerator based light sources: potential applications and requirements.” In: *Plasma Physics and Controlled Fusion* 56.8 (2014), p. 084015. ISSN: 0741-3335. DOI: 10.1088/0741-3335/56/8/084015.

[13] J. Ballam et al. “Total and partial photoproduction cross sections at 1.44, 2.8, and 4.7 GeV.” In: *Physical Review Letters* 23.9 (1969), pp. 498–501. ISSN: 00319007. DOI: 10.1103/PhysRevLett.23.498.

[14] David J. Gibson et al. “PLEIADES: A picosecond Compton scattering x-ray source for advanced backlighting and time-resolved material studies.” In: *Physics of Plasmas* 11.5 (2004), pp. 2857–2864. ISSN: 1070-664X. DOI: 10.1063/1.1646160.

[15] W. J. Brown et al. “Experimental characterization of an ultrafast Thomson scattering x-ray source with three-dimensional time and frequency-domain analysis.” In: *Physical Review Special Topics - Accelerators and Beams* 7.6 (2004), pp. 23–34. ISSN: 10984402. DOI: 10.1103/PhysRevSTAB.7.060702.

[16] Henry R. Weller et al. “Research opportunities at the upgraded HIγS facility.” In: *Progress in Particle and Nuclear Physics* 62.1 (2009), pp. 257–303. ISSN: 01466410. DOI: 10.1016/j.ppnp.2008.07.001.

[17] HIGS Collaboration. “HIGS Flux Performance Projection Total Flux [g / s] Collimated Flux FEL Comment CW Operation No-loss Mode : Loss Mode : Modes of HIGS Operation.” In: 2010 (2011), p. 7898.

[18] V. Petrillo et al. “Dual color x rays from Thomson or Compton sources.” In: *Physical Review Special Topics - Accelerators and Beams* 17.2 (2014), pp. 1–7. ISSN: 10984402. DOI: 10.1103/PhysRevSTAB.17.020706.

[19] Ovidiu Teşileanu, Daniel Ursescu, Răzvan Dabu, and Nicolae Victor Zamfir. "Extreme light infrastructure-nuclear physics." In: *Journal of Physics: Conference Series* 420.1 (2013). ISSN: 17426596. DOI: 10.1088/1742-6596/420/1/012157.

[20] Technical Design Report, Scientific Editor, Luca Serafini, Oscar Adriani, and Sebastiano Albergo. "Technical Design Report EuroGammaS proposal for the ELI-NP Gamma beam System." In: July (2014).

[21] T. Tajima and J. M. Dawson. "Laser electron accelerator." In: *Physical Review Letters* 43.4 (1979), pp. 267–270. ISSN: 00319007. DOI: 10.1103/PhysRevLett.43.267.

[22] Pisin Chen, J. M. Dawson, Huff R. W., and T. Katsouleas. "Acceleration of Electrons by the Interaction of a Bunched Electron Beam with a plasma." In: *Physical Review Letters* 54.7 (1985). ISSN: 03759601. DOI: 10.1016/0375-9601(91)90914-T. arXiv: arXiv:1011.1669v3.

[23] J B Rosenzweig. "Nonlinear plasma dynamics in the plasma wakefield accelerator." In: *Physical Review Letters* 58.6 (1987), pp. 555–558.

[24] T. Behnke et al. "The International Linear Collider Technical Design Report - Volume 1: Executive Summary." In: (2013). arXiv: 1306.6327.

[25] W. P. Leemans et al. "Interaction of relativistic electrons with ultrashort laser pulses: Generation of femtosecond X-rays and microprobing of electron beams." In: *IEEE Journal of Quantum Electronics* 33.11 (1997), pp. 1925–1933. ISSN: 00189197. DOI: 10.1109/3.641307.

[26] P. Catravas, E. Esarey, and W. P. Leemans. "Femtosecond x-rays from Thomson scattering using laser wakefield accelerators." In: *Measurement Science and Technology* 12.11 (2001), pp. 1828–1834. ISSN: 0957-0233. DOI: 10.1088/0957-0233/12/11/310.

[27] N. Hafz et al. "Femtosecond X-Ray Generation via the Thomson Scattering of a Terawatt Laser From Electron Bunches Produced From the LWFA Utilizing a Plasma Density Transition." In: *IEEE Transactions on Plasma Science* 31.6 II (2003), pp. 1388–1394. ISSN: 00933813. DOI: 10.1109/TPS.2003.820680.

[28] P. Tomassini, A. Giulietti, D. Giulietti, and L. A. Gizzi. "Thomson backscattering X-rays from ultra-relativistic electron bunches and temporally shaped laser pulses." In: *Applied Physics B: Lasers and Optics* 80.4-5 (2005), pp. 419–436. ISSN: 09462171. DOI: 10.1007/s00340-005-1757-x.

[29] F. V. Hartemann et al. "Compton scattering x-ray sources driven by laser wakefield acceleration." In: *Physical Review Special Topics - Accelerators and Beams* 10.1 (2007), pp. 1–8. ISSN: 10984402. DOI: 10.1103/PhysRevSTAB.10.011301.

[30] K. Ta Phuoc et al. "All-optical Compton gamma-ray source." In: *Nature Photonics* 6.5 (May 2012), pp. 308–311. ISSN: 1749-4885. DOI: 10.1038/nphoton.2012.82. arXiv: 1301.3973.

[31] S. Chen et al. "MeV-energy X rays from inverse compton scattering with laser-wakefield accelerated electrons." In: *Physical Review Letters* 110.15 (2013), pp. 1–5. ISSN: 00319007. DOI: 10.1103/PhysRevLett.110.155003.

[32] G. Sarri et al. "Ultrahigh brilliance multi-MeV Gamma-ray beams from nonlinear relativistic thomson scattering." In: *Physical Review Letters* 113.22 (2014), pp. 1–5. ISSN: 10797114. DOI: 10.1103/PhysRevLett.113.224801. arXiv: 1407.6980.

[33] N. D. Powers et al. "Quasi-monoenergetic and tunable X-rays from a laser-driven Compton light source." In: *Nature Photonics* 8.1 (2014), pp. 28–31. ISSN: 1749-4885. DOI: 10.1038/nphoton.2013.314.

[34] Cheng Liu et al. "Generation of 9 MeV γ-rays by all-laser-driven Compton scattering with second-harmonic laser light." In: *Optics Letters* 39.14 (2014), p. 4132. ISSN: 0146-9592. DOI: 10.1364/OL.39.004132.

[35] Cameron G.R. Geddes et al. "Compact quasi-monoenergetic photon sources from laser-plasma accelerators for nuclear detection and characterization." In: *Nuclear Instruments and Methods in Physics Research, Section B: Beam Interactions with Materials and Atoms* 350 (2015), pp. 116–121. ISSN: 0168583X. DOI: 10.1016/j.nimb.2015.01.013.

[36] Changhai Yu et al. "Ultrahigh brilliance quasi-monochromatic MeV γ-rays based on self-synchronized all-optical Compton scattering." In: *Scientific Reports* 6.January (2016), p. 29518. ISSN: 2045-2322. DOI: 10.1038/srep29518.

[37] Félicie Albert and Alec G R Thomas. "Applications of laser wakefield accelerator-based light sources." In: *Plasma Physics and Controlled Fusion* 58.10 (2016), p. 103001. ISSN: 0741-3335. DOI: 10.1088/0741-3335/58/10/103001.

[38] M. J. Hogan et al. "Plasma wakefield acceleration experiments at FACET." In: *New Journal of Physics* 12.5 (2010), p. 55030. ISSN: 13672630. DOI: 10.1088/1367-2630/12/5/055030.

[39] Vitaly Yakimenko et al. “FACET-II accelerator research with beams of extreme intensities.” In: (2016).

[40] Paul A. Walker et al. “Horizon 2020 EuPRAXIA design study.” In: *Journal of Physics: Conference Series* 874 (2017), p. 012029. DOI: 10.1088/1742-6596/874/1/012029.

[41] B. Hidding et al. “Ultracold electron bunch generation via plasma photocathode emission and acceleration in a beam-driven plasma blowout.” In: *Physical Review Letters* 108.3 (2012), pp. 1–5. ISSN: 00319007. DOI: 10.1103/PhysRevLett.108.035001.

[42] Irving Langmuir. “Oscillations in Ionized Gases.” In: *Proc. Natl. Acad. Sci. U.S.A.* 14 (1928), pp. 627–637.

[43] Jr. Lyman Spitzer. *Physics of fully ionized gases*. 2nd, Dover. Dover Publications, Inc., 2007. ISBN: 9780787979133.

[44] Timon Mehrling. “Theoretical and numerical studies on the transport of transverse beam quality in plasma-based accelerators.” PhD thesis. University of Hamburg, 2014.

[45] E. Esarey, C. B. Schroeder, and W. P. Leemans. “Physics of laser-driven plasma-based electron accelerators.” In: *Reviews of Modern Physics* 81.3 (2009), pp. 1229–1285. ISSN: 00346861. DOI: 10.1103/RevModPhys.81.1229.

[46] M. Reiser. *Theory and Design of Charged Particle Beams*. 2nd 2008. Weinheim: Wiley-VCH, 1994. ISBN: 9783527407415. DOI: 10.1002/9783527617623.

[47] L. V. Keldysh. “Ionization in the field of a string electromagnetic wave.” In: *Journal of Experimental and Theoretical Physics* 20.5 (1965), pp. 1307–1314. ISSN: 0038-5646. DOI: 10.1234/12345678.

[48] D. Bauer. “Plasma formation through field ionization in intense laser–matter interaction.” In: *Laser and Particle Beams* 21.04 (2003), pp. 489–495. ISSN: 0263-0346. DOI: 10.1017/S0263034603214026.

[49] Scientist303. *Braniac Alkali metals*. 2006.

[50] J. Bakos, A. Kiss, L. Szabó, and M. Tendler. “Light intensity dependence of the multiphoton ionization probability in the resonance case.” In: *Physics Letters A* 41.2 (1972), pp. 163–164. ISSN: 03759601. DOI: 10.1016/0375-9601(72)91095-X.

[51] Paul Scherkl. "High-Quality Radiation from Inverse Compton Scattering using Ultralow-Emittance Electron Bunches." Masters Thesis. University of Hamburg, 2015.

[52] S Augst, D D Meyerhofer, D Strickland, and S L Chin. "Laser Ionization of Noble-Gases By Coulomb-Barrier Suppression." In: *Journal Of The Optical Society Of America B-Optical Physics* 8.4 (1991), pp. 858–867. ISSN: 0740-3224. DOI: 10.1364/JOSAB.8.000858.

[53] Maxim V Ammosov, Nikolai B Delone, and Vladimir P Krainov. "Tunnel ionization of complex atoms and atomic ions in electromagnetic field." In: *Sov. Phys. JETP, 64:1191* (1986).

[54] D. Bauer. "Ejection energy of photoelectrons in strong-field ionization." In: *Physical Review A* 55.3 (1997), pp. 2180–2185. ISSN: 1050-2947. DOI: 10.1103/PhysRevA.55.2180.

[55] David L. Bruhwiler et al. "Particle-in-cell simulations of tunneling ionization effects in plasma-based accelerators." In: *Physics of Plasmas* 10.5 II (2003), pp. 2022–2030. ISSN: 1070664X. DOI: 10.1063/1.1566027.

[56] B. Hidding et al. "Beyond injection: Trojan horse underdense photocathode plasma wakefield acceleration." In: *AIP Conference Proceedings* 1507.May 2015 (2012), pp. 570–575. ISSN: 0094243X. DOI: 10.1063/1.4773760.

[57] Gennady Yudin and Misha Ivanov. "Nonadiabatic tunnel ionization: Looking inside a laser cycle." In: *Physical Review A* 64.1 (2001), p. 4. ISSN: 1050-2947. DOI: 10.1103/PhysRevA.64.013409.

[58] L. J. Kieffer and G. H. Dunn. "Electron Impact Ionization Cross-Section Data for Atoms, Atomic Ions, and Diatomic Molecules: I. Experimental Data." In: *Reviews of Modern Physics* 38.1 (1966). ISSN: 00205958. DOI: 10.1007/BF02082353.

[59] Wolfgang Lotz. "An empirical formula for the electron-impact ionization cross-section." In: *Zeitschrift fuer Physik* 206.2 (1967), pp. 205–211. ISSN: 14346001. DOI: 10.1007/BF01325928.

[60] Wolfgang Lotz. "Electron-impact ionization cross-sections and ionization rate coefficients for atoms and ions from hydrogen to calcium." In: *Zeitschrift fuer Physik* 216.3 (1968), pp. 241–247. ISSN: 14346001. DOI: 10.1007/BF01392963. arXiv: arXiv:1011.1669v3.

[61] Foster F. Rieke and William Prepejchal. “Ionization cross sections of gaseous atoms and molecules for high-energy electrons and positrons.” In: *Physical Review A* 6.4 (1972), pp. 1507–1519. ISSN: 10502947. DOI: 10.1103/PhysRevA.6.1507.

[62] S. P. Slinker, R. D. Taylor, and A. W. Ali. “Electron energy deposition in atomic oxygen.” In: *Journal of Applied Physics* 63.1 (1988), pp. 1–10. ISSN: 00218979. DOI: 10.1063/1.340491.

[63] H. Bethe. “Zur Theorie des Durchgangs schneller Korpuskularstrahlen durch Materie.” In: *Annalen der Physik* 397.3 (1930), pp. 325–400. DOI: https://doi.org/10.1002/andp.19303970303.

[64] J.J. Thomson. “Ionization by Moving Electrified Particles.” In: *Phil. Mag. S. 6* 23.136 (1912). ISSN: 1941-5982. DOI: 10.1080/14786440408637241.

[65] Tomonao Hosokai et al. “Optical guidance of terrawatt laser pulses by the implosion phase of a fast Z-pinch discharge in a gas-filled capillary.” In: *Optics Letters* 25.1 (2000), p. 10. ISSN: 0146-9592. DOI: 10.1364/ol.25.000010.

[66] W. P. Leemans et al. “GeV electron beams from a centimetre-scale accelerator.” In: *Nature Physics* 2.10 (2006), pp. 696–699. ISSN: 17452481. DOI: 10.1038/nphys418.

[67] A. J. Gonsalves, T. P. Rowlands-Rees, B. H P Broks, J. J A M Van Der Mullen, and S. M. Hooker. “Transverse interferometry of a hydrogen-filled capillary discharge waveguide.” In: *Physical Review Letters* 98.2 (2007). ISSN: 00319007. DOI: 10.1103/PhysRevLett.98.025002.

[68] V. Yakimenko et al. “Cohesive Acceleration and Focusing of Relativistic Electrons in Overdense Plasma.” In: *Physical Review Letters* 91.1 (2003), pp. 1–4. ISSN: 10797114. DOI: 10.1103/PhysRevLett.91.014802.

[69] J. Van Tilborg et al. “Active Plasma Lensing for Relativistic Laser-Plasma-Accelerated Electron Beams.” In: *Physical Review Letters* 115.18 (2015), pp. 1–5. ISSN: 10797114. DOI: 10.1103/PhysRevLett.115.184802.

[70] S. Steinke et al. “Multistage coupling of independent laser-plasma accelerators.” In: *Nature* 530.7589 (2016), pp. 190–193. ISSN: 0028-0836. DOI: 10.1038/nature16525.

[71] S. I. Krasheninnikov et al. “Plasma recombination and molecular effects in tokamak divertors and divertor simulators.” In: *Physics of Plasmas* 4.5 (1997), pp. 1638–1646. ISSN: 10897674. DOI: 10.1063/1.872268.

[72] D. R. BATES. “Electron Recombination in Helium.” In: *Physical Review* 77.718 (1950).

[73] A.L. Schmeltekopf and H. P. Broida. “Short-Duration Visible Afterglow in Helium.” In: *The Journal of Chemical Physics* 39.5 (1963), p. 1261. ISSN: 00219606. DOI: `10.1063/1.1734425`.

[74] A. E. Grün, E. Schopper, and B. Schumacher. “Electron Shadowgraphs and Afterglow Pictures of Gas Jets at Low Densities.” In: *Journal of Applied Physics* 24.12 (1953), pp. 1527–1528. ISSN: 0021-8979. DOI: `10.1063/1.1721218`.

[75] Einar Hinnov and Joseph G. Hirschberg. “Electron-ion recombination in dense plasmas.” In: *Physical Review* 125.3 (1962), pp. 795–801. ISSN: 0031899X. DOI: `10.1103/PhysRev.125.795`.

[76] John M. Dawson. “On the Production of Plasma by Giant Pulse Lasers.” In: *Physics of Fluids* 7.7 (1964), p. 981. ISSN: 00319171. DOI: `10.1063/1.1711346`.

[77] C.G. Durfee and H. M. Milchberg. “Light Pipe for High Intensity Laser Pulses.” In: *Physical Review Letters* 71.15 (1993), pp. 2409–2412. ISSN: 0031-9007. DOI: `10.1103/PhysRevLett.71.2409`.

[78] V. Narayanan, V. Singh, Pramod K. Pandey, Neeraj Shukla, and R. K. Thareja. “Increasing lifetime of the plasma channel formed in air using picosecond and nanosecond laser pulses.” In: *Journal of Applied Physics* 101.7 (2007). ISSN: 00218979. DOI: `10.1063/1.2713997`.

[79] Z. Henis, G. Milikh, K. Papadopoulos, and A. Zigler. “Generation of controlled radiation sources in the atmosphere using a dual femtosecond /nanosecond laser pulse.” In: *Journal of Applied Physics* 103.10 (2008). ISSN: 00218979. DOI: `10.1063/1.2927457`.

[80] B. Aune. “The Superconducting TESLA Cavities.” In: 3 (2000). DOI: `10.1103/PhysRevSTAB.3.092001`. arXiv: `0003011 [physics]`.

[81] Eric Esarey and Mark Pilloff. “Trapping and acceleration in nonlinear plasma waves.” In: *Physics of Plasmas* 2.5 (1995), p. 1432. ISSN: 1070664X. DOI: `10.1063/1.871358`.

[82] S. Corde et al. “Multi-gigaelectronvolt acceleration of positrons in a self-loaded plasma wakefield.” In: *Nature* 524.7566 (2015), pp. 442–445. ISSN: 0028-0836. DOI: `10.1038/nature14890`.

[83] E Adli et al. “Acceleration of electrons in the plasma wakefield of a proton bunch.” In: *Nature* 561 (2018), pp. 363–367. DOI: 10.1038/s41586-018-0485-4.

[84] P Sprangle, E Esarey, and A Ting. “Annexes Deng LiS LCA.” In: 64.17 (2011), pp. 2011–2014. ISSN: 1079-7114. DOI: 10.1103/PhysRevLett.64.2011.

[85] W. Lu, C. Huang, M. Zhou, W. B. Mori, and T. Katsouleas. “Nonlinear theory for relativistic plasma wakefields in the blowout regime.” In: *Physical Review Letters* 96.16 (2006), pp. 1–4. ISSN: 00319007. DOI: 10.1103/PhysRevLett.96.165002.

[86] P. Chen. “A possible final focusing mechanism for linear colliders.” In: *Particle Accelerators* 20.November (1987), p. 171.

[87] W. K H Panofsky and W. A. Wenzel. “Some considerations concerning the transverse deflection of charged particles in radio-frequency fields.” In: *Review of Scientific Instruments* 27.11 (1956), p. 967. ISSN: 00346748. DOI: 10.1063/1.1715427.

[88] J. B. Rosenzweig, N. Barov, M. C. Thompson, and R. B. Yoder. “Energy loss of a high charge bunched electron beam in plasma: Simulations, scaling, and accelerating wakefields.” In: *Physical Review Special Topics - Accelerators and Beams* 7.6 (2004), pp. 71–81. ISSN: 10984402. DOI: 10.1103/PhysRevSTAB.7.061302.

[89] L.M. Gorbunov and V.I. Kirsanov. “Excitation of plasma waves by an electromagnetic wave packet.” In: *Soviet Physics JETP* 66.2 (1987), pp. 290–294. ISSN: 0038-5646.

[90] J. B. Rosenzweig and Pisin Chen. “Beam optics of a self-focusing plasma lens.” In: *Physical Review D* 39.7 (1989), pp. 2039–2045. ISSN: 05562821. DOI: 10.1103/PhysRevD.39.2039.

[91] J. B. Rosenzweig, B. Breizman, T. Katsouleas, and J. J. Su. “Acceleration and focusing of electrons in two-dimensional nonlinear plasma wake fields.” In: *Physical Review A* 44.10 (1991). ISSN: 10502947. DOI: 10.1103/PhysRevA.44.R6189.

[92] A. Pukhov and J. Meyer-ter-Vehn. “Laser wake field acceleration: The highly non-linear broken-wave regime.” In: *Applied Physics B: Lasers and Optics* 74.4-5 (2002), pp. 355–361. ISSN: 09462171. DOI: 10.1007/s003400200795.

[93] K. V. Lotov. “Blowout regimes of plasma wakefield acceleration.” In: *Physical Review E* 69 (2004), 046405 (1–13). ISSN: 1539-3755. DOI: 10.1103/PhysRevE.69.046405.

[94] I. Kostyukov, A. Pukhov, and S. Kiselev. “Phenomenological theory of laser-plasma interaction in "bubble" regime.” In: *Physics of Plasmas* 11.11 (2004), pp. 5256–5264. ISSN: 1070664X. DOI: 10.1063/1.1799371.

[95] Johannes Thomas, Igor Yu. Kostyukov, Jari Pronold, Anton Golovanov, and Alexander Pukhov. “Non-linear theory of a cavitated plasma wake in a plasma channel for special applications and control.” In: *Physics of Plasmas* 23.5 (2016), p. 053108. ISSN: 1070-664X. DOI: 10.1063/1.4948712.

[96] Ian Blumenfeld et al. “Energy doubling of 42 GeV electrons in a metre-scale plasma wakefield accelerator.” In: *Nature* 445.7129 (2007), pp. 741–744. ISSN: 0028-0836. DOI: 10.1038/nature05538.

[97] Efthymios Kallos et al. “High-gradient plasma-wakefield acceleration with two subpicosecond electron bunches.” In: *Physical Review Letters* 100.7 (2008), pp. 3–6. ISSN: 00319007. DOI: 10.1103/PhysRevLett.100.074802.

[98] M. Litos et al. “High-efficiency acceleration of an electron beam in a plasma wakefield accelerator.” In: *Nature* 515.7525 (2014), pp. 92–5. ISSN: 1476-4687. DOI: 10.1038/nature13882.

[99] K L F Bane, Pisin Chent, and P B Wilson. “On Collinear Wake Field Acceleration.” In: *IEEE Nuclear Science Symposium Conference Record* NS-32.5 (1985).

[100] Pisin Chen, J. J. Su, J. M. Dawson, K. L F Bane, and P. B. Wilson. “Energy transfer in the plasma wake-field accelerator.” In: *Physical Review Letters* 56.12 (1986), pp. 1252–1255. ISSN: 00319007. DOI: 10.1103/PhysRevLett.56.1252.

[101] R. D. Ruth, A. W. Chao, P. L. Morton, and Wilson4. “A Plasma Wake Field Accelerator.” In: *Particle Accelerators* 17 (1985), pp. 171–189.

[102] C. Joshi et al. “High energy density plasma science with an ultrarelativistic electron beam.” In: *Physics of Plasmas* 9.5 (2002), pp. 1845–1855. ISSN: 1070664X. DOI: 10.1063/1.1455003.

[103] Erdem Oz. “Physics of Particle Trapping in Ultrarelativistic Plasma Wakes.” In: *Usc* December (2007).

[104] A. Pak et al. “Injection and trapping of tunnel-ionized electrons into laser-produced wakes.” In: *Physical Review Letters* 104.2 (2010), pp. 1–4. ISSN: 00319007. DOI: `10.1103/PhysRevLett.104.025003`.

[105] Alexander Knetsch. “Acceleration of laser-injected electron beams in an electron-beam driven plasma wakefield accelerator.” PhD thesis. University of Hamburg, 2017.

[106] G G Manahan et al. “Hot spots and dark current in advanced plasma wakefield accelerators.” In: *Physical Review Accelerators and Beams* 011303.011303 (2016), pp. 1–9. ISSN: 2469-9888. DOI: `10.1103/PhysRevAccelBeams.19.011303`.

[107] Ralph Assmann and Kaoru Yokoya. “Transverse beam dynamics in plasma-based linacs.” In: *Nuclear Instruments and Methods in Physics Research, Section A: Accelerators, Spectrometers, Detectors and Associated Equipment* 410.3 (1998), pp. 544–548. ISSN: 01689002. DOI: `10.1016/S0168-9002(98)00187-9`.

[108] Klaus Floettmann. “Some basic features of the beam emittance.” In: *Physical Review Special Topics - Accelerators and Beams* 6.3 (2003), pp. 80–86. ISSN: 10984402. DOI: `10.1103/PhysRevSTAB.6.034202`.

[109] R. Gholizadeh, T. Katsouleas, P. Muggli, C. Huang, and W. Mori. “Preservation of beam emittance in the presence of ion motion in future high-energy plasma-wakefield-based colliders.” In: *Physical Review Letters* 104.15 (2010), pp. 1–4. ISSN: 00319007. DOI: `10.1103/PhysRevLett.104.155001`.

[110] Klaus Floettmann. “Adiabatic matching section for plasma accelerated beams.” In: *Physical Review Special Topics - Accelerators and Beams* 17.5 (2014), pp. 1–7. ISSN: 10984402. DOI: `10.1103/PhysRevSTAB.17.054402`.

[111] P. Antici et al. “Laser-driven electron beamlines generated by coupling laser-plasma sources with conventional transport systems.” In: *Journal of Applied Physics* 112.044902 (2012). ISSN: 0021-8979. DOI: `10.1063/1.4740456`.

[112] T. Katsouleas et al. “Beam Loading in Plasma Accelerators.” In: *Particle Accelerators* 22.2 (1987), pp. 81–99. ISSN: 0093-3813. DOI: `10.1109/TPS.1987.4316687`.

[113] M. Tzoufras et al. “Beam loading in the nonlinear regime of plasma-based acceleration.” In: *Physical Review Letters* 101.14 (2008), pp. 1–4. ISSN: 00319007. DOI: `10.1103/PhysRevLett.101.145002`. arXiv: `0809.0227`.

[114] E. Brunetti et al. “Low emittance, high brilliance relativistic electron beams from a laser-plasma accelerator.” In: *Physical Review Letters* 105.21 (2010), pp. 3–6. ISSN: 00319007. DOI: `10.1103/PhysRevLett.105.215007`.

[115] G. R. Plateau et al. “Low-emittance electron bunches from a laser-plasma accelerator measured using single-shot X-ray spectroscopy.” In: *AIP Conference Proceedings* 1507.August (2012), pp. 278–283. ISSN: 0094243X. DOI: 10.1063/1.4773707.

[116] W. T. Wang et al. “High-Brightness High-Energy Electron Beams from a Laser Wakefield Accelerator via Energy Chirp Control.” In: *Physical Review Letters* 117.12 (2016), p. 124801. ISSN: 0031-9007. DOI: 10.1103/PhysRevLett.117.124801.

[117] G Golovin et al. “Intrinsic beam emittance of laser-accelerated electrons measured by x-ray spectroscopic imaging.” In: *Scientific reports* 6.April (2016), p. 24622. ISSN: 2045-2322. DOI: 10.1038/srep24622.

[118] Patrick G O’Shea. “Reversible and irreversible emittance growth.” In: *Physical Review E* 57.1 (1998).

[119] Simone Di Mitri. “On the Importance of Electron Beam Brightness in High Gain Free Electron Lasers.” In: *Photonics* 2.2 (2015), pp. 317–341. ISSN: 2304-6732. DOI: 10.3390/photonics2020317.

[120] Silvia Cipiccia et al. “Gamma-rays from harmonically resonant betatron oscillations in a plasma wake.” In: *Nature Physics* 7.11 (2011), pp. 867–871. ISSN: 1745-2473. DOI: 10.1038/nphys2090.

[121] X. L. Xu et al. “Phase-space dynamics of ionization injection in plasma-based accelerators.” In: *Physical Review Letters* 112.3 (2014), pp. 1–5. ISSN: 00319007. DOI: 10.1103/PhysRevLett.112.035003.

[122] T. Mehrling, J. Grebenyuk, F. S. Tsung, K. Floettmann, and J. Osterhoff. “Transverse emittance growth in staged laser-wakefield acceleration.” In: *Physical Review Special Topics - Accelerators and Beams* 15.11 (2012), pp. 1–7. ISSN: 10984402. DOI: 10.1103/PhysRevSTAB.15.111303.

[123] David H. Whittum, William M. Sharp, Simon S. Yu, Martin Lampe, and Glenn Joyce. “Electron-hose instability in the ion-focused regime.” In: *Physical Review Letters* 67.8 (1991), pp. 991–994. ISSN: 00319007. DOI: 10.1103/PhysRevLett.67.991.

[124] T. J. Mehrling, R. A. Fonseca, A. Martinez De La Ossa, and J. Vieira. “Mitigation of the Hose Instability in Plasma-Wakefield Accelerators.” In: *Physical Review Letters* 118.17 (2017), pp. 1–5. ISSN: 10797114. DOI: 10.1103/PhysRevLett.118.174801.

[125] J. Krall and G. Joyce. "Transverse equilibrium and stability of the primary beam in the plasma wake-field accelerator." In: *Physics of Plasmas* 2.4 (1995), pp. 1326–1331. ISSN: 1070664X. DOI: 10.1063/1.871344.

[126] E. Esarey, B. A. Shadwick, P. Catravas, and W. P. Leemans. "Synchrotron radiation from electron beams in plasma-focusing channels." In: *Physical Review E - Statistical, Nonlinear, and Soft Matter Physics* 65.5 (2002), pp. 1–15. ISSN: 15393755. DOI: 10.1103/PhysRevE.65.056505.

[127] N. Vafaei-Najafabadi et al. "Ionization injection and acceleration of electrons in a plasma wakefield accelerator at FACET." In: *AIP Conference Proceedings* (2016). DOI: 10.1063/1.4965654.

[128] E P Lee and R K Cooper. "General Envelope Equation for Cylindrically Symmetric Charged Particle Beams." In: *Part.Accel.* 7 (1976), pp. 83–95.

[129] S. G. Anderson, J. B. Rosenzweig, G. P. LeSage, and J. K. Crane. "Space-charge effects in high brightness electron beam emittance measurements." In: *Physical Review Special Topics - Accelerators and Beams* 5.1 (2002), pp. 12–23. ISSN: 10984402. DOI: 10.1103/PhysRevSTAB.5.014201.

[130] K. A. Marsh et al. "Beam matching to a plasma wake field accelerator using a ramped density profile at the plasma boundary." In: *Proceedings of the IEEE Particle Accelerator Conference* 2005.January 2014 (2005), pp. 2702–2704. DOI: 10.1109/PAC.2005.1591234.

[131] C. B. Schroeder et al. "Thermal emittance from ionization-induced trapping in plasma accelerators." In: *Physical Review Special Topics - Accelerators and Beams* 17.10 (2014), pp. 1–11. ISSN: 10984402. DOI: 10.1103/PhysRevSTAB.17.101301.

[132] Y. Xi, B. Hidding, D. Bruhwiler, G. Pretzler, and J. B. Rosenzweig. "Hybrid modeling of relativistic underdense plasma photocathode injectors." In: *Physical Review Special Topics - Accelerators and Beams* 16.3 (2013), pp. 1–9. ISSN: 10984402. DOI: 10.1103/PhysRevSTAB.16.031303.

[133] Grace G. Manahan et al. "Single-stage plasma-based correlated energy spread compensation for ultrahigh 6D brightness electron beams." In: *Nature Communications* 8 (2017), p. 15705. ISSN: 2041-1723. DOI: 10.1038/ncomms15705.

[134] B Hidding, G G Manahan, O Karger, A Knetsch, and G Wittig. "Ultrahigh brightness bunches from hybrid plasma accelerators as drivers of 5th generation light sources." In: *Journal of Physics B: Atomic, Molecular and Optical Physics* 47.234010 (2014). DOI: 10.1088/0953-4075/47/23/234010.

[135] B. Hidding et al. “Hybrid laser-plasma wakefield acceleration.” In: *AIP Conference Proceedings* 1299.November 2010 (2010), pp. 483–488. ISSN: 0094243X. DOI: 10.1063/1.3520370.

[136] T Heinemann et al. “Investigating the Key Parameters of a Staged Laser- and Particle Driven Plasma Wakefield Accelerator Experiment.” In: *Proceedings of IPAC2017* (2017). DOI: 10.18429/JACoW-IPAC2017-TUPIK010.

[137] A. Martinez De La Ossa et al. “Hybrid LWFA-PWFA staging as a beam energy and brightness transformer: Conceptual design and simulations.” In: *Philosophical Transactions of the Royal Society A: Mathematical, Physical and Engineering Sciences* 377.2151 (2019). ISSN: 1364503X. DOI: 10.1098/rsta.2018.0175.

[138] O. Klein and T. Nishina. “Über die Streuung von Strahlung durch freie Elektronen nach der neuen relativistischen Quantendynamik von Dirac.” In: *Zeitschrift f??r Physik* 52.11-12 (1929), pp. 853–868. ISSN: 14346001. DOI: 10.1007/BF01366453.

[139] Winthrop J. Brown and Frederic V. Hartemann. “Three-dimensional time and frequency-domain theory of femtosecond x-ray pulse generation through Thomson scattering.” In: *Physical Review Special Topics - Accelerators and Beams* 7.6 (2004), pp. 35–54. ISSN: 10984402. DOI: 10.1103/PhysRevSTAB.7.060703.

[140] Eric Esarey, S. K. Ride, and Phillip Sprangle. “Nonlinear Thomson scattering of intense laser pulses from beams and plasmas.” In: *Physical Review E* 48.4 (1993).

[141] J. D. Jackson. *Classical electrodynamics*. 3rd. New York: Wiley, 1999.

[142] J. Rosenzweig and O. Williams. “Limits on production of narrow band photons from inverse compton scattering.” In: *AIP Conference Proceedings* 877.March (2006), pp. 437–444. ISSN: 0094243X. DOI: 10.1063/1.2409167.

[143] I. Gadjev et al. “An inverse free electron laser acceleration-driven Compton scattering X-ray source.” In: *Scientific Reports* 9.532 (2019), pp. 1–10. ISSN: 2045-2322. DOI: 10.1038/s41598-018-36423-y.

[144] Changchun Sun. “Characterizations and diagnostics of Compton light source.” PhD thesis. 2009.

[145] V. Petrillo et al. “Polarization of x-gamma radiation produced by a Thomson and Compton inverse scattering.” In: *Physical Review Special Topics - Accelerators and Beams* 18.11 (2015), pp. 1–9. ISSN: 10984402. DOI: 10.1103/PhysRevSTAB.18.110701.

[146] V. Petrillo et al. “Photon flux and spectrum of γ-rays Compton sources.” In: *Nuclear Instruments and Methods in Physics Research, Section A: Accelerators, Spectrometers, Detectors and Associated Equipment* 693 (2012), pp. 109–116. ISSN: 01689002. DOI: `10.1016/j.nima.2012.07.015`.

[147] Stewart T. Boogert et al. “Micron-scale laser-wire scanner for the KEK Accelerator Test Facility extraction line.” In: *Physical Review Special Topics - Accelerators and Beams* 13.12 (2010), pp. 1–16. ISSN: 10984402. DOI: `10.1103/PhysRevSTAB.13.122801`.

[148] Axel Jochmann. “DEVELOPMENT AND CHARACTERIZATION OF A TUNABLE ULTRAFAST X-RAY SOURCE VIA INVERSE-COMPTON-SCATTERING.” In: September (2014).

[149] J. S. Reid and G. J. Milne. “A simple variable-wavelength X-ray monochromator.” In: *Journal of Applied Crystallography* 21.6 (1988), pp. 992–993. ISSN: 0021-8898. DOI: `10.1107/s0021889888007563`.

[150] W. P. Leemans et al. “Multi-Gev electron beams from capillary-discharge-guided subpetawatt laser pulses in the self-trapping regime.” In: *Physical Review Letters* 113.24 (2014), pp. 1–5. ISSN: 10797114. DOI: `10.1103/PhysRevLett.113.245002`.

[151] M Mirzaie et al. “Demonstration of self-truncated ionization injection for GeV electron beams.” In: *Scientific Reports* 5 (2015), p. 14659. ISSN: 2045-2322. DOI: `10.1038/srep14659`.

[152] J. P. Couperus et al. “Demonstration of a beam loaded nanocoulomb-class laser wakefield accelerator.” In: *Nature Communications* 8.1 (2017), p. 487. ISSN: 2041-1723. DOI: `10.1038/s41467-017-00592-7`. arXiv: `arXiv:1011.1669v3`.

[153] K. S. Yee. “Numerical Solution of Initial Boundary Value Problems Involving Maxwell’s Equations in Isotropic Media.” In: *IEEE Transactions on Antennas and Propagation* 14.3 (1966), pp. 302–307. DOI: `10.1007/978-3-662-44882-3_12`.

[154] R. Courant, K. Friedrichs, and H. Ley. “On the Partial Difference Equations of Mathematical Physics.” In: *IBM Journal of Research and Development* 11.2 (1967), pp. 215–134.

[155] J. P. Boris. “Relativistic plasma simulation-optimization of a hybrid code.” In: *Proceeding of Fourth Conference on Numerical Simulations of Plasmas* (1970), pp. 3–67.

[156] Chet Nieter and John R. Cary. "VORPAL: A versatile plasma simulation code." In: *Journal of Computational Physics* 196.2 (2004), pp. 448–473. ISSN: 00219991. DOI: 10.1016/j.jcp.2003.11.004.

[157] X. L. Xu et al. "Nanoscale Electron Bunching in Laser-Triggered Ionization Injection in Plasma Accelerators." In: *Physical Review Letters* 117.3 (2016), pp. 1–5. ISSN: 10797114. DOI: 10.1103/PhysRevLett.117.034801. arXiv: 1510.01445.

[158] B Godfrey. "Numerical Cherenkov Instabilities in Electromagnetic Particle Codes * Over the past several years the utility of particle-in-ceil computer simulation codes [l] in investigating highly complex plasma physics phenomena has been well established . Nonethel." In: *Jouranl of Computational Physics* 15 (1974), pp. 504–521.

[159] Andrew D. Greenwood, Keith L. Cartwright, John W. Luginsland, and Ernest A. Baca. "On the elimination of numerical Cerenkov radiation in PIC simulations." In: *Journal of Computational Physics* 201.2 (2004), pp. 665–684. ISSN: 00219991. DOI: 10.1016/j.jcp.2004.06.021.

[160] R. Lehe, A. Lifschitz, C. Thaury, V. Malka, and X. Davoine. "Numerical growth of emittance in simulations of laser-wakefield acceleration." In: *Physical Review Special Topics - Accelerators and Beams* (2013). DOI: 10.1103/PhysRevSTAB.16.021301.

[161] Benjamin M. Cowan, David L. Bruhwiler, John R. Cary, Estelle Cormier-Michel, and Cameron G.R. Geddes. "Generalized algorithm for control of numerical dispersion in explicit time-domain electromagnetic simulations." In: *Physical Review Special Topics - Accelerators and Beams* 16.4 (2013), pp. 1–10. ISSN: 10984402. DOI: 10.1103/PhysRevSTAB.16.041303.

[162] Ahmad Fahim Habib. "A Fith Generation Light Source Driven by Advanced Plasma Wakefield Accelerators." PhD thesis. University of Hamburg, 2017.

[163] S. Schulz et al. "Femtosecond all-optical synchronization of an X-ray free-electron laser." In: *Nature Communications* 6 (2015), p. 5938. ISSN: 2041-1723. DOI: 10.1038/ncomms6938.

[164] A E Gleason et al. "Ultrafast visualization of crystallization and grain growth in shock-compressed SiO2." In: *Nature Communications* 6 (2015).

[165] Eugenio Ferrari et al. "Widely tunable two-colour seeded free-electron laser source for resonant-pump resonant-probe magnetic scattering." In: *Nature Communications* 7 (2016), p. 10343. ISSN: 2041-1723. DOI: 10.1038/ncomms10343.

[166] Ulrike Frühling et al. "Single-shot terahertz-field-driven X-ray streak camera." In: *Nature Photonics* 3.9 (2009), pp. 523–528. ISSN: 1749-4885. DOI: 10.1038/nphoton.2009.160.

[167] K. Chouffani, F. Harmon, D. Wells, J. Jones, and G. Lancaster. "Laser-Compton scattering as a tool for electron beam diagnostics." In: *Laser and Particle Beams* 24.03 (2006), pp. 411–419. ISSN: 0263-0346. DOI: 10.1017/S0263034606060575.

[168] J. M. Krämer et al. "Making spectral shape measurements in inverse Compton scattering a tool for advanced diagnostic applications." In: *Scientific Reports* 8.1 (2018), pp. 1–11. ISSN: 20452322. DOI: 10.1038/s41598-018-19546-0.

[169] D. P. Umstadter. "United States Patent: Method and Apparatus for generating and accelerating ultrashort electron pulses." In: (1987), pp. 4–8.

[170] E. Esarey, R. Hubbard, W. Leemans, A. Ting, and P. Sprangle. "Electron Injection into Plasma Wakefields by Colliding Laser Pulses." In: *Physical Review Letters* 79.14 (1997), pp. 2682–2685. ISSN: 0031-9007. DOI: 10.1103/PhysRevLett.79.2682.

[171] J. Faure et al. "Controlled injection and acceleration of electrons in plasma wakefields by colliding laser pulses." In: *Nature* 444.7120 (2006), pp. 737–739. ISSN: 14764687. DOI: 10.1038/nature05393.

[172] F. Li et al. "Generating high-brightness electron beams via ionization injection by transverse colliding lasers in a plasma-Wakefield accelerator." In: *Physical Review Letters* 111.1 (2013), pp. 1–5. ISSN: 00319007. DOI: 10.1103/PhysRevLett.111.015003.

[173] X. Yan et al. "Subpicosecond electro-optic measurement of relativistic electron pulses." In: *Physical Review Letters* 85.16 (2000), pp. 3404–3407. ISSN: 00319007. DOI: 10.1103/PhysRevLett.85.3404.

[174] A. L. Cavalieri et al. "Clocking femtosecond x rays." In: *Physical Review Special Topics - Accelerators and Beams* 8.March (2005), pp. 1–4. ISSN: 10984402. DOI: 10.1103/PhysRevLett.94.114801.

[175] Paul Scherkl et al. "Plasma-photonic spatiotemporal synchronization of relativistic electron and laser beams." In: (Aug. 2019). arXiv: 1908.09263.

[176] C. G. Durfee, J. Lynch, and H. M. Milchberg. "Development of a plasma waveguide for high-intensity laser pulses." In: *Physical Review E* 51.3 (1995), pp. 2368–2389. ISSN: 1063651X. DOI: 10.1103/PhysRevE.51.2368.

[177] Eric Esarey, Phillip Sprangle, Jonathan Krall, and Antonio Ting. "Overview of plasma-based accelerator concepts." In: *IEEE Transactions on Plasma Science* 24.2 (1996), pp. 252–288. ISSN: 00933813. DOI: `10.1109/27.509991`.

[178] W. P. Leemans et al. "Laser-driven plasma-based accelerators: Wakefield excitation, channel guiding, and laser triggered particle injection." In: *Physics of Plasmas* 5.5 (1998), p. 1615. ISSN: 1070664X. DOI: `10.1063/1.872820`.

[179] C. L. Chen, C. C. Leiby, and L. Goldstein. "Electron temperature dependence of the recombination coefficient in pure helium." In: *Physical Review* 121.5 (1961), pp. 1391–1400. ISSN: 0031899X. DOI: `10.1103/PhysRev.121.1391`.

[180] A. E. Martirosyan et al. "Time evolution of plasma afterglow produced by femtosecond laser pulses." In: *Journal of Applied Physics* 96.10 (2004), pp. 5450–5455. ISSN: 00218979. DOI: `10.1063/1.1803920`.

[181] M. Moisan, A. Shivarova, and A. W. Trivelpiece. "Experimental investigations of the propagation of surface waves along a plasma column." In: *Plasma Physics* 24.11 (1982), pp. 1331–1400. ISSN: 00321028. DOI: `10.1088/0032-1028/24/11/001`.

[182] Andrey Elizarov and Vladimir Litvinenko. "Dynamics of shielding of a moving charged particle in a confined electron plasma." In: *Physical Review Special Topics - Accelerators and Beams* 18.4 (2015), pp. 1–20. ISSN: 10984402. DOI: `10.1103/PhysRevSTAB.18.044001`.

[183] Yunfeng Xi. "Ionization injection plasma wakefield acceleration." PhD thesis. University of California Los Angeles, 2016.

[184] Oliver S. Karger. "Pathways towards Ultra-high brightness electron beams." PhD thesis. University of Hamburg, 2019.

[185] R. L. Kelly. "Atomic and Ionic Spectrum Lines below 2000 Angstroms: Hydrogen through Krypton." In: *Journal of Physical and Chemical Reference Data* 16 (1987), Supplement 1.

[186] R Tarkeshian et al. "Transverse Space-Charge Field-Induced Plasma Dynamics for Ultraintense Electron-Beam Characterization." In: *Physical Review X* 8.2 (2018), p. 21039. ISSN: 2160-3308. DOI: `10.1103/PhysRevX.8.021039`.

[187] Aihua Deng et al. "Generation and acceleration of electron bunches from a plasma photocathode." In: *Nature Physics* (Nov. 2019). DOI: `10.1038/s41567-019-0610-9`.

[188] Bernhard Hidding et al. “First Measurements of Trojan Horse Injection in a Plasma Wakefield Accelerator.” In: *Proceedings of IPAC2017* TUYB1 (2017).

[189] N. Vafaei-Najafabadi et al. “Beam loading by distributed injection of electrons in a plasma wakefield accelerator.” In: *Physical Review Letters* 112.2 (2014), pp. 1–5. ISSN: 00319007. DOI: 10.1103/PhysRevLett.112.025001.

[190] Spencer Gessner et al. “Demonstration of a positron beam-driven hollow channel plasma wakefield accelerator.” In: *Nature Communications* 7 (2016), p. 11785. ISSN: 2041-1723. DOI: 10.1038/ncomms11785.

[191] S Z Green et al. “Laser ionized preformed plasma at FACET.” In: *Plasma Physics and Controlled Fusion* 56.8 (2014), p. 084011. ISSN: 0741-3335. DOI: 10.1088/0741-3335/56/8/084011.

[192] N Davidson, A A Friesem, and E Hasman. “Holographic axilens: high resolution and long focal depth.” In: *Optics letters* 16.7 (1991), pp. 523–5. ISSN: 0146-9592. DOI: 10.1364/OL.16.000523.

[193] E Adli et al. “Long-range attraction of an ultrarelativistic electron beam by a column of neutral plasma.” In: *New Journal of Physics* 18.10 (2016), p. 103013. ISSN: 1367-2630. DOI: 10.1088/1367-2630/18/10/103013.

[194] G. Wittig et al. “Optical plasma torch electron bunch generation in plasma wakefield accelerators.” In: *Physical Review Special Topics - Accelerators and Beams* 18.8 (2015), pp. 1–6. ISSN: 10984402. DOI: 10.1103/PhysRevSTAB.18.081304.

[195] Georg Wittig et al. “Electron beam manipulation, injection and acceleration in plasma wakefield accelerators by optically generated plasma density spikes.” In: *Nuclear Instruments and Methods in Physics Research Section A: Accelerators, Spectrometers, Detectors and Associated Equipment* (2016), pp. 1–5. ISSN: 01689002. DOI: 10.1016/j.nima.2016.02.027.

[196] Aleksandar Angelovski et al. “Evaluation of the cone-shaped pickup performance for low charge sub-10 fs arrival-time measurements at free electron laser facilities.” In: *Physical Review Special Topics - Accelerators and Beams* 18.012801 (2015), pp. 1–6. ISSN: 10984402. DOI: 10.1103/PhysRevSTAB.18.012801.

[197] N. Barov, J. B. Rosenzweig, M. E. Conde, W. Gai, and J. G. Power. “Observation of plasma wakefield acceleration in the underdense regime.” In: *Physical Review Special Topics - Accelerators and Beams* 3.1 (2000), pp. 1–10. DOI: 10.1103/physrevstab.3.011301.

[198] J. B. Rosenzweig et al. “Experimental observation of plasma wake-field acceleration.” In: *Physical Review Letters* 61.1 (1988), pp. 98–101. ISSN: 00319007. DOI: 10.1103/PhysRevLett.61.98.

[199] A. Oguchi et al. “Multiple self-injection in the acceleration of monoenergetic electrons by a laser wake field.” In: *Physics of Plasmas* 15.4 (2008). ISSN: 1070664X. DOI: 10.1063/1.2833593.

[200] S Y Kalmykov et al. “Controlled generation of comb-like electron beams in plasma channels for polychromatic inverse Thomson <i>γ</i> -ray sources.” In: *Plasma Physics and Controlled Fusion* 58.3 (2016), p. 034006. ISSN: 0741-3335. DOI: 10.1088/0741-3335/58/3/034006.

[201] M. Zeng et al. “Multichromatic narrow-energy-spread electron bunches from laser-Wakefield acceleration with dual-color lasers.” In: *Physical Review Letters* 114.8 (2015), pp. 1–5. ISSN: 10797114. DOI: 10.1103/PhysRevLett.114.084801. arXiv: 1406.7106.

[202] O. Lundh, C. Rechatin, J. Lim, V. Malka, and J. Faure. “Experimental measurements of electron-bunch trains in a laser-plasma accelerator.” In: *Physical Review Letters* 110.6 (2013), pp. 1–5. ISSN: 00319007. DOI: 10.1103/PhysRevLett.110.065005.

[203] N. Vafaei-Najafabadi et al. “Producing multi-coloured bunches through beam-induced ionization injection in plasma wakefield accelerator.” In: *Philosophical Transactions of the Royal Society A: Mathematical, Physical and Engineering Sciences* 377.2151 (2019). ISSN: 1364503X. DOI: 10.1098/rsta.2018.0184.

[204] B. Hidding et al. *Tunable Electron Multibunch Production in Plasma Wakefield Accelerators*. 2014. arXiv: 1403.1109.

[205] S M Wiggins et al. “High quality electron beams from a laser wakefield accelerator.” In: *Plasma Physics and Controlled Fusion* 52.12 (2010), p. 124032. ISSN: 0741-3335. DOI: 10.1088/0741-3335/52/12/124032.

[206] P. Emma et al. “Experimental demonstration of energy-chirp control in relativistic electron bunches using a corrugated pipe.” In: *Physical Review Letters* 112.3 (2014), pp. 1–5. ISSN: 00319007. DOI: 10.1103/PhysRevLett.112.034801.

[207] S. Antipov et al. “Experimental demonstration of energy-chirp compensation by a tunable dielectric-based structure.” In: *Physical Review Letters* 112.11 (2014), pp. 1–5. ISSN: 00319007. DOI: 10.1103/PhysRevLett.112.114801.

[208] Zhen Zhang et al. “Electron beam energy chirp control with a rectangular corrugated structure at the Linac Coherent Light Source.” In: *Physical Review Special Topics - Accelerators and Beams* 18.1 (2015), pp. 1–12. ISSN: 10984402. DOI: `10.1103/PhysRevSTAB.18.010702`.

[209] R. D’Arcy et al. “Tunable Plasma-Based Energy Dechirper.” In: *Physical Review Letters* 122.3 (2019), p. 34801. ISSN: 10797114. DOI: `10.1103/PhysRevLett.122.034801`.

[210] A. F. Habib. “PhD Thesis.” PhD thesis. University of Strathclyde, 2020.

[211] W. Lu et al. “A nonlinear theory for multidimensional relativistic plasma wave wakefields.” In: *Physics of Plasmas* 13.5 (2006). ISSN: 1070664X. DOI: `10.1063/1.2203364`.

[212] M. Tzoufras et al. “Beam loading by electrons in nonlinear plasma wakes.” In: *Physics of Plasmas* 16.5 (2009). ISSN: 1070664X. DOI: `10.1063/1.3118628`.